# Illuminating the Everblack: Dark Sector Searches with ATLAS

by

Tim Mathew

A dissertation accepted and approved in partial fulfillment of the
requirements for the degree of
Doctor of Philosophy
in Physics

Dissertation Committee:
David Strom, Chair
Stephanie Majewski, Advisor
Spencer Chang, Core Member
Scott Hansen, Institutional Representative

University of Oregon
Spring 2026

© 2026 Tim Mathew
This work, including text and images of this document but not including supplemental files (for example, not including software code and data), is licensed under a Creative Commons
**Attribution-NonCommercial-NoDerivs (United States) License.**



DISSERTATION ABSTRACT

Tim Mathew

Doctor of Philosophy in Physics

Title: Illuminating the Everblack: Dark Sector Searches with ATLAS

This dissertation presents two dark sector searches with the ATLAS experiment using proton-proton collision collected at the Large Hadron Collider (LHC), one with the full Run 2 dataset and one with the first 134.6 $\text{fb}^{-1}$ of Run 3 data. The first search is for dark mesons decaying into top and bottom quarks (*tttb* or *ttbb*), which is sensitive to a proposed Stealth Dark Matter scenario with a strongly coupled dark sector and a confining gauge group. This model contains a viable dark matter candidate in the form of a scalar baryon. The search targets both the all-hadronic and one-lepton final states of the top quark decays, with the one-lepton channel providing the strongest limits to date on this model. Dark pions with masses below 940 GeV are excluded for a ratio between the dark pion mass and the dark rho mass of 0.45, and masses below 740 GeV for a ratio of 0.25. The second search is for the exotic decay of the Higgs boson into a photon and a dark photon, which is motivated by several BSM models and provides an additional opportunity to probe a hypothetical dark sector. The analysis is optimized for the gluon-gluon fusion production channel, which has an order of magnitude larger cross-section than the vector boson fusion and associated production channels, and is made possible by the implementation of a new composite trigger that greatly increases the acceptance of gluon-gluon fusion events. The results of this search set the most stringent limits on the branching ratio of Higgs to a photon and dark photon to date, setting a combined upper limit on the branching ratio better

than 1%. The search for BSM physics in dark sectors will continue to be a major focus of the ATLAS physics program in the coming years, and the results of these searches will be used to guide future searches for dark matter at the LHC and beyond.

This dissertation includes previously published coauthored material.

CURRICULUM VITAE

NAME OF AUTHOR: Tim Mathew

GRADUATE AND UNDERGRADUATE SCHOOLS ATTENDED:

University of Oregon, Eugene, OR, USA
University of Washington, Seattle, WA, USA

DEGREES AWARDED:

Doctor of Philosophy, Physics, 2026, University of Oregon
Master of Science, Physics, 2023, University of Oregon
Bachelor of Science, Physics, 2019, University of Washington

AREAS OF SPECIAL INTEREST:

Beyond the Standard Model Physics
Machine Learning
Anomaly Detection

PROFESSIONAL EXPERIENCE:

Instructor, Pacific Learning Academy, 2019-2020
Owner, Empyrean, 2014-2017
Owner, Tim Mathew Painting, 2012-2017

GRANTS, AWARDS AND HONORS:

University of Oregon Lokey Dissertation Fellowship, 2026
US ATLAS ATC Award, 2024
Outstanding Leadership Award, UO Physics, 2024
Sigma Pi Sigma member, 2019–

PUBLICATIONS:

G. Othman and C. Wiseman and T. H. Burritt and J. A. Detwiler and M. P. Held and R. Henning and T. Mathew and D. Peterson and W. Pettus and G. Song and T. D. Van Wechel (2026). CAGE: An Internal Source Scanning Cryostat for HPGe Characterization. *arXiv*

ATLAS Collaboration (2024). Search for dark mesons decaying to top and bottom quarks in proton-proton collisions at $\sqrt{s} = 13$ TeV with the ATLAS detector, *JHEP* (pp. 5).

ACKNOWLEDGEMENTS

The path to completing this dissertation would not have been possible without the support and guidance of many friends, mentors, and family members. I am especially grateful to my advisor, Stephanie Majewski, for her guidance and support, and for pushing me to not give up when I easily could have. I would also like to thank my committee members Spencer Chang and David Strom for their valuable feedback and mentorship throughout this dissertation.

I am extremely grateful for the support, friendship, and guidance of the many friends and colleagues within ATLAS. I thank Jochen Heinrich for the research guidance, scotch recommendations, and Star Trek watch parties. I also thank Dani Koeck for the valuable discussions and allowing me to give her a hard time. Federica Piazza deserves thanks for guiding me through the complexities and challenges of the dark photon search, and bringing it to a timely and successful conclusion. I thank my mentors from BNL, Haider Abidi, Liza Brost, and Michael Begel, for believing in me and their invaluable advice.

From the University of Oregon, I am grateful to Claire Staley and Anne McGinley for their support. I also thank my graduate student colleagues for their friendship and support during classes. I thank my gaming squad for venting sessions and a much needed escape. To my closest friend, Michael Schmidt, thank you for your unwavering support and friendship, especially when times were challenging. To Gideon, my son, thank you for reminding me daily why I did this. Finally, I would like to thank my family for their love, sacrifice, and support.

To the creative geniuses who inspired me and we lost too soon,

Ryan

Chester

Chris

Mitch

Daniel

Neil

Diego

Justin

Kurt

Bo

Rest In Power.

TABLE OF CONTENTS

Chapter Page

I. INTRODUCTION . . . . . 31

II. THE STANDARD MODEL AND DARK SECTORS . . . . . 34

2.1. A Brief Overview of the Standard Model . . . . . 34

2.1.1. Electroweak Symmetry Breaking and the Higgs Mechanism . . 34

2.2. Evidence for Dark Matter and Beyond the Standard Model Physics . . . . . 37

2.2.1. Stealth Dark Matter and Dark Mesons . . . . . 39

2.2.2. The Dark Photon . . . . . 41

III. EXPERIMENTAL SETUP . . . . . 44

3.1. The Large Hadron Collider . . . . . 44

3.1.1. The Proton Acceleration Chain . . . . . 45

3.1.2. Proton-Proton Collisions and Luminosity . . . . . 48

3.2. The ATLAS Detector . . . . . 50

3.2.1. The ATLAS Coordinate System . . . . . 51

3.2.2. The Inner Detector . . . . . 53

3.2.3. The Calorimeter System . . . . . 55

3.2.3.1. Electromagnetic Calorimeters . . . . . 57

3.2.3.2. Hadronic Calorimeter . . . . . 59

3.2.3.3. Forward Calorimeter . . . . . 61

3.2.4. The Muon Spectrometer . . . . . 62

3.2.5. Magnet System . . . . . 64

3.2.6. Trigger and Data Acquisition (TDAQ) . . . . . 65

3.2.7. Changes for Run 3 . . . . . 67

Chapter Page

3.2.7.1. New Small Wheel . . . . . 68

3.2.7.2. Readout and TDAQ upgrades . . . . . 69

IV. HL-LHC AND ATLAS PHASE II UPGRADES . . . . . 73

4.0.1. ATLAS Global Trigger . . . . . 76

4.0.2. Topological Cell Clustering Algorithms . . . . . 77

4.0.2.1. ATLAS 420 and 422 algorithm . . . . . 78

4.0.2.2. 422 Scheme for the Global Trigger Topoclusters . . . 81

4.0.3. Unique Seed Cell Association Algorithm . . . . . 82

4.0.4. Physics Performance and Comparison . . . . . 85

4.0.4.1. Cluster Energies . . . . . 87

4.0.4.2. Cluster Multiplicity and Locations . . . . . 90

4.0.4.3. Cluster Missing Transverse Energy . . . . . 93

4.0.4.4. Reconstructed Jet Performance . . . . . 94

4.0.5. Trigger Performance . . . . . 95

4.0.5.1. Seed-Only Trigger Efficiencies . . . . . 97

4.0.6. Test Vectors . . . . . 100

4.0.7. Cell Neighbor and Translator Files . . . . . 102

4.0.7.1. Cells per Fiber . . . . . 102

4.1. Topological Cluster Algorithm Conclusions and Outlook . . . . . 107

V. A SEARCH FOR DARK MESONS DECAYING INTO TOP AND BOTTOM QUARKS . . . . . 109

5.1. Introduction . . . . . 109

5.2. ATLAS Detector . . . . . 114

5.3. Data and Simulated Event Samples . . . . . 116

5.3.1. Signal samples . . . . . 117

5.3.2. Background samples . . . . . 118

Chapter Page

5.3.2.1. $t\bar{t}$ background . . . 118

5.3.2.2. Other backgrounds . . . 121

5.4. Object and Event Selections . . . 123

5.5. Analysis Strategy . . . 129

5.5.1. All-hadronic channel . . . 129

5.5.2. One-lepton channel . . . 130

5.6. Background Estimate . . . 133

5.6.1. All-hadronic channel . . . 133

5.6.2. One-lepton channel . . . 137

5.7. Systematic Uncertainties . . . 138

5.7.1. Experimental uncertainties . . . 138

5.7.2. Modeling uncertainties in background simulations . . . 140

5.7.2.1. $t\bar{t}$ uncertainties . . . 140

5.7.2.2. $t\bar{t} + b\bar{b}$ uncertainties . . . 142

5.7.3. Data-driven background estimation uncertainties . . . 143

5.8. Statistical Analysis and Results . . . 143

5.8.1. All-hadronic channel . . . 144

5.8.2. One-lepton channel . . . 145

5.9. Interpretation . . . 148

5.10. Conclusion . . . 155

5.11. Multi-Lepton Channel Truth Study . . . 155

5.11.1. Signal Samples . . . 156

5.11.2. Signal Efficiencies . . . 158

5.11.3. Trigger Efficiencies . . . 158

5.11.4. Conclusions . . . 160

Chapter Page

5.12. Preselection yields for the all-hadronic channel . . . . . 161

5.13. Extended ABCD method for single bin SR estimate . . . . . 162

VI. A SEARCH FOR DARK PHOTONS FROM HIGGS DECAYS IN THE GLUON-GLUON FUSION PRODUCTION MODE . . . . . 168

6.1. Introduction . . . . . 168

6.2. Data and simulation . . . . . 170

6.3. Analysis trigger . . . . . 172

6.4. Event reconstruction . . . . . 175

6.5. Signature and backgrounds . . . . . 178

6.6. Event selection . . . . . 180

6.6.1. Baseline selection . . . . . 180

6.6.2. Signal Region . . . . . 181

6.7. Analysis strategy and background modelling . . . . . 186

6.7.1. Estimation of $e \rightsquigarrow \gamma$ . . . . . 187

6.7.2. Estimation of $j \rightsquigarrow \gamma$ . . . . . 189

6.8. Systematic uncertainties . . . . . 193

6.8.1. Experimental uncertainties . . . . . 194

6.8.2. Uncertainties on data-driven methods . . . . . 196

6.8.3. Theoretical uncertainties . . . . . 197

6.9. Statistical treatment and results . . . . . 197

6.9.1. Likelihood fitting . . . . . 197

6.9.2. TRExFitter Framework . . . . . 200

6.9.3. Walkthrough of the dark photon fit . . . . . 201

6.9.3.1. Control Regions . . . . . 202

6.9.3.2. Impact of the jets faking photons background . . . 203

Chapter Page

6.9.4. Simultaneous fit and results . . . 209

6.10. METNet Performance Studies . . . 214

6.11. Vertex Tagging Efficiency Studies . . . 219

6.11.1. Current vertex tagging performance and motivation . . . 220

6.11.2. Preliminary studies with a neural network classifier . . . 222

6.11.2.1. Neural network architecture and training . . . 222

6.11.2.2. Preliminary results and performance evaluation . . . 224

6.11.3. Future work and conclusions . . . 227

VII. CONCLUSION . . . 229

APPENDICES

A. SHELL COUNT STUDIES FOR THE USCA ALGORITHM . . . 233

A.1. Jet $p_T$ 2-D and Ratio Plots . . . 234

B. DARK MESON MC SAMPLES . . . 239

B.1. List of MC samples . . . 239

B.1.1. Signal samples . . . 239

C. N-DIMENSIONAL ABCD METHOD FOR THE DARK MESON SEARCH . . . 241

C.1. The extended ABCD method . . . 241

D. DARK PHOTON MC SAMPLES . . . 246

REFERENCES CITED . . . 249

LIST OF FIGURES


Figure Page

1. The Standard Model particles Dominguez (2015). The three generations of fermions are shown at left, the Higgs boson at the center, and the gauge bosons at right. . . . . 35

2. The observed rotation curve of galaxy M33 compared to the expected rotation curve from visible matter Corbelli and Salucci (2000) (left) and the Bullet Cluster showing the separation of dark matter and baryonic matter through gravitational lensing Massey, Kitching, and Richard (2010) (right). . . . 38

3. Dark meson production at leading order. The dominant production mechanism through kinetic mixing is shown on the left and middle, while Drell-Yan pair production is shown on the right. . . . . 41

4. Feynman diagrams that contribute to the $H_{\gamma\gamma_D}$ coupling at one loop level. The dark photon is denoted by $\gamma_D$, the Higgs boson by $H$, and the messenger fields by $S$. . . . . 43

5. CERN accelerator complexVanden Broeck (2019). The four main experiments are located at the interaction points highlighted in yellow. As of Run 3, the proton acceleration chain begins at LINAC4 highlighted in purple. . . . . 45

6. LHC dipole magnet schematic AC Team (1999) . . . . . 47

7. Average interactions per bunch crossing (pileup) recorded by the ATLAS detector during Runs 1 and 2, and the ongoing Run 3 data-taking periods ATLAS Collaboration (2025). . . . . 50

8. LHC and HL-LHC operation timeline CERN (2017), with integrated luminosities in blue along the bottom. . . . . 51

9. Schematic diagram of the Run 2 ATLAS detector and its sub-systems ATLAS Collaboration (2008). . . . . 52

10. Diagram of the ATLAS Inner Detector and its three subsystems ATLAS Collaboration (2008). . . . . 54

Figure Page

11. Diagram of the ATLAS calorimeter system labeled by subsystem ATLAS Collaboration (2008). . . . . 56

12. Accordion geometry of the ATLAS electromagnetic calorimeter with readout schematic (left) ATLAS Collaboration (2013). EM barrel layout with cells showing coverage in $\eta$ and $\phi$ (right) ATLAS Collaboration (1996a). . . . . 57

13. Pulse shape of LAr calorimeter signal to mitigate out-of-time pileup ATLAS Collaboration (2013a). . . . . 59

14. Tile calorimeter wedge module showing the scintillating tiles, steel absorber plates, and PMTs ATLAS Collaboration (2017d). . . . 60

15. Diagram of the ATLAS hadronic end cap calorimeter along with the EMEC and FCAL ATLAS Collaboration (1996a). . . . . 61

16. Schematic of the ATLAS Forward Calorimeter matrix structure ATLAS Collaboration (1996a). . . . . 62

17. Diagram of the ATLAS Muon Spectrometer chambers ATLAS Collaboration (2008). . . . . 63

18. Diagram of the ATLAS barrel solenoid and barrel and endcap toroidal magnets ATLAS Collaboration (2008). . . . . 64

19. Schematic of the ATLAS Trigger and Data Acquisition system showing the L1 trigger, HLT, and dataflow between systems and to permanent storage The ATLAS Collaboration (2016). . . . . 66

20. Schematic of the ATLAS detector in the Run 3 configuration, with the New Small Wheel highlightedATLAS Collaboration (2024a). . . . . 68

21. Diagram of the NSWs, including the support structure. ATLAS Collaboration (2013b). . . . . 69

22. Block diagram of the LAr Run 3 readout architecture, read upwards through the front end crates to the off-detector electronics ATLAS Collaboration (2024a). . . . . 70

23. Schematic of the ATLAS Run 3 Trigger and Data Acquisition system ATLAS Collaboration (2024a). . . . . 71

Figure Page

24. Schematic of the ITk, with the inner pixel layers in green and outer strip layers in blue. ATLAS Collaboration (2024b). . . . . 73

25. Schematic of the Run 4 TDAQ system ATLAS Collaboration (2017c). Detector data flows to the legacy L0Calo and L0Muon systems, as well as full granularity calorimeter informatoin to the Global Trigger. The Global Trigger passes trigger objects to the CTP for the final trigger decision. Events are then passed to the Event Filter for more detailed processing and a final storage decision. . . . . 75

26. Illustration of TDAQ with emphasis on the Global Trigger System. ATLAS Collaboration (2017c). . . . . 77

27. Cell $E_T$ for a background (left) and signal (right) sample. . . . . 79

28. ATLAS LAr and Tile calorimeter system, where cells segmented in $\eta$ and $\phi$ are used for topoclustering (left). Clustered cells from the FCAL calorimeter for a simulated dijet event using the 420 scheme (right). A closeup of the segmentation of cells in the LAr EM Barrel (bottom). . . . . 80

29. Diagram of the USCA algorithm, in 2 dimensions for simplicity. $2\sigma$ cells are in green and $4\sigma$ in red. The central $4\sigma$ cell is the seed for the current cluster, and there are 3 shells of growth. The cluster for the top left $4\sigma$ cell is merged into current cluster. . . . . 83

30. A USCA cluster after 1,2, and 3 shells of growth. The cell volumes are scaled by their energy. Courtesy of Ryan Stuve. . . . . 84

31. Percent of cell overlap per event for background (left) and signal (right) samples. . . . . 84

32. A map of $2\sigma$ (left) and $4\sigma$ (right) cell locations in the first two LAr Calorimeter layers in $\eta$, $\phi$ space from an HH4b sample. . . . . 85

33. Global Trigger Performance framework. . . . . 86

34. Cluster $E_T$ for background JZ0 (left) and HH $\rightarrow$ 4b (right). . . . . 88

35. The leading 50 clusters in $E_T$ for background JZ0 (top left) and HH $\rightarrow$ 4b (top right). Total $E_T$ distributions for background JZ0 (bottom left) and HH $\rightarrow$ 4b (bottom right) . . . . . 89

36. Cluster $\eta$ for background JZ0 (left) and HH $\rightarrow$ 4b (right). . . . . 91

Figure Page

37. Cluster locations for the 50 leading $E_T$ clusters for background JZ0 (left) and HH $\rightarrow$ 4b (right). . . . . 91

38. Cluster multiplicity for background JZ0 (left) and HH $\rightarrow$ 4b (right). . . 92

39. Number of cells per cluster for background JZ0 (left) and HH $\rightarrow$ 4b (right). . . . . 92

40. Cluster MET for background JZ0 (top) and HH $\rightarrow$ 4b (bottom) split into x and y components. . . . . 94

41. Jet $p_T$ for background JZ0 (left) and HH $\rightarrow$ 4b (right). . . . . 95

42. Jet $\eta$ for background JZ0 (left) and HH $\rightarrow$ 4b (right). . . . . 95

43. Fixed-threshold jet trigger efficiencies. The x-axis is the offline reconstructed jet $p_T$ from 420 clusters. . . . . 97

44. Rate plots using the JZ0 sample for single and multijets with a target rate of 60 kHz highlighted. . . . . 98

45. Fixed rate jet trigger turn on curves. A rate of 60 kHz was chosen for all single and multijet triggers. . . . . 98

46. Seed-only rate plots using the JZ0 sample for single and multijets with a target rate of 60 kHz highlighted. . . . . 99

47. Seed-only fixed rate jet trigger turn on curves. A rate of 60 kHz was chosen for all single and multijet triggers. . . . . 100

48. Example of `coe` test vector file with cell $E_T$ converted to 10 bit binary strings (left). Comparison of cell $E_T$ directly from the GTP output `root` file to cell $E_T$ from the test vector file (right). . . . . 101

49. Example of `coe` file with list of 2 shells of neighbors for every potential seed cell within $|\eta| < 3.2$ (top). Visualization of a specific seed cell and 1 shell of neighbors (bottom left) and 2 shells of neighbors (bottom right). . . . . 103

50. The lookup table `coe` file with online, offline, and GEP cell IDs. . . . . 104

51. Number of $2\sigma$ (top left) and $4\sigma$ (top right) cells per LASP fiber for the JZ0 sample. A leading 420 jet $p_T$ cut at 50 GeV is applied for the bottom plots. . . . . 105

Figure Page

52. Number of $2\sigma$ (top left) and $4\sigma$ (top right) cells per LASP fiber for the HH $\rightarrow$ 4b sample. A leading 420 jet $p_T$ cut at 50 GeV is applied for the bottom plots. . . . . 106

53. Examples of leading Feynman diagrams of dark pion pair production. The diagram in a shows resonant production via kinetic mixing with the $W$-field resulting in either a neutral or charged dark rho meson, a mixing with the $B$-field that can only result in a neutral dark rho meson is also possible, b shows Drell–Yan-type pair production of dark pions, and c shows an illustrative diagram of the dark pion decay into a top and a bottom quark for dark pion production. . . . . 111

54. Pair-production cross-sections for dark pions as a function of dark pion mass for four different values of $\eta_{\mathrm{D}}$ in a an $\mathrm{SU}(2)_{\mathrm{L}}$ model and b an $\mathrm{SU}(2)_{\mathrm{R}}$ model. The dashed colored lines indicate the contribution of the resonant production mode to the total dark pion production cross-section. . . . . 113

55. Branching fractions of the available decays of dark pions from gaugephobic $\mathrm{SU}(2)_{\mathrm{L}}$ and $\mathrm{SU}(2)_{\mathrm{R}}$ models are shown for a neutral dark pions and b positively charged dark pions. Channels with small branching fractions are suppressed for clarity. . . . 113

56. Mass of the a leading and b sub-leading large-$R$ jet for all simulated backgrounds overlaid with three example distributions for various signal points after preselection in the all-hadronic channel. Also shown is a simplified data-driven estimate of the multijet background which was created by taking the event yields for data and subtracting all simulated backgrounds from it. Statistical uncertainties stemming from MC are indicated by the shaded region. The SR is to the right of the vertical line in both the subfigures. Individual SR bins select sub-regions of leading and sub-leading large-$R$ jet mass for improved background discrimination. The last bin contains the overflow. . . . . 131

Figure Page

57. Normalized distributions of a $\Delta R(\ell, b_2)$ and b $m_{bb,\min\Delta R}$ for all simulated backgrounds with two example signal distributions overlaid after the one-lepton channel preselection. Statistical uncertainties stemming from MC are indicated by a shaded region, but are not visible on the scale of the $y$-axis. The vertical dashed lines indicate the selection requirements applied to events in the SR, CR and VR, as indicated by the labels. . . . . 132

58. Normalized distributions of $m_{\mathrm{J}^{\mathrm{had}}} + m_{\mathrm{J}^{\mathrm{lep}}}$ for all simulated backgrounds overlaid with two example distributions for various signal points after the one-lepton channel preselection. Statistical uncertainties stemming from MC are indicated by a shaded region, but are not visible on the scale of the $y$-axis. . . . . 133

59. Region labels for the 16 regions used in the data-driven multijet estimate in the all-hadronic channel. Region $S$ labels the SR, regions $B$, $C$, $E$ and $I$ are used for the ABCD extrapolation, regions $D$, $F$, $G$, $H$, $J$ and $O$ are used to compute correlation correction factors, and regions $K$, $L$, $M$ and $N$ are validation regions. The background estimate is performed independently for all nine SR bins. . . . . 134

60. The four all-hadronic channel validation regions $K$, $L$, $M$ and $N$ from Figure 59 for each of the nine SR mass bins with the following naming convention: the leading large-$R$ jet lower mass boundary in GeV is followed by the sub-leading large-$R$ jet lower mass boundary. The shaded region indicates the uncertainty on the background estimate in each bin that includes the statistical uncertainties from the limited sample sizes in data and simulation as well as a multijet non-closure systematic uncertainty, as detailed in Section 5.7. . . . . 137

Figure Page

61. Comparison of the events yields in data and the background prediction after the fit under the background-only hypothesis in all bins of the all-hadronic SR. The dashed line is stacked onto the SM background and shows an example $SU(2)_L$ signal with $\eta_D = 0.25$ and $m_{\pi_D} = 500$ GeV. The uncertainty bands contain all statistical and systematic uncertainties. The horizontal axis labels reflect the different SR bins, with the first number indicating the lower boundary of the leading large-$R$ jet mass bin and the second number the lower boundary of the sub-leading large-$R$ jet mass bin. . . . . 145

62. Comparison of the events yields in data and the background prediction in the SRs, CRs, and VRs in the one-lepton channel, after the fit to data in all CRs and SRs under the background-only hypothesis. The uncertainty bands contain all statistical and systematic uncertainties. Two example $SU(2)_L$ signal points are overlaid in the SRs. . . . . 146

63. Distributions of $m_{\mathbb{J}^{had}} + m_{\mathbb{J}^{lep}}$ in a SR_5j3b, b SR_5j4b, c SR_6j3b, d SR_6j4b, e SR_7j3b, and f SR_7j4b, after the fit to data in all CRs and SRs under the background-only hypothesis. Two example $SU(2)_L$ signal point with $\eta_D = 0.25$ and $m_{\pi_D} = 400$ GeV is stacked on top of the background. The uncertainty bands contain all statistical and systematic uncertainties. The dashed line in the ratio panel shows the ratio of signal plus background event yields over just background event yields. . . . . 147

64. Observed (solid line) and expected (dashed line) limits on the dark pion production cross-section as a function of dark pion mass using the $CL_S$ method for all $SU(2)_L$ models in four slices of $\eta_D$: a $\eta_D$=0.45, b $\eta_D$=0.35, c $\eta_D$=0.25, and d $\eta_D$=0.15. The surrounding shaded bands correspond to one and two standard deviations around the expected limit. The overlaid theory line shows the theoretical dark pion cross-section prediction Kribs, Martin, Ostdiek, and Tong (2019). . . . . 150

Figure Page

65. Observed (solid line) and expected (dashed line) exclusion contours at 95% CL in the $\eta_D$–$m_{\pi_D}$ plane for $SU(2)_L$ signal models in the a all-hadronic and b one-lepton channel. Masses that are within the contours are excluded, as indicated by the hatched area. An uncertainty band corresponding to the $\pm 1\sigma$ variation on the expected limit is also indicated. The shaded area in a and the innermost shaded area in b indicates the phase space previously excluded through re-interpretation of other collider searches presented in Ref. Butterworth, Corpe, Kong, Kulkarni, and Thomas (2022). The outermost shaded area in b indicates the phase space excluded by the analysis in the all-hadronic channel and is identical to the observed limit shown in a. . . . . 151

66. Most relevant final states for pair-produced dark pions from a gaugephobic $SU(2)_L$ models and b gaugephobic $SU(2)_R$ models. . . . . 156

67. Branching fractions of the most relevant decay channels over the full dark pion mass range for neutral dark pions in a and for positively charged dark pions in b. Not all possible decay channels are drawn and channels with small branching fractions are suppressed for clarity. About one third of dark pions in the $SU(2)_L$ models are neutral, resulting in the *tttb* event signature being twice as likely as the *ttbb* signature. For $SU(2)_R$ models only the *ttbb* final state appears. . . . . 156

68. Multi-lepton channel signal efficiencies for $SU(2)_L$ (left) and $SU(2)_R$ (right) out of 10,000 events. The blue gridpoints are the expected efficiencies for comparison. . . . . 159

69. Absolute multi-lepton trigger efficiencies as a function of the dark pion mass and $\eta$ out of 10,000 events. $SU(2)_L$ is plotted on the left and $SU(2)_R$ on the right. . . . . 159

70. Weighted exclusive multi-lepton trigger events for the full $SU(2)_L$ (left) $SU(2)_R$ (right) gridpoints. . . . . 160

Figure Page

71. All-hadronic preselection yield and efficiency for SU2L signal points. The signal region has been optimized for $\eta = 0.25$ and $m_{\pi_D} = 500$ GeV. SU2R is not targeted in the all hadronic channel due to the low cross section at large $\pi_D$ and $\rho_D$ masses in this model. Note that these plots were created with the old luminosity tag corresponding to 139 fb$^{-1}$, however we expect differences with the new luminosity tag at 140 fb$^{-1}$ to be small. . . . . 166

72. Regions used for ABCD method. . . . . 167

73. Data - MC and QCD estimates for VR ABCD regions. The ABCD estimate shown is 2D, 3D or 4D depending on region. . . . . 167

74. Feynman diagrams illustrating the Higgs boson production via gluon-gluon fusion process (a), vector-boson fusion (b), and Higgsstrahlung (c), all followed by the decay into a photon and a dark photon ($H \to \gamma\gamma_D$). The hatched circle in the $H\gamma\gamma_D$ vertex represents the interaction through messenger fields. . . . . 169

75. Trigger efficiency curves as function of $m_T$ (a), $p_T^\gamma$ (b), and $p_T^{\text{miss}}$ (c), for data, MC simulation of the dominant background $W\gamma$ and total background. The *baseline* selections are applied together with the selection $\Delta\phi(E_T^{\text{miss}}, E_T^\gamma) > 1.25$. Events selected by single-muon baseline trigger, containing one photon and one muon treated as invisible in the evaluation of $p_T^{\text{miss}}$ and $m_T$, are used. . . . . 174

76. Fraction of events with correct primary vertex (PV) for the $H \to \gamma\gamma_d$ signals and for different background processes, with different selections applied: baseline selection are shown in blue and green, signal region (SR) selections are shown in orange and red. No selection on the BDT$_{\text{vertex}}$ is applied for the blue and orange dots, while BDT$_{\text{vertex}} \geq 0.1$ is applied for the green and red ones. . . . . 181

Figure Page

77. Schematic overview of the signal (SR), control (CR), validation (VR) and probe (PR) regions used in the analysis. Different colours correspond to different final states: events with one isolated photons are selected in the SR (continuous lines), CRs (dashed lines) and VRs (dotted lines), while events with single electron or non isolated photon are used for the corresponding PRs. Data in the PRs are scaled by the fake factors indicated by the blue and green arrows ($f_{e\gamma}$ and $f_{j\gamma}$) to estimate the $j \rightsquigarrow \gamma$ and $e \rightsquigarrow \gamma$ contribution in each analysis region. . . . . 185

78. Invariant mass for reconstructed $\gamma e$ and $\gamma\mu$ pairs from data, the latter being rescaled such to match its sidebands to those of the former. The vertical dashed lines limit the window used to compute $f_{e\gamma}$, while the vertical dotted lines mark the sidebands used for the renormalization of the $\gamma\mu$ distribution. . 188

79. Comparison between data and pre-fit background estimates in the low $m_T$ VR. The uncertainty includes both statistical and systematic contributions from the $e \rightsquigarrow \gamma$ and $j \rightsquigarrow \gamma$ data-driven methods. . . . . 190

80. Isolation distributions for reconstruted photons, used for the $j \rightsquigarrow \gamma$ background estimate. The figure displays the distribution from the $\texttt{Loose}'$ photon sample (enriched of $j \rightsquigarrow \gamma$), and an example of extrapolated distribution for the $\texttt{Tight}$ sample ($\texttt{Loose}'(\rightarrow \texttt{Loose}''_a) \rightarrow \texttt{Tight}$), using a $\texttt{Loose}''_a$ sample to compute $R_m$ and $R_w$. The two dashed vertical lines mark the "isolated" ($\Upsilon < 0.022$) and the "non-isolated" ($\Upsilon > 0.1$) regions. The figure also shows the observed and extrapolated distributions for a different $\texttt{Loose}''_b$ sample. . . . . 192

81. Comparison between data and pre-fit background estimates in the low $\mathcal{S}_{p_T^{\text{miss}}}$ CR (a) and the low $\Delta\phi$ VR (b), enriched of $j \rightsquigarrow \gamma$. The uncertainty includes both statistical and systematic contributions from the $e \rightsquigarrow \gamma$ and $j \rightsquigarrow \gamma$ data-driven methods. . . . . 193

82. Prefit distribution of the transverse mass $m_T$ in the signal region, with Asimov sample. . . . . 202

83. Prefit distributions of the transverse mass $m_T$ in the control regions. . . 204

Figure Page

84. Ranking of the nuisance parameters in the fit, showing the impact of each nuisance parameter on the signal strength $\mu$ (left). Correlation matrix of the fit parameters (right). Both plots are with the low $E_{\mathrm{T}}^{\mathrm{miss}}$ significance validation region included in the fit. . . . . 205

85. Prefit (left) and postfit (right) distributions of the transverse mass $m_T$ in the low $E_{\mathrm{T}}^{\mathrm{miss}}$ significance validation region. The fit confirms that the low $E_{\mathrm{T}}^{\mathrm{miss}}$ significance region is stable, and can be safely used to constrain the jets faking photons background. . . . . 206

86. Postfit distributions of the transverse mass $m_T$ in the low $E_{\mathrm{T}}^{\mathrm{miss}}$ significance control region with data (left) and Asimov samples (right). The background expectations are stable with all configurations of the fit, and the data is well modeled. . . . . 207

87. Ranking of the nuisance parameters in the fit after including the low $E_{\mathrm{T}}^{\mathrm{miss}}$ significance control region, showing the impact of each nuisance parameter on the signal strength $\mu$ (right). Correlation matrix of the fit parameters, showing the correlations between the signal strength $\mu$ and the normalization factors of the backgrounds (left). Both plots are with the low $E_{\mathrm{T}}^{\mathrm{miss}}$ significance control region included in the fit. . . . . 208

88. Normalization factor pulls of the $W\gamma$ and $Z\gamma$ backgrounds with the low $E_{\mathrm{T}}^{\mathrm{miss}}$ significance control region included in the fit (left) and without it (right). The normalization factors are consistent between the two fits, showing that the inclusion of the low $E_{\mathrm{T}}^{\mathrm{miss}}$ significance control region does not bias the fit results. . . . . 208

89. Distribution of $m_T$ for data and for the expected SM background after the background-only fit, in the SR (a) and CRs (b), (c), and (d). The $H \to \gamma\gamma_d$ signal with $\mathrm{BR}_{\gamma\gamma_d} = 1\%$ is shown as a dashed red line, including the ggF, VBF, WH and ZH channels. The pre-fit prediction is overlaid as a dashed blue line. The uncertainties include both the statistical and the systematic component determined by the multiple-bin fit. The lower panel shows the ratio of data to expected background event yields post-fit (black dots) and pre-fit (dashed blue line). . . . . 211

Figure Page

90. Observed data and post-fit background yields in the SR, CRs, and VRs after the background-only fit. The expected signal yields are overlaid assuming $\mathrm{BR}_{\gamma\gamma_d} = 10\%$ for visualisation purposes. The lower panel shows the signal contamination, defined as $1 + S/B$, where $S$ denotes the signal yield with $\mathrm{BR}_{\gamma\gamma_d} = 1\%$ and $B$ the total background yield. . . . . 212

91. Summary of the 95% CL upper limits on $\mathrm{BR}_{\gamma\gamma_d}$, achieved by the Run-2 searches (top three rows: $ZH$ ATLAS Collaboration (2022d), VBF ATLAS Collaboration (2021e), and their combination ATLAS Collaboration (2024)) and by the present analysis (4th row). The overall Run2+Run3 combination is displayed in the bottom row. . . . . 213

92. $E_T^{\mathrm{miss}}$ distribution (a) for METNet (blue), the tight WP (red), and truth (green) for $Z \to \mu\mu$ + jets. The resolution (b) is shown for all events in solid blue rectangles (METNet) and red triangles (tight WP), and plus marks and asterisks for good and bad reconstructed vertices respectively. . . . 216

93. $E_T^{\mathrm{miss}}$ distributions for METNet (blue), the tight WP (red), and truth (green) for: (a) ggF $H \to \gamma\gamma_D$, (b) $\gamma$ + jets fragmentation, (c) $Z \to \mu\mu$ + jets, and (d) $Z \to \nu\nu + \gamma$. Analysis preselections applied. . . . . 217

94. Resolution as a function of $N_{\mathrm{PV}}$ for METNet (blue) and the tight WP (red) for: (a) ggF $H \to \gamma\gamma_D$, (b) $\gamma$ + jets fragmentation, (c) $Z \to \mu\mu$ + jets, and (d) $Z \to \nu\nu + \gamma$. Analysis preselections applied. . . . . 218

95. Diagram of a hard scatter jet and photon and a pile-up vertex with a jet, with the hard scatter vertex correctly identified as the primary vertex (left) and incorrectly identified as the pile-up vertex (right). The misidentification of the primary vertex leads to a significant miscalculation of the $E_{\mathrm{T}}^{\mathrm{miss}}$. . . . . 221

96. The reconstructed z position of the primary vertex plotted against the true z position of the hard-scatter vertex for signal events. The diagonal line represents perfect vertex tagging, while the gaussian distribution around the diagonal line represents misidentification. . . . . 221

97. Diagram of the linear fit performed using the z and R positions of the photon showers and the z positions of the three primary vertex candidates (left). Actual line of best fit example for a signal event (right). The star is the true vertex, and the $\chi^2$ value from this fit is used as an input to the neural network classifier. . . . . 223

98. Distribution of the photon pointing variable for correctly identified vertices and incorrectly identified vertices in the background slice. The photon pointing variable shows good separation between correctly identified vertices and incorrectly identified vertices, with correctly identified vertices having a more peaked distribution around zero, while incorrectly identified vertices have a broader distribution. . . . . 225

99. Predicted probabilities from the neural network classifier for candidates split into correctly identified vertices and incorrectly identified vertices, for both the training with preselections (bottom) and without preselections (top), and split by background (left) and signal (right). The classifier shows good separation between the true PV candidates and pile-up vertices, especially in the background slice. . . . . 226

100. Table of the vertex tagging efficiency for the standard vertex tagging method and the neural network classifier, for both the training with preselections and without preselections, and split by background and signal. The neural network classifier shows a significant improvement in vertex tagging efficiency compared to the standard method, especially in the background slice. . . . . 227

101. The $\Delta z$ between the reconstructed primary vertex and the true vertex for both the standard vertex tagging method (solid) and the neural network classifier (dashed) with preselections applied, and split by background (red) and signal (blue). The neural network classifier shows a significant improvement in the $\Delta z$ distribution, with a sharper peak around zero for correctly identified vertices, especially in the background slice. . . . . 228

102. Extrapolation search sensitivity for a dark meson signal point with a 600 GeV dark pion in Run 3 that was not excluded in the all-hadronic channel of Run 2 as a function of luminosity (top). A conservative 50% multijet systematic uncertainty is included. $H_T$ trigger efficiencies as a function of dark pion mass and mass ratio $m_{\pi_D}/m_{\rho_D}$ (bottom). . . . . 230

A.103 Cluster $E_T$ plots for a HH $\rightarrow$ 4b sample with 1-4 shells used during the algorithm growth stage. . . . . 234

A.104 Cluster multiplicities, $\eta$, and positions for a HH $\rightarrow$ 4b sample with 1-4 shells used during the algorithm growth stage. . . . . 235

A.105 Reconstructed jet $p_T$ for a HH $\rightarrow$ 4b sample with 1-4 shells used during the algorithm growth stage. . . . . 236

A.106 Fixed threshold trigger efficiency curves for leading and 3rd leading jets using a HH $\rightarrow$ 4b sample with 1-4 shells used during the algorithm growth stage. . . . . 236

A.107 2-D Comparisons between the leading 6 in $p_T$ reconstructed jets from USCA and 422 clusters for background (top) and HH $\rightarrow$ 4b (bottom). The plots are divided between 2-shell (left) and 3-shell (right) USCA jets. . . . . 237

A.108 Ratio of USCA jet $p_T$ over 422 jet $p_T$ as a function of 422 jet $p_T$. Background (top) and HH $\rightarrow$ 4b (bottom) samples are shown divided between 2-shell (left) and 3-shell (right) USCA jets. . . . . 238

A.109 Ratio of USCA jet $p_T$ over 420 jet $p_T$ as a function of 420 jet $p_T$ for a background sample. . . . . 238

C.1. 4D ABCD estimate region definitions. These labels have been chosen to agree with the notation used in ATLAS Collaboration (2016a). Tag definitions are described in the main body in table 6. . . . . 241

C.2. Regions used in a conventional 2D ABCD estimate. Figure taken from Kasieczka, Nachman, Schwartz, and Shih (2021). Discriminating variables are f and g in this plot. . . . . 242

LIST OF TABLES

Table Page

1. Gauge representations of the Standard Model fermion fields. The three fermion generations are not shown, as all generations have the same quantum numbers. . . . . 35

2. Physics simulated samples used for topocluster studies . . . . . 87

3. Binary encoding conversion to 10 bit strings. The first 2 bits represent the energy range, the other 8 bits are the index in that range. This format is subject to change as of March 2024. . . . . 101

4. Overview of the configuration of all nominal background samples used in the analysis; details and definitions are provided in the text. . . . . 118

5. Summary of the preselection criteria for the all-hadronic and one-lepton channels, in terms of the number of baseline and signal leptons, $R = 0.4$ and $R = 1.2$ jets, number of $b$-jets, and $H_{\mathrm{T}}$. The definitions of the physics objects for the two channels are given in the text. Signal leptons constitute a subset of the baseline leptons. . . . . 129

6. Summary of selection criteria for the SR ("Tag selection"). Nine bins are defined in the leading large-$R$ jet vs. sub-leading large-$R$ jet mass plane. The inverted selection ("Anti-tag selection") is also defined for use in the data-driven multijet extrapolation described in Section 5.6.1. . . . . 131

7. Observed and predicted event yields after the fit under the background-only hypothesis in all nine all-hadronic SR mass bins. The name of each column corresponds to the SR bins: the leading large-$R$ jet lower mass boundary in GeV is followed by the sub-leading large-$R$ jet lower mass boundary; the same convention is used in Figure 61. The quoted uncertainties contain statistical and systematic components. The total post-fit uncertainty can be smaller than the sum in quadrature of the different components due to correlations resulting from the fit to data. . . . . 152

Table Page

8. Observed and predicted event yields after the fit under the background-only hypothesis in the six SR bins in the one-lepton channel. The name of each column corresponds to the bins described in Section 5.5.2, identified with the number of jets followed by the number of $b$-jets. The quoted uncertainties contain statistical and systematic components. The total post-fit uncertainty can be smaller than the sum in quadrature of the different components due to correlations resulting from the fit to data. . . . . 153

9. Impact of different categories of systematic uncertainty in the one-lepton channel, for two signal benchmarks, relative to the total uncertainty on the fitted signal strength. For each category, the fit is repeated with the corresponding group of nuisance parameters fixed to their best-fit values and the impact for each category is evaluated as the quadrature difference between the signal strength uncertainty in the new fit and in the nominal one, divided by the uncertainty in the nominal fit. The contribution from the statistical uncertainty and the systematic one, further separated into the global instrumental and theoretical uncertainties, are shown. The total systematic uncertainty is different from the sum in quadrature of the different groups due to the correlations among the nuisance parameters in the fit. . . . . 154

10. Summary of the preselection cuts used in the all-hadronic channel. . . . 161

11. All-hadronic preselection yields for data and Monte Carlo samples. . . . 162

12. All-hadronic preselection cutflow for data and all considered simulated backgrounds at 140 $\text{fb}^{-1}$ integrated luminosity. . . . . 163

13. All-hadronic binned tag selections applied to each signal-region bin. . . . . 164

14. The configurations used for event generation of signal and background MC samples. The matrix element (ME) order refers to the order in the strong coupling constant of the perturbative calculation in the MC event generation. PDF refers to the parton density libraries used with the generator. The tune refers to the underlying-event tune of the parton shower model. . . . . 173

Table Page

15. Overview of the sequential overlap removal procedure applied to reconstructed objects and the corresponding matching criteria based on the $\Delta R$ separation and shared Inner Detector (ID) tracks. . . . . 178

16. Description of the input features of the vertex BDT, in order of importance. . . . . 182

17. Summary of the selections applied in the signal (SR) and control (CR) regions. In the CRs with muons, the $E_{\mathrm{T}}^{\mathrm{miss}}$ is recomputed treating muons as invisible particles. . . . . 184

18. Objects and data samples used for the $e \rightsquigarrow \gamma$ background. In the electron probe region (PR) an electron replaces the photon. . . . . 187

19. Impact of each category of uncertainty on the signal yields, as obtained through the covariance matrix decomposition method. . . . 194

20. Expected 95% CL limits on $\mathcal{B}(H \rightarrow \gamma\gamma_d)$ at $-2\sigma$, $-1\sigma$, median, $+1\sigma$, and $+2\sigma$, with and without the low $E_{\mathrm{T}}^{\mathrm{miss}}$ significance control region included in the fit. There is a roughly 10% improvement in the expected limits when the low $E_{\mathrm{T}}^{\mathrm{miss}}$ significance control region is included. . . . . 209

21. Data and background yields in the SR and CRs, after the background-only fit. Uncertainties include statistical and systematic components. . . . . 212

22. MC samples used for METNet studies. . . . . 215

23. Features used for training the neural network classifier to improve vertex tagging efficiency. . . . . 223

B.1. List of all used MC16a signal samples with associated TOPQ1 and TOPQ4 derivation tags, cross sections, number of produced events and equivalent integrated luminosity. . . . . 240

D.1. List of signal MCd samples used in this analysis. . . . . 246

D.2. List of $\gamma jets$ MC23d and MC23e samples used in this analysis. . . . . 247

D.3. List of $W\gamma/Z\gamma$ MC23d and MC23e samples used in this analysis . . . . 248

D.4. List of $W/Z$ MC23d and MC23e samples used in this analysis. . . . . 248

# CHAPTER I

# INTRODUCTION

Humanity is driven to understand the nature of the universe, leading to great efforts and achievements in theoretical and experimental physics. One of these great achievements, a combined effort of many across decades and through multiple experiments, is the formulation of a framework to describe the fundamental particles and their interactions. This framework is known as the Standard Model (SM) of particle physics. Complete in its ability to describe and predict the observed phenomena of the particles it contains, it remains the starting point for virtually every investigation in particle physics. Some of the most recent confirmations of the SM are the top quark observation at Fermilab in 1995 by the D0 and CDF experiments CDF Collaboration (1995); D0 Collaboration (1995) and the Higgs boson discovery at CERN in 2012 by the ATLAS and CMS experiments ATLAS Collaboration (2012a); CMS Collaboration (2012). Recent measurements of the W boson mass, which initially showed a significant deviation from the SM prediction, have also been updated with new measurements that are consistent with the SM ATLAS Collaboration (2024a); CDF Collaboration (2022), further confirming that the SM is able to withstand intense scrutiny.

Despite its successes, however, the Standard Model is known to be incomplete in regards to several observations. We know that over 85% of the matter in the observable universe is in the form of dark matter (DM), which does not have any observed interactions with the SM and thus must be explained with new physics. Additionally, at certain energy scales, the SM requires neutrinos to be massless, which is contradicted by neutrino oscillation observations. The extensions to the SM and discussion needed to explain neutrino masses are beyond the scope

of this thesis. The matter-antimatter asymmetry observed in the universe is also not fully explained by the SM, requiring some new mechanism to generate the observed abundance of matter. A strongly-coupled theory of quantum gravity is unable to be incorporated into the SM, and there is no explanation within the SM for dark energy at the scales observed in cosmology. These shortcomings and others motivate searches for physics beyond the Standard Model (BSM).

This thesis focuses on two specific BSM searches with the ATLAS detector at the Large Hadron Collider (LHC) at CERN. Motivated by two different approaches to explaining dark matter, the first search is for dark mesons decaying into top and bottom quarks Kribs, Martin, and Tong (2019b), and the second search is for dark photons from Higgs decays in the gluon-gluon fusion production mode Biswas, Gabrielli, and Mele (2022). Both models are explained in more detail in Chapter 2.2.2, along with an overview of the Standard Model and the motivation for BSM physics. The production cross sections for the these signals are $\sim 10^{13}$ times smaller than the total inelastic proton-proton cross section at the LHC, so these searches require sophisticated analysis techniques to separate the signal from the overwhelming background. Chapter III gives an overview of the experimental methods used in these searches, including a description of the ATLAS detector and how the LHC provides an unprecedented center of mass energy for proton-proton collisions. The LHC will enter a new phase of operation in the coming years, with the High-Luminosity LHC (HL-LHC) upgrade providing a significant increase in luminosity and the ATLAS Phase II upgrade improving the detector capabilities to handle the increased pile-up and radiation damage. Chapter IV gives an overview of the HL-LHC and ATLAS Phase II upgrades, and the impact they will have on the physics reach of the ATLAS experiment. The two

searches for dark mesons and dark photons are described in Chapters V and VI, respectively. My primary contributions to the dark meson search include a study of generated physics events in the multi-lepton channel, verifying preselection yields for the all-hadronic channel, verifying the 4-d ABCD method for the all-hadronic channel, and assisting in the development of the analysis and plotting frameworks for the one-lepton channel. As a main contributor to the dark photon search, I was heavily involved in the development and implementation of the fitting regions for the statistical analysis, validation of the background estimation methods and vertex BDT, optimization of the signal region, studies to improve the primary vertex selection, and studies of a new neural network method to reconstruct $E_{\mathrm{T}}^{\mathrm{miss}}$. Concluding remarks and future outlook are given in Chapter VII.

# CHAPTER II

# THE STANDARD MODEL AND DARK SECTORS

## 2.1 A Brief Overview of the Standard Model

The Standard Model is a quantum field theory (QFT) describing known particles and three of the four fundamental forces of nature, the strong, electromagentic (EM), and weak forces through fermion fields interacting via gauge boson fields. These fields are colloquially referred to as particles, with the fermions as the matter particles and the gauge bosons as the force carriers. Fermion field masses are generated through interactions with the Higgs field via the Higgs mechanism, and the broken electroweak symmetry gives mass to the weak gauge bosons as well. The fermions are spin 1/2 particles, the force carriers are spin 1 particles, and the Higgs boson is a spin 0 particle. Fermions are further classified as quarks and leptons, with quarks charged under both the strong and electroweak interactions, while leptons only interact via the electroweak interaction. All SM particles are visualized in Fig. 1.

As a gauge theory, the SM is invariant under the symmetry group $SU(3)_C \times SU(2)_L \times U(1)_Y$. $SU(3)_C$ describes the strong interaction with color charge $C$, and $SU(2)_L \times U(1)_Y$ describes the electroweak interaction with weak isospin $L$, since weak charge currents only interact with left-handed fermions, and hypercharge $Y$ acting on right and left-handed particles to give the observed electric charge of particles. Table 1 summarizes the gauge representations of the SM fermions under these symmetry groups.

### 2.1.1 Electroweak Symmetry Breaking and the Higgs Mechanism.

In the SM, the electroweak symmetry $SU(2)_L \times U(1)_Y$ is unbroken at high energies. The gauge fields associated with this symmetry are the $W^1$,

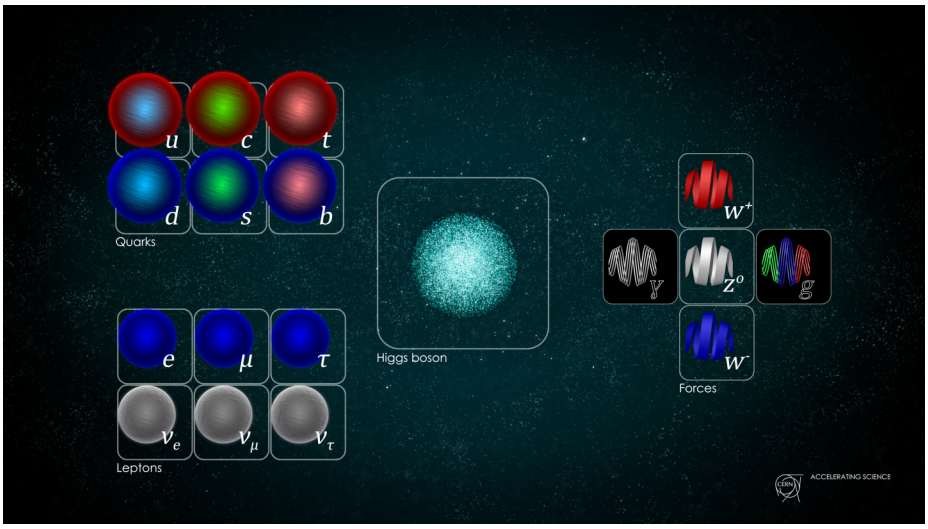


*Figure 1.* The Standard Model particles Dominguez (2015). The three generations of fermions are shown at left, the Higgs boson at the center, and the gauge bosons at right.

| Particle | $SU(3)_C$ | $SU(2)_L$ | $U(1)_Y$ |
|---|---|---|---|
| Left-handed quark doublet $Q_L$ | 3 | 2 | 1/6 |
| Right-handed up quark $u_R$ | 3 | 1 | 2/3 |
| Right-handed down quark $d_R$ | 3 | 1 | -1/3 |
| Left-handed lepton doublet $L_L$ | 1 | 2 | -1/2 |
| Right-handed electron $e_R$ | 1 | 1 | -1 |

Table 1. Gauge representations of the Standard Model fermion fields. The three fermion generations are not shown, as all generations have the same quantum numbers.

$W^2$, and $W^3$ bosons for $SU(2)_L$ and the $B$ boson for $U(1)_Y$. However, at low energies, the Higgs field spontaneously breaks this symmetry to the electromagnetic symmetry $U(1)_{EM}$, giving mass to the weak gauge bosons and fermions. This is accomplished through the introduction of a complex scalar doublet field $\phi$ into the SM

$$V(\phi) = \frac{1}{2}\mu^2\phi^\dagger\phi + \frac{1}{4}\lambda(\phi^\dagger\phi)^2, \tag{2.1}$$

which has stationary points at $\phi^\dagger\phi = 0, -\mu^2/\lambda$. For $\mu^2 < 0$ and $\lambda > 0$, the minimum at 0 is unstable. Even if the field is initially at 0, the field would evolve into the non-zero minima, spontaneously breaking the electroweak symmetry since all non-zero minima are degenerate. Choosing $v = \sqrt{-\mu^2/\lambda}$ as the vacuum expectation value (vev) of the Higgs field, we can write the Higgs field in unitary gauge as

$$\phi = \frac{1}{\sqrt{2}} \begin{pmatrix} 0 \\ v + H(x) \end{pmatrix}, \tag{2.2}$$

With $v \approx 246$ GeV and $H(x)$ the physical Higgs boson field. Plugging Eq. 2.2 into the SM Lagrangian gives mass terms for the weak gauge bosons and fermions, with the photon remaining massless, as well as a mass term for the Higgs boson itself. The $W^3$ boson mixes with the $B$ boson to give the physical $Z$ and $\gamma$ bosons, while the $W^1$ and $W^2$ bosons combine to form the $W^\pm$ bosons. The masses of the weak gauge bosons are given by

$$m_W = \frac{1}{2}vg, \quad m_Z = \frac{1}{2}v\sqrt{g^2 + g'^2}, \tag{2.3}$$

where $g$ and $g'$ are the $SU(2)_L$ and $U(1)_Y$ coupling constants, respectively. Fermion masses are generated through Yukawa interactions with the Higgs field, with the mass of a fermion $f$ given by

$$m_f = \frac{y_f v}{\sqrt{2}}, \tag{2.4}$$

where $y_f$ is the Yukawa coupling of the fermion to the Higgs field. With the Higgs field incorporated into the SM, tri and quartic self-interactions of the Higgs boson are also generated, with the Higgs boson mass given by

$$m_H = \sqrt{2\lambda} v. \tag{2.5}$$

The discovery of the Higgs boson at the LHC with a mass of approximately 125 GeV ATLAS Collaboration (2012a); CMS Collaboration (2012) confirms a viable candidate for the SM Higgs boson. However, there are still many properties of the Higgs and electroweak symmetry breaking that remain to be measured and understood, including the Higgs self-couplings and possible couplings to BSM particles.

## 2.2 Evidence for Dark Matter and Beyond the Standard Model Physics

As mentioned previously, there are several observations that the Standard Model is unable to explain, motivating searches for physics beyond the Standard Model. One of the most compelling pieces of evidence for BSM physics is the existence of dark matter. Astrophysical and cosmological observations provide strong evidence through the gravitational effects of dark matter on visible matter. This includes galaxy rotation curves Rubin, Ford, and Thonnard (1980), gravitational lensing Massey et al. (2010), and the cosmic microwave background (CMB) anisotropies Hu and Dodelson (2002). In particular, the rotation curve of galaxy M33, where the observed rotation curve does not match the expectation due

to visible matter, indicates the presence of additional unseen mass, attributed to dark matter. The observation of the Bullet Cluster, where galaxies have collided and the dark matter component has been observed through gravitational lensing and is separate from the baryonic matter, provides clear evidence for the existence of dark matter. Both examples can be seen in Fig. 2.

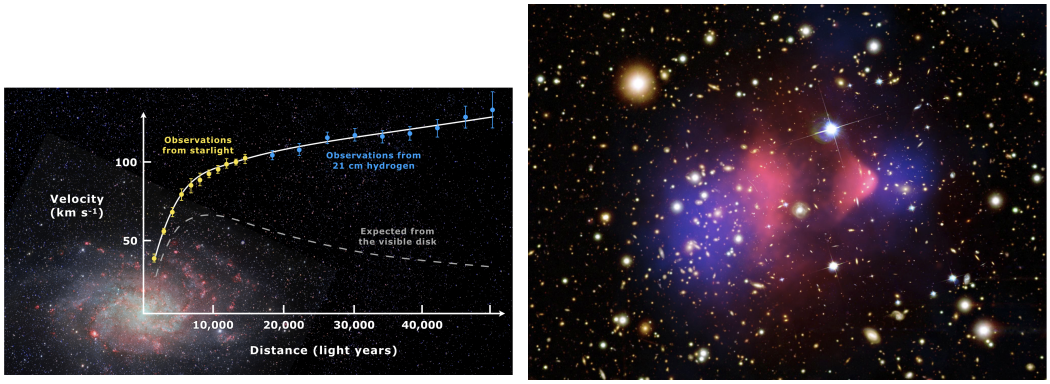


*Figure 2.* The observed rotation curve of galaxy M33 compared to the expected rotation curve from visible matter Corbelli and Salucci (2000) (left) and the Bullet Cluster showing the separation of dark matter and baryonic matter through gravitational lensing Massey et al. (2010) (right).

Current attempts to explain these observations through modifications to gravity have not been successful in explaining all observed phenomena, leading to the conclusion that dark matter is most likely composed of new, yet-undiscovered particles. In addition to observational evidence, large scale structure formation and simulations of galaxy formation also require the presence of dark matter to match observations Vogelsberger, Marinacci, Torrey, and Puchwein (2020). A universe without dark matter would not have the necessary gravitational potential wells to form galaxies and other large scale structures within the time scales of our universe, and the observed distribution of galaxies match simulations incorporating ΛCDM cosmology. While the evidence is strong, the exact physical nature of dark matter remains unknown as of now. Dark matter must meet several criteria from

current observational constraints, however, including being stable on cosmological timescales, non-baryonic, having weak or no interactions with electromagnetic radiation, and the correct relic abundance to account for the observed dark matter density in the universe. These criteria have led to many proposed candidates for dark matter particles, including weakly interacting massive particles (WIMPs), axions, and sterile neutrinos, among others. It is possible that dark matter might be contained within a dark sector, with its own particles and interactions, accessible to the Standard Model only through so-called portal interactions. The Higgs boson is a prime candidate for such a portal, given its unique properties, coupling to mass, and the current constraints on the Higgs to invisible branching ratio. In order to explore these possibilities experimentally, there must be some particle(s) that mediate the interactions between the dark sector and the Standard Model, and have an accessible mass scale for current experiments such as the LHC. This section will discuss two possible dark sector models that could be probed through Higgs portal interactions at the LHC: the dark meson sector of stealth dark matter and a dark photon model.

**2.2.1 Stealth Dark Matter and Dark Mesons.** Dark matter has eluded direct detection thus far, with increasingly stringent limits being placed on the interaction cross section of dark matter with Standard Model particles. This has led to the creation and exploration of models where the absence of an experimental signature so far is a natural consequence of the model itself. One such area of dark sector models is stealth dark matter Kribs and Neil (2016b), which posits a new confining non-Abelian gauge group, similar to quantum chromodynamics (QCD), with dark fermions that are charged under the dark gauge group and transform as vector-like representations of the SM electroweak group.

The specific dark meson model explored in this thesis is detailed in Ref. Kribs, Martin, and Tong (2019b). The dark matter candidate in this model is a composite baryonic scalar of an $SU(N)_D$ strongly interacting dark sector, with $N$ being even. The lightest baryonic scalar is stable due to an accidental $U(1)_{darkbaryon}$ symmetry of the dark sector, making it a viable dark matter candidate. The dark fermions also form mesonic bound states, called dark mesons, that could be accessible at the LHC. These dark mesons are previously unconstrained by existing searches due to the nature of BSM searches that typically require high MET or high mass resonances while the dark meson mass regime is lower.

This new dark sector contains at least one triplet of dark pions and dark rhos, $(\pi_D^{\pm}, \pi_D^0)$ and $(\rho_D^{\pm}, \rho_D^0)$, which are pseudoscalars and vectors respectively. Charged under the electroweak interaction and $SU(N)_D$, the dark fermions break the global chiral symmetry of the dark sector, leading to the decay of the dark pions and rhos to Standard Model particles through electroweak interactions. The dark meson model has a custodial Higgs symmetry with SU(2) dark flavor symmetry, which protects the electroweak $T$ parameter from large corrections. The Lagrangian is thus

$$\mathcal{L}_{darksector} = \mathcal{L}_{kinetic} + \mathcal{L}_{mass} + \mathcal{L}_{\pi_D,\rho_D} + \mathcal{L}_{kineticmixing} + \mathcal{L}_{decay}, \tag{2.6}$$

and includes kinetic terms, mass terms, dark meson interaction terms, kinetic mixing terms between the dark sector and SM gauge bosons, and decay terms for the dark mesons to SM particles.

Searches for dark mesons at the LHC can be parameterized by the dark pion mass $m_{\pi_D}$, along with the ratio of the dark pion mass to the dark rho mass,

$$\eta = \frac{m_{\pi_D}}{m_{\rho_D}} \tag{2.7}$$

If $\eta < 0.5$, the dark rho can decay to two dark pions with a branching fraction near 1, while if $\eta > 0.5$, the dark rho decays to pairs of SM fermions. The electroweak portal between the dark sector and SM is primarily through the kinetic mixing term,

$$\mathcal{L}_{kineticmixing} = \frac{\epsilon}{2}\rho^a_{D,\mu\nu}F^{a\mu\nu}. \tag{2.8}$$

Two mixing models are allowed, $\mathrm{SU}(2)_R$ and $\mathrm{SU}(2)_L$, with the former having the dark rho mix with the full SM $W$ boson triplet and the latter having the dark rho mix with the B field only. The $\mathrm{SU}(2)_L$ model has a significantly higher cross section, and is thus the focus of Chapter V. Fig. 3 shows the relevant Feynman diagrams for dark meson production at leading order, both through kinetic mixing and via Drell-Yan production. The resonant production via kinetic mixing is the dominant production mode, with the dark pions decaying to SM top and bottom quarks.

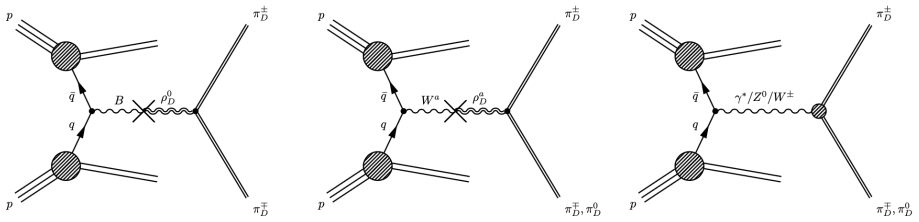


*Figure 3.* Dark meson production at leading order. The dominant production mechanism through kinetic mixing is shown on the left and middle, while Drell-Yan pair production is shown on the right.

**2.2.2 The Dark Photon.** Another extension to the Standard Model that has gained traction in recent years and allows access to a dark sector is

through the introduction of a new $U(1)_D$ gauge symmetry, with the associated gauge boson being the dark photon, $\gamma_D$. The dark photon can either be massless or massive, with the former being the focus of this thesis. For a massive dark photon, kinetic mixing between the dark photon and the SM hypercharge gauge boson $B$ is allowed. A massless dark photon cannot couple at tree level to any SM particles, and interacts via messenger fields of dimension higher than 4. The generic Lagrangion for the SM U(1) and the dark $U(1)_D$ is given by

$$\mathcal{L} = -\frac{1}{4}F_{\mu\nu}F^{\mu\nu} - \frac{1}{4}F'_{\mu\nu}F'^{\mu\nu} + \frac{\epsilon}{2}F_{\mu\nu}F'^{\mu\nu} + \frac{1}{2}m^2_{\gamma_D}A'_\mu A'^\mu + J^\mu_{EM}A_\mu + J^\mu_{dark}A'_\mu, \quad (2.9)$$

where $F_{\mu\nu}$ and $F'_{\mu\nu}$ are the field strength tensors for the SM photon and dark photon, respectively, $\epsilon$ is the kinetic mixing parameter, $m_{\gamma_D}$ is the mass of the dark photon, and $J^\mu_{EM}$ and $J^\mu_{dark}$ are the electromagnetic and dark currents, respectively. Assuming $m_{\gamma_D} = 0$, we can cancel the kinetic mixing term through a field redefinition, leaving the dark photon with no tree-level couplings to SM particles. This redifinition is done by defining new fields $A_\mu$ and $A'_\mu$ as follows:

$$\begin{pmatrix} A'^\mu \\ A^\mu \end{pmatrix} = \begin{pmatrix} \frac{1}{\sqrt{1-\epsilon^2}} & 0 \\ -\frac{\epsilon}{\sqrt{1-\epsilon^2}} & 1 \end{pmatrix} \begin{pmatrix} \cos\theta & -\sin\theta \\ \sin\theta & \cos\theta \end{pmatrix} \begin{pmatrix} \tilde{A}^\mu_d \\ \tilde{A}^\mu \end{pmatrix}, \quad (2.10)$$

where $\tilde{A}^\mu_d$ and $\tilde{A}^\mu$ are the new fields after the redefinition, and $\theta$ is a mixing angle that can diagonolize the kinetic terms. Since $\theta$ can take any arbitry angle without a dark photon mass term, interactions between the dark photon and SM particles only happen through higher order operators.

The dark photon model of interest in VI is a minimal model that assumes a generic messenger sector that allows for interactions between the dark photon and the SM through the afformentioned higher order operators Biswas et al. (2022). The doublet messenger fields, denoted by $S_i$, carry both SM and dark $U(1)_D$

charges, and generate an interaction between the dark photon and the SM at the one loop level. An interaction Lagrangian for this model can be written as

$$\mathcal{L}_{int} = \lambda_S S_0(\tilde{H}^\dagger S_L^U S_R^U + H^\dagger S_L^D S_R^D) + h.c. \tag{2.11}$$

where $\lambda$ is a universal coupling, the $S_0$ is a singlet scalar field with a vev, and $S_{L,R}^U$ and $S_{L,R}^D$ are the doublet up-type and down-type messenger fields, respectively. This vev is similar to the Higgs vev described in Section 2.1.1, and allows for the messenger fields to acquire mass and generate the necessary interactions between the dark photon and the SM. Once the scalar field $S_0$ acquires a vev, the messenger fields acquire mass and generate trilinear couplings between the dark photon and the SM Higgs boson at one loop level, $H\gamma\gamma_D$ and $H\gamma_D\gamma_D$, with couplings proportional to $\mu_S = \lambda_S < S_0 >$. After electroweak symmetry breaking, a mixing term between the left and right messenger fields is generated, proportional to $\mu_S\nu$ where $\nu$ is the Higgs vev. Feynman diagrams that contribute to the $H_{\gamma\gamma_D}$ coupling are shown in Fig. 4.

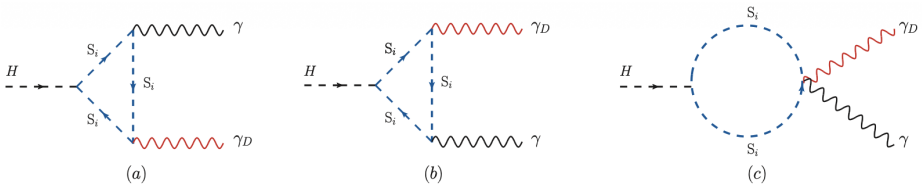


*Figure 4.* Feynman diagrams that contribute to the $H_{\gamma\gamma_D}$ coupling at one loop level. The dark photon is denoted by $\gamma_D$, the Higgs boson by $H$, and the messenger fields by $S$.

# CHAPTER III

# EXPERIMENTAL SETUP

The results presented in this thesis were obtained with the ATLAS detector located at the Large Hadron Collider (LHC) during the Run 2 and Run 3 data-taking periods. Section 3.1 will describe the LHC complex and beamline, while the ATLAS detector in the Run 2 configuration will be described in section 3.2. ATLAS underwent upgrades during the LHC's second long shutdown (LS2) from 2019-2021, and the detector in the Run 3 configuration will be described in section 3.2.7. Hardware and software upgrades of the ATLAS detector for the High-Luminosity LHC (HL-LHC) will be discussed in chapter IV.

## 3.1 The Large Hadron Collider

The LHC Evans and Bryant (2008), located near Geneva, Switzerland, is the world's largest and most powerful particle accelerator. It collides protons at a center-of-mass (COM) energy of 13.6 TeV during Run 3 operations, with plans to reach its design energy of 14 TeV in the High-Luminosity LHC (HL-LHC) era. The two opposing beams of protons travel in a 27-kilometer ring of superconducting magnets and are made to collide at four evenly spaced interaction points highlighted in Fig. 5 every 25 ns. There are 2 general-purpose detectors, ATLAS ATLAS Collaboration (2008) and CMS CMS Collaboration (2008), and 2 specialized detectors, LHCb LHCb Collaboration (2008) and ALICE The ALICE Collaboration (2008), located at the interaction points to observe and record the results of the proton-proton collisions. Of particular note, the LHC has made it possible for the ATLAS and CMS collaborations to discover the Higgs boson in 2012 ATLAS Collaboration (2012a); CMS Collaboration (2012).

Currently in Run 3, the LHC has operated since 2009, with two long shutdowns between runs to allow for upgrades to the accelerator complex and detectors. Run 1 took place from 2010 to 2013 at center-of-mass energies of 7 and 8 TeV, while Run 2 took place from 2015 to 2018 at a center-of-mass energy of 13 TeV. The High-Luminosity LHC (HL-LHC) is scheduled to begin operations in 2030 after a third long shutdown to upgrade the LHC and detectors to handle and take advantage of the large increase in luminosity.

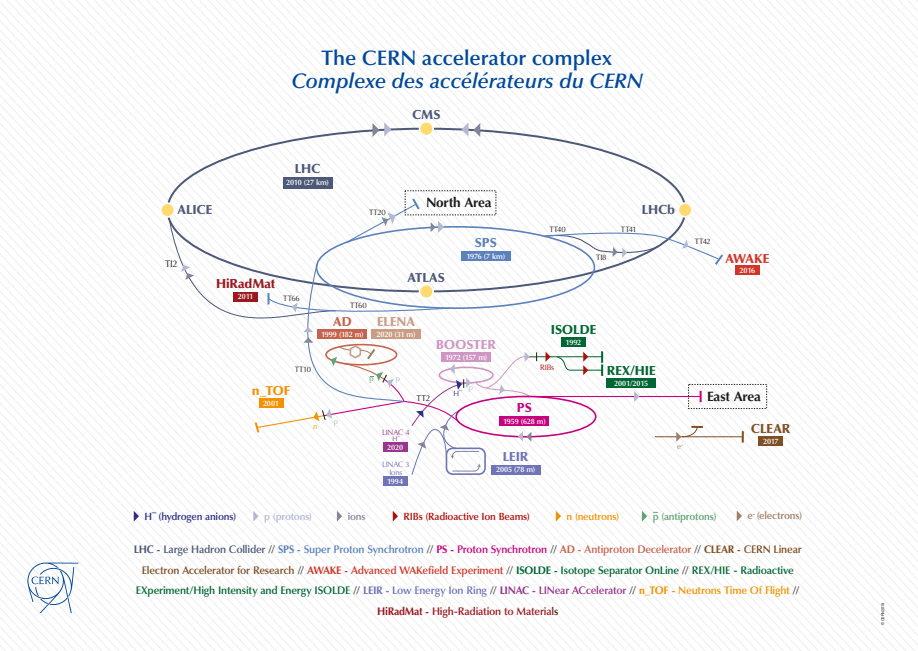


*Figure 5.* CERN accelerator complexVanden Broeck (2019). The four main experiments are located at the interaction points highlighted in yellow. As of Run 3, the proton acceleration chain begins at LINAC4 highlighted in purple.

**3.1.1 The Proton Acceleration Chain.** The CERN accelerator complex prepares and accelerates protons before injecting them into the LHC as seen in Fig. 5. Prior to Run 3, hydrogen gas is ionized to produce protons, which are then accelerated to an energy of 50 MeV in the linear accelerator (LINAC2) before being injected into the Proton Synchrotron Booster (PSB). Run 3 replaced

LINAC2 with LINAC4, which accelerates negative hydrogen ions (H-) to 160 MeV before being injected into the PSB. Next, a series of synchrotrons furthers the acceleration process: the PSB accelerates protons to 2 GeV, followed by the Proton Synchrotron (PS) with 26 GeV, and finally the Super Proton Synchrotron (SPS) where protons reach an energy of 450 GeV. Within the PS, the protons are grouped into bunches containing $10^{11}$ protons each, and these bunches are split into opposing beams in the SPS. The two beams are finally ready to be injected into the LHC for the final acceleration up to 6.5 TeV per beam in Run 2, and 6.8 TeV per beam in Run 3. The beams collide at the 4 interaction points every 25 ns, resulting in a maximum of 40 million collisions per second.

Each system in the chain uses radio-frequency (RF) cavities for acceleration, while the synchrotrons also include magnetic dipoles for beam steering and magnetic quadrupoles for focusing. Since protons are charged particles, RF cavities use oscillating electric fields to accelerate them. These cavities are shaped to resonate at frequencies that match the timing of the proton bunches, accelerating them forward while keeping the bunches tightly packed. The frequency is gradually increased as the protons gain energy, imparting a "pull" as they enter the cavity and a "push" as they exit. The bunches are also shaped longitudinally by the RF cavities. This is done by having the protons encounter the fields at the crest of the wave, slightly pushing the forward protons back and the trailing protons forward, keeping the bunches compact and compressed. There are 8 RF cavities in the LHC ring, providing a total of 16 MV per turn at 400 MHz to reach the final energy of 6.8 TeV per beam. RF cavities must be cooled down to 4.5K using liquid helium to maintain their superconducting state and operating efficiency.

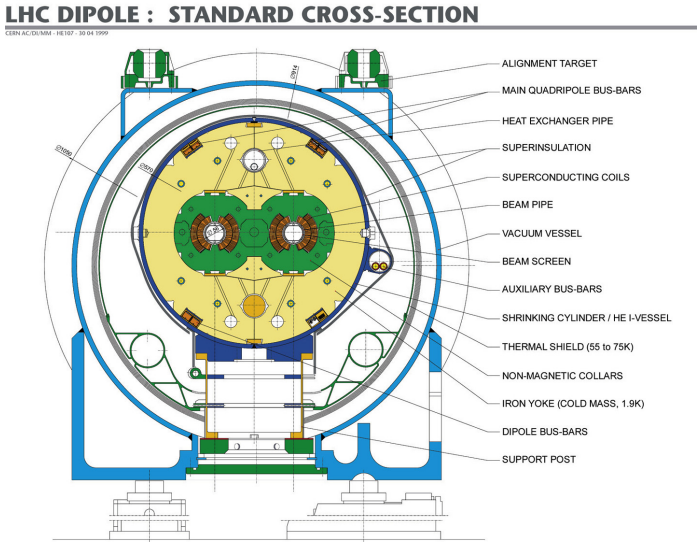


*Figure 6.* LHC dipole magnet schematic AC Team (1999)

Opposite polarity fields applied by dipole magnets shown in Fig. 6 bend the beam trajectories along the ring in opposing directions. This design allows for the opposing beams to circulate in separate beam pipes within the same magnet structure, reducing the overall size of the beam pipe to fit within the LEP tunnel. The 1232 dipole magnets are superconducting as well, and the specially designed NbTi Rutherford wires are cooled to 1.9K with liquid helium, generating magnetic fields up to 8.3 T. While the overall shape of the LHC is circular, the path is more accurately described by straight sections with bends at the dipoles. The PSB, PS, and SPS use superconducting dipole magnets similarly, with field strengths of .087, 1.24, and 2.02 T, respectively Tommasini (2010). The quadrupole magnets focus the beams in these straight sections, keeping protons tightly packed and prepared for collision at the interaction points. Single quadrupole magnets focus on one axis while defocusing the other, so they are arranged in sequences of alternating orientations.

### 3.1.2 Proton-Proton Collisions and Luminosity.

Once the two proton beams reach their target energy and are prepared for collision by the focusing magnets, they are directed to cross paths at the interaction points. There are 2808 equally spaced bunches in each beam, colliding at the interaction points with a frequency of 40 MHz (every 25 ns). The number of proton collisions is characterized by the luminosity and cross section:

$$N = \sigma \mathcal{L}, \tag{3.1}$$

where $\sigma$ is the cross section of the proton-proton interaction process, and $\mathcal{L}$ is the luminosity integrated over a time interval. The inelastic proton-proton cross section at a center-of-mass energy of 13 TeV is approximately 80 mb (1 mb $= 10^{-27}$ cm$^2$) Aaboud, Aad, Abbott, et al. (2016). The equation is also valid for a rate of events, where $N$ is replaced by $\frac{dN}{dt}$ and $\mathcal{L}$ is replaced by the instantaneous luminosity $\mathcal{L}_{inst}$. The instantaneous luminosity depends on properties of the LHC beams and is given by:

$$\mathcal{L}_{inst} \propto \frac{N^2 f_{rev}}{4\epsilon\beta^*}, \tag{3.2}$$

where $N$ is the number of protons per bunch, $f_{rev}$ is the revolution frequency of the beams, $\epsilon$ is the normalized transverse beam emittance, and $\beta^*$ is the beta function at the interaction point. The emittance characterizes the spread of the beam in position and moment space, while beta is a measure of the magnetic focusing strength at the interaction point. $\epsilon$ and $\beta^*$ have units of length, so the instantaneous luminosity has units of cm$^{-2}$s$^{-1}$. The beams are designed to collide at a slight crossing angle, giving a gamma and geometric factor which are ommitted

here for simplicity. Given nominal values of $N = 1.15 \times 10^{11}$ protons per bunch, $f_{rev} = 11.245$ kHz, $\epsilon = 3.75$ $\mu$m, and $\beta^* = 0.55$ m, the approximate LHC instantaneous luminosity is $1 \times 10^{34}$ cm$^{-2}$s$^{-1}$ CERN (2004). This design luminosity was surpassed in Run 2 and Run 3, reaching peak instantaneous luminosities above $2.1 \times 10^{34}$ cm$^{-2}$s$^{-1}$.

A more tractable measure of proton-proton collisions is the interactions per bunch crossing, as shown in Fig. 7. Within the ATLAS detector, the average interactions per bunch crossing $\langle\mu\rangle$ was 35 in Run 2, and has reached values above 60 in Run 3. While higher pileup increases the likelihood of a collision of interest, the extra interactions in a bunch crossing create outgoing particles or jets that need to be addressed during event reconstruction. This effect is known as pileup, scales with instantaneous luminosity, and must be accounted for when reconstructing events or physics objects within a detector. Pileup can be in-time, where multiple interactions occur within the same bunch crossing, or out-of-time, where interactions from previous bunch crossings are recorded in the current window due to detector response times.

With Run 3 coming to an end in mid 2026, the LHC will undergo a third long shutdown to prepare for the HL-LHC era, planned to begin in 2030 as shown in Fig. 8. The HL-LHC will increase the instantaneous luminosity to $7.5 \times 10^{34}$ cm$^{-2}$s$^{-1}$, with a goal of reaching the design center-of-mass energy of 14 TeV and collecting up to 3000 fb$^{-1}$ of integrated luminosity over a decade of operation CERN (2017). Pileup is expected to reach an average of 200 interactions per bunch crossing, requiring significant upgrades to the LHC and experiments to handle and take advantage of the factor of 4 increase in pileup.

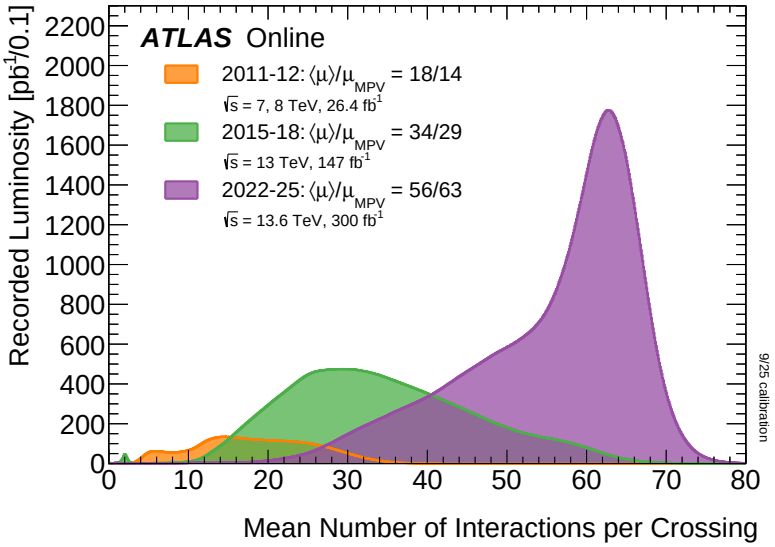


*Figure 7.* Average interactions per bunch crossing (pileup) recorded by the ATLAS detector during Runs 1 and 2, and the on-going Run 3 data-taking periods ATLAS Collaboration (2025).

Chapter IV will discuss the HL-LHC and corresponding upgrades to ATLAS in more detail.

### 3.2 The ATLAS Detector

The ATLAS detector is a general purpose detector at Point 1 of the LHC ring. It is designed to detect and measure the scattering products of collisions provided by the LHC. Cylindrical in design, it is symmetric about the z-axis, and measures approximately 25 m in height and 44 m in length, with a total mass of about 7000 tons. ATLAS Collaboration (2008). ATLAS consists of several detector subsystems, magnets, and cryostats arranged in layers around the interaction point, as shown in Fig. 9. The first detector layer surrounding the interaction point is the Inner Detector (ID) which tracks charged particles. Around the ID are multiple calorimeter systems which measure and absorb the energy of all Standard Model particles except muons and neutrinos. The final detector component is the Muon

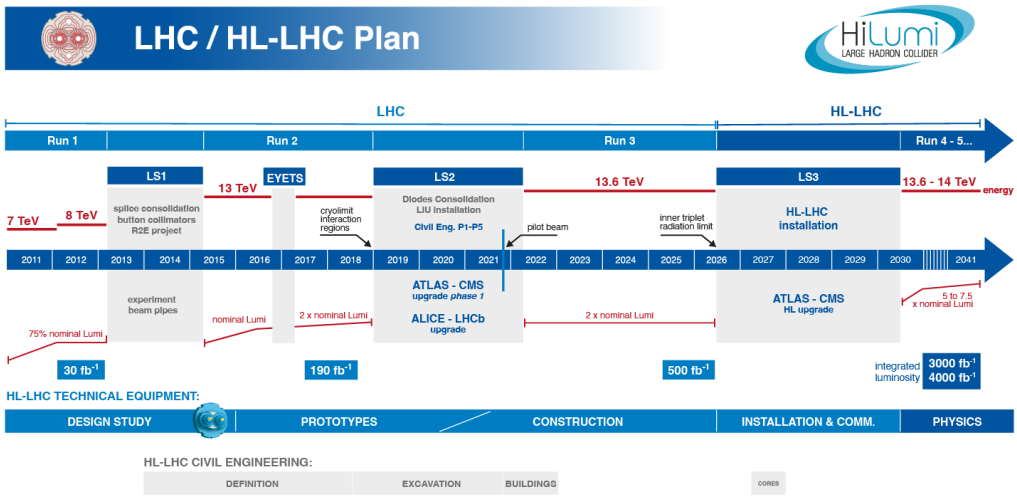


*Figure 8.* LHC and HL-LHC operation timeline CERN (2017), with integrated luminosities in blue along the bottom.

Spectrometer (MS) which tracks muons as they pass through ATLAS. The detector systems are divided into barrel and end cap regions, with the barrel covering the region perpendicular to the beamline and the end caps covering regions parallel to the beamline. This design allows for near $4\pi$ coverage around the interaction point, and is sensitive to a wide range of particle signatures, motivated partly by the prediction that the Higgs boson would decay to multiple final states. There are two main magnet systems in ATLAS: a solenoid magnet surrounding the ID, and a toroidal magnet surrounding the calorimeters and sections of the MS. Bathing sections of the detector in strong magnetic fields allows for the measurement of charged particle momenta by curving their trajectories. A vital off-detector system is the Trigger and Data Acquisition (TDAQ) system, which takes input from the detector components and selects interesting collision events for further analysis.

**3.2.1 The ATLAS Coordinate System.** ATLAS uses a right-handed coordinate system with its origin at the interaction point, $\hat{y}$ pointed

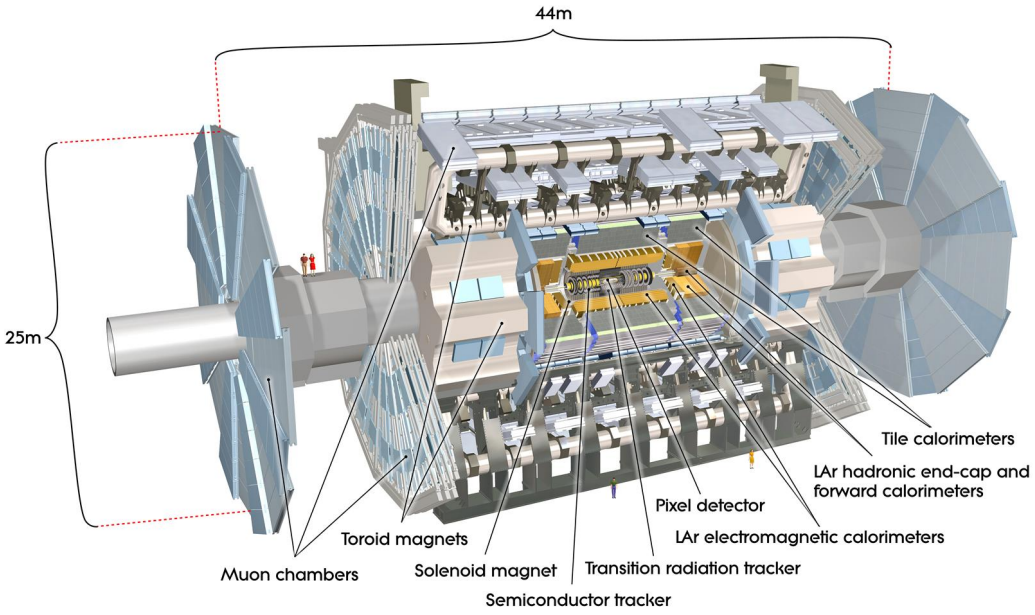


*Figure 9.* Schematic diagram of the Run 2 ATLAS detector and its sub-systems ATLAS Collaboration (2008).

upwards, $\hat{x}$ pointed radially inward towards the center of the LHC ring, and $\hat{z}$ pointed along the beamline. The cylindrical symmetry of the detector and typical particle trajectories often motivates the use of two angular coordinates with $\theta$ the angle from the $\hat{z}$ axis, and $\phi$ the azimuthal angle in the transverse (x-y) plane.

To better describe particle trajectories in a flat geometry, the pseudorapidity $\eta$ replaces the polar angle $\theta$ and is defined as:

$$\eta = -\ln\left(\tan\left(\frac{\theta}{2}\right)\right) \tag{3.3}$$

Pseudorapidity is valid in the highly relativistic conditions of the LHC where $pc \gg mc^2$, and has the advantage of being invariant under Lorentz boosts along the beam axis. A common measure of distance in the detector, since it is also invariant under boosts along the beam axis, is $\Delta R$ defined as:

$$\Delta R = \sqrt{(\Delta\eta)^2 + (\Delta\phi)^2} \tag{3.4}$$

Since the LHC collides protons essentially head-on, they have an initial transverse energy of zero. It is therefore useful to define and measure physical quantities in the transverse plane, such as transverse momentum $p_T$ and missing transverse energy $E_T^{miss}$ often referred to as MET.

**3.2.2 The Inner Detector.** The ID is the innermost detector system seen in Fig. 10, tracking charged particle trajectories as they emerge from the interaction point with minimal energy loss as they pass through ATLAS Collaboration (1997a). It is composed of three subsystems and covers an $\eta$ range of $|\eta| < 2.5$. The whole ID is immersed in a 2T magnetic field provided by the solenoid magnet.

Tracking is performed by measuring the charge, position, and timing of charged particles. As a charged particle passes through a layer of the ID, it ionizes the detector material, creating electron-hole pairs. Each layer is under high voltage, and these free charges are collected to provide a *hit* in the detector. Combining hits from multiple layers allows for the reconstruction of the particle trajectory, or *track*. The direction of curvature of the track due to the magnetic field gives the charge of the particle, while the radius of curvature gives the momentum. Tracks are also traced back to the beamline to identify the vertex of the associated particle. If a track does not originate from the beamline, it might have originated from a secondary vertex, indicating the decay of a long-lived particle or as a product of a parent particle decay.

The innermost subsystem is the Pixel Detector ATLAS Collaboration (1998), starting at a distance of 33.25 mm from the beamline and extending

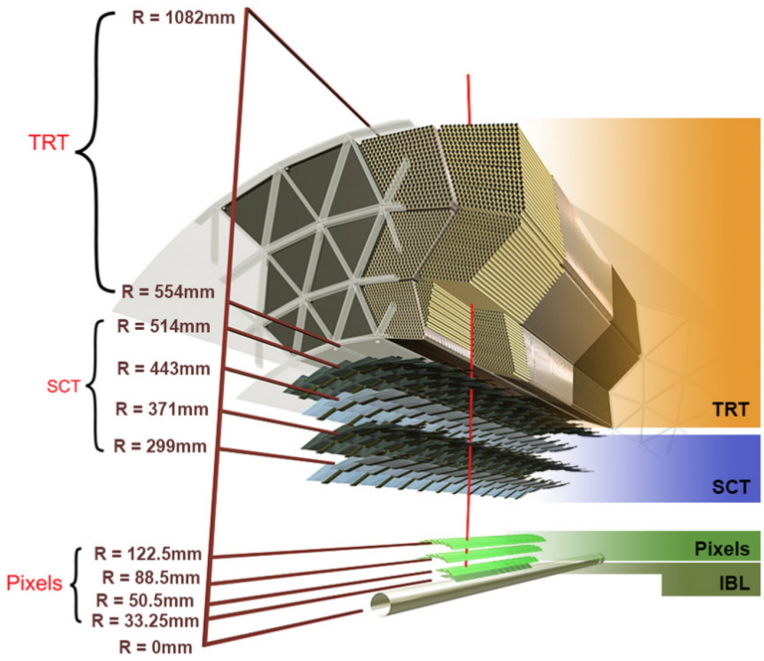


*Figure 10.* Diagram of the ATLAS Inner Detector and its three subsystems ATLAS Collaboration (2008).

to 122.5 mm. It is composed of layers of 92 million silicon pixel sensors, each measuring 50 $\mu$m by 400-600 $\mu$m in size. Sensors are stacked in four overlapping layers in the barrel region, and 3 disks on each end cap providing coverage out to $|\eta| < 2.5$. The overlapping geometry provides a granularity of approximately 10 $\mu$m. The closest layer to the beamline is the Insertable B-Layer (IBL), which was added in 2014 for Run 2 operation and beyond ATLAS Collaboration (2010a). The purpose of the IBL upgrade is to improve the resolution of secondary vertices and thus $b$-tagging performance, as well as further suppress pileup vertices.

Surrounding the Pixel Detector is the Semiconductor Tracker (SCT) ATLAS Collaboration (2014c) at a radial distance of 122.5 mm to 520 mm, composed of silicon microstrip sensors. SCT sensors are arranged in pairs of back-to-back strips and are larger than pixel sensors. There are four SCT barrel layers out to

$|\eta| < 1$, and nine end cap disks on each side extending coverage to $|\eta| < 2.5$. The precision of the SCT is approximately 16 $\mu$m in the r-$\phi$ direction and 580 $\mu$m in the z direction.

The outermost subsystem of the ID is the Transition Radiation Tracker (TRT) ATLAS Collaboration (2008), extending from a radial distance of 563 mm to 1066 mm. It uses a completely different technology than the inner two systems, consisting of 298,304 drift tubes, or straws. Each straw is a 4 mm diameter tube filled with an ionizing gas mixture and a central grounded wire made of gold plated tungsten. The gas mixture is 70% Xe, 27% $CO_2$, and 3% $O_2$. Extending out to $|\eta| < 2.0$, the TRT has a barrel section with straws parallel to the beamline, and two end cap sections with straws arranged radially, and provides $\sim$ 36 additional hits to improve tracking. As particles pass through the polypropylene material between straws, they emit transition radiation, which ionizes the gas in the straws. The larger size of the TRT provides a better measurement of the bend of tracks in the magnetic field, improving momentum resolution.

**3.2.3 The Calorimeter System.** The purpose of the ATLAS calorimeter system is to absorb and measure the energy of particles after they pass through the ID. There are two main sampling calorimeter technologies used in ATLAS, Liquid Argon (LAr) and scintillating tiles (Tile), composing multiple layers as shown in Fig. 28. LAr calorimeters are used in the electromagnetic (EM) barrel, hadronic and EM end caps (HEC and EMEC), and the forward calorimeter (FCAL). The Tile barrel and extended barrel use scintillating tiles, and are for hadronic object reconstruction. With over 188,000 readout channels, the calorimeter system covers the range $|\eta| < 4.9$ ATLAS Collaboration (1996a). The calorimeters were designed to fully contain particle showers up to a few

TeV in energy and provide identification of electrons and photons. Hadronic showering primarily occurs in the Tile systems, but jet reconstruction takes input from all calorimeters. Muons and neutrinos are the only particles that escape the calorimeters with minimal energy loss, however, muons are tracked in the MS and neutrinos can be inferred from the missing transverse energy in an event.

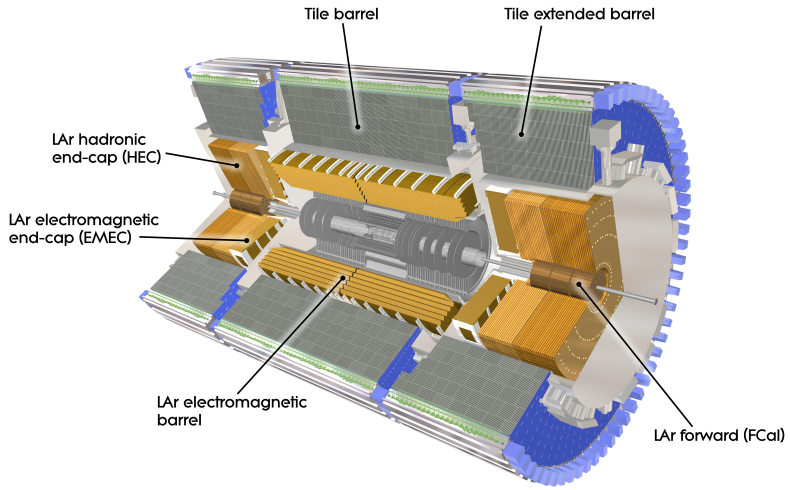


*Figure 11.* Diagram of the ATLAS calorimeter system labeled by subsystem ATLAS Collaboration (2008).

Sampling calorimetry involves alternating layers of dense absorbing material and active sensing material. Absorbing layers induce particle showers by scattering the incoming particle(s). The particle showers interact with the active layers through ionization or scintillation, allowing for multiple measurements of energy deposition as they pass through the calorimeter. The calorimeter resolution within ATLAS is generally parameterized as:

$$\frac{\sigma_E}{E} = \frac{a}{\sqrt{E}} \oplus \frac{b}{E} \oplus c \tag{3.5}$$

and depends on stochastic effects ($a$), electronic noise ($b$), and other detector effects ($c$). In practice, resolution varies between calorimeter subsystems, but typical values for jets range from 6-25% for 20 GeV $< E <$ 300 GeV ATLAS Collaboration (2020b).

***3.2.3.1 Electromagnetic Calorimeters.*** The ATLAS EM calorimeters ATLAS Collaboration (1996a) primarily measure the energy of electrons and photons, and are sectioned into a barrel and two end cap regions, extending out to a radius of 2 m. All regions use LAr as the active material and lead as the absorber, chosen for its high Z value, with radiation lengths of 24 $X_0$ in the barrel and 26 $X_0$ in the end caps. The barrel covers the region $|\eta| < 1.475$, while the two end cap sections cover $1.375 < |\eta| < 3.2$. An accordion geometry is used for the lead absorbers as shown in Fig. 12, with LAr filling the gaps between sheets. Electrodes are placed in the LAr gaps and are sectioned into "cells" in $\eta$ and $\phi$ to provide highly granular spatial resolution. This design allows for full $\eta$-$\phi$ coverage and fast signal collection.

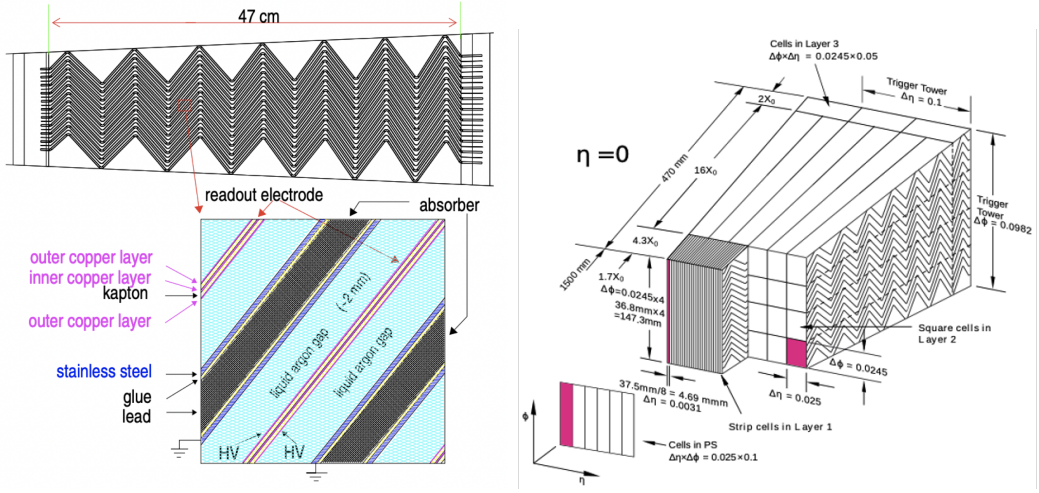


*Figure 12.* Accordion geometry of the ATLAS electromagnetic calorimeter with readout schematic (left) ATLAS Collaboration (2013). EM barrel layout with cells showing coverage in $\eta$ and $\phi$ (right) ATLAS Collaboration (1996a).

There are three layers in the barrel region, with an additional presampler in front of the barrel to allow for energy loss corrections due to material in front of the calorimeter. As electrons and photons pass through the layers, they interact with the lead absorbers, producing a shower of more electrons and photons primarily through Bremsstrahlung and pair production. This cascade continues, with measurements and showering occuring in turns until all the energy is absorbed. The first layer has very fine granularity in $\eta$-$\phi$, $0.003 \times 0.1$, to distinguish between single photons and overlapping photons from $\pi^0$ decays. Most of the energy is deposited in the second layer as it is the thickest, with a trade off between slightly lower $\eta$ granularity than layer one, but higher $\phi$ granularity at $0.025 \times 0.025$. The third layer is thinner and collects the tail ends of showers with a granularity of $0.050 \times 0.025$. The EM end caps have a similar accordion geometry and layer structure, with an additional presampler between the barrel and end caps, but are arranged in a disk shape to cover the forward regions. EMEC cells are segmented in cells that have varying granularity with $\eta$ and layer and are larger than barrel cells. There are over 170,000 readout channels in the EM calorimeters.

The readout of the EM calorimeters is delayed by the ion drift time in the LAr, which varies between 450-600 ns depending on the layer ATLAS Collaboration (2010c). This delayed signal is longer than the LHC collision rate of 24 ns, necessitating the use of pulse shaping to mitigate out-of-time pileup from previous bunch crossings. Analog circuits in the front end electronics use a bipolar shaping filter to create a sharply peaked pulse and long negative tail as shown in Fig. 13. The triangle shape is the ionization drift inside the detector. A capacitively coupled input forces the shaped pulse to have a total integral of zero, canceling out contributions from out-of-time pileup.

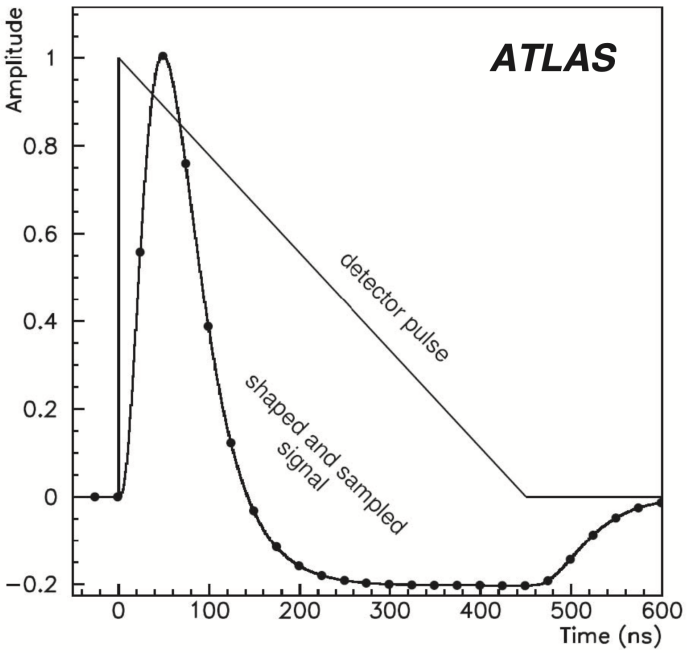


*Figure 13.* Pulse shape of LAr calorimeter signal to mitigate out-of-time pileup ATLAS Collaboration (2013a).

***3.2.3.2 Hadronic Calorimeter.*** The physically largest component of the ATLAS calorimeter system is the hadronic calorimeters, which capture and measure the energy of hadrons. Particles such as charged and neutral pions, kaons, and protons punch through the EM calorimeters and interact via the strong interaction with nuclei in the absorber material, producing hadronic showers. These showers are commonly described through the interaction length $\lambda$, where a hadron has a $1 - \frac{1}{e}$ chance of interacting with a nucleus. Composed of the Tile calorimeter in the range $|\eta| < 1.475$, and the HEC in $1.475 < |\eta| < 3.2$, scintillators and LAr are used respectively. The detector extends out to $\sim 17$ interaction lengths in Tile and $\sim 11$ interaction lengths in the HEC.

The Tile calorimeter ATLAS Collaboration (1996b) uses steel as the absorber and plastic scintillating tiles as the active material as shown in Fig. 14, with a radius from 2.28 m to 4.25 m. It takes its name from the rectangular plastic

scintillating tiles that are arranged in layers between steel absorber plates. When shower particles passes through the tiles, they excite molecules in the plastic, which in turn emit photons as they return to their ground state. Photons are then collected by wavelength shifting fibers and directed to photomultioplier tubes (PMTs) which convert the light to a voltage signal, and is proportional to the energy deposited in the tile. Tiles are grouped together by the PMTs into cells with coarser granularity than the EM calorimeters due to the larger size of hadronic showers, with $\eta \times \phi$ sizes of $0.1 \times 0.1$ in the barrel and $0.1 \times 0.2$ in the extended barrel.

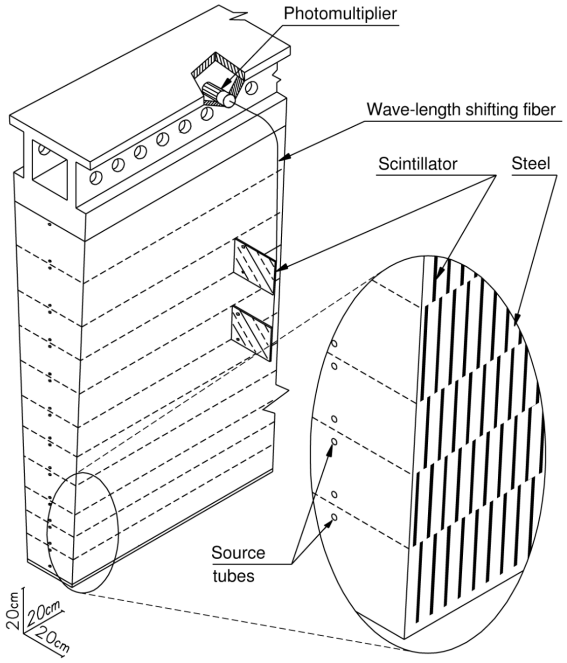


*Figure 14.* Tile calorimeter wedge module showing the scintillating tiles, steel absorber plates, and PMTs ATLAS Collaboration (2017d).

Just past the EMEC in $z$ is the HEC, which is similar in design to the EM calorimeters, using LAr as the active material and copper as the absorber ATLAS Collaboration (1996a) arranged in the accordion geometry. As seen in Fig. 15, each

end cap has two wheels contained in the same cryostat as the EMEC and FCAL. The cells also vary in size depending on $\eta$ and layer due to the wheel geometry.

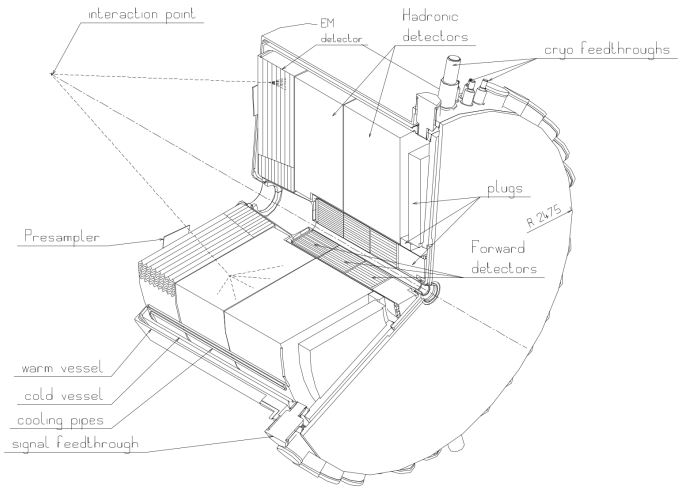


*Figure 15.* Diagram of the ATLAS hadronic end cap calorimeter along with the EMEC and FCAL ATLAS Collaboration (1996a).

***3.2.3.3 Forward Calorimeter.*** The Forward Calorimeter (FCAL) ATLAS Collaboration (1996a) covers the extreme forward region of $3.1 < |\eta| < 4.9$ and is designed to withstand the high radiation dose and particle flux. Using similar LAr technology as the EM and HEC, the FCAL is composed of three modules arranged in series along the beamline and integrated in the same cryostat as the EMEC and HEC as shown in Fig. 15. The first section is made of copper, while the other two are made of tungsten. Each contains a matrix of small concentric rods and tubes, with the rods held at high voltage and the gap between filled with LAr as seen in Fig. 16.

The LAr gap between a rod and tube contains a polyether ether ketone (PEEK) spacer to maintain a gap of $\sim 260$ $\mu$m in the first module and $\sim 500$ $\mu$m in the other two modules for fast and uniform signal collection. A dense absorber with matrix cells is necessary to contain the high energy particle showers in this region,

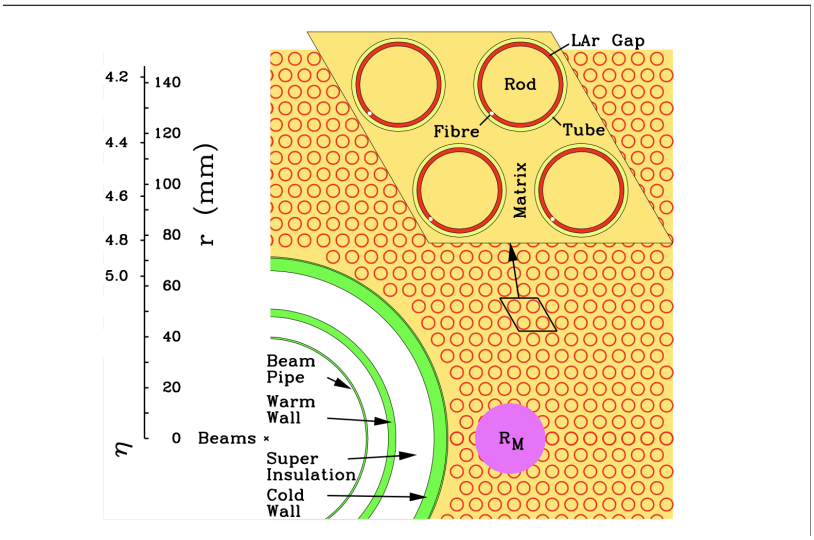


*Figure 16.* Schematic of the ATLAS Forward Calorimeter matrix structure ATLAS Collaboration (1996a).

with interaction lengths of $\sim$ 8 in the copper module and $\sim$ 10 in the tungsten modules.

**3.2.4 The Muon Spectrometer.** The outermost detector subsystem is the Muon Spectrometer (MS) ATLAS Collaboration (1997b), which tracks muons since they pass through ATLAS with minimal energy loss, and measures their momenta. There are multiple layers of tracking chambers using different technologies with coverage out to $|\eta| < 2.7$ as shown in Fig. 17, arranged in a barrel and two end cap regions. A toroid magnet system provides the magnetic field for momentum measurements, and is placed between layers of the MS. Monitored Drift Tubes (MDT) are the most common tracking chambers in the MS, covering the full $\eta$ range. All three barrel layers and the two outermost end cap layers use MDTs. The MDTs are composed of 3 cm diameter aluminum tubes filled with a gas mixture of 93% Ar and 7% $CO_2$, with an anode wire held at high voltage running through the tube. Cathode Strip Chambers (CSC) are used in the forward regions near the end cap toroids where there is a higher occupancy and radiation

dose, covering $2.0 < |\eta| < 2.7$. These chambers are multi-wire proportional chambers with segmented cathode strips to provide a precise position measurement. All MDT and CSC chambers were constructed with a high precision mechanical assembly and aligned using an in situ optical alignment system to meet the design tracking resolution.

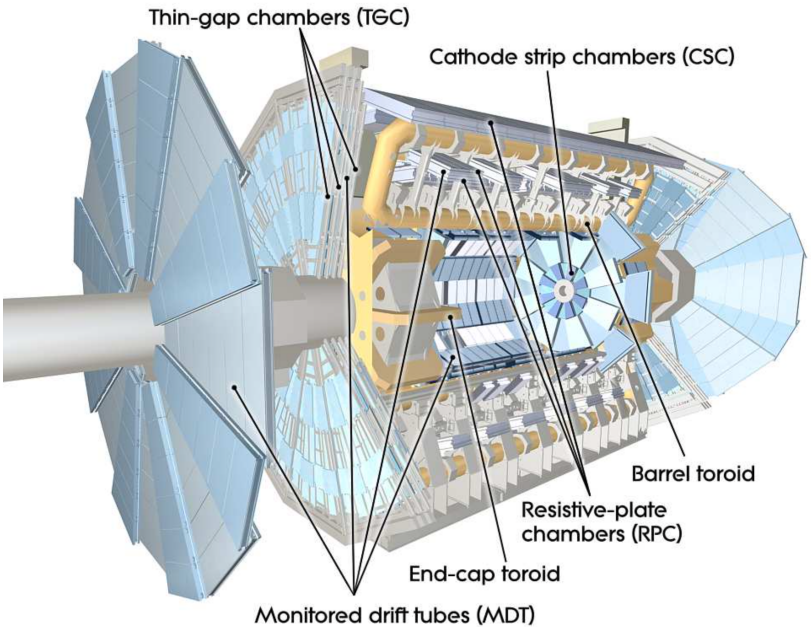


*Figure 17.* Diagram of the ATLAS Muon Spectrometer chambers ATLAS Collaboration (2008).

In the barrel region, Resistive Plate Chambers (RPC) are used for muon triggering. The RPCs are composed of two parallel resistive plates with a gap inbetween filled with tetrafluoroethane gas. Readout strips on the outside of the plates provide $x$ and $y$ track measurements. The inner RPC layers are used for a low $p_T$ trigger, while the combined layers are used for a high $p_T$ trigger. While the RPCs provide a fast response for triggering, they have a coarser spatial resolution than the MDTs. Triggering in the end caps is provided by Thin Gap Chambers (TGC) covering $|\eta|$ out to 2.4. TGCs are similar to the CSCs, with a smaller gap

between the anode wires and cathode planes to provide a fast response time. The inner TGC layers provide a measurement of $\phi$ for tracking, while the outer layers are used for high and low $p_T$ triggering.

**3.2.5 Magnet System.** The ATLAS magnet system is composed of a solenoid magnet surrounding the ID, and a toroidal magnet system surrounding the calorimeters and sections of the MS ATLAS Collaboration (2008). All magnet systems use superconducting coils cooled to 4.5 K with liquid helium, and are shown in Fig. 18. The solenoid magnet provides a 2T magnetic field for the ID, allowing for momentum and charge measurements as particles pass through with minimal magnet material interaction. It covers the range $|\eta| < 2.5$ and is 5.3 m in length with a diameter of 2.5 m.

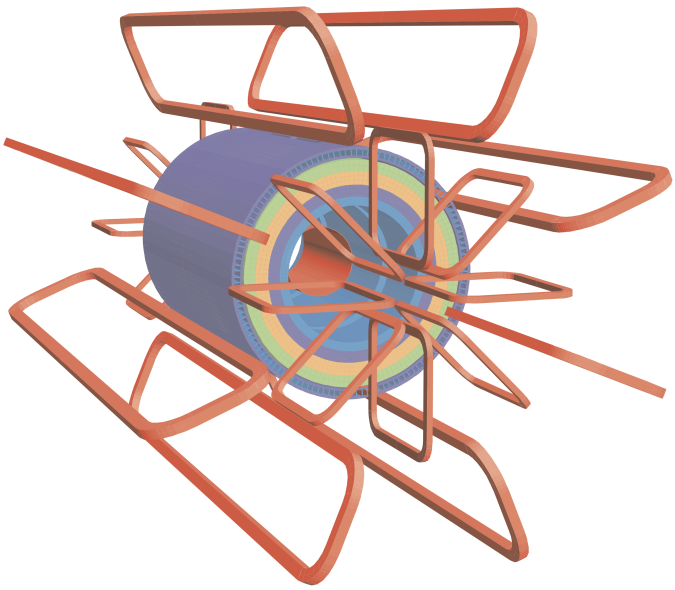

*Figure 18.* Diagram of the ATLAS barrel solenoid and barrel and endcap toroidal magnets ATLAS Collaboration (2008).

The toroidal magnet system is composed of a barrel toroid and two end cap toroids. The barrel toroid is made of eight superconducting coils arranged symmetrically around the beamline inbetween the outer calorimeters and the muon

chambers, providing a magnetic field up to 3.5 T in the MS barrel region. The two end cap toroids are each made of eight superconducting coils arranged in a disk shape, providing a magnetic field up to 5 T in the MS end cap regions.

**3.2.6 Trigger and Data Acquisition (TDAQ).** At the LHC bunch crossing rate of 40 MHz, ATLAS produces an enormous amount of data at a rate of over 1 PB per second if all detector information were to be recorded. Storing and processing this amount of data is not feasible, so a trigger system is implemented to select events based on distinctive features or characteristics that indicate physics processes of interest. The ATLAS Trigger and Data Acquisition (TDAQ) system The ATLAS Collaboration (2016) utilizes a two-level trigger system to reduce the 40 MHz LHC bunch crossing rate to a manageable 1 kHz in Run 2 for offline storage and analysis. It is important to note that while 1 kHz is the target rate, the actual rate is allowed to be higher in practice, and there are multiple streams of physics data. Events are selected based on trigger signatures designed to capture the interesting physics while rejecting backgrounds, optimized for the computing and storage resources available. Triggers are prioritized based on physics goals and needs of analysis groups, with high event yield triggers prescaled to reduce their rate. The TDAQ system can be seen in Fig. 19.

In Run 2, the first level trigger (L1) is a hardware-based system that primarily uses information from the calorimeters and muon spectrometer, L1Calo and L1Muon, to make a decision within 2.5 $\mu$s ATLAS Collaboration (2017h). The 40 MHz collision rate is reduced to a maximum of 100 kHz before data is sent to the high level trigger (HLT). L1Calo uses LAr and Tile calorimeter information to identify electrons, photons, and jets using coarse granularity trigger towers of size $0.1 \times 0.1$ in $\eta$-$\phi$. Fast algorithms identify high energy deposits and apply

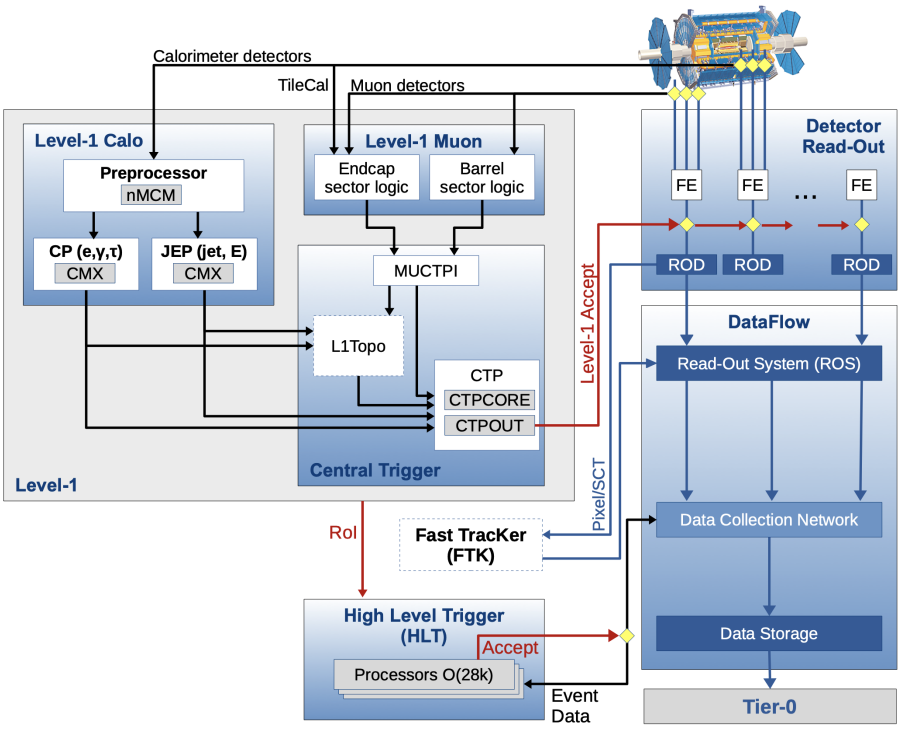


*Figure 19.* Schematic of the ATLAS Trigger and Data Acquisition system showing the L1 trigger, HLT, and dataflow between systems and to permanent storage The ATLAS Collaboration (2016).

isolation criteria to select EM objects within a region of interest (ROI). L1Muon uses hits from the RPCs and TGCs to identify muon candidates and measure their transverse momentum for triggering within $|\eta| < 2.4$. The reconstructed trigger objects (TOBs) are sent to the L1 central trigger processor where a decision is made based on programmable trigger menus. If an event is accepted, data and an associated ROI are sent to the HLT for further processing.

The HLT is a software level trigger that further reduces the L1 acceptance rate of 100 kHz to  1 kHz for permanent storage ATLAS Collaboration (2017h). This is implemented on a large computing farm using offline-like algorithms to reconstruct physics objects within the ROIs identified by L1. Events are distributed to HLT nodes where ATLAS reconstruction software within Athena processes the data. High granularity readout from all detector subsystems, including tracking information, and more sophisticated algorithms allow for better reconstruction and identification for a final trigger decision based on HLT trigger menus. The HLT uses a two-step process, where a fast first step rejects the majority of events, and is followed by a precision reconstruction step for the remaining events. Accepted events are sent to the dataflow system where they are assembled and formatted for permanent storage.

**3.2.7 Changes for Run 3.** The ATLAS detector underwent several upgrades during the Long Shutdown 2 (LS2) from 2019-2021 in preparation for Run 3 data-taking ATLAS Collaboration (2024a). New electronic readout systems were installed in the LAr and Tile calorimeters to handle higher trigger rates and improve performance. The New Small Wheels (NSWs) in the MS end caps replaced the existing Small Wheels, with the data recorded using new readout electronics. With the incorporation of the NSW and the new LAr and Tile readout systems,

the trigger system was also upgraded to utilize higher granularity information at L1 while maintaining the 100 kHz acceptance rate. ATLAS in the Run 3 configuration can be seen in Fig. 20.

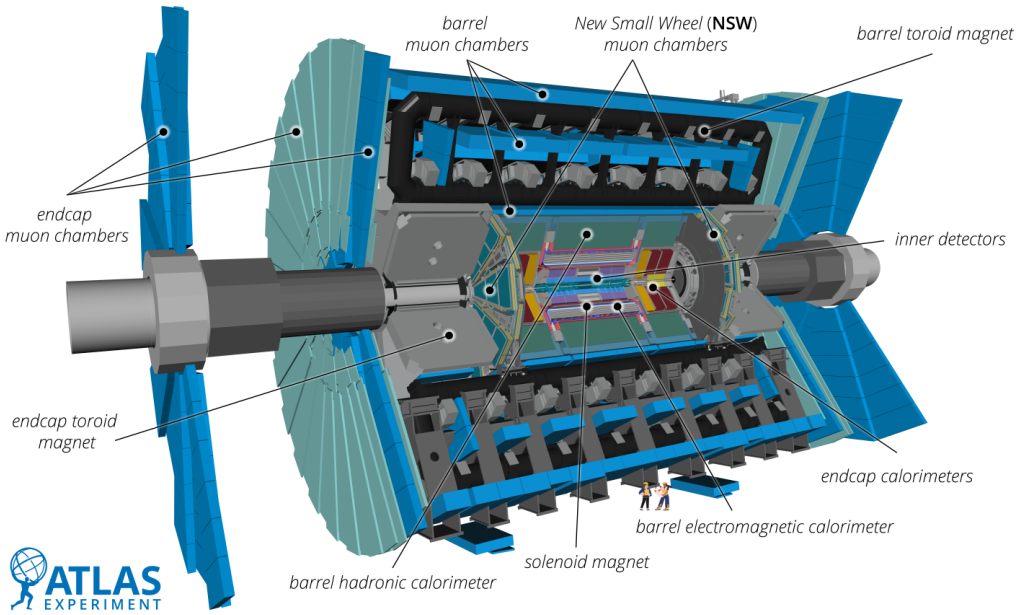


*Figure 20.* Schematic of the ATLAS detector in the Run 3 configuration, with the New Small Wheel highlightedATLAS Collaboration (2024a).

***3.2.7.1 New Small Wheel.*** The largest hardware upgrade to ATLAS for Run 3 was the installation of the New Small Wheel (NSW) in the MS end caps ATLAS Collaboration (2013b), seen in Fig. 21. Designed to withstand the high particle flux and meet the triggering and tracking needs of Run 3 and beyond, two new technologies were implemented in the NSW. The first is small-strip Thin Gap Chambers (sTGC), while the second is micro-mesh gaseous structure (Micromegas) detectors. The sTGCs are multi-wire proportional chambers similar to the existing TGCs, but with smaller strip pitches and wire spacing to provide higher spatial resolution. Micromegas technology permits very thin planar gaseous detectors, with the traditional planes of HV wires replaced by a metallic micro-mesh. These

allow for improved azimuthal resolution and precision tracking, thus increasing the trigger resolution and background rejection. A lower $p_T$ threshold for muon triggering is also achievable with the NSW while maintaining an acceptable trigger rate.

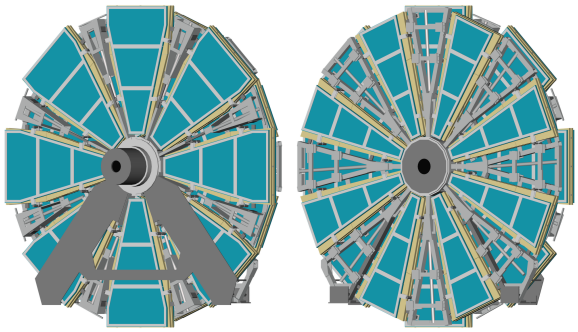

*Figure 21.* Diagram of the NSWs, including the support structure. ATLAS Collaboration (2013b).

***3.2.7.2 Readout and TDAQ upgrades.*** During Runs 1 and 2, calorimeter signals were sent to the trigger system in trigger towers of size 0.1 × 0.1 in $\eta$-$\phi$. A new digital trigger path was installed in the LAr calorimeter readout system during LS2, allowing for the use of supercells with finer granularity of up to 0.025 × 0.1 in $\eta$-$\phi$ at L1 ATLAS Collaboration (2013a). The trigger path utilizes new front-end boards, LAr Trigger Digitizer Boards (LTDB), to digitize and process the supercell signals. To support the LTDBs, modifications to the Front End Crates and the Front End Boards were made to sum cells with within supercells. The full Run 3 readout architecture for the LAr calorimeter can be seen in Fig. 22.

Off detector electronics were also upgraded to readout the LTDBs. The Front-End Link eXchange (FELIX) system over optical links configures and monitors the LTDBs, while the readout is handled by the LAr Digital Processing System (LDPS).

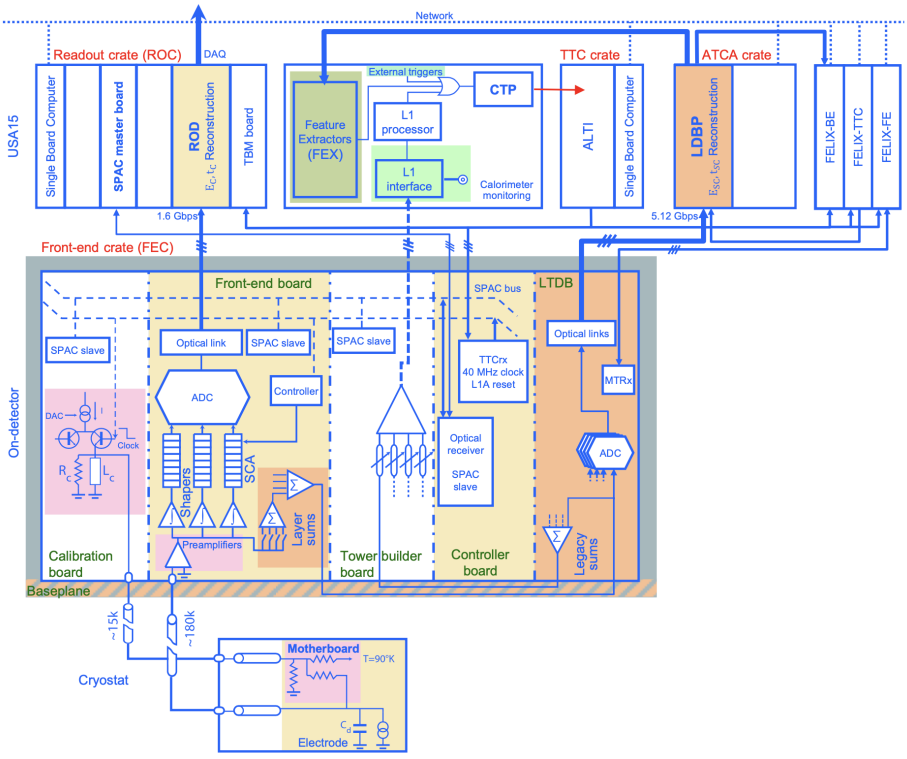


*Figure 22.* Block diagram of the LAr Run 3 readout architecture, read upwards through the front end crates to the off-detector electronics ATLAS Collaboration (2024a).

With full detector information available and higher granularity calorimeter data at L1, the TDAQ system was also upgraded for Run 3, and an overview can be seen in Fig. 23.

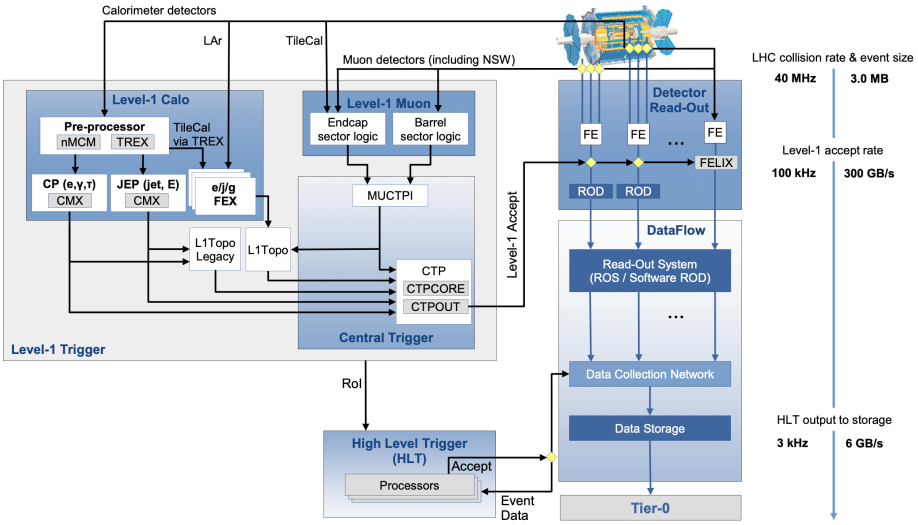


*Figure 23.* Schematic of the ATLAS Run 3 Trigger and Data Acquisition system ATLAS Collaboration (2024a).

While the two-level trigger architecture remains the same, both the L1 and HLT systems were improved to support the new detector readout from the calorimeters and NSW and advance the ATLAS physics goals for Run 3. Within the L1 system, new feature extractor (FEX) boards exploit the higher granularity calorimeter data to perform more advanced object reconstruction and identification. These include the eFEX for electrons, photons, and taus; jFEX for jets, taus, and $E_T^{\text{miss}}$; gFEX for large-R jets, $E_T^{\text{miss}}$, and the scalar sum of transverse momenta of jets, ($H_T$). The FEXes use custom FPGA-based hardware to implement fast algorithms for reconstruction within the L1 latency budget. Tile calorimeter energies are now digitized by the Tile REciever EXchange (TREX) board. The L1Muon system was also upgraded to incorporate the NSW data for improved muon triggering in the end cap regions. The HLT was refined to handle the data

more efficiently and implement more advanced algorithms. FELIX is used to route data more efficiently to the HLT servers running software readout drivers. New software support of multi-threading within the HLT allows for operation at higher event rates, 3 kHz, without reaching computing resource limits.

# CHAPTER IV

## HL-LHC AND ATLAS PHASE II UPGRADES

The LHC will undergo a series of upgrades during Long Shutdown 3; the High Luminosity LHC (HL-LHC) is planned to begin operations in 2030. The accelerator upgrades will aid in providing experiments with 10 times the integrated luminosity compared to previous runs after 12 years of HL-LHC data taking, with instantaneous luminosities in the range of $\mathcal{L} = 5 - 7.5 \times 10^{34}$ cm$^{-2}$ s$^{-1}$ and approximately 200 interactions per bunch crossing. The HL-LHC upgrade necessitates changes to ATLAS to not only manage, but take advantage of the increase in particle interactions and efficiently store events of interest to the physics goals. The largest upgrade to ATLAS is the complete replacement of the Inner Detector with a new all-silicon Inner Tracker (ITk) ATLAS Collaboration (2017a), which will provide higher granularity tracking and has the ability to withstand the higher collision rates and subsequent radiation doses. As seen in Fig. 24, the ITk will consist entirely of pixel detectors, with the innermost layers being high granularity pixel detectors, and the outer layers being strip detectors.

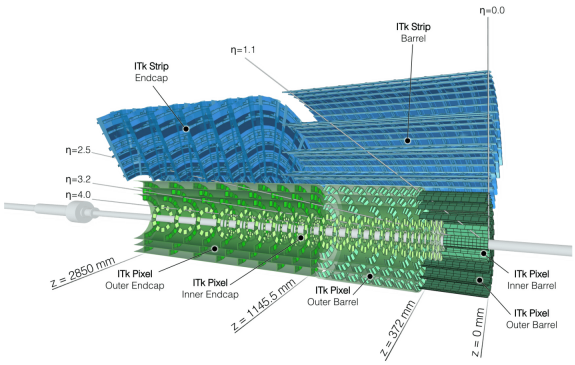


*Figure 24.* Schematic of the ITk, with the inner pixel layers in green and outer strip layers in blue. ATLAS Collaboration (2024b).

A completely new subsystem, the High-Granularity Timing Detector (HGTD) ATLAS Collaboration (2020a), will be installed in front of the end cap calorimeters to provide precision timing information for pile-up mitigation. The TDAQ system, which includes dataflow from the detectors to permanent storage and event selections, will receive a complete overhaul in order to take full advantage of the higher pileup and manage unprecedented data rates ATLAS Collaboration (2017c). An overview schematic of the Run 4 TDAQ system is shown in Fig. 25. Changes to the LAr and Tile readout system are necessary to achieve full granularity calorimeter information at the trigger level ATLAS Collaboration (2017b, 2017d). The muon system will also receive upgrades to the trigger with the incorporation of MDT detector information to the level 1 Muon trigger. In addition, muon readout and trigger electronics will be completely replaced ATLAS Collaboration (2024a).

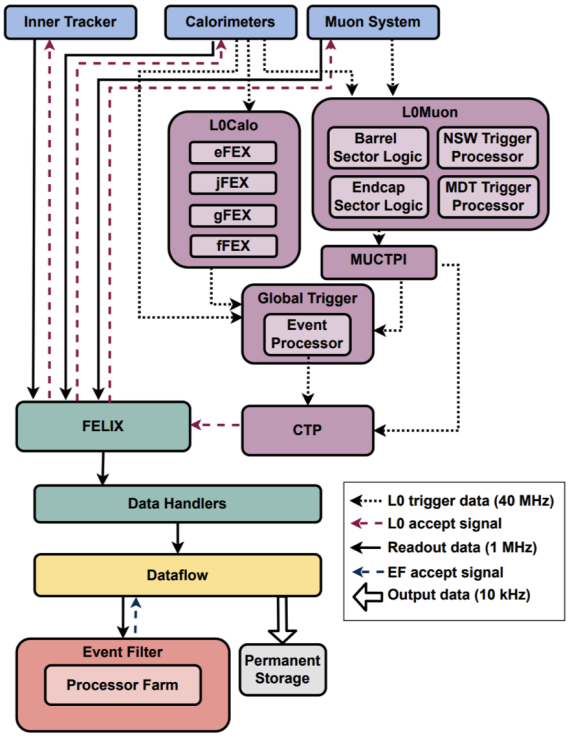


*Figure 25.* Schematic of the Run 4 TDAQ system ATLAS Collaboration (2017c). Detector data flows to the legacy L0Calo and L0Muon systems, as well as full granularity calorimeter informatoin to the Global Trigger. The Global Trigger passes trigger objects to the CTP for the final trigger decision. Events are then passed to the Event Filter for more detailed processing and a final storage decision.

#### 4.0.1 ATLAS Global Trigger.

ATLAS will rely on a Level-0 hardware trigger, called the Global Trigger within TDAQ, that reduces the event rate to 1 MHz. The purpose of the Global Trigger is to bring offline-inspired algorithms to the Level-0 trigger system, improving trigger object definitions for final selection in the central trigger processor (CTP). As seen in Figure 26, Muon data and full granularity cell data from LAr and Tile (hadronic calorimeter), along with the legacy L0Calo trigger objects, will be sent to the Global Trigger at a rate of 40 MHz through a series of time-multiplexers (MUX). The MUX will distribute events tagged by bunch crossing ID (BCID) to the Global Event Processors (GEPs) 48 events at a time, where they will be processed in parallel. Each GEP node is housed on a Xilinx Versal Premium 1802 Field Programmable Gate Array (FPGA), allowing for flexible and optimized firmware to be run. The current best estimate for total time the GEPs have to process an event is 4.27$\mu$s, and the maximum possible value for processing time is 5.72$\mu$s Begel and Sankey (2021). After the GEPs process an event, it is passed to the demultiplexing CTP interface where the final trigger decision is made. If an event passes the CTP, it will reach the Event Filter, which will store data at a rate of 10kHz on tape ATLAS Collaboration (2017c).

The following upgrade sections discuss the development and performance studies of the topological clustering algorithm to be implemented in the Global Trigger.

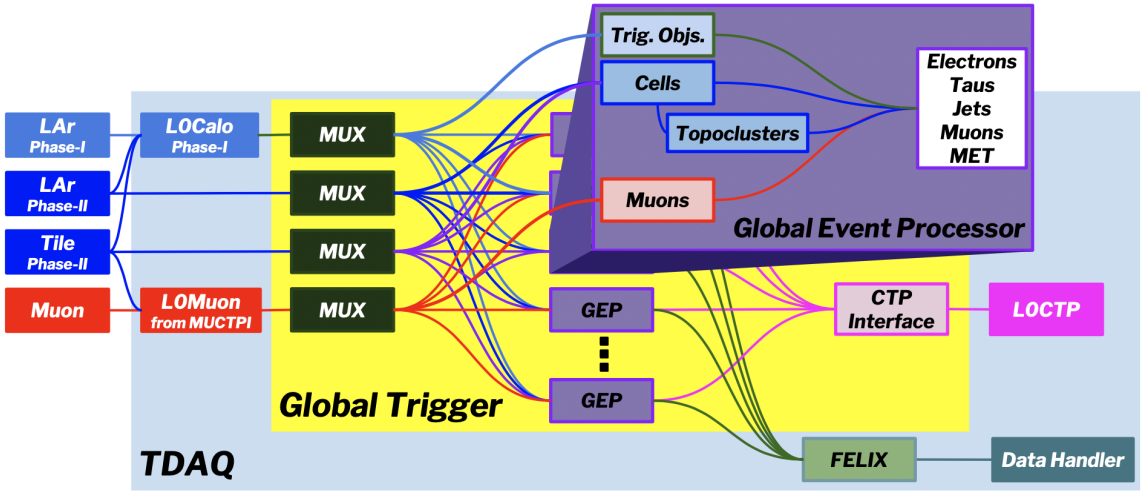


*Figure 26.* Illustration of TDAQ with emphasis on the Global Trigger System. ATLAS Collaboration (2017c).

#### 4.0.2 Topological Cell Clustering Algorithms.

Topological clusters (topoclusters) are three-dimensional groups of neighboring calorimeter cells within ATLAS ATLAS Collaboration (2017j). The goal of grouping cell signals together from an event is to separate physics signals from background electronic noise and pile-up. Formation of clusters is based on signal significance of the cells, and where cells are in relation to others in $\eta$, $\phi$, and across layers. The neighboring cells energies are summed, and the location of the resulting cluster can be determined from the cell locations and energies. Clusters may contain the full or fractional detector response to a particle shower, or the merged response to nearby particles, depending on the types of particles and their energies. These clusters are the basis of jet and tau reconstruction, and vital for identifying electrons, muons, and photons. They are also necessary inputs for energy flow observables such as missing transverse momentum. As with jets, the algorithm used greatly affects the physical representation of the cluster. Two common topoclustering algorithms are the "420" and "422" schemes.

#### *4.0.2.1 ATLAS 420 and 422 algorithm.*

ATLAS utilizes a robust offline topoclustering method called the "420" scheme, which groups segmented sections of the calorimeters, or cells, into clusters based on various levels of signal significance:

$$\varsigma_{cell}^{EM} = \frac{E_{cell}^{EM}}{\sigma_{noise,cell}^{EM}} \tag{4.1}$$

,

where $E_{cell}^{EM}$ is the cell signal and $\sigma_{noise,cell}^{EM}$ is the quadrature sum of the cell electronics and pile-up noise. These signals are measured on the electromagnetic (EM) energy scale, and corrections for hadrons must be added later ATLAS Collaboration (2017j). For the studies, a multijet background sample, JZ0W, and a signal sample, HH $\rightarrow$ 4b, are used for the performance studies in this paper, and are described in more detail in Section 4.0.4. A distribution of cell transverse energies ($E_T$) is shown in Fig. 27 for reference. Clusters are formed using the following selection variables:

$$|\varsigma_{cell}^{EM}| > S \text{ primary seed threshold,} \tag{4.2}$$

$$|\varsigma_{cell}^{EM}| > N \text{ threshold for growth control,} \, and \tag{4.3}$$

$$|\varsigma_{cell}^{EM}| > P \text{ principal cell filter.} \tag{4.4}$$

For the 420 scheme, $S = 4$, $N = 2$, and $P = 0$. A cluster starts with a seed cell satisfying Eq. 4.2, and cells adjacent to the seed passing the criteria in Eqs. 4.3 and 4.4 are added to the cluster. If one of these newly clustered cells passes Eqs. 4.3, its neighbors are collected if they satisfy at least Eq. 4.4. This process repeats, where neighbors of cells that pass Eqs. 4.3 are added to the cluster. A

cluster is made for each seed cell, called a proto-cluster, and these proto-clusters are merged or split using a weighting calculation until clusters are finalized ATLAS Collaboration (2017j). An example of clusters from the 420 scheme are shown in Fig. 28.

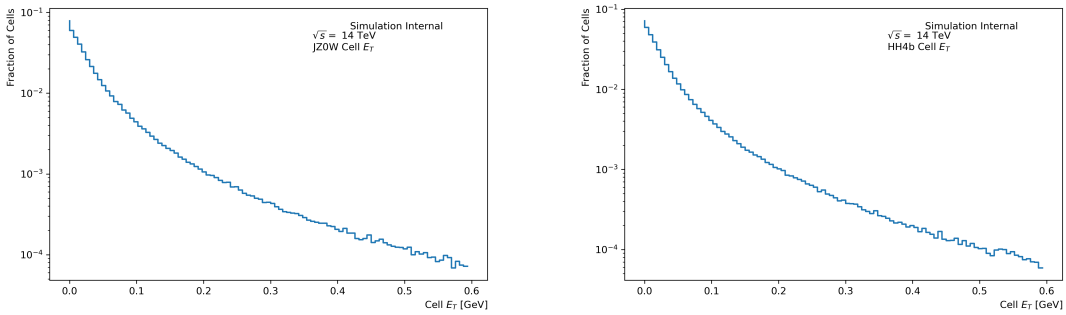


*Figure 27.* Cell $E_T$ for a background (left) and signal (right) sample.

422 clusters are also available for use in ATLAS offline analysis. The process for growing clusters is the same as the 420, except in the growth control parameter, which is now $P = 2$. This means that only neighboring cells that have $|E| > 2\sigma^{EM}_{noise,cell}$ can be added to a cluster. In terms of performance, there have not been many in-depth comparisons between 420 and 422 clusters or reconstructed observables from them. This study has the added benefit of conducting some of these studies as a byproduct, and the results are discussed in Sections 4.0.4 and 4.0.5.

Since the selection variables only rely on the absolute value of cell significance, negative cell signals can be used in clustering. This comes from pile-up and electronic noise fluctuations. Clusters seeded from negative cell energies are used for noise diagnostics offline, and are included in the list of clusters within the ATLAS software framework `athena`.

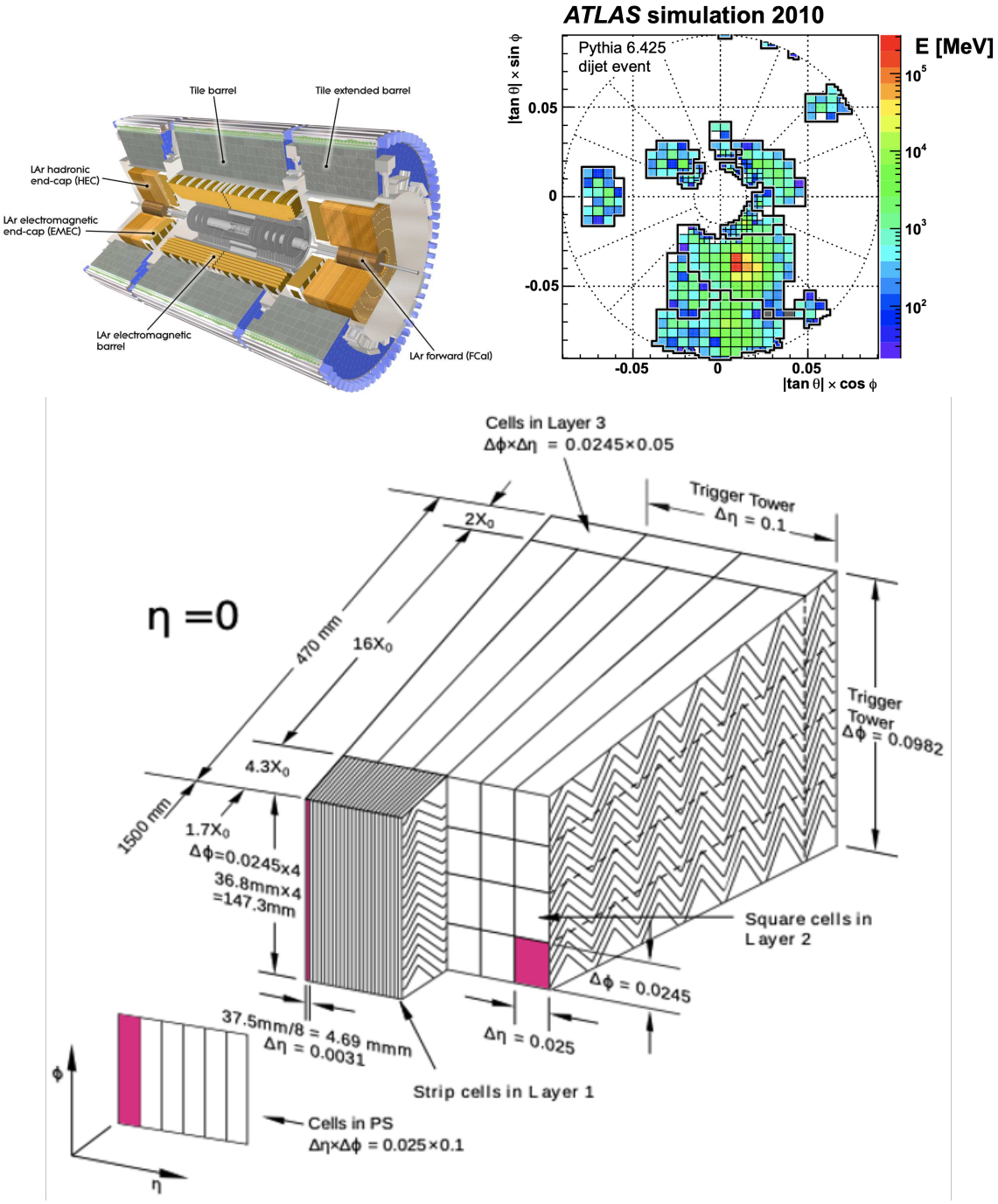


*Figure 28.* ATLAS LAr and Tile calorimeter system, where cells segmented in $\eta$ and $\phi$ are used for topoclustering (left). Clustered cells from the FCAL calorimeter for a simulated dijet event using the 420 scheme (right). A closeup of the segmentation of cells in the LAr EM Barrel (bottom).

#### *4.0.2.2 422 Scheme for the Global Trigger Topoclusters.*

With access to the full granularity cell information from the LAr and Tile calorimeters, seen in Fig. 28, the GEPs will reconstruct topoclusters online, which will then be included in the Trigger Objects (TOBs) for trigger algorithms downstream. The location and energy information in the topoclusters are especially important for the anti-$k_t$ jet-finding trigger. The planned version of topoclustering on the GEPs will follow the offline "422" scheme described above with a few notable differences. Given the challenging time constraints the Global Trigger has to process events, a balance between speed and accuracy in topocluster reconstruction is needed. The calorimeters are also limited in how fast they can output cell information, and will only be passing positive energy cells with $E_T$ above $2\sigma$, or "zero-suppressed" data. 422-like algorithms output fewer clusters per event and fewer cells per cluster than the 420 scheme, and is more ideal for the Global Trigger. A comprehensive split/merge step for the global trigger clustering algorithm would take considerably more resources, and is proven to be unnecessary for the current algorithm as shown in Section 4.0.3.

The GEPs will be given 2 lists of noise-suppressed cell index "masks" for topoclustering, cells above $4\sigma$ and $2\sigma$, along with the full raw cell $E_T$ data. This differs from the 422 and 420 clusters which use full cell energy. It is important to note that topoclustering on the GEPs will only be made out to $|\eta| < 3.2$. Topoclusters will be reconstructed in less than 2 $\mu$s and output TOBs will contain the topoclusters $E_T$, $p_{x,y,z}$, max $E_T$ cell $\eta$ and $\phi$, and the constituent cell IDs. The current topoclustering algorithm candidate, Unique Seed Cell Association (USCA), is designed to perform similarly to the 422 algorithm while maintaining simplicity and efficiency for the Global Trigger.

**4.0.3 Unique Seed Cell Association Algorithm.** The USCA algorithm is designed to be similar to the offline "422" version in `athena` and uses only zero-suppressed cells from $4\sigma$ and $2\sigma$ lists. Neighboring cells are defined to be those physically nearby in the same layer, or that overlap in $\eta$ and $\phi$ in adjacent calorimeter layers. For a specific cell, the neighboring cells are defined as "shell 1" around the cell. The neighbors of the cells in shell 1 are labeled as "shell 2" relative to the original cell and so on for each new shell. Only the cluster $E_T$ is calculated, coming from the sum of cell $E_T$s. $\eta$, and $\phi$ are simply taken from the highest energy cell in the cluster, while the 422 and 420 algorithms use cluster moments to calculate the cluster location ATLAS Collaboration (2017j). The major steps of the USCA algorithm, as seen in Fig. 29, are seeding and adding direct neighbors, fixed shell growth, and seed merging. From here on, "$n$-shell clusters" refers to the number of iterations in the fixed shell growth step.

- Seeding and Adding Direct Neighbors:
  - Start with a $4\sigma$ seed from the list.
  - Every neighboring cell is considered to be in shell 1, and cells above $2\sigma$ are added to the cluster.
- Fixed Shell Growth:
  - For each new cell added to shell 1, check if it has neighboring cells above $2\sigma$ and add them to the cluster. This is now a 2 shell proto-cluster
  - Repeat for "n" iterations, creating a "$n$ shell proto-cluster".
- Seed Merging:
  - After all seeds have a proto-cluster, iterate through the list of clusters.

* If the current proto-cluster contains seed cells from other proto-clusters, merge cells from those proto-clusters to the current proto-cluster.
* Remove merged proto-clusters from the list and move to next proto-cluster.

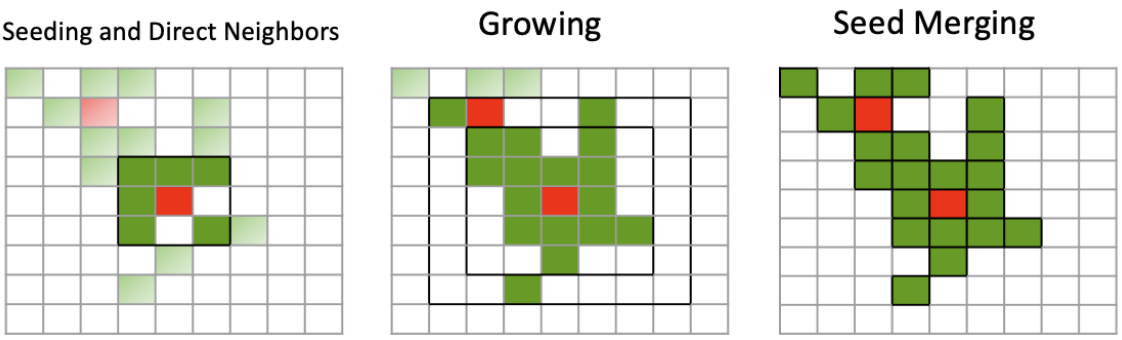


*Figure 29.* Diagram of the USCA algorithm, in 2 dimensions for simplicity. $2\sigma$ cells are in green and $4\sigma$ in red. The central $4\sigma$ cell is the seed for the current cluster, and there are 3 shells of growth. The cluster for the top left $4\sigma$ cell is merged into current cluster.

A 3-dimensional visualization of a USCA cluster with different shells is shown in Fig. 30 for reference. All seeds make proto-clusters, but a cluster may or may not contain more than one seed. If clusters with 2 shells or more are produced, and a seed does not have any cells above $2\sigma$ in its 1st shell, it will not add any potential $2\sigma$ cells from its 2nd shell. This is not common for signal events since particle showers tend to leave a trail of energy deposits through the detector, not singular pockets of energy.

Splitting does not become vital to prevent overly large clusters since there are only a fixed number of shells in the growing stage, as compared to the offline 422 and 420 algorithms. This is observed in a typical spread of $2\sigma$ and $4\sigma$ cells from an HH4b sample in the LAr calorimeters, shown in Fig. 32. It is possible for $2\sigma$ cells on the edges of clusters to be double-counted. If two separate clusters

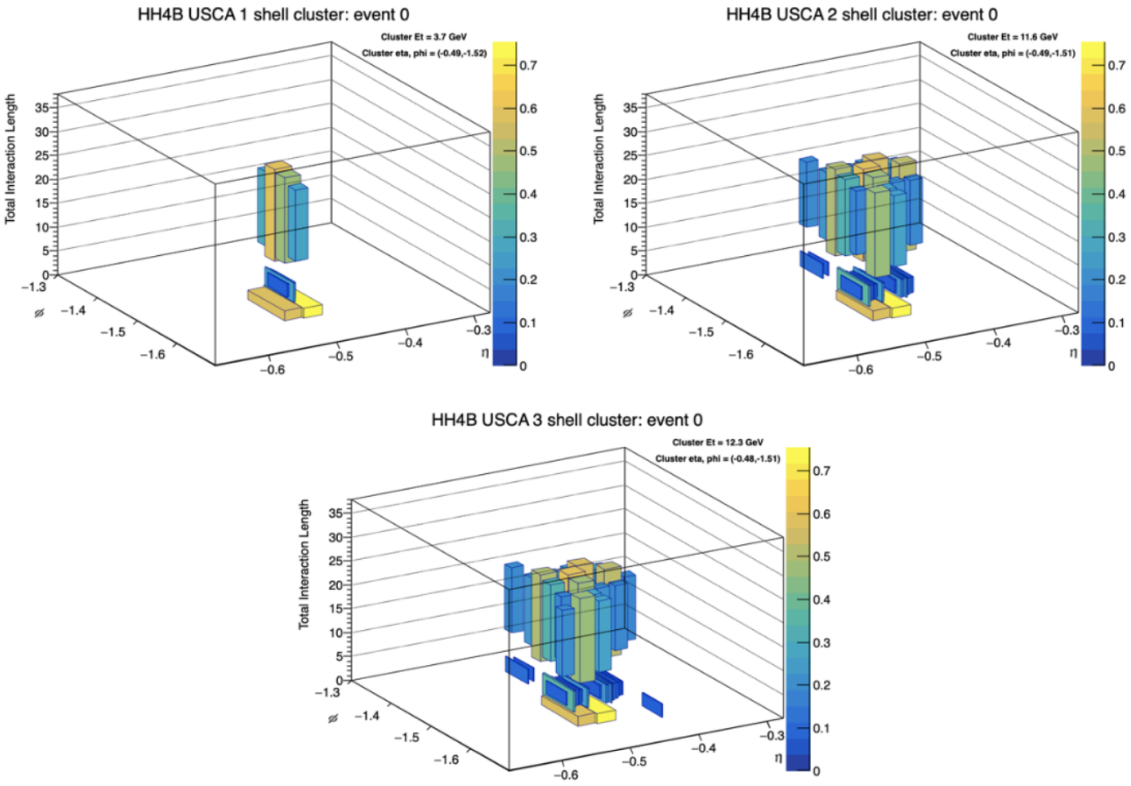


*Figure 30.* A USCA cluster after 1,2, and 3 shells of growth. The cell volumes are scaled by their energy. Courtesy of Ryan Stuve.

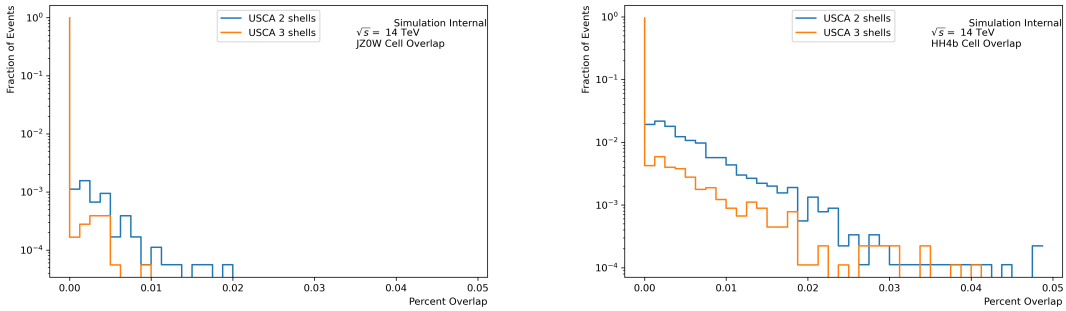


*Figure 31.* Percent of cell overlap per event for background (left) and signal (right) samples.

are nearby and not close enough to share seeds, but have shared $2\sigma$ cells in their outer shells, this will cause overlapping clusters and the double-counting of cells. This happens rarely since there are usually enough $4\sigma$ seeds nearby to resolve this issue in the merging step. Fig. 31 shows the percent of total cells that are double-counted per event for background and signal samples on a log scale. Virtually all events have less than .05% percent of total cells shared, with only a handful out of thousands having more than a few cells overlapping.

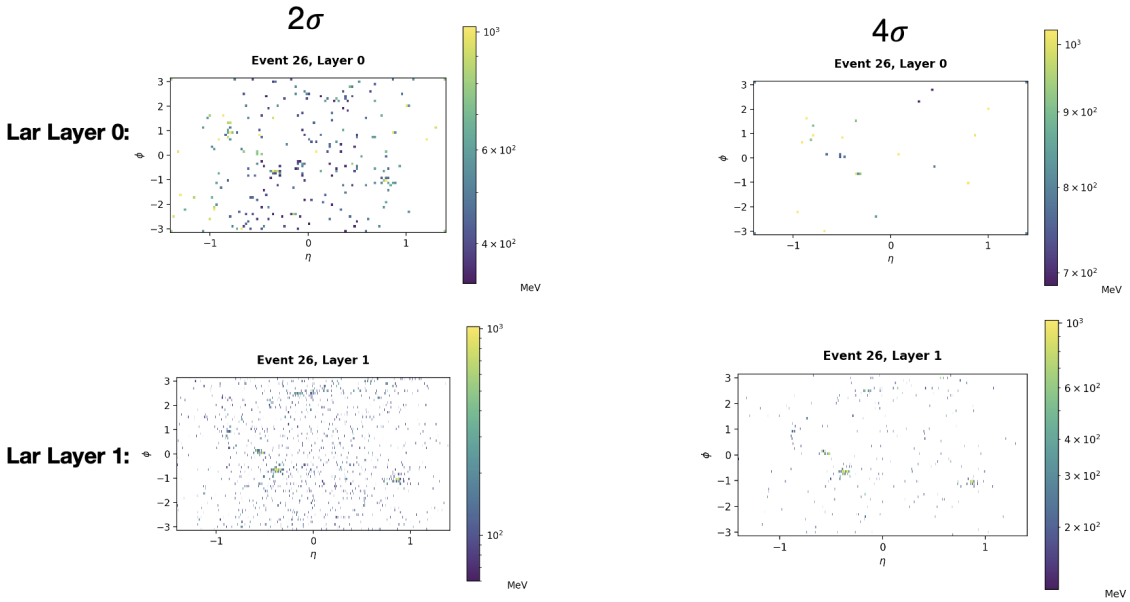


*Figure 32.* A map of $2\sigma$ (left) and $4\sigma$ (right) cell locations in the first two LAr Calorimeter layers in $\eta$, $\phi$ space from an HH4b sample.

#### 4.0.4 Physics Performance and Comparison.

The USCA algorithm is implemented in the Global Trigger Performance (GTP) package in `athena` release 21.9.26 found on this fork[1] in the athena/Trigger/TrigL0GepPerf folder. The GTP framework was created by collaborators for developers to run performance studies on custom trigger algorithms. It also includes ATLAS offline

[1] *https://gitlab.cern.ch/tmathew/athena.git*

algorithms, including the 422 and 420 clusters, for comparison studies. The main goal of the GTP package is to allow algorithms to be written more easily in `C++` and then interface them with the ATLAS analysis framework `athena`. The framework can be setup following instructions from the Global Trigger Performance documentation[2]. The USCA algorithm is currently stored on a separate fork of `athena` 21.9. With release 21 of `athena` having been deprecated in 2024, the GTP framework was moved to release 24, however, the workflow remains the same. A diagram of the GTP workflow is shown in Fig. 33.

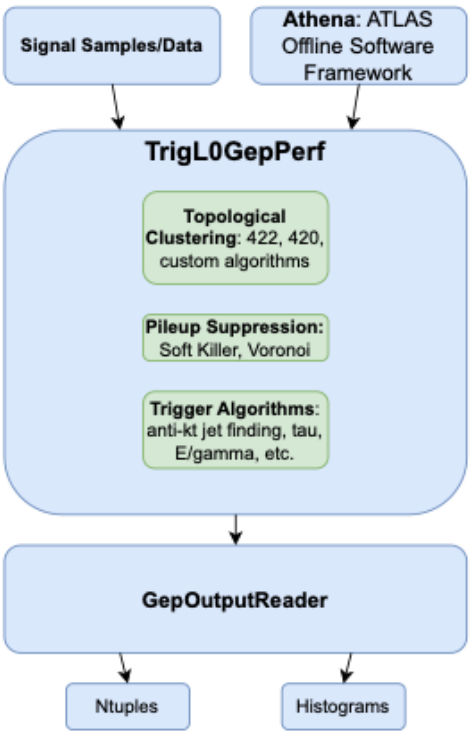


*Figure 33.* Global Trigger Performance framework.

[2] *https://globaltrigperf.docs.cern.ch*

The primary samples used for the physics performance studies are a signal HH $\rightarrow$ 4b[3], and background JZ0[4], which are described in Table 2. Both were generated at a center of mass energy of $\sqrt{s} = 14$ TeV and average pileup of $\langle\mu\rangle = 200$.

Table 2. Physics simulated samples used for topocluster studies

| Physics Process | Sample Name | Number of Events |
|---|---|---|
| HH $\rightarrow$ 4b | mc15_14TeV.600463.PhPy8EG_PDF4LHC15_HH4b_cHHH01d0.recon.AOD.e8222_s3654_s3657_r12442 | 9000 |
| JZ0 | mc15_14TeV.800290.Py8EG_A14NNPDF23LO_jetjet_JZ0WithSW.recon.AOD.e8185_s3595_s3600_r12065 | 18000 |
| $t\bar{t}$ | mc15_14TeV.600012.PhPy8EG_A14_ttbar_hdamp258p75_nonallhad.recon.AOD.e8185_s3595_s3600_r12063 | 8200 |

As noted above, the Global Trigger is planned to only have access to cells within $|\eta| < 3.2$, and the following plots are made with 422 and 420 clusters within those $\eta$ bounds unless otherwise stated. There is also a minimum cluster $E_T$ requirement of 1 GeV applied to all clusters before they are sent to other algorithms. The motivation of this transverse selection is to improve the jet reconstruction performance and reduces background noise and pile-up. This selection is applied before splitting for the 420 and 422 clusters, and cannot be changed currently because of how the GTP framework interfaces with `athena` algorithms. The two candidate versions of the USCA clusters are with 2 and 3 shells, which is reflected in the performance plots in the following section. Some initial studies that led to narrowing down from 1-5 shells are in Appendix A.

***4.0.4.1 Cluster Energies.*** The primary metrics of the USCA algorithm performance is comparing the various cluster variables to that of the 422 and 420 algorithms. The cluster $E_T$ will be included in the TOBs within the Global Trigger and is the most natural place to begin studying physics performance. USCA clusters from 2 and 3 shells are shown in Figure 34 for

[3] *HH $\rightarrow$ 4b sample*

[4] JZ0 sample

signal and background. The distributions are clearly similar, with the only major

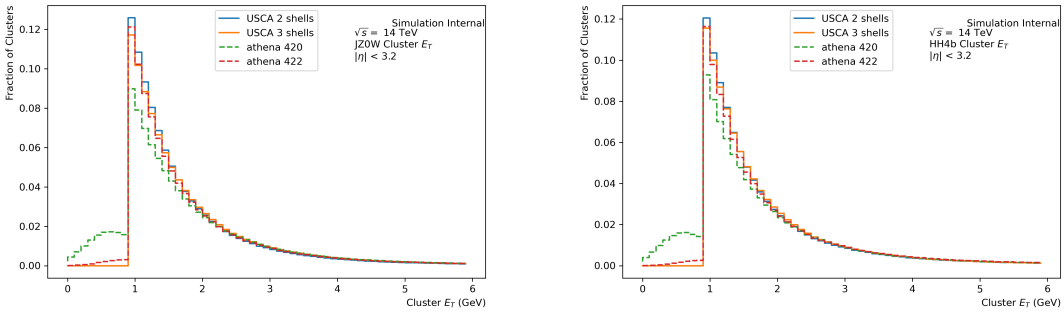


*Figure 34.* Cluster $E_T$ for background JZ0 (left) and HH $\rightarrow$ 4b (right).

difference being the transverse energies below 1 GeV for the 420 and 422 clusters from splitting. As mentioned above, splitting of the athena 422 and 420 clusters happens after the 1 GeV cut, explaining the small distribution of clusters below 1 GeV. This is a very small fraction of the total clusters, and is not expected to have a significant effect on physics performance. The USCA clusters have $E_T$ values close to the 422 clusters, while the 420 clusters have a distribution that leans to slightly higher values on average due to there being more cells in the sums, although the difference is small, again due to the fact that large clusters are split. The differences between the USCA and 420 or 422 clusters becomes more apparent at high energy.

The leading 50 clusters in $E_T$ are shown in Fig. 35. For high energy, large $\Delta R$, or close-by particle showers, the USCA clustering algorithm will have more high $E_T$ clusters on average because there is no splitting. This effect is heightened with a larger shell count in the growing stage, and is seen in the separation of the 3-shell distribution compared to its 2-shell counterpart or the 420 and 422 algorithms.

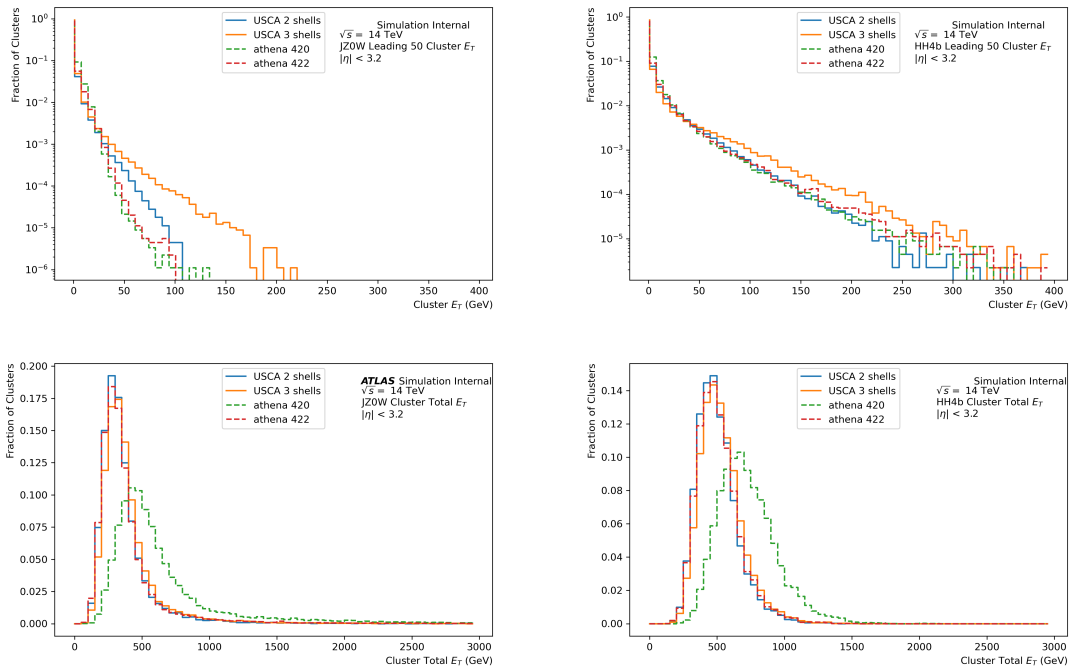


*Figure 35.* The leading 50 clusters in $E_T$ for background JZ0 (top left) and HH $\rightarrow$ 4b (top right). Total $E_T$ distributions for background JZ0 (bottom left) and HH $\rightarrow$ 4b (bottom right)

The sum of all cluster transverse energies is shown in Fig. 35. USCA cluster total $E_T$ closely matches the 422 clusters and is lower than the 420 clusters as expected. Without the edge $0 < E_T < 2\sigma$ cells, the 422 and USCA clusters will be a few hundred GeV less than the 420 clusters with $\sqrt{s} = 14$ TeV collisions, as seen in the plot. The difference between 2 or 3 shells is small since most cells that would get picked up by a cluster are included in a cluster, even though the growing stage is 1 less iteration. The reason for this is because cells with high energy are necessarily nearby, so even though there might be more clusters on average for the 2-shell USCA algorithm compared to the 3-shell, there are enough seeds to grab nearby $2\sigma$ cells that should be in a cluster. There is also evidence from cluster multiplicity studies that using higher shell counts for the USCA clusters does not lead to significantly larger clusters, again supporting the conclusion that high energy cells are close enough to be picked up in 2 or 3 iterations of growing.

***4.0.4.2 Cluster Multiplicity and Locations.*** Accurate cluster locations improve jet reconstruction and capturing detector response to particle showers. The USCA cluster $\eta$ and $\phi$ are taken from the highest $E_T$ cell and does not exactly match the location of 422 or 420 clusters as defined by the cluster moment calculations. Even with this difference, the cluster $\eta$ distributions are similar for the USCA and 422 algorithms as seen in Fig. 36. The 420 distribution is flatter, with more clusters having values away from 0. This could be from the splitting, since the number of clusters near a specific $\eta$ value would double for each split cluster.

Cluster locations for a single background or signal event are shown in Fig. 37, with the dots scaled by energy. While there are minor differences, the majority of clusters are overlapping between the different algorithms, and the difference

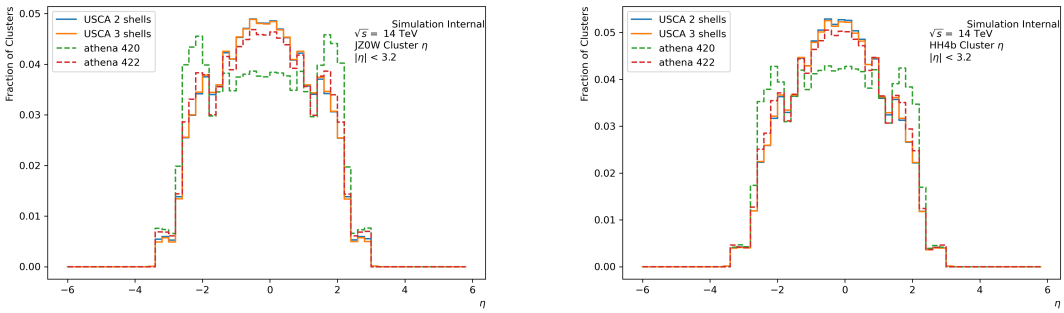


*Figure 36.* Cluster $\eta$ for background JZ0 (left) and HH $\rightarrow$ 4b (right).

in how cluster $\eta$ and $\phi$ are calculated does not lead to large discrepancies in location. After looking into the leading 50 cluster energies in more detail, the main differences between algorithms come from the selection of the leading 50 clusters. Specifically, clusters near either side of the cut-off, $\sim$ 40 to $\sim$ 60, may be ordered differently for each algorithm.

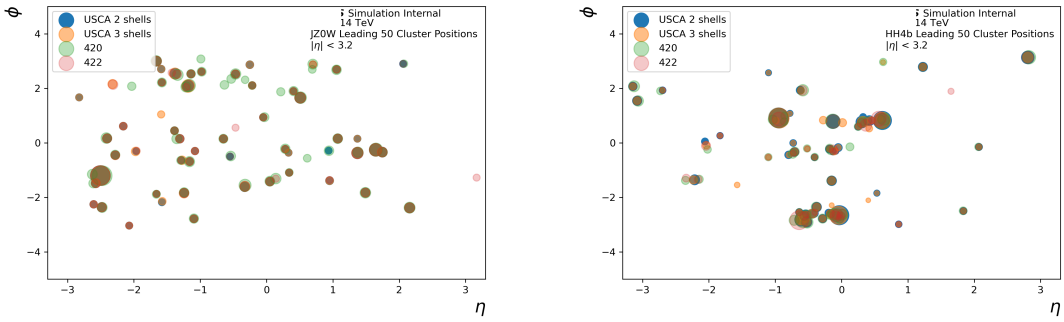


*Figure 37.* Cluster locations for the 50 leading $E_T$ clusters for background JZ0 (left) and HH $\rightarrow$ 4b (right).

For 422-like clusters, initial evidence that splitting may not be necessary is seen in cluster multiplicity studies. The growing stage is limited compared to the 420 algorithm, leading to less physically large clusters. The 420 merging stage will merge clusters that have shared edge cells, so two nearby particle showers can become merged into a large cluster just from one shared cell that has energy

less than $2\sigma$, thus the splitting step becomes important. Limited bandwidth and

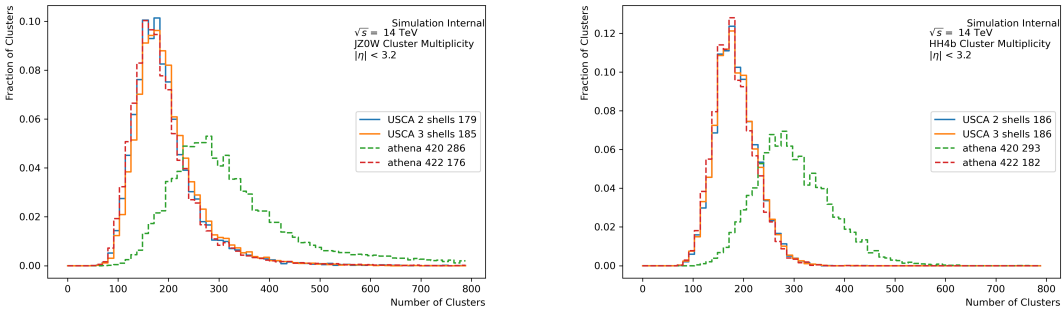


*Figure 38.* Cluster multiplicity for background JZ0 (left) and HH $\rightarrow$ 4b (right).

latency within the Global Trigger requires the topoclustering algorithm to balance computation time and physics performance. Cluster multiplicity is shown for signal and background in Fig. 38. It is clearly seen that even without a splitting step, the multiplicity is almost identical between 422 and USCA clusters, based on the gaussian mean of the distributions. The conclusion from the study is that the splitting step in the 422 clusters rarely finds multiple local maxima within a cluster, and the USCA clusters perform similarly. This also supports the earlier statement that the differences between the 2- and 3-shell USCA clusters is minimal, meaning that the merging step counteracts the smaller growing stage.

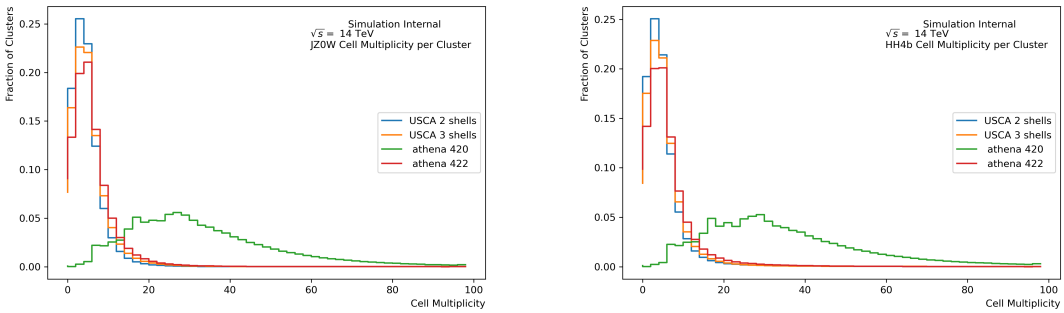


*Figure 39.* Number of cells per cluster for background JZ0 (left) and HH $\rightarrow$ 4b (right).

The expected number of cells per cluster is plotted in Fig. 39. The USCA clusters again have distributions that are similar to the 422. In the 420 cluster scheme, there are a much higher number of cells per cluster. This coupled with the cluster multiplicity provides concrete numbers to estimate bandwidth usage and computation time. Even though 2- to 3-shell clusters can have more than 25 cells before merging, the plots show that on average, post-merged clusters have roughly half that number or less for signal and background events. There are many lower energy clusters from background/pileup interactions, and only using $2\sigma$ cells limits growth of the clusters. Signal events may also not create physically large clusters since the particles tend to be collimated into a smaller R regions with high energy deposits in a smaller number of cells. The number of larger R clusters in signal events seems to be smaller, especially since this usually means the cluster has essentially captured most of the detector's response to the particle and is the only cluster used in the reconstruction of the resulting jet. In Fig. 32, energies from signal particle showers are seen to be grouped together in smaller R regions, supporting these arguments.

#### *4.0.4.3 Cluster Missing Transverse Energy.*

Clusters will be given as inputs to the missing $E_T$ (MET) algorithms on the Global Trigger, specifically for calculating the MET soft term. Cluster MET is not directly used for physics or trigger performance, but is included here as a preliminary step for more detailed studies to be done by the MET trigger group. The MET is calculated as the vector sum of all cluster $E_T$, and the plots shown in Fig. 40 are divided into the x and y components. Nothing stands out in the distributions, and again, it is seen that the USCA clusters perform similarly to the 422 clusters. For background or HH $\rightarrow$ 4b events, it is not expected to see large amounts of MET, and it may be

interesting to explore the MET distributions for a signal sample that would expect a larger amount from neutrinos or a dark matter candidate.

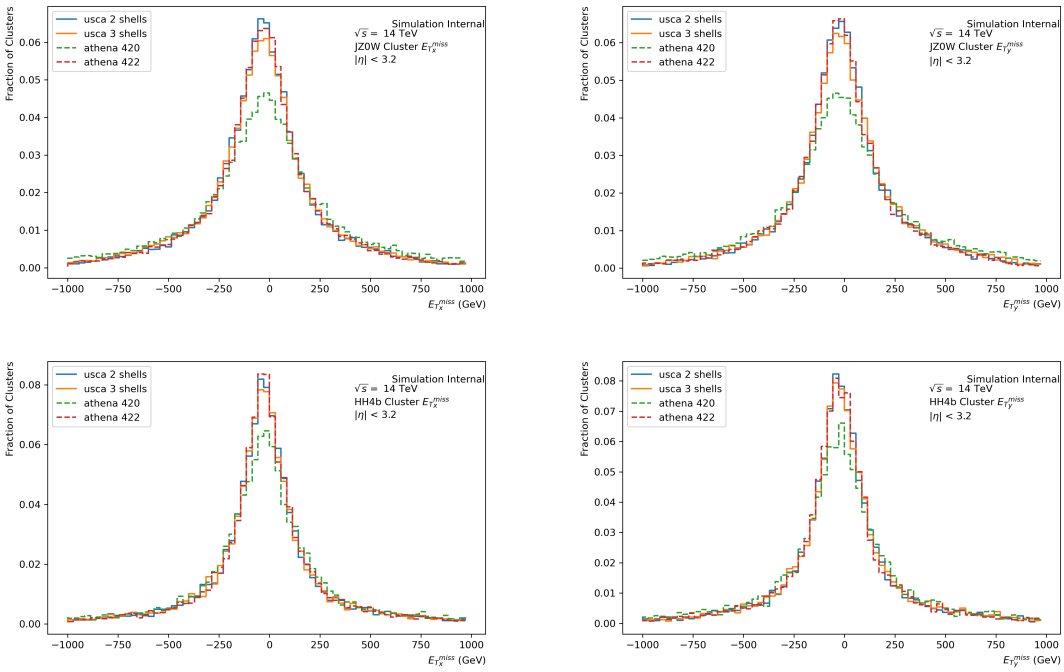


*Figure 40.* Cluster MET for background JZ0 (top) and HH → 4b (bottom) split into x and y components.

#### *4.0.4.4* ***Reconstructed Jet Performance.*** Jets for all clustering algorithms are reconstructed using the offline athena anti-$k_T$ algorithm. Future studies should use the USCA clusters as inputs to the Global Trigger jet reconstruction algorithm candidates, such as the cone jets algorithm implemented by collaborators. Jet $p_T$ is shown in Fig. 41 for background and signal samples. Distributions of the jet $p_T$ reconstructed from USCA clusters is very similar to the 422 jets, which is especially obvious on the log scale. This is not surprising given the similarities between the clusters themselves. If there are comparable clusters by location and $E_T$, then the resulting jets should be similar in location, energy, and number. The USCA and 422 jet $p_T$ distributions from JZ0 events diverge from their

420 counterparts, especially in the 24-125 GeV range. This may come from the higher spread in energy deposits from background processes, but most importantly the USCA and 422 jets behave similarly.

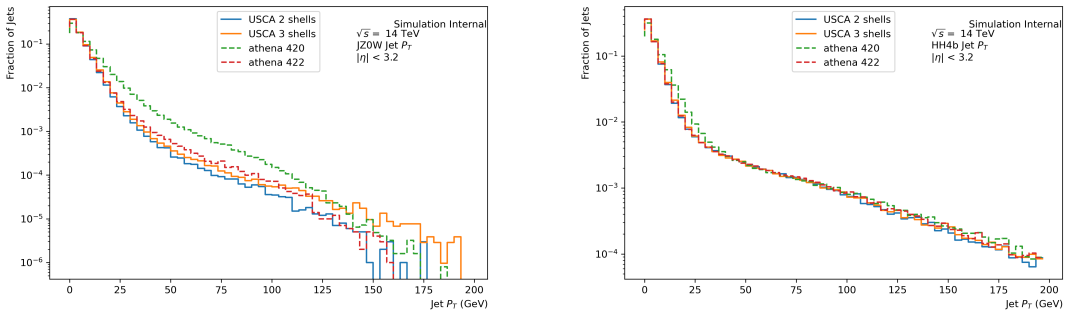


*Figure 41.* Jet $p_T$ for background JZ0 (left) and HH $\rightarrow$ 4b (right).

The $\eta$ distributions of reconstructed jets can be seen in Fig. 42, and again the distributions are similar between USCA and 422, with the 420 jets having a flatter profile because there is more splitting, allowing for jet locations that span the physical detector gaps. These dips are seen in the cluster $\eta$ plots as well, and are a direct consequence of the cluster positions.

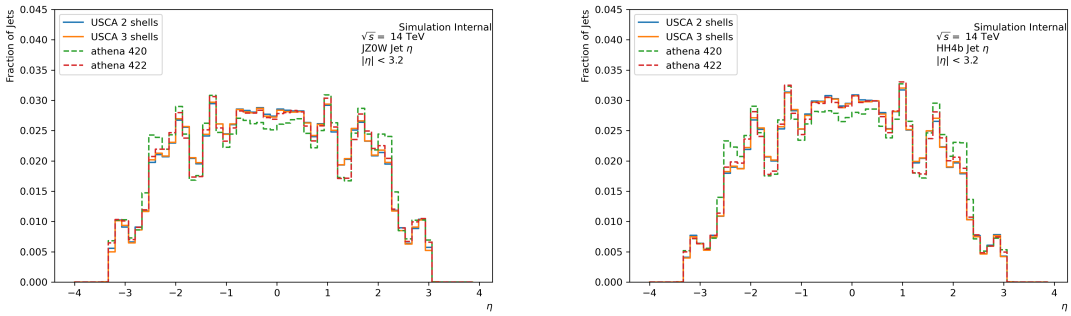


*Figure 42.* Jet $\eta$ for background JZ0 (left) and HH $\rightarrow$ 4b (right).

**4.0.5 Trigger Performance.** The main metric for Global Trigger algorithms is the trigger efficiencies and performance, especially since the goal is to improve useful event collection from the detector. For the trigger efficiency plots

show in this section, anti-k$_T$ jets with $R = 0.4$ are reconstructed from USCA, 422, and 420 clusters. The baseline jets for comparison are from the 420 clusters, and all trigger efficiency curves are shown as a function of this reconstructed offline jet $p_T$. There are two measures of trigger efficiency used in the plots, both fixed-threshold and at a fixed-rate of 60 kHz. Only jets within $\eta$ <2.5 are shown to reduce the amount of high $p_T$ jets that flood the rates in the higher $\eta$ regions of the detector. How a trigger "turns on", the steepness of the curve, is related to the resolution of the reconstructed jet $p_T$ and is the subject of interest in this section.

Fig. 43 shows the fixed-threshold trigger efficiencies for single and multi-jet triggers, with thresholds taken from the current Run 3 trigger thresholds. USCA jets perform similarly to the 422 jets, with slightly steeper turn-on curves for the 3-shell algorithm. All triggers are fully efficient within roughly 30 GeV of the thresholds despite the shallower turn-ons for the 2-shell jets. This is to be expected since 3-shell USCA clusters can more accurately represent 422 clusters, especially if the 422 clusters are large. Higher shell counts, 4 to 5 shells, show diminishing returns for USCA clusters.

Rate plots using jets from the JZ0 sample are shown in Fig. 44 for all 4-jet triggers. The $p_T$ cuts at the 60 kHz rate are almost identical between the 3-shell USCA jets and the 422 jets, with the 2-shell USCA jets having slightly lower cuts. There are no major deviations in the plots between USCA and 422 jets. The cuts are reflected in the trigger efficiency plots at fixed-rate seen in Fig. 45. The difference in turn-on steepness becomes more pronounced for the 2-shell USCA jets, which have shallower curves then their 3-shell counterparts, although this may be improved with a calibration of the USCA jets. To really study this difference, jet $p_T$ resolution plots should be made in the next iteration of cluster performance

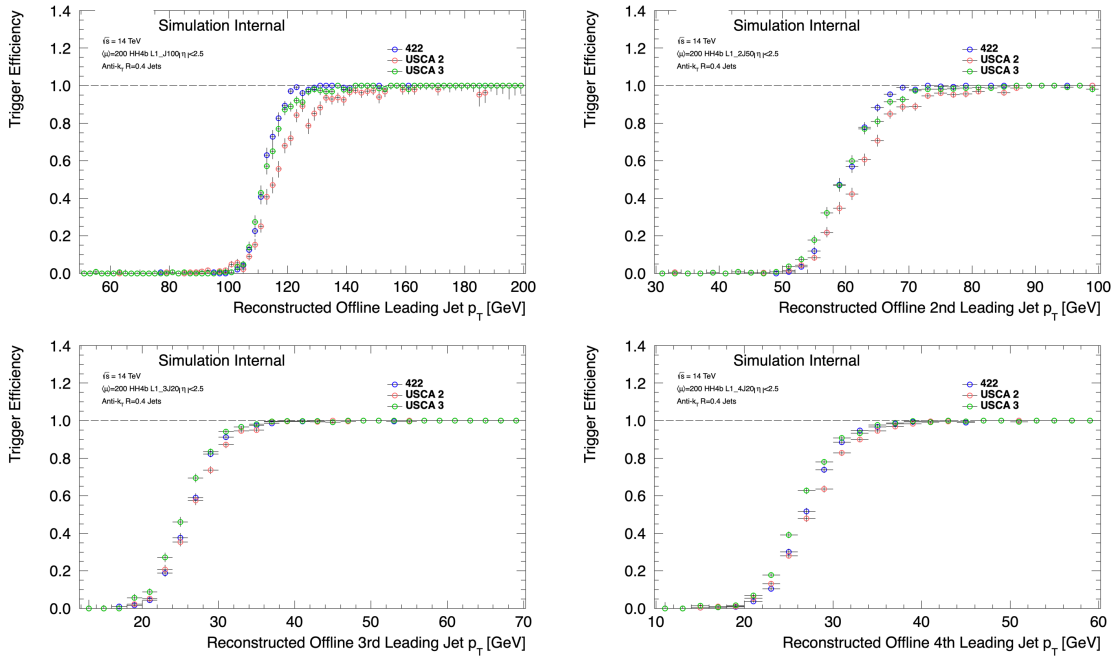


*Figure 43.* Fixed-threshold jet trigger efficiencies. The x-axis is the offline reconstructed jet $p_T$ from 420 clusters.

studies. It is expected to see a difference in the resolution of the 2-shell vs 3-shell or 422 jets leading to the shallower turn-ons.

#### *4.0.5.1 Seed-Only Trigger Efficiencies.*

For commissioning the Global Trigger, a simple option is to build and use seed-only clusters for downstream algorithms. Only $4\sigma$ cells would be used as inputs to the clustering algorithm, outputting ultra pileup suppressed clusters for the jet reconstruction algorithm. Preliminary physics performance plots were made to test the viability of triggering on these jets during commissioning. The seed-only clusters are referred to as proto-clusters in the plots. Rate plots for jets from these seed-only clusters are shown in Fig. 46 in comparison to the regular 422 jets. Thresholds are much lower as expected, with all $p_T$ thresholds below 50 GeV. Efficiency plots are shown in Fig. 47 using the aforementioned thresholds at fixed-rate. The turn-ons are very slow, especially for the multi-jet triggers that have ranges of $\tilde{4}0$ GeV before becoming

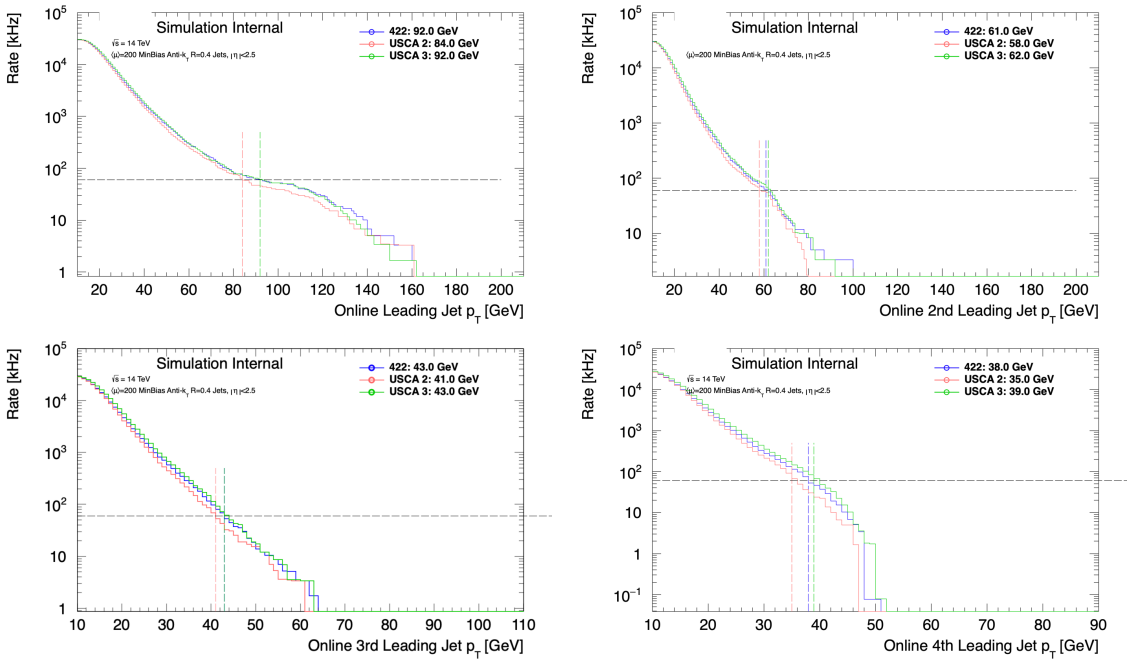


*Figure 44.* Rate plots using the JZ0 sample for single and multijets with a target rate of 60 kHz highlighted.

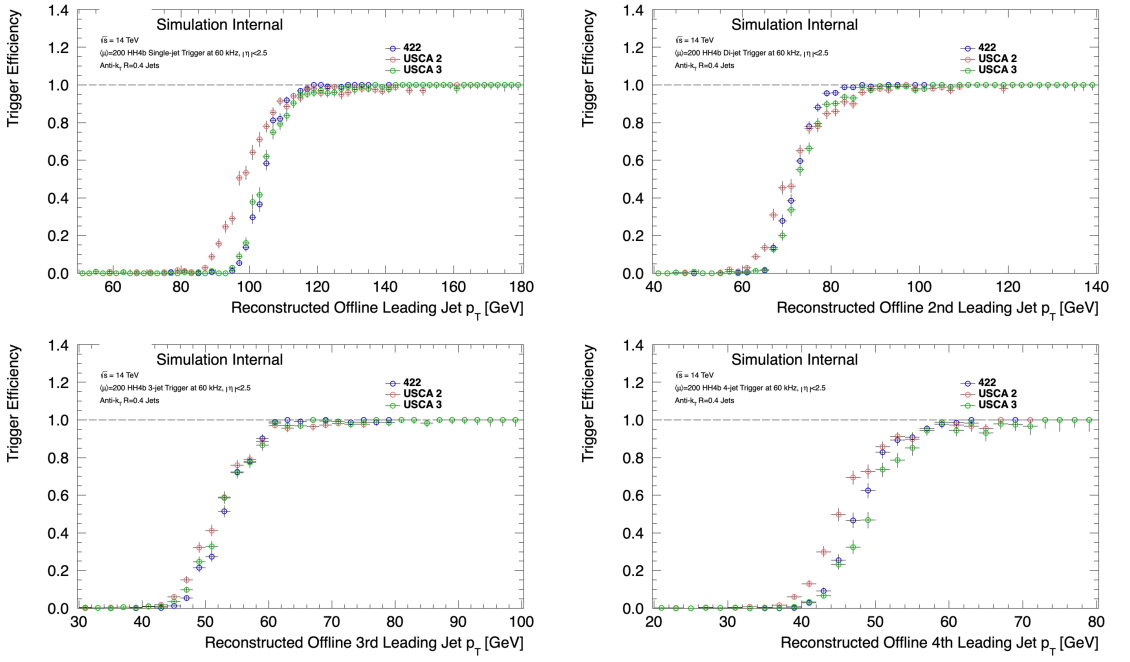


*Figure 45.* Fixed rate jet trigger turn on curves. A rate of 60 kHz was chosen for all single and multijet triggers.

fully efficient. However, from these studies alone, the seed-only clusters may be sufficient for commissioning. The single jet trigger with an online threshold of 50 GeV should be efficient enough to reconstruct jets from signal events with offline transverse momenta of 115 GeV or above.

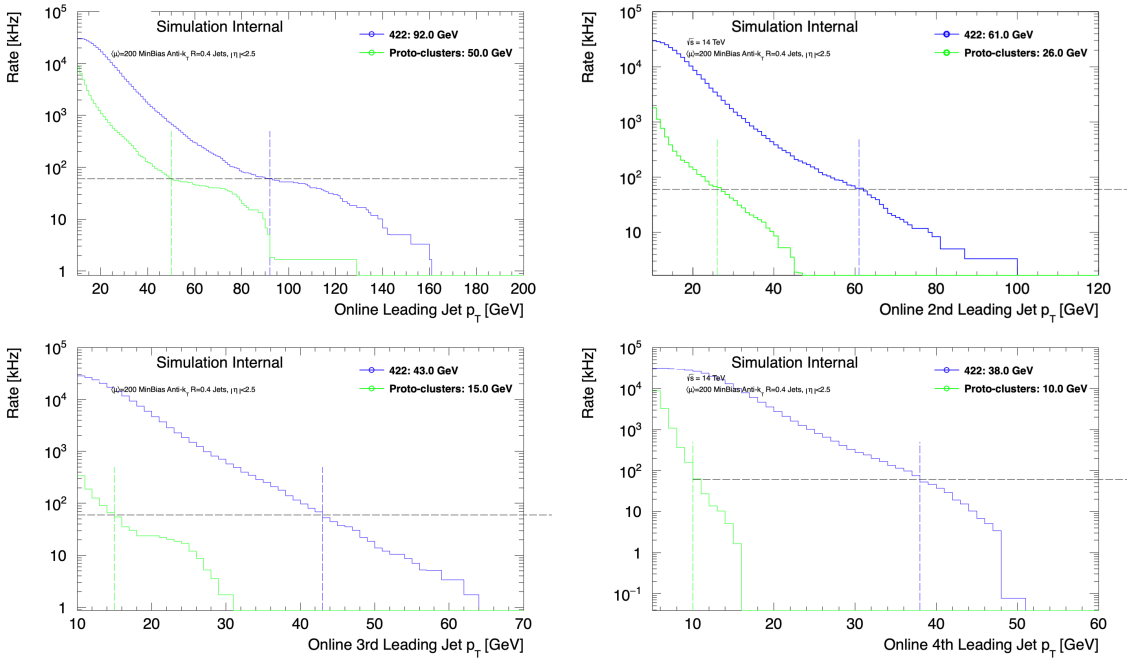


*Figure 46.* Seed-only rate plots using the JZ0 sample for single and multijets with a target rate of 60 kHz highlighted.

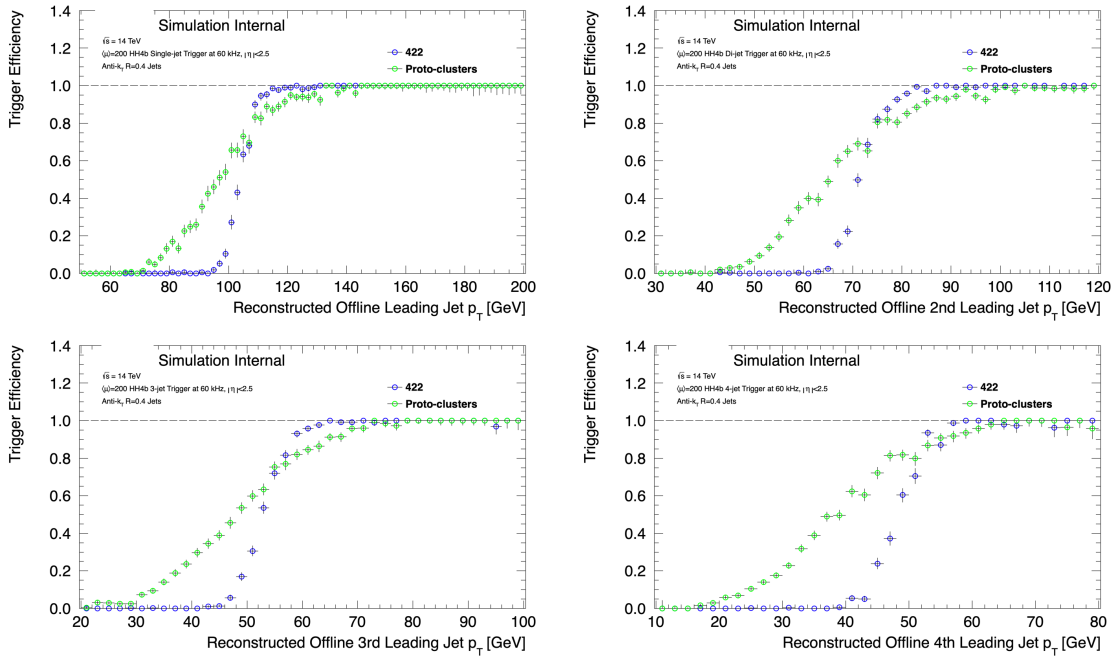


*Figure 47.* Seed-only fixed rate jet trigger turn on curves. A rate of 60 kHz was chosen for all single and multijet triggers.

**4.0.6 Test Vectors.** Part of the development process for the Global Trigger involves running firmware simulations in Verilog on test-bench FPGAs. Files called "test vectors" containing cell or cluster level information are created to validate the firmware. Starting with HH4b and JZ0W simulated physics samples with $\langle\mu\rangle = 200$, cell information is extracted using the GTP framework, and output to `root` files. A stand-alone `python` package [5] encodes the cell $E_T$ into 10-bit binary strings following Table 3, and the cell IDs (which contains position information) into 32-bit strings organized by event and position in $\eta$ and $\phi$ space. The $E_T$ strings are output to one test vector file, and the corresponding IDs to another file, both in `coe` format. The test vectors mimic the register size of input

[5] *https://gitlab.cern.ch/tmathew/topo_code*

to the FPGAs: 128 bits wide, and 256 bits deep. An example of a test vector containing cell $E_T$ is shown in Fig. 48.

Table 3. Binary encoding conversion to 10 bit strings. The first 2 bits represent the energy range, the other 8 bits are the index in that range. This format is subject to change as of March 2024.

| Leading 2 bits | Low (MeV) | High (MeV) | Step (MeV) |
|---|---|---|---|
| 00 | 32 | 1024 | 3.875 |
| 01 | 1024 | 8192 | 28 |
| 10 | 8192 | 65536 | 224 |
| 11 | 65536 | 524288 | 1792 |

Validation of, and studies with the test vectors were conducted to ensure accuracy and track the amount of expected data coming to the Global Trigger. Cell $E_T$ from the `coe` files were compared to the original data, and plotted in Fig. 48 as well. The data replication and translation to binary works as expected. Approximately 2.3% and .44% of cells are above $2\sigma$ and $4\sigma$ respectively for the HH4b sample. These values give the firmware engineers an expectation of data size for useful signal events. A future task is to create output test vectors for topoclusters, which will contain clusters in TOB format for downstream trigger algorithms.

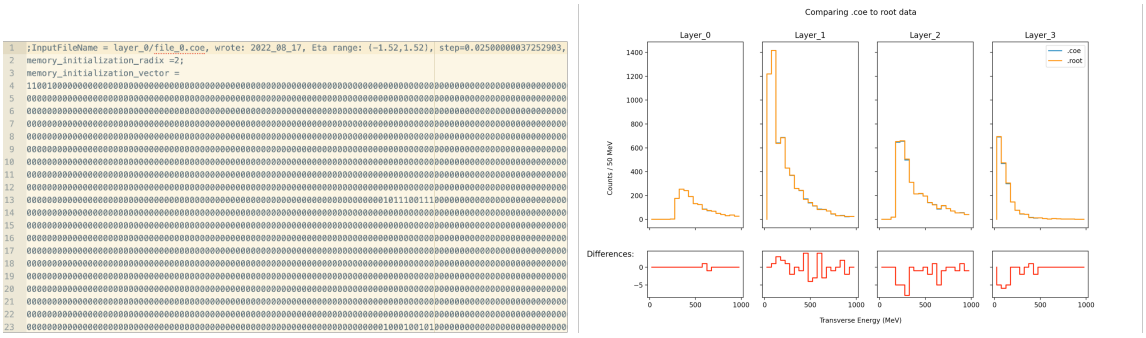


*Figure 48.* Example of `coe` test vector file with cell $E_T$ converted to 10 bit binary strings (left). Comparison of cell $E_T$ directly from the GTP output `root` file to cell $E_T$ from the test vector file (right).

**4.0.7 Cell Neighbor and Translator Files.** A common file format for testing and development for FPGA firmware is the `coe` file, which is a text file with hexadecimal values that can be read into the firmware as a lookup table or test vector. The newest iteration of `coe` files includes a lookup table of 2 shells of neighbors for every cell within $|\eta| < 3.2$. Seen in Fig. 49, the 32 bit online cell IDs are used, and the file has a 64 bit width. The first column is the potential seed cell's online ID, the second column is the first neighboring cell ID. Every line after is the list of other neighbors in the last 32 bits, while the first 32 bits are zero padded. This repeats for the next potential seed cell when the first 32 bits are non-zero again. 179,304 calorimeter cells are within the $\eta$ boundary, and most have on average $\tilde{2}5$ neighboring cells in their 2 shells, depending on the region of the calorimeter. A cross check was done on the `coe` file, seen in the middle of Fig. 49. A 3-D visualization of a seed cell with 1 shell of neighbors, and a visualization of 2 shells of neighbors is shown.

The other new file is a lookup table that translates from online cell ID or offline cell ID to the new internal GEP ID for each cell that will be sent to the Global Trigger. The current GEP ID format is an 18 bit ID: 5 bits for which mux the cell arrives on, 6 bits for the specific fiber, and 7 bits for the channel identifier of the cell. There are a maximum of 128 channels per fiber. The lookup table is also shown in Fig. 50, with the first 64 bits of each row the offline and online cell IDs, and the last 18 bits the GEP cell IDs.

***4.0.7.1 Cells per Fiber.*** LAr will only have the bandwidth to send 32 $2\sigma$ cells per fiber. This is in order of cells on each front-end board, not by energy, and the effects of this have not been studied yet. For higher energy particle showers, there could be a loss of cells. The latest test vector study was plotting the

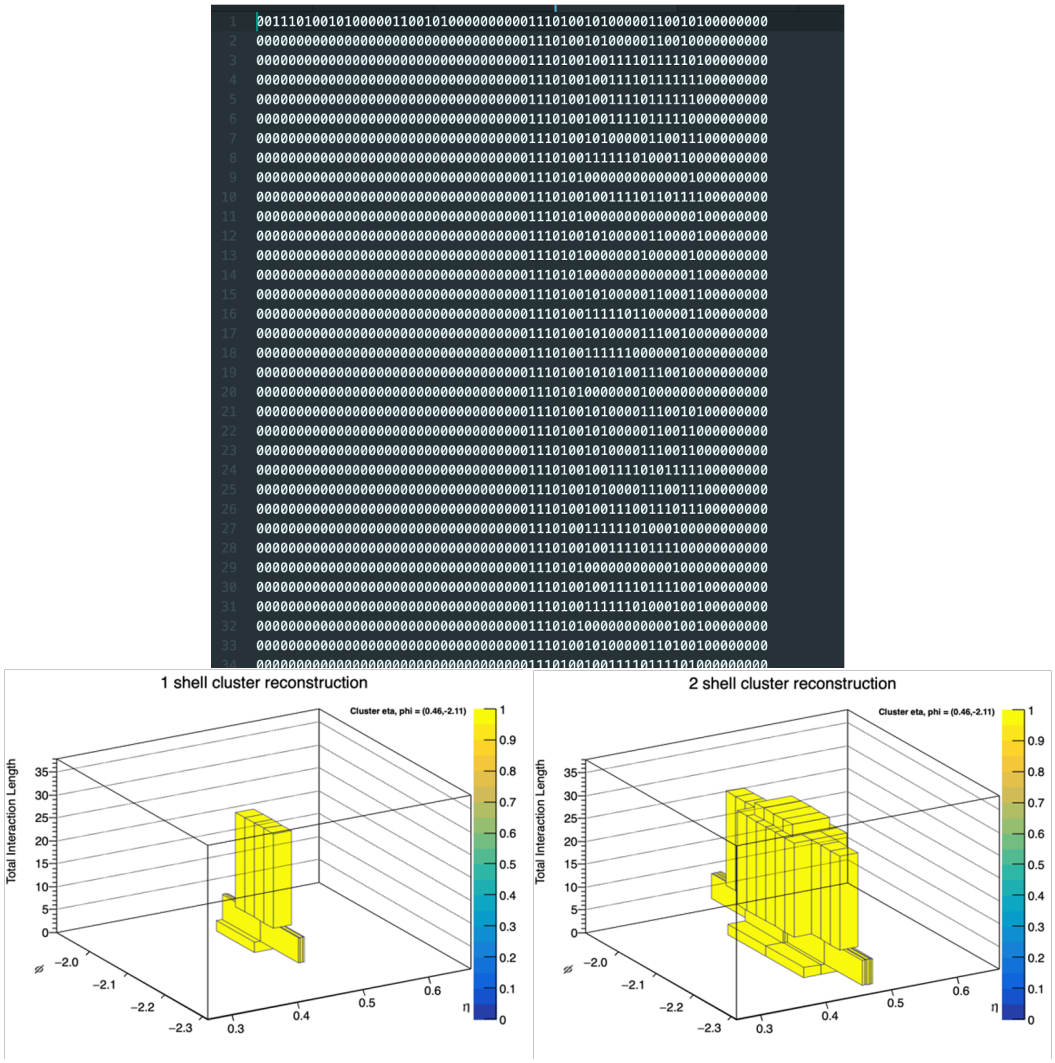


*Figure 49.* Example of `coe` file with list of 2 shells of neighbors for every potential seed cell within $|\eta| < 3.2$ (top). Visualization of a specific seed cell and 1 shell of neighbors (bottom left) and 2 shells of neighbors (bottom right).

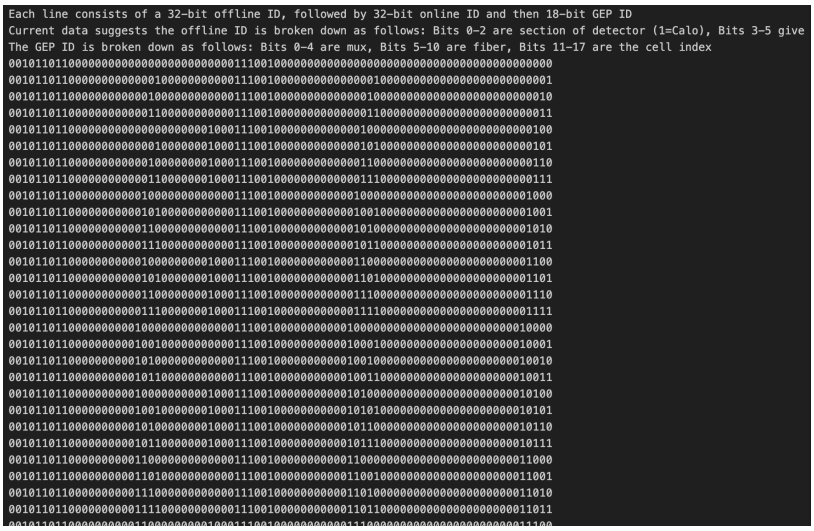


*Figure 50.* The lookup table `coe` file with online, offline, and GEP cell IDs.

number of $2\sigma$ and $4\sigma$ cells per LASP fiber using a background and signal sample, and the GEP cell IDs. As seen in Fig. 51, most fibers have fewer than 32 $2\sigma$ cells on average for the background sample. There are even fewer $4\sigma$ cells per fiber, but there are some fibers well above 32. In the bottom plots, only events that have a 420 jet with $p_T > 50$ GeV are plotted, which increases the average number of cells per fiber by removing many of the empty fibers. The same plots are shown in Fig. 52 for the HH $\rightarrow$ 4b sample, with notably fewer cells per fiber with and without the jet $p_T$ cut. As discussed in section 4.0.4, the signal particle showers tend to be more collimated, which will help limit the loss of cells being sent to the Global Trigger. This effect needs to be propagated to the clusters to see how the cluster growing stage is affected and subsequently the jet triggering efficiencies.

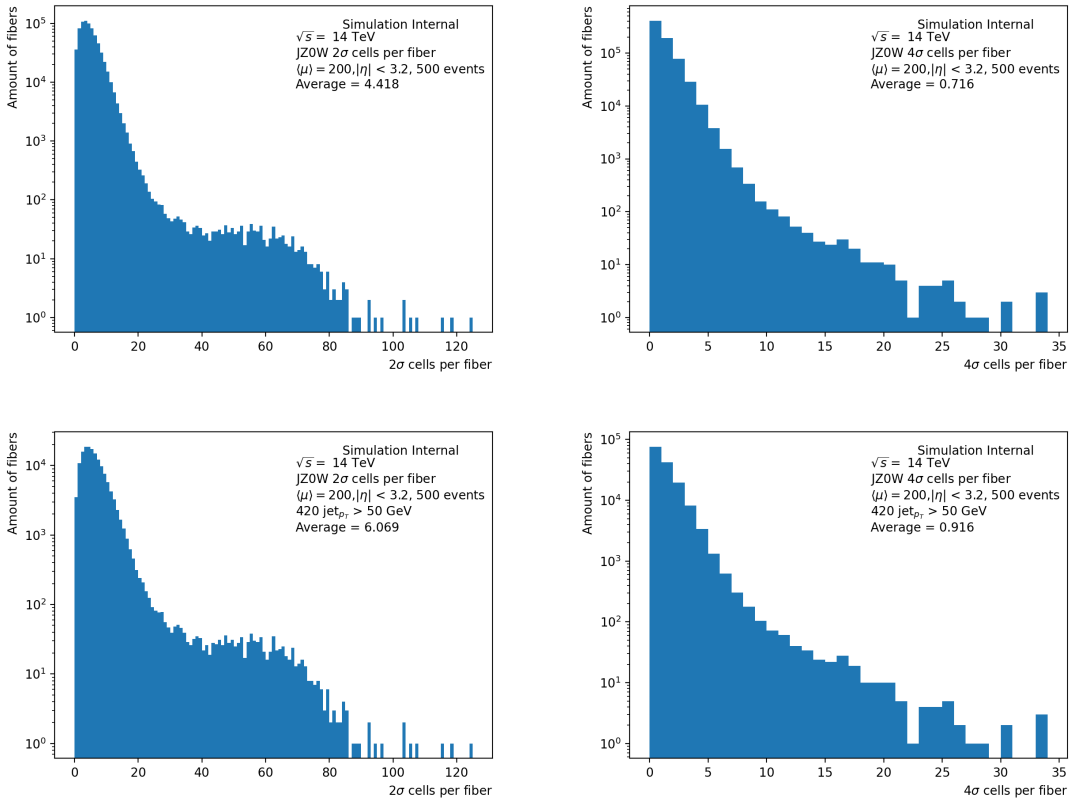


*Figure 51.* Number of $2\sigma$ (top left) and $4\sigma$ (top right) cells per LASP fiber for the JZ0 sample. A leading 420 jet $p_T$ cut at 50 GeV is applied for the bottom plots.

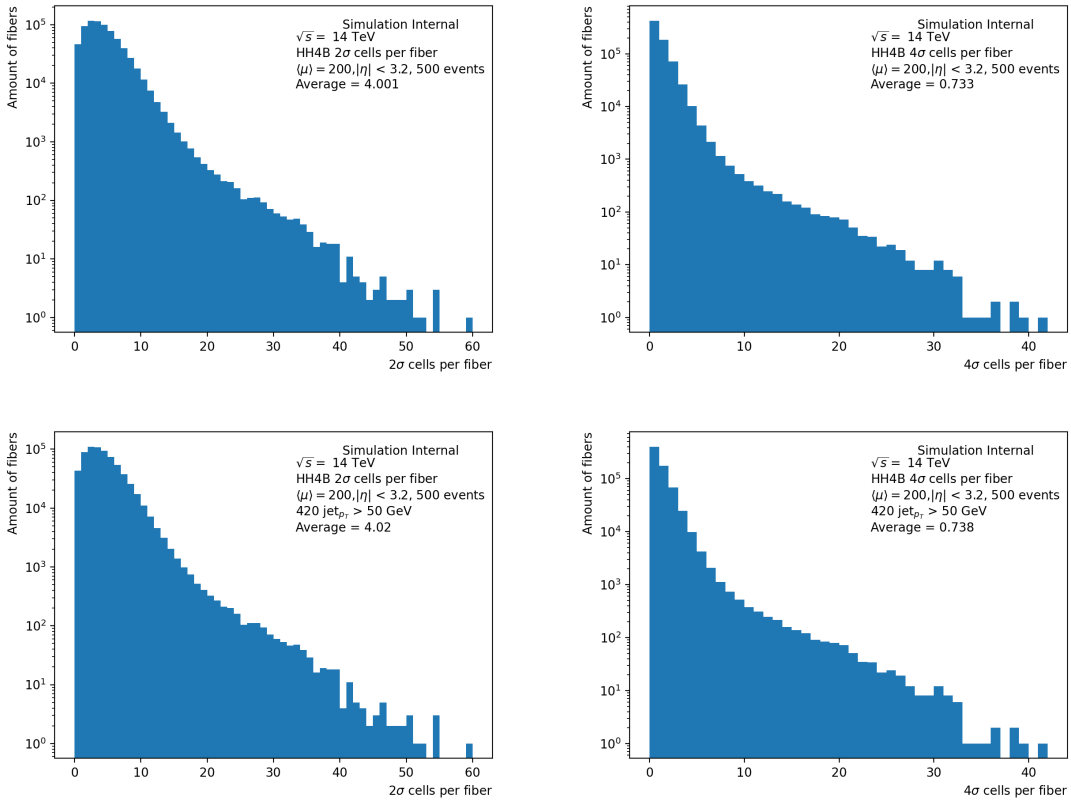


*Figure 52.* Number of $2\sigma$ (top left) and $4\sigma$ (top right) cells per LASP fiber for the HH $\rightarrow$ 4b sample. A leading 420 jet $p_T$ cut at 50 GeV is applied for the bottom plots.

## 4.1 Topological Cluster Algorithm Conclusions and Outlook

Topological clusters are formed first on the Global Trigger and are used as inputs for many vital algorithms, including jet and tau reconstruction, pileup suppression, topotowers, and isolation-type variable calculations. Thus an efficient and optimized topoclustering algorithm that maximizes physics performance is required by the Global Trigger. The USCA clustering algorithm is currently the first and most ideal software emulation of the Global Trigger firmware clustering algorithm. Based on the findings in the above studies, the 3-shell USCA algorithm would be the best choice if there were no bandwidth or memory constraints and enough clock cycles available. However, the 2-shell version still performs comparable to the 422 algorithm in terms of trigger efficiencies, with only a small change in jet energy resolution and speed of the trigger turn-on. It is thus the official recommendation of these studies to start implementing a firmware algorithm that most closely resembles the 2-shell USCA algorithm. Future studies are needed on the clustering algorithm to fully understand the physics performance and there is room to further optimize the software version of the algorithm. As of this writing, Global Trigger integration tests are being conducted at CERN with a modified version of clustering called cell towers. These towers are formed by summing the $E_T$ of all cells in a 0.1 x 0.1 $\eta$-$\phi$ region, and are used as inputs to pileup suppression and the jet reconstruction algorithm instead of clusters for the time being. It is expected that the cell towers will be used for commissioning the Global Trigger and initial data taking. The Global Trigger is primarily a firmware project, and its dynamic nature allows for implementation of the USCA algorithm in firmware at a later time with some modifications to optimize for latency and bandwidth. Steps to incorporate the USCA algorithm, or one like it, onto the

GEPs can be taken in parallel to the current integration tests with continued software and firmware studies.

# CHAPTER V

# A SEARCH FOR DARK MESONS DECAYING INTO TOP AND BOTTOM QUARKS

This chapter includes a previously published co-authored paper ATLAS Collaboration (2024b), with credit belonging to the ATLAS collaboration. The author of this thesis contributed to the analysis in multiple areas including a truth study of the multi-lepton channel, verifying preselection yields for the all-hadronic channel, verifying the 4-d ABCD method for the all-hadronic channel, and assisting in the development of the analysis and plotting frameworks for the one-lepton channel. After the paper in sections 5.1–5.10, additional details on the multi-lepton channel truth study, preselection yields, and the 4-d ABCD method are included in sections 5.11.4, 5.12, and 5.13, respectively.

## 5.1 Introduction

The Standard Model (SM) can be extended by a new strongly-coupled, confining gauge theory with fermion representation which transforms under the electroweak group. The appeal of such an extension is that dark matter can arise in the form of composite mesons or baryons of the new strongly-coupled theory. In addition, these models often exhibit an automatic accidental symmetry protecting against dark matter decay. Consequently, candidates for strongly-coupled dark matter include dark mesons, dark quarkonia-like states, glueballs and dark baryons Butterworth et al. (2022); Kribs and Neil (2016a). The search presented here targets one set of models incorporating this concept: Stealth Dark Matter Lattice Strong Dynamics (LSD) Collaboration (2015). Here, the new strongly-coupled dark sector consists of vector-like fermions that can transform under the new dark group but also interact with both the

electroweak sector of the SM and the Higgs boson. The result is the emergence of a quantum chromodynamics (QCD)-like dark sector as the direct analog to the QCD meson and baryon sector. This leads to several intriguing phenomenological consequences: as long as the vector-like mass is dominant over the chiral mass, the new dark sector is only weakly constrained by precision electroweak or Higgs coupling measurements, while the Higgs interactions break the dark sector global symmetry and thus allow dark mesons to decay into pure SM states Kribs, Martin, Ostdiek, and Tong (2019). This search focuses on the low-energy effective theories developed in Ref. Kribs, Martin, and Tong (2019a), which incorporate the leading interactions between dark mesons of a strongly-coupled $SU(2)$ dark flavor symmetry preserving dark sector and the SM. These models contain a stable dark scalar baryon which could account for the stable dark matter observed in cosmological measurements Lattice Strong Dynamics (LSD) Collaboration (2015).

The simplified model targeted in this search contains only the two phenomenologically relevant sets of dark mesons: a lighter pseudoscalar triplet of dark pions, $\pi_{\mathrm{D}}$, and an additional triplet of dark rho vector mesons, $\rho_{\mathrm{D}}$, which are both expected at a scale around or slightly above the electroweak scale. Following standard theoretical assumptions, the triplets are completely mass-degenerate and the dark sector can be fully described by three parameters: the mass of the dark pions $m_{\pi_D}$, the mass of the dark rho mesons $m_{\rho_D}$, and the number of dark colors $N_D$. Since the phenomenological consequences remain unchanged for values of $N_D$ that are not excessively large, $N_D$ is fixed to $N_D = 4$ throughout this search following the typical choice made for Stealth Dark Matter Lattice Strong Dynamics (LSD) Collaboration (2015).

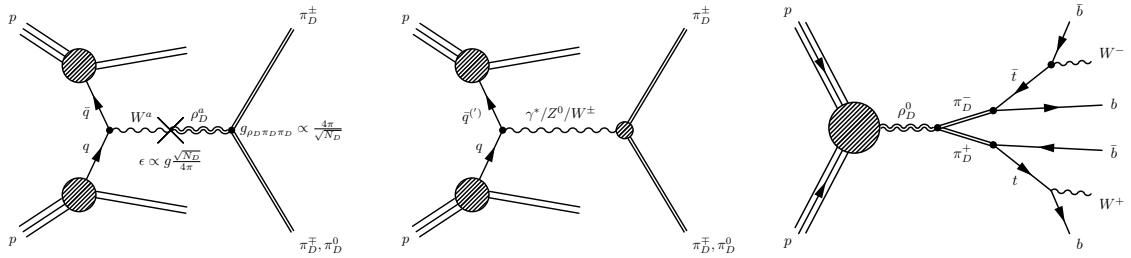


*Figure 53.* Examples of leading Feynman diagrams of dark pion pair production. The diagram in a shows resonant production via kinetic mixing with the $W$-field resulting in either a neutral or charged dark rho meson, a mixing with the $B$-field that can only result in a neutral dark rho meson is also possible, b shows Drell–Yan-type pair production of dark pions, and c shows an illustrative diagram of the dark pion decay into a top and a bottom quark for dark pion production.

Contrary to QCD, the vector-like nature of the dark sector allows to either gauge the full $\mathrm{SU(2)_L}$ weak interaction symmetry group or just the underlying $U(1)$ group, which leads to two distinct models of kinetic mixing of dark mesons with the SM, $\mathrm{SU(2)_L}$ and $\mathrm{SU(2)_R}$. The phenomenological consequences manifest themselves in the allowed decay channels and production cross-sections of dark pions, where the $\mathrm{SU(2)_L}$ models result in considerably larger cross sections than the $\mathrm{SU(2)_R}$ models. Dark pions are always pair-produced either via Drell–Yan-type processes or resonantly via kinetic mixing of SM electroweak gauge bosons with the $\rho_\mathrm{D}$ that then subsequently decays into a pair of dark pions, as shown in Figure 53. The kinetic mixing parameter $\epsilon$ depends on the number of dark colors as shown in Figure 53a (see also Ref. Kribs, Martin, Ostdiek, and Tong (2019)). Throughout nearly all of the parameter space investigated in this search, the resonant production dominates the production of dark pions. Once the choice of $N_D = 4$ is made, the production cross-section depends trivially on the ratio of the dark pion and dark rho-meson masses, for which the symbol $\eta_\mathrm{D} = m_{\pi_\mathrm{D}}/m_{\rho_\mathrm{D}}$ is used, equivalent to the $\eta$ defined in Ref. Kribs, Martin, Ostdiek, and Tong (2019). For

gaugephobic $SU(2)_L$ models, a given dark pion mass and $\eta_D$-parameter fully specify the model, including the dark pion decay branching fractions.

This search considers only models with $\eta_D < 0.5$ where the decay $\rho_D^{\pm,0} \to \pi_D^{\pm}\pi_D^{0,\mp}$ has a branching fraction of nearly 1.0, while for models with $\eta_D > 0.5$ this decay is kinematically forbidden and the dark rho meson can only decay to pairs of leptons or quarks. Previous searches for resonances in the dilepton spectrum both in ATLAS ATLAS Collaboration (2017i) and CMS CMS Collaboration (2018) have placed strong constraints on such models Kribs, Martin, Ostdiek, and Tong (2019). The bounds for models with $\eta_D < 0.5$ are considerably weaker Butterworth et al. (2022). This is the first search in any collider experiment optimized for this specific type of model.

Figure 54 shows the pair-production cross-sections for dark pions in $SU(2)_L$ and $SU(2)_R$ models. The contribution of resonant production to the total production cross-section is indicated by the dashed lines. A variety of different decay channels are open to dark pions in the available parameter space. The most relevant channels and their branching fractions are shown in Figure 67. For gaugephobic models the decay to top and bottom quarks dominates at high masses, while decays to bottom and charm quarks, $\tau$-leptons and gauge bosons are relevant at lower dark pion masses.

This search is the result of the analysis of 140 fb$^{-1}$ of proton–proton ($pp$) collisions collected by the ATLAS detector during Run 2 of the Large Hadron Collider (LHC). Since the dark pions are pair-produced in the model considered, the experimental signatures are either three top quarks and one bottom quark ($tttb$) or two top quarks and two bottom quarks ($ttbb$)[1]. About one third of dark

[1]The label "$tttb$" is used to indicate both $t\bar{t}t\bar{b}$ as well as its charge conjugate, $t\bar{t}\bar{t}b$; whereas "$ttbb$" refers to $t\bar{t}b\bar{b}$.

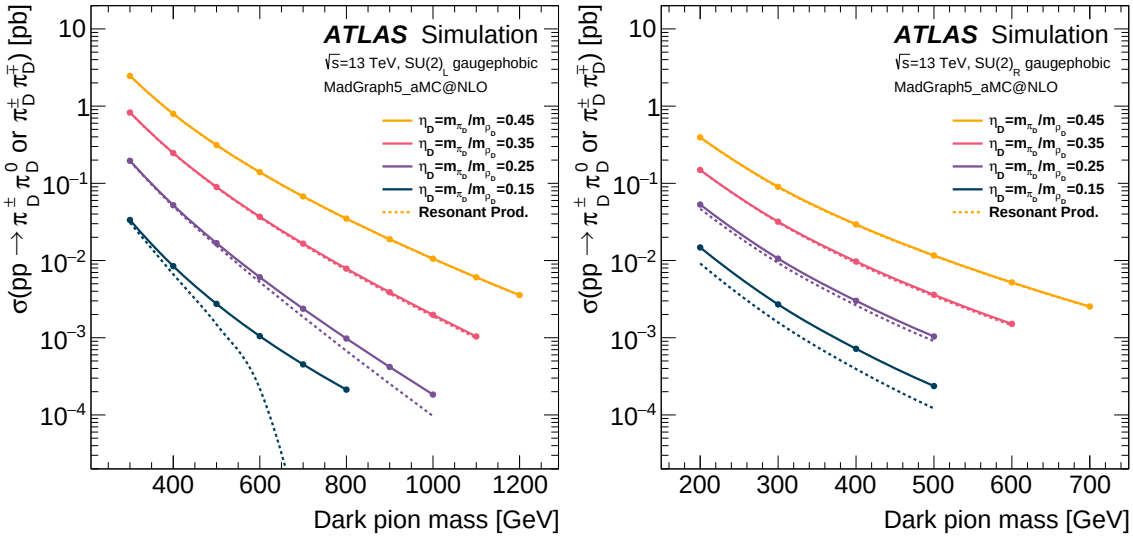


*Figure 54.* Pair-production cross-sections for dark pions as a function of dark pion mass for four different values of $\eta_D$ in a an $SU(2)_L$ model and b an $SU(2)_R$ model. The dashed colored lines indicate the contribution of the resonant production mode to the total dark pion production cross-section.

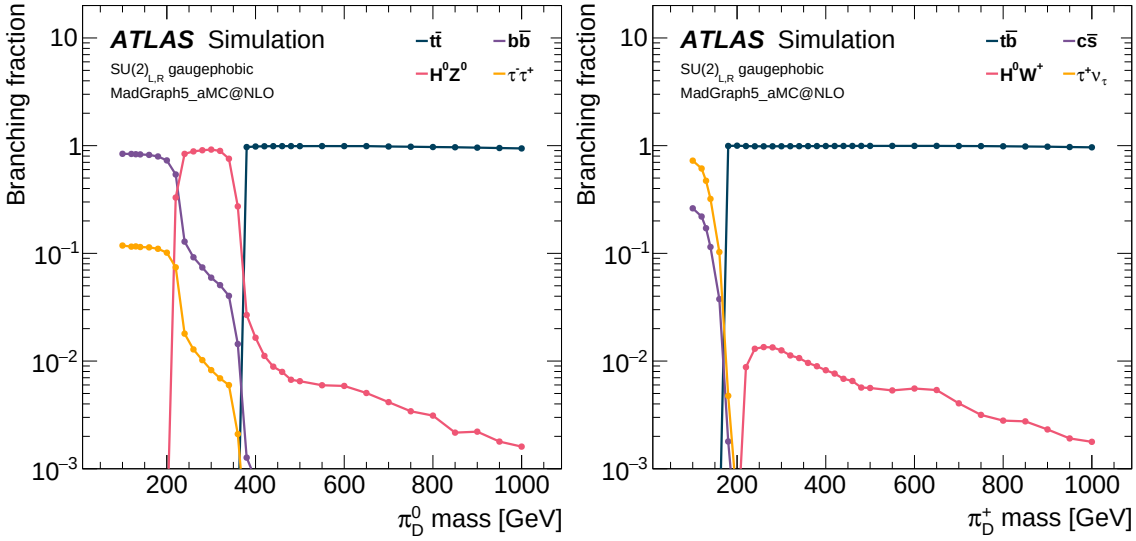


*Figure 55.* Branching fractions of the available decays of dark pions from gaugephobic $SU(2)_L$ and $SU(2)_R$ models are shown for a neutral dark pions and b positively charged dark pions. Channels with small branching fractions are suppressed for clarity.

pions in the $\mathrm{SU}(2)_\mathrm{L}$ models are neutral, resulting in the *tttb* event signature being twice as likely as the *ttbb* signature. These processes can give rise to several different final states depending on the hadronic or semileptonic decay mode of each of the top quarks. The search is performed in the *all-hadronic* channel, targeting fully hadronic top quark decays where the signal results in eight to ten jets of which at least four originate from bottom quarks, and in the *one-lepton* channel, corresponding to final states with exactly one electron or muon in addition to up to four jets from b-quarks.

The results are interpreted as limits on the production cross-section of dark pion pairs as a function of $m_{\pi_\mathrm{D}}$ and $\eta_\mathrm{D}$.

## 5.2 ATLAS Detector

The ATLAS detector ATLAS Collaboration (2008) at the LHC covers nearly the entire solid angle around the collision point.[2] It consists of an inner tracking detector surrounded by a thin superconducting solenoid, electromagnetic and hadronic calorimeters, and a muon spectrometer incorporating three large superconducting air-core toroidal magnets.

The inner-detector system (ID) is immersed in a 2 T axial magnetic field and provides charged-particle tracking in the range $|\eta| < 2.5$. The high-granularity silicon pixel detector covers the vertex region and typically provides four measurements per track, the first hit generally being in the insertable B-layer (IBL) installed before Run 2 Abbott et al. (2018); ATLAS Collaboration

[2]ATLAS uses a right-handed coordinate system with its origin at the nominal interaction point (IP) in the center of the detector and the $z$-axis along the beam pipe. The $x$-axis points from the IP to the center of the LHC ring, and the $y$-axis points upwards. Polar coordinates $(r, \phi)$ are used in the transverse plane, $\phi$ being the azimuthal angle around the $z$-axis. The pseudorapidity is defined in terms of the polar angle $\theta$ as $\eta = -\ln\tan(\theta/2)$ and is equal to the rapidity $y = \frac{1}{2}\ln\left(\frac{E+p_z c}{E-p_z c}\right)$ in the relativistic limit. Angular distance is measured in units of $\Delta R \equiv \sqrt{(\Delta y)^2 + (\Delta\phi)^2}$.

(2010a). It is followed by the SemiConductor Tracker (SCT), which usually provides eight measurements per track. These silicon detectors are complemented by the transition radiation tracker (TRT), which enables radially extended track reconstruction up to $|\eta| = 2.0$. The TRT also provides electron identification information based on the fraction of hits (typically 30 in total) above a higher energy-deposit threshold corresponding to transition radiation.

The calorimeter system covers the pseudorapidity range $|\eta| < 4.9$. Within the region $|\eta| < 3.2$, electromagnetic calorimetry is provided by barrel and endcap high-granularity lead/liquid-argon (LAr) calorimeters, with an additional thin LAr presampler covering $|\eta| < 1.8$ to correct for energy loss in material upstream of the calorimeters. Hadronic calorimetry is provided by the steel/scintillator-tile calorimeter, segmented into three barrel structures within $|\eta| < 1.7$, and two copper/LAr hadronic endcap calorimeters. The solid angle coverage is completed with forward copper/LAr and tungsten/LAr calorimeter modules optimized for electromagnetic and hadronic energy measurements respectively.

The muon spectrometer (MS) comprises separate trigger and high-precision tracking chambers measuring the deflection of muons in a magnetic field generated by the superconducting air-core toroidal magnets. The field integral of the toroids ranges between 2.0 and 6.0 T m across most of the detector. Three layers of precision chambers, each consisting of layers of monitored drift tubes, cover the region $|\eta| < 2.7$, complemented by cathode-strip chambers in the forward region, where the background is highest. The muon trigger system covers the range $|\eta| < 2.4$ with resistive-plate chambers in the barrel, and thin-gap chambers in the endcap regions.

The luminosity is measured mainly by the LUCID–2 Avoni et al. (2018) detector that records Cherenkov light produced in the quartz windows of photomultipliers located close to the beampipe.

Events are selected by the first-level trigger system implemented in custom hardware, followed by selections made by algorithms implemented in software in the high-level trigger ATLAS Collaboration (2017h). The first-level trigger accepts events from the 40 MHz bunch crossings at a rate below 100 kHz, which the high-level trigger further reduces in order to record complete events to disk at about 1 kHz.

A software suite ATLAS Collaboration (2024) is used in data simulation, in the reconstruction and analysis of real and simulated data, in detector operations, and in the trigger and data acquisition systems of the experiment.

## 5.3 Data and Simulated Event Samples

This analysis is performed using data from $pp$ collisions with $\sqrt{s} = 13\,\text{TeV}$ recorded by the ATLAS detector in 2015–2018. Only events for which all relevant subsystems were operational are considered. The data correspond to an integrated luminosity of $140.1 \pm 1.2\,\text{fb}^{-1}$ ATLAS Collaboration (2022c).

Monte Carlo (MC) simulated event samples are used for the estimate of background from SM processes and to model the targeted signal models. The details of the event generation are provided in Sections 5.3.1 and 5.3.2 for signal and background samples, respectively. The generation of all simulated event samples includes the effect of multiple $pp$ interactions per bunch crossing, as well as changes in detector response due to interactions in bunch crossings before or after the one containing the hard interaction, modeled by overlaying simulated inelastic events on the physics event. These two effects are referred to as pileup. The

simulated event samples are processed with the GEANT4-based ATLAS detector simulation ATLAS Collaboration (2010b); GEANT4 Collaboration, Agostinelli, et al. (2003). All samples are weighted to match the pileup distribution observed in data and are processed with the same reconstruction algorithms as data.

**5.3.1 Signal samples.** Signal samples are generated in a grid over a two-dimensional space, varying the dark pion mass $m_{\pi_{\mathrm{D}}}$ between $300 - 1200$ GeV and the $\eta_{\mathrm{D}}$-parameter between $0.15 - 0.45$. The matrix element calculation for the pair production of dark pions is performed at next-to-leading order (NLO) in QCD based on the model described in Ref. Kribs, Martin, Ostdiek, and Tong (2019) using MADGRAPH5_AMC@NLO v2.4.3 Alwall et al. (2014) interfaced with PYTHIA.212 Sjöstrand et al. (2015) for the modeling of parton showering, hadronization and underlying event using the A14 set of tuned parameters ("tune") ATLAS Collaboration (2014a) and the NNPDF2.3 Ball et al. (2013a) set of parton distribution functions (PDF).

The decays of bottom and charm hadrons are simulated using the EVTGEN v1.6.0 program Lange (2001). An additional set of signal samples, with parameter values near the expected exclusion contour of the all-hadronic channel, is generated at NLO in QCD using MADGRAPH5_AMC@NLO v2.9.9 Alwall et al. (2014) interfaced with PYTHIA.306 Bierlich et al. (2022) using the A14 tune and NNPDF2.3 PDF set. Kinematic distributions match in both setups. All signal cross-sections are extracted from MADGRAPH5_AMC@NLO v2.9.9. The number of dark colors $N_D$ is set to 4 for all signal points. The dark pion decays are simulated using the narrow width approximation and contain all possible decay channels from Figure 67.

Table 4. Overview of the configuration of all nominal background samples used in the analysis; details and definitions are provided in the text.

| Process | Generator | PDF | Showering | Tune | Cross section |
|---|---|---|---|---|---|
| $t\bar{t}$ | POWHEG-BOX v2 | NNPDF3.0NLO | PYTHIA | A14 | NNLO+NNLL |
| $t\bar{t}+b\bar{b}$ | POWHEG-BOX-RES | NNPDF3.0NLO | PYTHIA | A14 | NLO |
| $V$ + jets | SHERPA v2.2.11 | NNPDF3.0NNLO | SHERPA | Def. | NLO |
| Single top | POWHEG-BOX v2 | NNPDF3.0NLO | PYTHIA | A14 | NLO+NNLL |
| $t\bar{t}t\bar{t}$ | MADGRAPH5_AMC@NLO v2.4.3 | NNPDF3.1NLO | PYTHIA | A14 | NLO |
| $t\bar{t}V$ | MADGRAPH5_AMC@NLO v2.3.3 | NNPDF3.0NLO | PYTHIA | A14 | NLO |
| $t\bar{t}H$ | POWHEG-BOX v2 | NNPDF3.0NLO | PYTHIA | A14 | NLO |
| Other $t\bar{t}X$ | MADGRAPH5_AMC@NLO | NNPDF2.3 | PYTHIA | A14 | NLO |
| Multiboson | SHERPA v2.2.1/v2.2.2 | NNPDF3.0NNLO | SHERPA | Def. | NLO |

**5.3.2 Background samples.** The dominant SM background process in the all-hadronic channel is multijet production. This background is estimated with data-driven methods while MC simulation is used to estimate the remaining SM processes. The background in the one-lepton channel is estimated from MC simulations and is dominated by top quark pair-production ($t\bar{t}$), often in association with heavy-flavor quarks ($t\bar{t}$ + HF). Other important backgrounds are the production of a vector boson in association with jets ($V$ + jets) and single top-quark production (single top) which is dominated by the associated production of a top quark with a $W$ boson but also contains single top-quark production in the $s-$ and $t-$channels. Smaller background contributions stem from $t\bar{t}$ produced in association with additional bosons or quarks ($t\bar{t}t\bar{t}$, $t\bar{t}V$, $t\bar{t}H$, and other $t\bar{t}X$) and multiboson production. The configurations used to produce the background samples are described below and are summarized in Table 4. For all background samples, except those generated with SHERPA, the EVTGEN v.1.6.0 or v1.7.0 program is used to simulate the decays of bottom and charm hadrons.

***5.3.2.1 $t\bar{t}$ background.*** The production of $t\bar{t}$ events is modeled using the POWHEG-BOX v2 Alioli, Nason, Oleari, and Re (2010); Frixione, Nason, and Oleari (2007); Frixione, Ridolfi, and Nason (2007); Nason (2004) generator that

provides matrix elements at NLO in QCD with the NNPDF3.0NLO Ball et al. (2015); Carrazza, Forte, Kassabov, Latorre, and Rojo (2015) set PDFs and the $h_{\text{damp}}$ parameter, which controls the matching in POWHEG and effectively regulates the high-$p_{\text{T}}$ radiation against which the $t\bar{t}$ system recoils, set to 1.5 $m_{\text{top}}$ ATLAS Collaboration (2016h). The functional form of the renormalization and factorization scales are set to the default scale $\sqrt{m_{\text{top}}^2 + p_{\text{T}}^2}$. The events are interfaced with PYTHIA.230 for the parton shower and hadronization, using the A14 set of tuned parameters and the NNPDF2.3 PDF set. The $t\bar{t}$ sample is normalized to the cross section prediction at next-to-next-to-leading order (NNLO) in QCD including the resummation of next-to-next-to-leading-logarithmic (NNLL) soft-gluon terms calculated using TOP++2.0 Bärnreuther, Czakon, and Mitov (2012); Beneke, Falgari, Klein, and Schwinn (2012); Cacciari, Czakon, Mangano, Mitov, and Nason (2012); Czakon, Fiedler, and Mitov (2013); Czakon and Mitov (2012, 2013, 2014). For $pp$ collisions at a center-of-mass energy of $\sqrt{s} = 13$ TeV, this cross section corresponds to $\sigma(t\bar{t})_{\text{NNLO+NNLL}} = 832 \pm 51$ pb using a top-quark mass of $m_{\text{top}} = 172.5$ GeV.

The inclusive $t\bar{t}$ sample described above is complemented by a dedicated sample in which a pair of top quarks is produced in association with two $b$-quarks. Events are simulated with the POWHEG-BOX-RES Ježo, Lindert, Moretti, and Pozzorini (2018) generator and OPENLOOPS Buccioni et al. (2019); Cascioli, Maierhöfer, and Pozzorini (2012); Denner, Dittmaier, and Hofer (2017), using a pre-release of the implementation of this process in POWHEG-BOX-RES provided by the authors Ježo (2019), with the NNPDF3.0NLO PDF set. It is interfaced with PYTHIA.240, using the A14 set of tuned parameters and the NNPDF2.3 PDF set. The four-flavor scheme is used with the $b$-quark mass set to 4.95 GeV. The

factorization scale and $h_{\text{damp}}$ parameter are both set to $0.5 \times \Sigma_{i=t,\bar{t},b,\bar{b},j} m_{\text{T},i}$, and the renormalization scale is set to $\sqrt[4]{m_{\text{T}}(t) \cdot m_{\text{T}}(\bar{t}) \cdot m_{\text{T}}(b) \cdot m_{\text{T}}(\bar{b})}$. This $t\bar{t} + b\bar{b}$ sample is used in the one-lepton channel where the dominant background comes from $t\bar{t}$ production, whereas the multijet-dominated all-hadronic channel relies on the five-flavor scheme inclusive sample alone.

Previous studies have seen improved agreement between data and prediction in $t\bar{t}$ events, particularly for the top-quark $p_{\text{T}}$ distribution, when comparing with NNLO calculations ATLAS Collaboration (2016c). Top-quark pair differential calculations at NNLO QCD accuracy including electroweak (EW) corrections have become available Czakon et al. (2017). Hence, a small improvement to the modeling is incorporated by correcting the $t\bar{t}$ and the $t\bar{t} + b\bar{b}$ samples to match their top/antitop-quark $p_{\text{T}}$ and the top-quark mass distribution to the accuracy predicted at NNLO in QCD and NLO in EW.

Events in the $t\bar{t}$ and $t\bar{t} + b\bar{b}$ samples are classified according to the flavor of the particle jets not originating from the top quark. The particle jets are reconstructed from the simulated stable particles using the anti-$k_t$ algorithm Cacciari, Salam, and Soyez (2008, 2012) with a radius parameter $R = 0.4$, and are required to have $p_{\text{T}} > 15$ GeV and $|\eta| < 2.5$. Events are labeled as $t\bar{t}+ \geq 1b$ if at least one particle jet is matched within $\Delta R < 0.4$ to $b$-hadrons with $p_{\text{T}} > 5$ GeV that do not arise from the decay of top quarks. In the remaining events, if at least one particle jet is matched within $\Delta R < 0.4$ to additional $c$-hadrons with $p_{\text{T}} > 5$ GeV, the events are classified as $t\bar{t}+ \geq 1c$. All other events are labeled as $t\bar{t} +$ light. The $t\bar{t} + b\bar{b}$ sample is used for the $t\bar{t}+ \geq 1b$ category meaning that all $t\bar{t} +$ light and $t\bar{t}+ \geq 1c$ events are rejected from this sample. Likewise, only the $t\bar{t} +$ light and $t\bar{t}+ \geq 1c$ events are retained from the inclusive $t\bar{t}$ sample.

***5.3.2.2 Other backgrounds.*** The production of $V$ + jets is simulated with the SHERPA v2.2.11 Bothmann et al. (2019) generator using NLO matrix elements for up to two partons, and leading-order (LO) matrix elements for up to five partons calculated with the Comix Gleisberg and Höche (2008) and OPENLOOPS libraries. They are matched with the SHERPA parton shower Schumann and Krauss (2008) using the MEPS@NLO prescription Catani, Krauss, Webber, and Kuhn (2001); Höche, Krauss, Schönherr, and Siegert (2012, 2013); Höche, Krauss, Schumann, and Siegert (2009) and the set of tuned parameters developed by the SHERPA authors. The HESSIAN NNPDF3.0NNLO PDF set is used and the samples are normalized to a prediction that is NNLO in QCD Anastasiou, Dixon, Melnikov, and Petriello (2004).

The associated production of a top quark with a $W$ bosons ($tW$) is modeled using the POWHEG-BOX v2 Alioli et al. (2010); Frixione, Nason, and Oleari (2007); Nason (2004); Re (2011) generator at NLO in QCD using the five-flavor scheme and the NNPDF3.0NLO PDF set. The diagram removal scheme Frixione, Laenen, Motylinski, White, and Webber (2008) is used to remove interference and overlap with $t\bar{t}$ production. The related uncertainty is estimated by comparing with an alternative sample generated using the diagram subtraction scheme ATLAS Collaboration (2016h); Frixione et al. (2008). Single top-quark $t$-channel production is modeled using the POWHEG-BOX v2 Alioli et al. (2010); Frederix, Re, and Torrielli (2012); Frixione, Nason, and Oleari (2007); Nason (2004) generator at NLO in QCD using the four-flavor scheme and the corresponding NNPDF3.0NLO PDF set. Single top-quark $s$-channel production is modeled using the POWHEG-BOX v2 Alioli, Nason, Oleari, and Re (2009); Alioli et al. (2010); Frixione, Nason, and Oleari (2007); Nason (2004) generator at NLO in QCD in the five-flavor

scheme with the NNPDF3.0NLO PDF set. All single top-quark events are processed through Pythia.230 using the A14 tune and the NNPDF2.3 PDF set.

The production of $t\bar{t}t\bar{t}$ events is modeled using the MadGraph5_aMC@NLO v2.4.3 generator which provides matrix elements at NLO in QCD with the NNPDF3.1NLO Ball et al. (2015) PDF set. The functional form of the renormalization and factorization scales is set to $0.25\times\sum_i\sqrt{m_i^2+p_{\mathrm{T},i}^2}$, where the sum runs over all the particles generated from the matrix element calculation, following Ref. Frederix, Pagani, and Zaro (2018). Top quarks are decayed at LO using MadSpin Artoisenet, Frederix, Mattelaer, and Rietkerk (2013); Frixione, Laenen, Motylinski, and Webber (2007) to preserve all spin correlations. The events are interfaced with Pythia.230 for the parton shower and hadronization, using the A14 set of tuned parameters and the NNPDF2.3 PDF set.

The production of $t\bar{t}V$ events is modeled using the MadGraph5_aMC@NLO v2.3.3 generator at NLO in QCD with the NNPDF3.0NLO PDF set. The events are interfaced to Pythia.210 using the A14 tune and the NNPDF2.3 PDF set.

The production of $t\bar{t}H$ events is modeled using the Powheg-Box v2 Alioli et al. (2010); Frixione, Nason, and Oleari (2007); Frixione, Ridolfi, and Nason (2007); Hartanto, Jäger, Reina, and Wackeroth (2015); Nason (2004) generator at NLO in QCD with the NNPDF3.0NLO PDF set. The events are interfaced to Pythia.230 using the A14 tune and the NNPDF2.3 PDF set.

Further rare top-quark-pair backgrounds $ttt$, $t\bar{t}ZZ$, $t\bar{t}WW$, $t\bar{t}WZ$, $t\bar{t}WH$ and $t\bar{t}HH$ are all produced using the NLO in QCD MadGraph5_aMC@NLO generator interfaced with Pythia using the A14 set of tuned parameters and scaled to NLO cross sections de Florian et al. (2016).

Samples of diboson final states ($VV$) are simulated with the Sherpa v2.2.1 or v2.2.2 Bothmann et al. (2019) generator depending on the process, including off-shell effects and Higgs-boson contributions, where appropriate. Semileptonic final states, where one boson decays leptonically and the other hadronically, are generated using matrix elements at NLO accuracy in QCD for up to one additional parton and at LO accuracy for up to three additional parton emissions. Samples for the loop-induced processes $gg \rightarrow VV$ are generated using LO-accurate matrix elements for up to one additional parton emission. The matrix element calculations are matched and merged with the Sherpa parton shower based on Catani–Seymour dipole factorization Gleisberg and Höche (2008); Schumann and Krauss (2008) using the MEPS@NLO prescription. The virtual QCD corrections are provided by the OpenLoops library. The NNPDF3.0NNLO PDF set is used, along with the dedicated set of tuned parton-shower parameters developed by the Sherpa authors.

### 5.4 Object and Event Selections

For each event, interaction vertices are reconstructed from ID charged particle tracks, where the tracks are required to have transverse momenta ($p_{\mathrm{T}}$) greater than 500 MeV ATLAS Collaboration (2015b). Candidates for the primary vertex are required to have at least two associated tracks. If multiple vertices are reconstructed, the vertex with the largest sum of the squares of the transverse momenta of associated tracks is taken as the primary vertex. Events that fail the primary vertex reconstruction are rejected.

Electrons are reconstructed from energy deposits in the electromagnetic calorimeter that are matched to charged-particle tracks in the ID ATLAS Collaboration (2019d). They are identified using a likelihood-based (LH)

identification which employs calorimeter and tracking information to discriminate between electrons and jets and that combines this likelihood and the likelihood of it originating from background processes into a single discriminant. Only electron candidates with $p_{\mathrm{T}} > 10$ GeV within $|\eta| < 1.37$ or $1.52 < |\eta| < 2.47$ are considered. Electrons are required to be well isolated using criteria based on the properties of the topological clusters in the calorimeter and of ID tracks around the reconstructed electron. Further requirements of $|z_0 \sin\theta| < 0.5$ mm and $|d_0|/\sigma(d_0) < 5$ are placed on the longitudinal and transverse impact parameters to select electrons originating from the primary vertex. Electrons are further categorized as "baseline" or "signal". For the all-hadronic channel, baseline electrons are identified by the *LooseAndBLayer* likelihood-based identification working point and are required to fulfill the *Loose* isolation criteria ATLAS Collaboration (2019d, 2019e). Events containing a baseline electron candidate satisfying these baseline criteria are rejected. For the one-lepton channel, baseline electrons are identified with the *Medium* working point ATLAS Collaboration (2019d) and are not subject to any isolation requirement. Signal electrons are identified by the *Tight* working point and are subject to the *Tight* track-based isolation criteria ATLAS Collaboration (2019d). The $p_{\mathrm{T}}$-requirement of the signal electrons is increased to $p_{\mathrm{T}} > 28$ GeV. Signal electrons constitute a subset of the baseline electrons.

Muon candidates are reconstructed by combining tracks in the MS with tracks in the ID and are subject to cut-based identification criteria which are based on the numbers of hits in the different ID and MS subsystems, and on the significance of the charge-to-momentum ratio $q/p$ ATLAS Collaboration (2021d). All muon candidates are required to be within the acceptance region of the ID at $|\eta| < 2.5$ and to have $p_{\mathrm{T}} > 10$ GeV. Muons are required to satisfy isolation

requirements based on the properties of ID tracks around the reconstructed muon ATLAS Collaboration (2021d). Similarly to electrons, requirements on the longitudinal and transverse impact parameters, $|z_0 \sin\theta| < 0.5$ mm and $|d_0|/\sigma(d_0) < 3$, are also applied. Baseline muons are identified in the all-hadronic channel by the *Loose* quality working point and are required to fulfill the *Loose* isolation criteria ATLAS Collaboration (2021d). Events containing a muon candidate satisfying these baseline criteria are rejected. In the one-lepton channel, baseline muons are identified by the *Medium* quality working point ATLAS Collaboration (2021d) and are not subject to any isolation criteria. For the selection of signal muons the *Medium* quality working point is applied and the muon candidates are required to fulfill the *Tight* isolation criteria based on the $p_T^{\text{varcone30}}$ variable defined in Ref. ATLAS Collaboration (2021d) and have $p_{\text{T}} > 28$ GeV. Signal muons constitute a subset of the baseline muons. Events are selected for the one-lepton channel if they contain exactly one signal and no additional baseline leptons (electrons or muons).

Jet candidates are reconstructed using a particle-flow reconstruction algorithm ATLAS Collaboration (2017f) combining charged particle tracks from the ID and three-dimensional topological energy clusters ATLAS Collaboration (2017j) in the calorimeter. Jets are reconstructed using the anti-$k_t$ algorithm Cacciari et al. (2008) implemented in the FastJet package Cacciari, Salam, and Soyez (2012) with a fixed radius parameter $R = 0.4$ using charged constituents associated with the primary vertex and neutral particle flow objects as inputs. In order to minimize the contribution from pileup jets, a requirement on the jet-vertex tagger ATLAS Collaboration (2016e) is made for jets with $p_{\text{T}}$ below 60 GeV.

Slight differences in the efficiency of the association of jets to vertices in data and simulation are addressed by applying scale factors to simulation. Jet energy scale corrections, derived from MC simulation, are used to calibrate the average energies of jet candidates to the scale of their constituent particles ATLAS Collaboration (2020b). Remaining differences between data and simulated events are evaluated and corrected for using in situ techniques, which exploit the transverse momentum balance between a jet and a reference object such as a photon, $Z$ boson, or multijet system in data. After these calibrations, all jets in the event with $p_{\mathrm{T}} > 20$ GeV must satisfy a set of loose jet-quality requirements ATLAS Collaboration (2013c) designed to reject jets originating from sporadic bursts of detector noise, large coherent noise or isolated pathological cells in the calorimeter system, hardware issues, beam-induced background or cosmic-ray muons ATLAS Collaboration (2015a). In the one-lepton channel, the jets are required to satisfy $|\eta| < 2.5$, while in the all-hadronic channel, they are required to satisfy $|\eta| < 2.8$ to match the $\eta$ range of the $H_T$ trigger. If these jet requirements are not met, the jet is discarded.

Jets are tagged as containing a $b$-hadron ($b$-tagged) by a deep neural network algorithm trained on a simulated hybrid sample composed of $t\bar{t}$ and $Z' \rightarrow t\bar{t}$ events ATLAS Collaboration (2017g, 2022b) at a working point corresponding to a 77% $b$-jet efficiency, as measured on an inclusive $t\bar{t}$ sample. This working point has a rejection factor of 5 and 170 on charm and light-flavored jets, respectively. Flavor-tagging efficiency differences between data and simulation are corrected by a reweighting procedure detailed in Refs. ATLAS Collaboration (2019a, 2019b, 2021c).

To resolve any reconstruction ambiguities between electrons, muons and jets, an overlap removal procedure is applied in a prioritized sequence, based on baseline leptons and jets, as follows. First, if an electron shares the same ID track with another electron, the electron with lower $p_{\mathrm{T}}$ is discarded, and then any electron sharing the same ID track with a muon is rejected. Next, jets are rejected if they lie within $\Delta R = 0.2$ of an electron. Similarly, jets within $\Delta R = 0.2$ of a muon are rejected if the jet has fewer than three associated tracks or if the muon is matched to the jet through ghost association Cacciari et al. (2008). Finally, electrons that are close to a remaining jet are discarded if their distance from the jet is $\Delta R < 0.4$, while for muons the distance is $\Delta R < \min(0.4, 0.04 + 10\ \mathrm{GeV}/p_{\mathrm{T}})$.

Large-$R$ jets are reclustered from the calibrated $R = 0.4$ jets described above using the anti-$k_t$ algorithm with a fixed radius parameter of $R = 1.2$ Nachman, Nef, Schwartzman, Swiatlowski, and Wanotayaroj (2015). The large-$R$ jets aim to fully contain the dark pion decay products and the $R$ parameter is optimized for the dark pion mass range of the targeted signal points. For the one-lepton channel the signal lepton is added to the $R = 0.4$ jet collection before the reclustering, which then proceeds in the same way as in the all-hadronic channel. After reclustering, the large-$R$ jet containing the lepton is referred to as $J^{\mathrm{lep}}$ and the leading fully hadronic large-$R$ jet $J^{\mathrm{had}}$. Both large-$R$ jets originate from the same reclustering procedure, ensuring there is no overlap between the two.

Events are selected for the all-hadronic channel using triggers on $H_{\mathrm{T}}$, defined as the scalar sum of the transverse momenta of all the reconstructed jets in the event with $|\eta_{\mathrm{jet}}| < 2.8$ ATLAS Collaboration (2016f). The $H_{\mathrm{T}}$-trigger threshold was 850 GeV in 2015 and the first half of 2016, and was increased to 1000 GeV in the latter half of 2016 for the remainder of Run 2. Since the trigger decision

is based on $H_{\mathrm{T}}$ computed from trigger-level jet momenta (which lack a detailed calibration), the triggers show a slow onset behavior with respect to $H_{\mathrm{T}}$ computed from jet momenta of fully calibrated jets. A requirement of $H_{\mathrm{T}} > 1150$ GeV ensures that the trigger is fully efficient to minimize systematic uncertainties resulting from imprecise modeling of the onset behavior in simulation. The $H_{\mathrm{T}}$ variable computed from fully calibrated jets is used for the remainder of this search.

Events are selected for the one-lepton channel using a combination of single-lepton triggers ATLAS Collaboration (2020d, 2020e, 2020f, 2021a). The single-lepton triggers require the presence of a muon or an electron with $p_{\mathrm{T}}$ higher than a certain threshold and, in some cases, impose identification and lepton-isolation requirements. The lowest $p_{\mathrm{T}}$ threshold was 24 (20) GeV for electrons (muons) during the 2015 data-taking period and 26 GeV for both electrons and muons in the data-taking periods from 2016 to 2018. The efficiencies of the single-lepton triggers range between 20% and 50% in the simulated signal samples. To account for small differences in the single-lepton trigger efficiency between data and simulation, all triggered simulated events receive an event weight to match data.

The analysis strategy relies on the reconstruction of each dark pion using a large-$R$ jet. In the all-hadronic channel, events are required to have six or more $R = 0.4$ jets with $p_{\mathrm{T}} > 25$ GeV, in addition to the $H_{\mathrm{T}} > 1150$ GeV requirement and the lepton veto. At least three jets within the ID acceptance ($|\eta| < 2.5$) must be $b$-tagged. At least two large-$R$ jets with jet mass $m_{\mathrm{jet,R=1.2}} > 190$ GeV are required in all events. Events for the one-lepton channel are required to have at least five jets, out of which at least three have to be $b$-tagged, and to have $H_{\mathrm{T}} > 300$ GeV. Here the $H_{\mathrm{T}}$ is defined similar to the all-hadronic channel, however only jets with $|\eta_{\mathrm{jet}}| < 2.5$ are considered. Events passing all selection requirements listed here

Table 5. Summary of the preselection criteria for the all-hadronic and one-lepton channels, in terms of the number of baseline and signal leptons, $R = 0.4$ and $R = 1.2$ jets, number of $b$-jets, and $H_{\mathrm{T}}$. The definitions of the physics objects for the two channels are given in the text. Signal leptons constitute a subset of the baseline leptons.

| Variable | All-hadronic channel | One-lepton channel |
|---|---|---|
| $\mathrm{N_{lep}}$ (baseline) | 0 | 1 |
| $\mathrm{N_{lep}}$ (signal) | - | 1 |
| $\mathrm{N_{jets}}$ ($R = 0.4$) | $\geq 6$ | $\geq 5$ |
| $\mathrm{N_{jets}}$ ($R = 1.2$) | $\geq 2$ | - |
| $\mathrm{N_{}b\text{-jets}}$ | $\geq 3$ | $\geq 3$ |
| $H_{\mathrm{T}}$ | $\geq 1150$ GeV | $\geq 300$ GeV |

are considered preselected for the analysis. The preselection requirements are summarized for both the analysis channels in Table 5.

### 5.5 Analysis Strategy

Preselected events are separated into signal, control, and validation regions based on the properties of the large-$R$ and small-$R$ jets in the event, as well as the signal lepton for the one-lepton channel. Signal regions (SRs) are signal-enriched regions while the control regions (CRs) are used to estimate the SM background contributions. The validation regions (VRs) are used to validate the background estimation methods. The analysis strategies for the all-hadronic and one-lepton channels are detailed below.

**5.5.1 All-hadronic channel.** In the all-hadronic channel, the leading two large-$R$ jets define the overall SR, where the leading large-$R$ jet satisfies $m_{\mathrm{jet,R=1.2}} > 300$ GeV and the sub-leading large-$R$ jet satisfies $m_{\mathrm{jet,R=1.2}} > 250$ GeV as shown in Figure 56 for distributions after preselection. To suppress multijet events containing, for example, gluon to $b\bar{b}$ splitting, a selection on $m_{bb}/p_{\mathrm{T},bb}$, defined as the ratio of the mass to the transverse momentum of the pair of $b$-tagged jets closest to the center of the large-$R$ jet, is applied to both large-$R$ jets. In signal events $m_{bb}/p_{\mathrm{T},bb}$ is expected to take on larger values than in background events,

thus a cut of $m_{bb}/p_{\mathrm{T},bb} > 0.25$ is required. Further, both large-$R$ jets must satisfy a $bb_i$ tag, where the $\Delta R$ between the leading ($i = 1$) or sub-leading ($i = 2$) large-$R$ jet and the second closest $b$-tagged jet, defined as $\Delta R\,(j, b_2)$, is less than 1.0 and thus both $b$-tagged jets are well contained within the volume of the large-$R$ jet. This variable is designed to suppress $t\bar{t}$ events where the second closest $b$-jet arises from the other top quark in the event and can thus have a large $\Delta R$ with the large-$R$ jet. In signal, on the other hand, the decay products of the dark pion always include two $b$-quarks no matter whether the $tttb$ or $ttbb$ final state is considered and the $\Delta R$ therefore tends to be small. The overall SR is then subdivided into nine separate bins in the leading versus sub-leading large-$R$ jet mass plane. A large-$R$ jet is considered $\pi_{D,i}$ tagged if its mass falls into one of the nine mass bins. The SR requires both large-$R$ jets to satisfy both tagging selections (i.e. both jets must be $bb_i$ and $\pi_{D,i}$ tagged). The events where the two leading large-$R$ jets satisfy only one or two out of the four possible tags form the CRs used for the data-driven multijet extrapolation; events that satisfy three tags allow for a validation of the method and thus form the VRs. The SR selection criteria are summarized in Table 6.

**5.5.2 One-lepton channel.** Events satisfying the preselection requirements for the one-lepton channel are categorized into SRs, CRs and VRs based on two kinematic variables defined in terms of the properties of the small-$R$ and large-$R$ jets. The first variable, $\Delta R(\ell, b_2)$, is defined as the angle between the lepton in the event and the second closest $b$-jet to this lepton and aims to suppress $t\bar{t}$ background similar to $\Delta R\,(j, b_2)$ in the all-hadronic channel. The kinematics of the second $b$-jet as distinguishing characteristic of signal events is also utilized for the second variable, $m_{bb,\mathrm{min}\Delta R}$, defined as the invariant mass of the two $b$-jets in the event that are closest to each other. This is effective for discriminating high

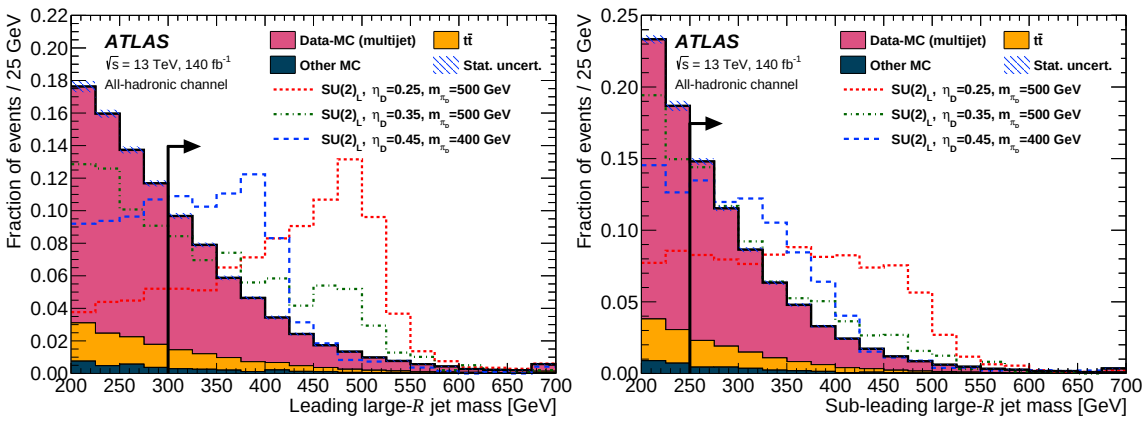


*Figure 56.* Mass of the a leading and b sub-leading large-$R$ jet for all simulated backgrounds overlaid with three example distributions for various signal points after preselection in the all-hadronic channel. Also shown is a simplified data-driven estimate of the multijet background which was created by taking the event yields for data and subtracting all simulated backgrounds from it. Statistical uncertainties stemming from MC are indicated by the shaded region. The SR is to the right of the vertical line in both the subfigures. Individual SR bins select sub-regions of leading and sub-leading large-$R$ jet mass for improved background discrimination. The last bin contains the overflow.

Table 6. Summary of selection criteria for the SR ("Tag selection"). Nine bins are defined in the leading large-$R$ jet vs. sub-leading large-$R$ jet mass plane. The inverted selection ("Anti-tag selection") is also defined for use in the data-driven multijet extrapolation described in Section 5.6.1.

| | Tag | Variable | Tag selection | Anti-tag selection |
|---|---|---|---|---|
| Both large-$R$ jets | | $m_{bb}/p_{\mathrm{T},bb}$ | $> 0.25$ | $> 0.25$ |
| Leading large-$R$ jet | $bb_1$ | $\Delta R\,(j, b_2)$ | $< 1.0$ | $\geq 1.0$ |
| Sub-leading large-$R$ jet | $bb_2$ | $\Delta R\,(j, b_2)$ | $< 1.0$ | $\geq 1.0$ |
| Leading large-$R$ jet | $\pi_{D,1}$ | $m_{\mathrm{jet,R=1.2}}$ | $[300-325$ GeV, $325-400$ GeV, $> 400$ GeV$]$ | $\leq 300$ GeV |
| Sub-leading large-$R$ jet | $\pi_{D,2}$ | $m_{\mathrm{jet,R=1.2}}$ | $[250-300$ GeV, $300-350$ GeV, $> 350$ GeV$]$ | $\leq 250$ GeV |

dark pion mass signal points against background in which the two $b$-quarks closest to each other come e.g. from gluon splitting. The distributions of these variables

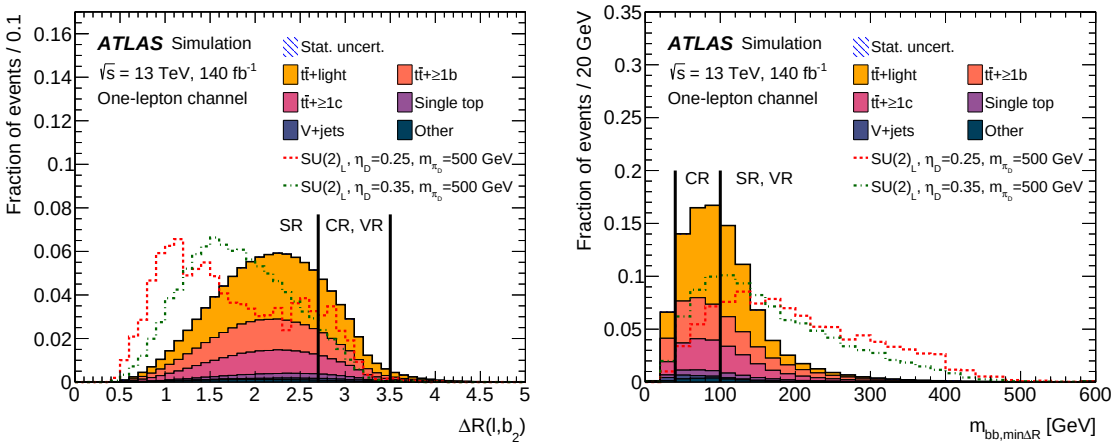


*Figure 57.* Normalized distributions of a $\Delta R(\ell, b_2)$ and b $m_{bb,\min\Delta R}$ for all simulated backgrounds with two example signal distributions overlaid after the one-lepton channel preselection. Statistical uncertainties stemming from MC are indicated by a shaded region, but are not visible on the scale of the $y$-axis. The vertical dashed lines indicate the selection requirements applied to events in the SR, CR and VR, as indicated by the labels.

in signal and background MC simulations are shown in Figure 57 for preselected events.

The SR is defined by requiring $\Delta R(\ell, b_2) < 2.7$ and $m_{bb,\min\Delta R} > 100$ GeV. A CR for the $t\bar{t}$ +HF background is defined by the requirements 2.7 ¡ $\Delta R(\ell, b_2)$ ¡ 3.5, and 40 GeV ¡ $m_{bb,\min\Delta R}$ ¡ 100 GeV, thus ensuring orthogonality to the SR. This region is used to correct for mismodeling in $t\bar{t}$ +HF events and has a background composition similar to that in the SR. Typical signal contamination in the CR, from signal points that are not already excluded through re-interpretation of other collider searches Butterworth et al. (2022), is below 1%. The $t\bar{t}$ +HF background estimate is validated in a VR defined by the requirements 2.7 ¡ $\Delta R(\ell, b_2)$ ¡ 3.5, and $m_{bb,\min\Delta R}$ ¿ 100 GeV, making it orthogonal to both the SR and the CR while also exhibiting a background composition similar to that of the SR and CR.

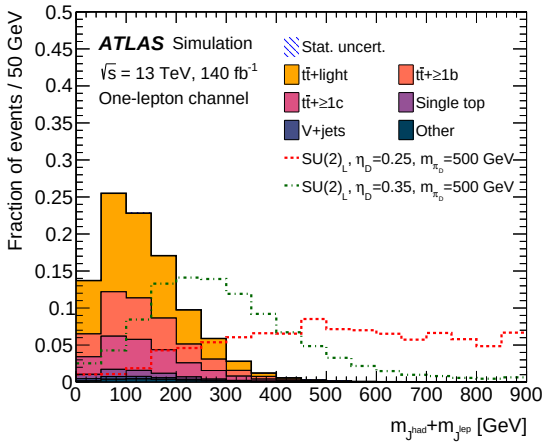


*Figure 58.* Normalized distributions of $m_{\mathbb{J}^{\text{had}}} + m_{\mathbb{J}^{\text{lep}}}$ for all simulated backgrounds overlaid with two example distributions for various signal points after the one-lepton channel preselection. Statistical uncertainties stemming from MC are indicated by a shaded region, but are not visible on the scale of the $y$-axis.

The statistical analysis in the one-lepton channel relies on a profile-likelihood fit to the distribution of the sum of the masses of the reclustered jets, described in Section 5.4, $m_{\mathbb{J}^{\text{had}}} + m_{\mathbb{J}^{\text{lep}}}$. This discriminating variable is shown in Figure 58 for preselected events. For the fit, all events are further classified into regions split into bins based on the number of jets and $b$-jets in the event. Six bins are defined labeled XR_5j3b, XR_5j4b, XR_6j3b, XR_6j4b, XR_7j3b and XR_7j4b, where the number before the 'j' indicates the number of jets, the number before the 'b' the number of $b$-jets and 'X' can take on the values 'S' for an SR, 'C' for a CR and 'V' for a VR bin. In all cases, the highest jet or $b$-jet multiplicity is inclusive, e.g. the region CR_7j4b is a CR that contains events with $\geq 7$ jets and $\geq 4$ $b$-jets.

## 5.6 Background Estimate

**5.6.1 All-hadronic channel.** The dominant background for the analysis in the all-hadronic channel originates from multijet events and constitutes about $75\% - 85\%$ of the total background in each SR bin. A data-driven method




*Figure 59.* Region labels for the 16 regions used in the data-driven multijet estimate in the all-hadronic channel. Region $S$ labels the SR, regions $B$, $C$, $E$ and $I$ are used for the ABCD extrapolation, regions $D$, $F$, $G$, $H$, $J$ and $O$ are used to compute correlation correction factors, and regions $K$, $L$, $M$ and $N$ are validation regions. The background estimate is performed independently for all nine SR bins.

is used to estimate this background, while MC simulation is used to account for the remaining sub-dominant SM processes as described in Section 5.3. Typical ABCD multijet extrapolations are based on two discriminating variables. Here, however, an extended ABCD method is employed that relies on four instead of two discriminating variables, which allows the correction of correlations between pairs of discriminating variables and provide validation regions close to the SR selection.

The multijet background is estimated by extrapolating from regions with small leading and sub-leading $m_{\text{jet,R=1.2}}$ and large $\Delta R\,(j, b_2)$ to SR bins with large leading and sub-leading $m_{\text{jet,R=1.2}}$ and small $\Delta R\,(j, b_2)$. The method is similar to the one detailed in Ref. ATLAS Collaboration (2018). To this end, two additional anti-tags denoted by a slashed tag label (with orthogonal selections to the already described $bb_i$ and $\pi_{D,i}$ tags) are defined. The tag $\not bb_i$ inverts the $bb_i$ selection, while $\not\pi_{D,i}$ places upper requirements on the large-$R$ jet mass, as summarized in Table 6. The combinations of possible tags and anti-tags in an event result in 16 separate regions shown in Figure 59. The extended ABCD method extrapolates from regions with one tag to each of the nine SR bins. Two-tag regions are used to determine correlation correction factors and three-tag regions are used for validation of the multijet estimate.

The concept of the extended ABCD method is detailed here by explicitly stating the computations for one VR, however, analogous derivations have to be carried out for all SRs and VRs. Considering only region $K$ in Figure 59, a 2-variable ABCD estimate for this region would be computed in the standard way through $\hat{K} = \frac{J \cdot D}{B}$, where $J$, $D$ and $B$ are the number of data events minus the number of simulated events in the respective regions. If $\pi_{D,1}$ and $\pi_{D,2}$ are uncorrelated, $\hat{K}$ would be a valid estimate. However, if $\pi_{D,1}$ and $\pi_{D,2}$ are correlated, then $\hat{K}$ needs to be corrected by a correlation factor ($k$-factor). As long as there is no significant additional three-tag correlation with the $bb_2$ tag, this correlation factor, $k_{\pi_{D,1},\pi_{D,2}}$, can be measured from $\frac{F \cdot A}{C \cdot E}$ since $\frac{K \cdot B}{J \cdot D} = \frac{F \cdot A}{C \cdot E}$. Thus,

$$\hat{K} = \frac{J \cdot D}{B} \cdot \frac{F \cdot A}{C \cdot E} = \frac{J \cdot D}{B} \cdot k_{\pi_{D,1},\pi_{D,2}} \ . \tag{5.1}$$

One can also consider the estimate of region $K$ using a three-variable ABCD estimate computed with two correlation correction factors:

$$\hat{K} = \frac{J \cdot C}{A} \cdot k_{\pi_{D,1},\pi_{D,2}} \cdot k_{\pi_{D,1},bb_2} \ , \tag{5.2}$$

where $k_{\pi_{D,1},bb_2} = \frac{D \cdot A}{B \cdot C}$. Substituting this correlation factor into Eq. (5.2) yields once again Eq. (5.1). All other $k$-factors can be defined according to the same principle as $k_{\pi_{D,1},\pi_{D,2}}$ and $k_{\pi_{D,1},bb_2}$.

The final multijet background estimate requires a four-variable ABCD estimate $\hat{S}'$ that is computed from data minus event counts from MC simulated backgrounds in the regions $B$, $C$, $E$, and $I$ where exactly one tag is applied and region $A$ with no applied tags according to

$$\hat{S}' = \frac{B \cdot C \cdot E \cdot I}{A^3} \ . \tag{5.3}$$

This estimate is then multiplied by six $k$-factors to correct for correlations between tags,

$$\hat{S} = \hat{S}' \cdot k_{\pi_{D,1},bb_1} \cdot k_{\pi_{D,2},bb_2} \cdot k_{\pi_{D,1},bb_2} \cdot k_{\pi_{D,2},bb_1} \cdot k_{\pi_{D,1},\pi_{D,2}} \cdot k_{bb_1,bb_2} \ . \tag{5.4}$$

If the selection criteria defined by these tags are independent from each other then the expectation value of the corresponding $k$-factor will be 1. Correlation factors around 1.5 are observed between the $\pi_{D,1}$ and $bb_1$ tags as well as the $\pi_{D,2}$ and $bb_2$ tags. The $bb_1$ and $bb_2$ tags are highly correlated with a $k$-factor of 0.1 due to the preselection requirement of three $b$-tagged jets. This could be mitigated by requiring four $b$-tagged jets, however, this would result in low statistics and high signal contamination for the four-variable ABCD extrapolation regions.

Typical signal contaminations in the extrapolation regions are less than 5% and small compared to the uncertainty applied to the multijet background discussed in Section 5.7. The method is validated through the closure of the estimate in the four 3-tag validation regions $K$, $L$, $M$ and $N$. Figure 60 compares data to estimated background yields for each validation region in each bin of the SR. If significant 3-tag correlations occurred, a discrepancy between multijet estimate and data yields should be visible in the validation regions. However, all data yields are compatible with the background estimate within the uncertainty bands for all validation regions. The uncertainty includes a non-closure systematic uncertainty, which by design covers non-linear correlations and the impact of multijet estimation regions with low statistics. It ranges between 33% and 57% and is derived and discussed in Section 5.7. The procedure was further validated by performing signal injection tests as well as stability tests over time, under variation of the selection criteria and with scaled simulated background contributions. In all

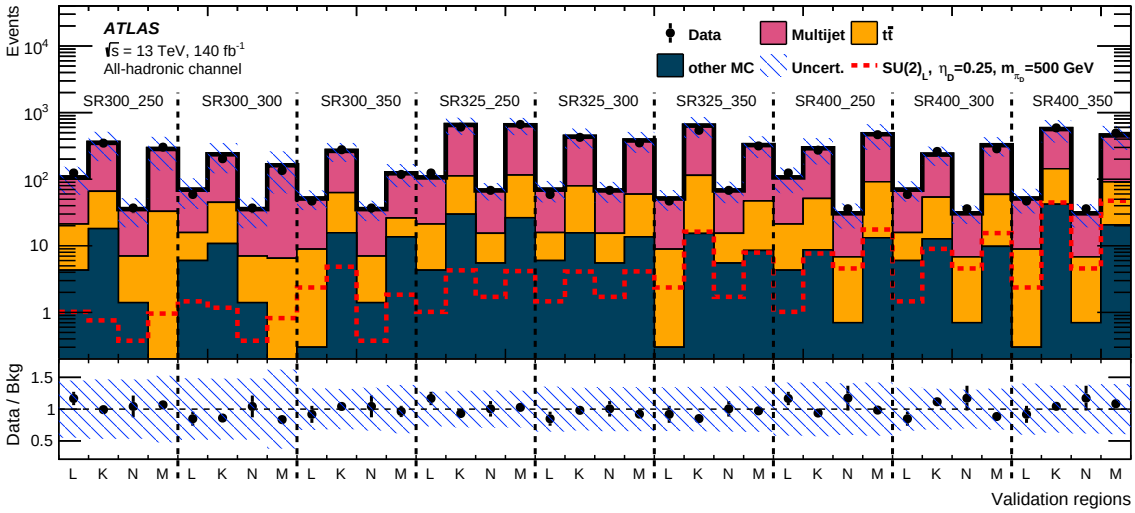


*Figure 60.* The four all-hadronic channel validation regions $K$, $L$, $M$ and $N$ from Figure 59 for each of the nine SR mass bins with the following naming convention: the leading large-$R$ jet lower mass boundary in GeV is followed by the sub-leading large-$R$ jet lower mass boundary. The shaded region indicates the uncertainty on the background estimate in each bin that includes the statistical uncertainties from the limited sample sizes in data and simulation as well as a multijet non-closure systematic uncertainty, as detailed in Section 5.7.

cases the resulting background estimates where stable and thus consistent with the nominal estimate.

**5.6.2 One-lepton channel.** The background in the one-lepton channel is estimated from MC simulations using the samples described in Section 5.3 and is dominated by $t\bar{t}$ production in association with light-flavor or heavy-flavor quarks. This background is estimated by using the inclusive $t\bar{t}$ sample complemented by the dedicated $t\bar{t} + b\bar{b}$ sample, with events categorized into $t\bar{t}+ \geq 1b$, $t\bar{t}+ \geq 1c$ and $t\bar{t}$ + light as described in Section 5.3. The $t\bar{t}$ +HF background that populates the SR is known from previous studies to be underestimated by the current MC predictions ATLAS Collaboration (2019h). This mismodeling is corrected by keeping the normalization of these backgrounds unconstrained in the profile-likelihood fit to the $m_{\mathbb{J}^{\mathrm{had}}} + m_{\mathbb{J}^{\mathrm{lep}}}$ distribution. To this

end, the $t\bar{t}+ \geq 1c$ and $t\bar{t}+$ light contributions are combined and two normalization factors are fit depending on whether in addition to $t\bar{t}$ any $b$-quarks are present in the event. In this categorization, the combination of the $t\bar{t}+ \geq 1c$ and $t\bar{t}+$ light backgrounds is referred to as $t\bar{t}+$ nb. The resulting background estimates for the SR, CR and VR are presented in Section 5.8.2.

## 5.7 Systematic Uncertainties

The predicted signal and background event yields in the SR bins are affected by various sources of systematic uncertainties stemming from instrumentation, the data-driven multijet estimation and theoretical considerations. For the all-hadronic channel, the total uncertainty is dominated by the uncertainty on the multijet background estimate. In the one-lepton channel, the theoretical sources of uncertainty on the background modeling dominate the total uncertainty.

**5.7.1 Experimental uncertainties.** The uncertainty in the combined 2015–2018 integrated luminosity is 0.83% ATLAS Collaboration (2022c), obtained using the LUCID-2 detector Avoni et al. (2018) for the primary luminosity measurements, complemented by measurements using the ID and calorimeters. A systematic variation that might be introduced by the reweighting of simulated samples to match the pileup profile observed in data is estimated by varying the scale factor applied to the pileup distributions. The onset of the $H_{\mathrm{T}}$ trigger used in the all-hadronic channel was studied and potential effects of mismodeling were evaluated. All three of these uncertainties were found to have a negligible impact on the analysis ($< 1\%$ in the all-hadronic channel, and ranking from $< 1\%$ to a few percent depending on the signal in the one-lepton channel).

Slight performance differences between data and simulation in lepton reconstruction, identification and isolation are corrected by the application of

scale factors that are estimated from tag-and-probe experiments in data and simulation ATLAS Collaboration (2019d, 2021d). The impact of lepton momentum scale corrections is evaluated by $\pm 1\sigma$ scale variations. For resolution uncertainties the lepton energy or momentum is smeared. In total seven (twelve) separate variations for electrons (muons) are considered. The impact of lepton uncertainties is less than 1% in both channels.

The determination of the jet energy scale and resolution is done by combining information from collision data, test beam data and simulation as described in Ref. ATLAS Collaboration (2020b). Effects from jet flavor composition, single-particle response and pileup are considered. In the one-lepton channel, 29 parameters are evaluated for scale variations, while 13 parameters are evaluated for jet $p_{\mathrm{T}}$ resolution systematic uncertainties. In the all-hadronic channel the variations are simplified since the data-driven background estimation method largely compensates yield changes by different systematic variations and causes most of the systematic uncertainties to be negligibly small. As such, 23 parameters arise from scale variations, while for jet $p_{\mathrm{T}}$ resolution systematic uncertainties 8 parameters are evaluated. The impact of these uncertainties on the final result is small, ranging between $<$ 1% to about 4% in the all-hadronic channel, and remaining $<$ 10% in the one-lepton channel.

Uncertainties on the corrections of $b$-tagging efficiency differences between data and simulation are derived from dedicated flavor-enriched subsets of the data ATLAS Collaboration (2019a). Also considered are uncertainties due to the mis-tagging of $c$-jets ATLAS Collaboration (2021c) and light-flavor jets ATLAS Collaboration (2019b). Additionally, variations to extrapolate the measured uncertainties to the high-$p_{\mathrm{T}}$ region are considered for both channels ATLAS

Collaboration (2021f). The impact of flavor-tagging systematic uncertainties is less than 1% on the final result in the all-hadronic channel, while a larger contribution is observed in the one-lepton channel, reaching values of the order of 10%.

**5.7.2 Modeling uncertainties in background simulations.** For the all-hadronic channel, uncertainties in modeling of the $t\bar{t}$ background are included. For the one-lepton channel, uncertainties in modeling the $t\bar{t}$, $t\bar{t}$ + $b\bar{b}$, and single top-quark backgrounds are included. All other simulated backgrounds are negligible in both channels and no systematic uncertainties are assigned to them. For the single top-quark background, a 30% normalization uncertainty is applied ATLAS Collaboration (2022a) with an impact ranging between $< 1\%$ and a few percent. Details on the $t\bar{t}$ and $t\bar{t} + b\bar{b}$ uncertainties are described below.

***5.7.2.1*** $t\bar{t}$ ***uncertainties.*** Several uncertainties in the theoretical modeling of the $t\bar{t}$ background samples are considered. In the one-lepton channel the $t\bar{t}$ theory systematic uncertainties apply only on the $t\bar{t}$ + light and $t\bar{t}+ \geq 1c$ background components as they are estimated from the five-flavor scheme $t\bar{t}$ sample, while the $t\bar{t}+ \geq 1b$ background has dedicated systematic uncertainties.

Missing higher order contributions in perturbative expansion of the $t\bar{t}$ production cross-section are estimated by adding in quadrature contributions from renormalization and factorization scale variations, which are obtained by independently varying the parameters $\mu_R$ and $\mu_F$ by a factor 0.5 and 2.0 and taking the envelope. Uncertainties on the choice of PDF set used for event simulation are estimated by using the PDF4LHC and NNPDF error sets following the PDF4LHC prescription Botje et al. (2011) and taking the envelope. The initial-state radiation (ISR) modeling is estimated by variations of the strong coupling constant $\alpha_S$ through the VAR3C tune variation. The amount of final-state radiation (FSR)

in an event is estimated by varying the factorization scale by factors 0.5 and 2.0 inside PYTHIA. To assess the uncertainty in the matching of NLO matrix elements to the parton shower, the nominal sample is compared to an alternative sample obtained setting the `pthard` PYTHIA parameter to 1 (the default is 0). This parameter regulates the definition of the vetoed region of the showering, important to avoid holes and overlaps in the phase space filled by POWHEG and PYTHIA. This recommendation follows the description included in Ref. Höche, Mrenna, Payne, Preuss, and Skands (2022). The alternative sample was produced using POWHEG interfaced with PYTHIA.306 using the NNPDF2.3 PDF set and the A14 set of tuned parameters. The impacts of using a different parton shower and hadronization model were evaluated by comparing the nominal $t\bar{t}$ sample with another event sample produced with the POWHEG-BOX v2 generator. For the parton shower variation the NNPDF3.0NLO PDF set was used, while events in the sample used to estimate the impact of the hadronization model were interfaced with HERWIG 7.04 Bähr et al. (2008); Bellm et al. (2016), using the H7UE set of tuned parameters Bellm et al. (2016) and the MMHT2014LO PDF set Harland-Lang, Martin, Motylinski, and Thorne (2015). The impact of a variation of the $h_{\text{damp}}$ parameter is assessed by comparing the nominal samples to an alternative set of samples for which $h_{\text{damp}}$ is set to $3m_{\text{top}}$.

All alternative samples used to derive the systematic uncertainties are corrected to match the NNLO in QCD and NLO in EW predictions of the top/antitop-quark $p_{\text{T}}$ and the top-quark mass distribution using the procedure outlined in Section 5.3.2.1. A systematic uncertainty associated with this reweighting itself is derived from the maximum and minimum 7-point scale variations, independently for the top/antitop-quark $p_{\text{T}}$ and the top-quark mass.

The variations are taken into account in the final statistical fit by including them as scale variations on the $t\bar{t}$ background.

To avoid over-constraining the $t\bar{t}$ modeling nuisance parameters in the one-lepton channel, the theoretical systematic uncertainties are treated as uncorrelated among $t\bar{t}$ + light and $t\bar{t}+ \geq 1c$, jet and $b$-jet multiplicity bins, and between their shape and acceptance components.

The impact of $t\bar{t}$ modeling uncertainties on the final result is found to range between $< 1\%$ and 10%.

***5.7.2.2*** $t\bar{t} + b\bar{b}$ ***uncertainties.*** Theory uncertainties on the $t\bar{t} + b\bar{b}$ sample are only applied to the $t\bar{t}+ \geq 1b$ component in the one-lepton channel, as all other $t\bar{t}$ components are estimated from the bulk $t\bar{t}$ sample.

The scale, PDF, ISR, and FSR uncertainties for the $t\bar{t} + b\bar{b}$ sample are derived in the same way as the bulk $t\bar{t}$ sample. The impacts of using a different parton shower and hadronization model are evaluated by comparing the nominal $t\bar{t}$ sample to another sample produced with the Powheg-Box v2 generator. For the parton shower variation the NNPDF3.0NLO PDF set was used, while events in the sample estimating the impact of the hadronization model were interfaced with Herwig 7.1, using the H7.1-Default set of tuned parameters and the MMHT2014lo PDF set Harland-Lang et al. (2015).

The matching uncertainty is evaluated by comparing the nominal sample with an alternative sample obtained by setting the `pthard` Pythia parameter to 1. The alternative sample was produced using Powheg interfaced with Pythia.307 using the NNPDF2.3 PDF set and the A14 set of tuned parameters.

The $t\bar{t} + b\bar{b}$ uncertainty nuisance parameters are treated as uncorrelated between the different regions of jet and $b$-jet multiplicities and are further split up

into their shape and acceptance components to avoid over-constraining them in the fit. They constitute the dominant systematic contribution in the one-lepton channel, with an impact on the final results ranging from 1% to about 30%.

**5.7.3 Data-driven background estimation uncertainties.** In the all-hadronic channel, the dominant systematic uncertainty originates from the multijet estimation method. Deviations of the ratio between data and SM estimate from unity in the VRs, denoted by $k_{VR} = (\text{data} - \text{MC})/\text{multijet}$, are used to estimate a non-closure systematic uncertainty. These $k$-factors are a measure of the remaining correlations between 3-tags in the multijet estimation method and are expected to be close to unity. The statistical uncertainties on the $k$-factors $\sigma_{k_{VR}}$ are added in quadrature so that the final multijet uncertainty is calculated according to:

$$\sigma_{ABCD} = \sqrt{\left(1 - \prod_{VR} k_{VR}\right)^2 + \sum_{VR} \sigma_{k_{VR}}^2} \quad , \tag{5.5}$$

where the first term under the square root describes the non-closure component of the systematic uncertainty calculated from the $k$-factors and the second term the statistical uncertainty summed up in quadrature over all four VRs. The statistical component dominates in most regions and is driven by region $H$ in Figure 59 which has the lowest number of events. The computation is done separately for each bin of the SR producing values ranging from 33% to 57%. The uncertainty in each SR mass bin is treated as fully uncorrelated with the other SR mass bins thus yielding a conservative estimate.

## 5.8 Statistical Analysis and Results

Signal hypotheses are evaluated against the data by performing profile-likelihood fits in each analysis channel. The set of nuisance parameters $\theta$ that corresponds to the systematic uncertainties is scaled in such a fashion that, before

the fit, all individual uncertainties $j$ have $\theta_j = 0$. In addition, the uncertainties of these nuisance parameters $\sigma$ are scaled to fulfill $\sigma_j = 1$ before fitting. Defining $\gamma$ as the set of statistical uncertainties with $\gamma_i$ the uncertainty on the number of predicted events of a specific bin $i$, the set is scaled to be a factor around 1. The profile-likelihood fit is then performed by minimizing the quantity $q(\mu) = -2\log\mathcal{L}$, where the likelihood $\mathcal{L}$ is defined as

$$\mathcal{L}(\mu,\theta|S,B,N) = \prod_{i\in\text{bins}} \mathcal{P}\left(N_i|\mu S_i + B_i\right) \times \mathcal{P}\left(S_i + B_i|\gamma_i\right) \prod_{j\in\text{syst.}} \mathcal{G}\left(\theta_j,\sigma_j\right) \qquad (5.6)$$

with $N$ being the number of data events, $S$ the predicted number of signal events and $B$ the expected number of background events. Statistical and systematic uncertainties are taken to be Poissonian ($\mathcal{P}$) and Gaussian ($\mathcal{G}$) distributed parameters, respectively. The fit is evaluated using the RooFit Verkerke and Kirkby (2003) package with the minimization conducted with the Minuit2 package Hatlo et al. (2005), which yields the optimal values for $\mu$ and the set of parameters $\theta_i$, $\gamma_i$ and $\sigma_i$ in a signal plus background fit.

**5.8.1 All-hadronic channel.** The fit in the all-hadronic channel is performed over all nine SR bins simultaneously. Since the multijet estimate constrains background to the data, most systematic uncertainties (other than from the multijet estimate) have limited impact on the final result and all systematic uncertainties below 1% are ignored. Surviving uncertainties are kept as nuisance parameters in the fit. Because simulated backgrounds constitute less than 20% of the total SM background in the SR, no CRs are used to scale the simulated estimates.

Figure 61 shows the distributions in all SR bins after fitting. No significant pulls or constraints are observed for the fitted nuisance parameters. The results are also summarized in Table 7. As can be seen the data are very well described by

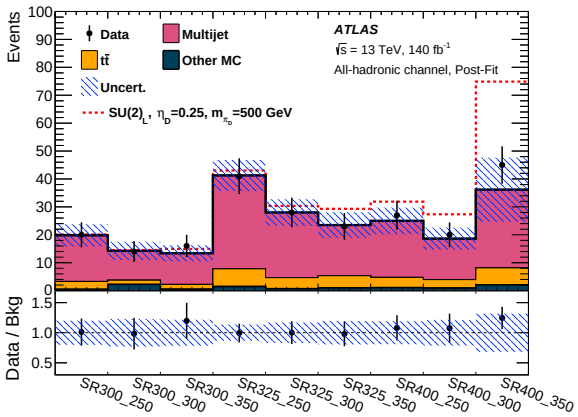


*Figure 61.* Comparison of the events yields in data and the background prediction after the fit under the background-only hypothesis in all bins of the all-hadronic SR. The dashed line is stacked onto the SM background and shows an example $\mathrm{SU}(2)_\mathrm{L}$ signal with $\eta_\mathrm{D} = 0.25$ and $m_{\pi_\mathrm{D}} = 500$ GeV. The uncertainty bands contain all statistical and systematic uncertainties. The horizontal axis labels reflect the different SR bins, with the first number indicating the lower boundary of the leading large-$R$ jet mass bin and the second number the lower boundary of the sub-leading large-$R$ jet mass bin.

the background-only hypothesis with no significant excess of events above the SM prediction.

**5.8.2 One-lepton channel.** In the one-lepton channel, a profile-likelihood fit is performed to the binned $m_{\mathbb{J}^\mathrm{had}} + m_{\mathbb{J}^\mathrm{lep}}$ spectrum in the six SRs and the six CRs defined based on jet and $b$-jet multiplicity requirements, simultaneously. As already indicated in Section 5.6.2, two independent normalization factors are used for the $t\bar{t}$ background depending on whether in addition to $t\bar{t}$ any $b$-quarks are present in the event. These two normalization factors are denoted by $k(t\bar{t}+ \geq 1b)$ and $k(t\bar{t} + 0b)$. To avoid over-constraining the background modeling nuisance parameters, the theoretical systematic uncertainties are treated as uncorrelated among different $t\bar{t}$ flavors, jet and $b$-jet multiplicity bins, and between their shape and acceptance components.

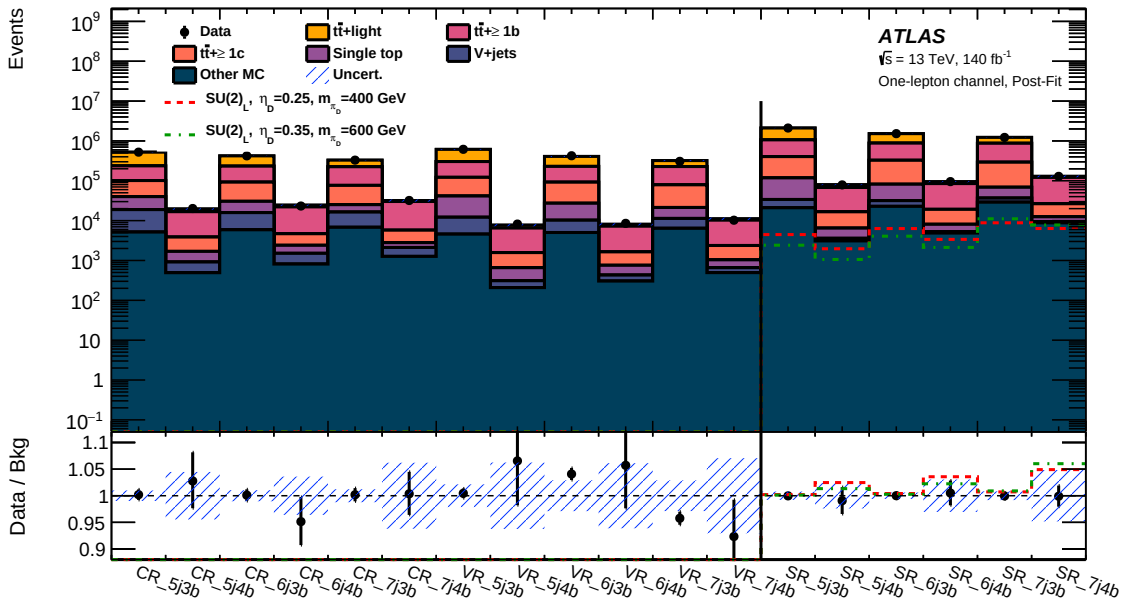


*Figure 62.* Comparison of the events yields in data and the background prediction in the SRs, CRs, and VRs in the one-lepton channel, after the fit to data in all CRs and SRs under the background-only hypothesis. The uncertainty bands contain all statistical and systematic uncertainties. Two example $\mathrm{SU}(2)_{\mathrm{L}}$ signal points are overlaid in the SRs.

The event yields for all SRs, CRs and VRs are shown after a fit to the data under the background-only hypothesis in Figure 62. The corresponding distributions of $m_{\mathbb{J}^{\mathrm{had}}} + m_{\mathbb{J}^{\mathrm{lep}}}$ are shown in Figure 63 for all jet and $b$-jet multiplicity bins of the SR. The SM background estimate is in good agreement with data after the background-only fit. The post-fit normalization factors for the $t\bar{t}$ background components are $k(t\bar{t} + 0b) = 0.92^{+0.09}_{-0.08}$ and $k(t\bar{t} + \geq 1b) = 1.60^{+0.19}_{-0.17}$. No pulls greater than $1\sigma$ are observed for the fitted nuisance parameters, with only some constraints in the nuisance parameters describing the theoretical modeling. Data and post-fit background event yields are shown in Table 8. Good agreement between the background prediction and data is observed in all regions.

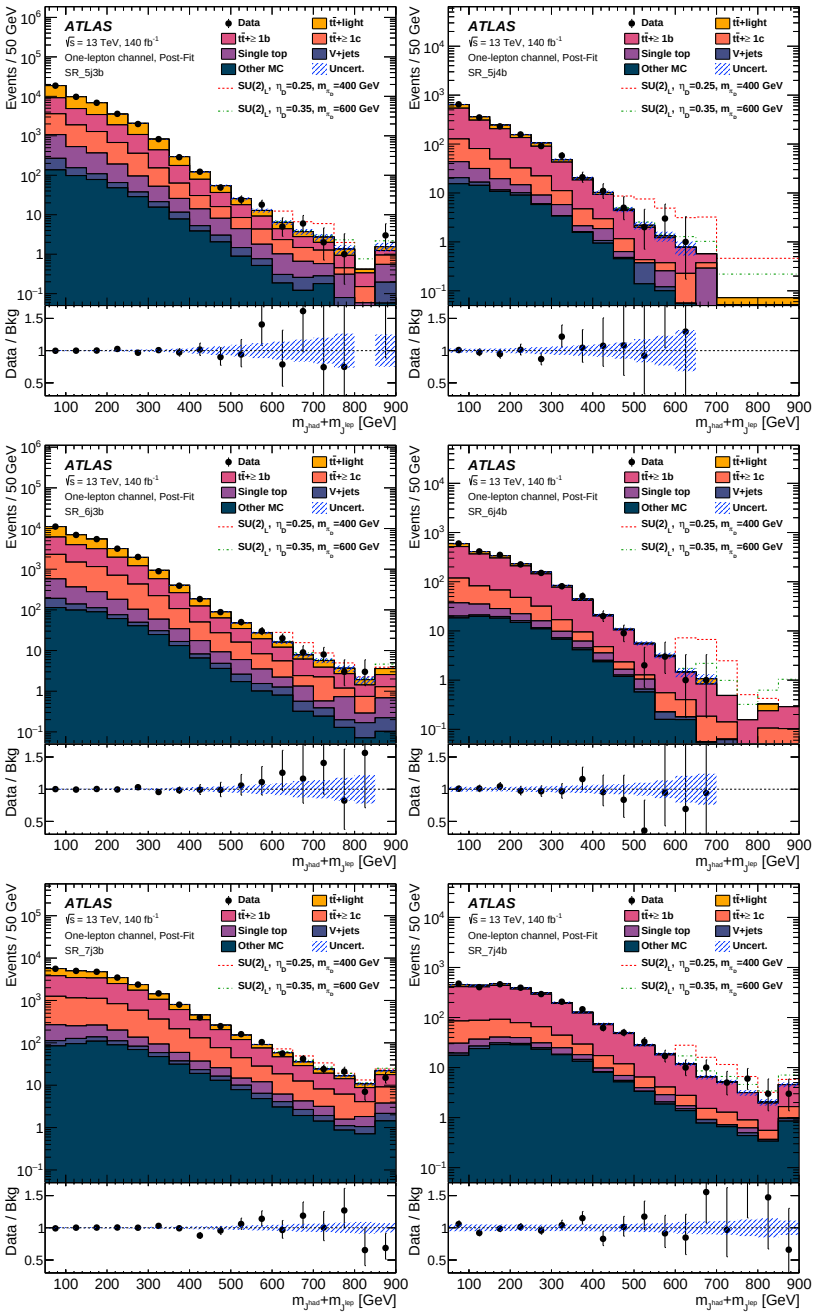


*Figure 63.* Distributions of $m_{\mathbb{J}^{\text{had}}} + m_{\mathbb{J}^{\text{lep}}}$ in a SR_5j3b, b SR_5j4b, c SR_6j3b, d SR_6j4b, e SR_7j3b, and f SR_7j4b, after the fit to data in all CRs and SRs under the background-only hypothesis. Two example $\mathrm{SU}(2)_{\mathrm{L}}$ signal point with $\eta_{\mathrm{D}} = 0.25$ and $m_{\pi_{\mathrm{D}}} = 400$ GeV is stacked on top of the background. The uncertainty bands contain all statistical and systematic uncertainties. The dashed line in the ratio panel shows the ratio of signal plus background event yields over just background event yields.

## 5.9 Interpretation

The results are used to set 95% confidence level (CL) upper limits on the dark pion pair production cross-sections following the $CL_S$ technique Read (2002). Upper limits on the dark pion production cross-sections are shown in Figure 64 for four slices of $\eta_D$. The impacts of the different systematic uncertainties, described in Section 5.7, on the signal strength, defined as the signal cross-section normalized to the theoretical prediction, of two benchmark signals are summarized in Table 9: the analysis is limited by the systematic uncertainty, with dominant contribution from the theoretical sources of uncertainty on the background modeling.

Using the predicted dark pion pair production cross-sections, the limits can be translated into limits on dark pion masses in the two-dimensional $\eta_D$–$m_{\pi_D}$ plane. The exclusion contour obtained from the all-hadronic channel for the $SU(2)_L$ model is shown in Figure 65a. No dark pion masses can be excluded for $\eta_D = 0.15$. For $\eta_D = 0.25$ the exclusion covers the mass range 280 GeV $< m_{\pi_D} <$ 520 GeV (expected 280 GeV $< m_{\pi_D} <$ 540 GeV), while for $\eta_D = 0.35$, dark pions with masses $m_{\pi_D} <$ 430 GeV are excluded (expected $m_{\pi_D} <$ 450 GeV). The exclusion contour obtained from the one-lepton channel for $SU(2)_L$ is shown in Figure 65b and is observed to fully cover the all-hadronic limit and significantly extend the probed phase space for this dark meson model. Since the all-hadronic limit is completely contained within the one-lepton limit, there is no expected gain from a combination of the two channels. Dark pion masses with $m_{\pi_D} <$ 940 GeV can be excluded for $\eta_D = 0.45$, $m_{\pi_D} <$ 720 GeV are excluded for $\eta_D = 0.35$ and for $\eta_D = 0.25$ the mass region $m_{\pi_D} <$ 740 GeV is excluded. The results significantly extend the phase space previously excluded through re-interpretation of other collider searches Butterworth et al. (2022). In the $SU(2)_R$ model, cross sections are significantly smaller than for

$SU(2)_L$ and therefore none of the channels have sensitivity to this model with the current data sample.

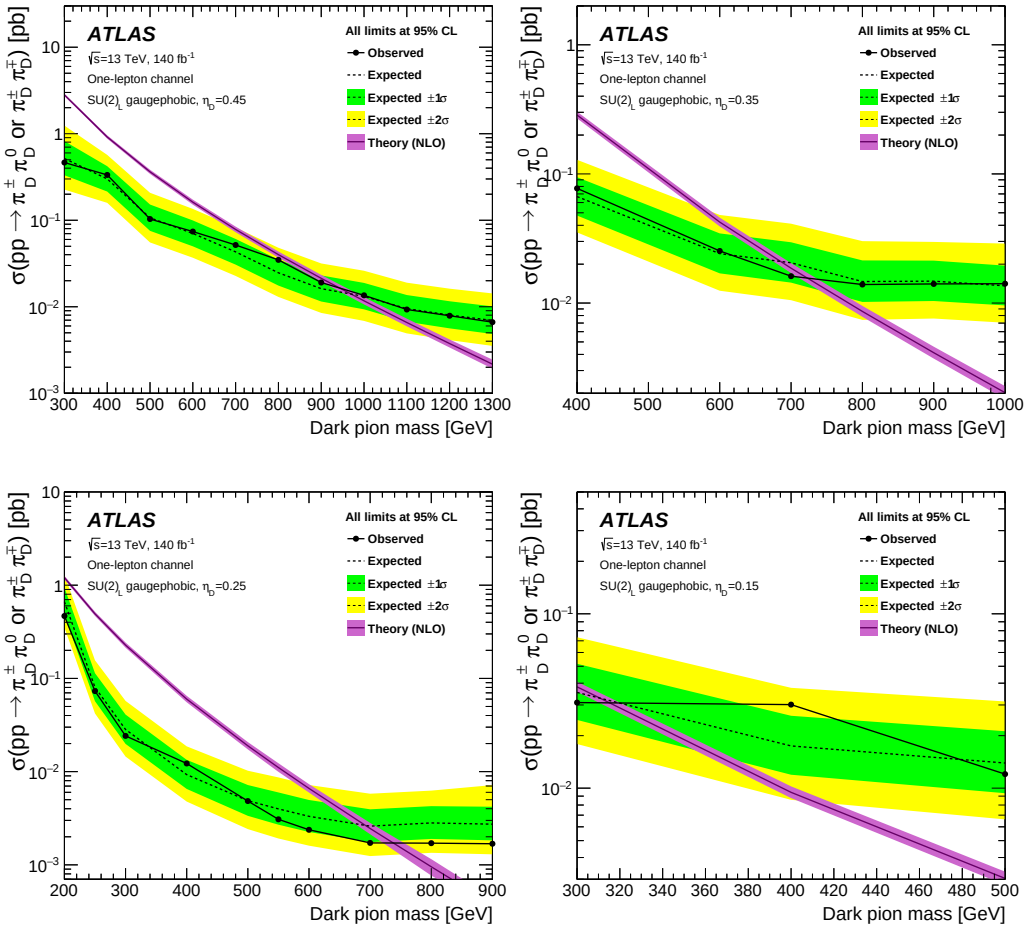


*Figure 64.* Observed (solid line) and expected (dashed line) limits on the dark pion production cross-section as a function of dark pion mass using the $CL_S$ method for all $SU(2)_L$ models in four slices of $\eta_D$: a $\eta_D$=0.45, b $\eta_D$=0.35, c $\eta_D$=0.25, and d $\eta_D$=0.15. The surrounding shaded bands correspond to one and two standard deviations around the expected limit. The overlaid theory line shows the theoretical dark pion cross-section prediction Kribs, Martin, Ostdiek, and Tong (2019).

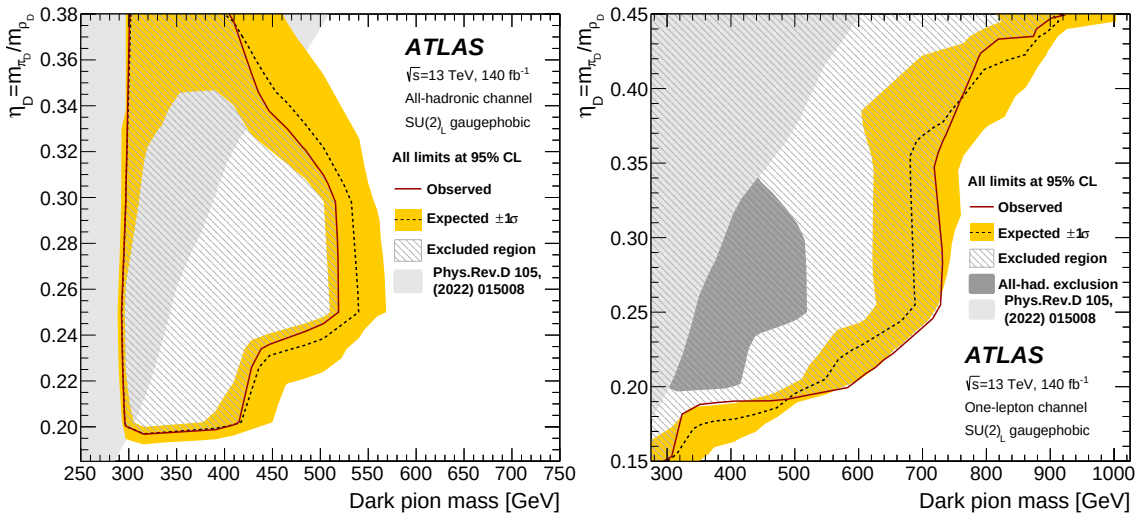


*Figure 65.* Observed (solid line) and expected (dashed line) exclusion contours at 95% CL in the $\eta_{\mathrm{D}}$–$m_{\pi_D}$ plane for $\mathrm{SU}(2)_{\mathrm{L}}$ signal models in the a all-hadronic and b one-lepton channel. Masses that are within the contours are excluded, as indicated by the hatched area. An uncertainty band corresponding to the $\pm 1\sigma$ variation on the expected limit is also indicated. The shaded area in a and the innermost shaded area in b indicates the phase space previously excluded through re-interpretation of other collider searches presented in Ref. Butterworth et al. (2022). The outermost shaded area in b indicates the phase space excluded by the analysis in the all-hadronic channel and is identical to the observed limit shown in a.

Table 7. Observed and predicted event yields after the fit under the background-only hypothesis in all nine all-hadronic SR mass bins. The name of each column corresponds to the SR bins: the leading large-$R$ jet lower mass boundary in GeV is followed by the sub-leading large-$R$ jet lower mass boundary; the same convention is used in Figure 61. The quoted uncertainties contain statistical and systematic components. The total post-fit uncertainty can be smaller than the sum in quadrature of the different components due to correlations resulting from the fit to data.

| | SR300_250 | SR300_300 | SR300_350 |
|---|---|---|---|
| V+jets | $< 0.01$ | $1.97 \pm 0.89$ | $0.28 \pm 0.06$ |
| Single top | $0.12 \pm 0.07$ | $0.00 \pm 0.03$ | $< 0.01$ |
| $t\bar{t} + X$ | $0.30 \pm 0.04$ | $0.21 \pm 0.09$ | $0.17 \pm 0.04$ |
| $t\bar{t}$ | $2.9 \pm 1.9$ | $1.6 \pm 1.1$ | $1.78 \pm 0.76$ |
| Multijet | $16.5 \pm 4.3$ | $10.5 \pm 3.6$ | $11.1 \pm 3.1$ |
| Total SM | $19.8 \pm 4.0$ | $14.2 \pm 3.3$ | $13.4 \pm 2.9$ |
| Data | 20 | 14 | 16 |

| | SR325_250 | SR325_300 | SR325_350 |
|---|---|---|---|
| V+jets | $0.74 \pm 0.64$ | $0.12 \pm 0.18$ | $0.19 \pm 0.16$ |
| Single top | $0.36 \pm 0.06$ | $0.12 \pm 0.13$ | $0.27 \pm 0.15$ |
| $t\bar{t} + X$ | $0.35 \pm 0.06$ | $0.44 \pm 0.11$ | $0.50 \pm 0.07$ |
| $t\bar{t}$ | $6.4 \pm 3.6$ | $4.0 \pm 2.0$ | $4.4 \pm 2.1$ |
| Multijet | $33.4 \pm 6.7$ | $23.3 \pm 5.2$ | $18.1 \pm 5.0$ |
| Total SM | $41.2 \pm 5.6$ | $28.0 \pm 4.8$ | $23.5 \pm 4.6$ |
| Data | 41 | 28 | 23 |

| | SR400_250 | SR400_300 | SR400_350 |
|---|---|---|---|
| V+jets | $0.71 \pm 0.55$ | $< 0.01$ | $1.19 \pm 0.30$ |
| Single top | $< 0.01$ | $0.47 \pm 0.08$ | $0.11 \pm 0.02$ |
| $t\bar{t} + X$ | $0.34 \pm 0.07$ | $0.40 \pm 0.07$ | $0.73 \pm 0.10$ |
| $t\bar{t}$ | $3.7 \pm 1.8$ | $3.1 \pm 2.5$ | $6.1 \pm 3.9$ |
| Multijet | $20.2 \pm 5.3$ | $14.7 \pm 4.6$ | $28 \pm 12$ |
| Total SM | $25.0 \pm 4.8$ | $18.6 \pm 4.0$ | $36 \pm 11$ |
| Data | 27 | 20 | 45 |

Table 8. Observed and predicted event yields after the fit under the background-only hypothesis in the six SR bins in the one-lepton channel. The name of each column corresponds to the bins described in Section 5.5.2, identified with the number of jets followed by the number of $b$-jets. The quoted uncertainties contain statistical and systematic components. The total post-fit uncertainty can be smaller than the sum in quadrature of the different components due to correlations resulting from the fit to data.

| | SR_5j3b | SR_5j4b | SR_6j3b |
|---|---|---|---|
| $t\bar{t}+\geq 1b$ | $12400 \pm 2600$ | $1150 \pm 180$ | $9400 \pm 1800$ |
| $t\bar{t}+\geq 1c$ | $5900 \pm 500$ | $230 \pm 40$ | $5400 \pm 600$ |
| $t\bar{t}+$ light | $23100 \pm 1900$ | $270 \pm 70$ | $14300 \pm 1200$ |
| Single top | $1800 \pm 500$ | $59 \pm 18$ | $1080 \pm 330$ |
| V+jets | $274 \pm 30$ | $10.2 \pm 1.5$ | $192 \pm 22$ |
| Other MC | $416 \pm 15$ | $61 \pm 4$ | $465 \pm 17$ |
| Total SM | $10500 \pm 100$ | $402 \pm 20$ | $8430 \pm 110$ |
| Data | 10462 | 403 | 8438 |

| | SR_6j4b | SR_7j3b | SR_7j4b |
|---|---|---|---|
| $t\bar{t}+\geq 1b$ | $1210 \pm 120$ | $9900 \pm 2500$ | $1900 \pm 400$ |
| $t\bar{t}+\geq 1c$ | $247 \pm 45$ | $5400 \pm 800$ | $350 \pm 90$ |
| $t\bar{t}+$ light | $220 \pm 50$ | $8500 \pm 1500$ | $180 \pm 50$ |
| Single top | $59 \pm 18$ | $710 \pm 220$ | $66 \pm 21$ |
| V+jets | $7.7 \pm 1.2$ | $170 \pm 20$ | $14.9 \pm 1.9$ |
| Other MC | $99 \pm 6$ | $620 \pm 40$ | $187 \pm 14$ |
| Total SM | $477 \pm 22$ | $6600 \pm 120$ | $640 \pm 40$ |
| Data | 465 | 6598 | 641 |

Table 9. Impact of different categories of systematic uncertainty in the one-lepton channel, for two signal benchmarks, relative to the total uncertainty on the fitted signal strength. For each category, the fit is repeated with the corresponding group of nuisance parameters fixed to their best-fit values and the impact for each category is evaluated as the quadrature difference between the signal strength uncertainty in the new fit and in the nominal one, divided by the uncertainty in the nominal fit. The contribution from the statistical uncertainty and the systematic one, further separated into the global instrumental and theoretical uncertainties, are shown. The total systematic uncertainty is different from the sum in quadrature of the different groups due to the correlations among the nuisance parameters in the fit.

| Category | $\mathrm{SU(2)_L}$, $\eta_\mathrm{D} = 0.25$, $m_{\pi_D} = 400$ GeV | $\mathrm{SU(2)_L}$, $\eta_\mathrm{D} = 0.35$, $m_{\pi_D} = 700$ GeV |
|---|---|---|
| Luminosity | 0.03 | 0.05 |
| Pileup | 0.05 | 0.09 |
| Flavor tagging | 0.28 | 0.26 |
| Leptons | 0.01 | 0.04 |
| Jets | 0.08 | 0.14 |
| $t\bar{t}+ \geq 1b$ | 0.26 | 0.53 |
| $t\bar{t}+ \geq 1c$ | 0.12 | 0.18 |
| $t\bar{t}+$ light | 0.13 | 0.17 |
| Top $p_\mathrm{T}$ NNLO reweighting | 0.08 | 0.09 |
| Single top | 0.06 | 0.06 |
| Statistical | 0.28 | 0.24 |
| Instrumental | 0.30 | 0.30 |
| Theory | 0.38 | 0.63 |

## 5.10 Conclusion

Results from a search for dark mesons originating from strongly-coupled, $SU(2)$ dark flavor symmetry conserving models and decaying to top and bottom quarks are reported. The analysis is based on the full Run 2 data sample of proton-proton collisions at $\sqrt{s} = 13$ TeV recorded by the ATLAS detector at the LHC, corresponding to an integrated luminosity of 140 fb$^{-1}$. The search is performed in the all-hadronic channel, where the event signature results in eight to ten jets of which at least four originate from bottom quarks, and in the one-lepton channel, corresponding to final states with one electron or muon in addition to jets. In the all-hadronic channel, a data-driven technique is used to estimate the predominant multijet background. In the one-lepton channel, the dominant background comes from $t\bar{t}$ production and is estimated from MC simulations.

No excess above the SM background expectation is observed. The strongest exclusion limits are obtained from the one-lepton channel. For $\mathrm{SU(2)_L}$ signals with $m_{\pi_\mathrm{D}}/m_{\rho_D} = 0.45$, dark pions with masses $m_{\pi_\mathrm{D}} < 940$ GeV are excluded, while for $m_{\pi_\mathrm{D}}/m_{\rho_D} = 0.25$ the exclusion covers the mass range $m_{\pi_\mathrm{D}} < 740$ GeV. These results constitute the first direct collider constraints on this type of model, and significantly extend the phase space previously excluded through re-interpretation of other collider searches.

## 5.11 Multi-Lepton Channel Truth Study

As seen in figure 66, decays with 2 or more leptons constitute a small fraction of *ttbb* and *tttb* final states. The purpose of these studies is to investigate the benefits of adding the multi-lepton channel to the aforementioned Run 2 iteration of the dark meson analysis, or a potential Run 3 update of the analysis. Although the fractions are small, the potential of making the one-lepton channel

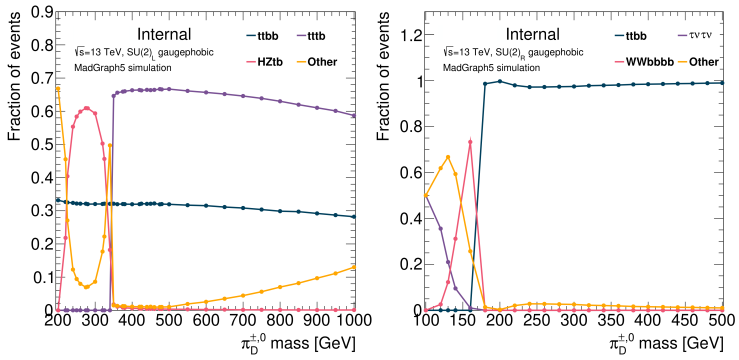


*Figure 66.* Most relevant final states for pair-produced dark pions from a gaugephobic $\mathrm{SU}(2)_\mathrm{L}$ models and b gaugephobic $\mathrm{SU}(2)_\mathrm{R}$ models.

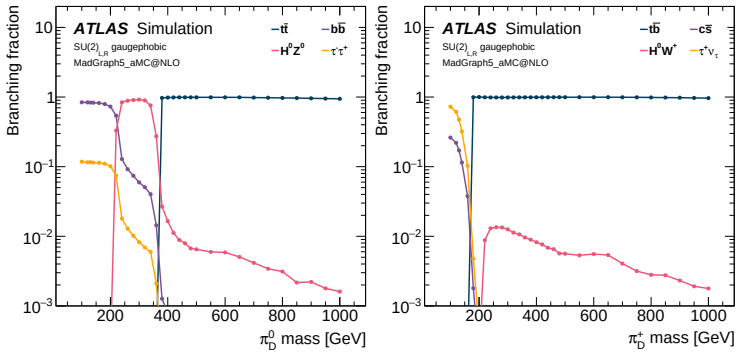


*Figure 67.* Branching fractions of the most relevant decay channels over the full dark pion mass range for neutral dark pions in a and for positively charged dark pions in b. Not all possible decay channels are drawn and channels with small branching fractions are suppressed for clarity. About one third of dark pions in the $\mathrm{SU}(2)_\mathrm{L}$ models are neutral, resulting in the *tttb* event signature being twice as likely as the *ttbb* signature. For $\mathrm{SU}(2)_\mathrm{R}$ models only the *ttbb* final state appears.

inclusive is worth investigating to boost the sensitivity if the cost in backgrounds is not significant, however, it was not deemed justified to investigate backgrounds after conducting these studies. The $H_T$ and single-lepton triggers have high efficiencies for the signal, but there are some events that do not pass either. Signal and trigger efficiencies are calculated, then a final estimate of events that pass multi-lepton triggers, but do not pass the $H_T$ or single-lepton triggers is presented.

**5.11.1 Signal Samples.** Dark pions can be pair-produced resonantly via the production of a dark rho or in Drell-Yann-type processes. Both production

channels are simulated in MadGraph5_aMC@NLO v2.4.3 Alwall et al. (2014), where the matrix elements are calculated to NLO, interfaced with Pythia.212 Sjöstrand, Mrenna, and Skands (2008) for hadronisation and showering using production tags `e8005` for $\mathrm{SU(2)_L}$ and `e8207` for $\mathrm{SU(2)_R}$ samples in `athena r19`. Signal parameters were chosen to cover the relevant areas in ($m_{\pi_D}$,$\eta$) space for $\mathrm{SU(2)_L}$ and $\mathrm{SU(2)_R}$ models. The number of dark colours $N_D$ was set to 4 for all signal points, the dark pion decays were simulated using the narrow width approximation. All events are passed through a detailed simulation of the ATLAS detector in Geant4 ATLAS Collaboration (2010b); GEANT4 Collaboration et al. (2003), where the detailed configuration is listed in tag `s3126`. The same reconstruction algorithms and the same `athena` software release is used for simulation and data. To mimic the pileup conditions during data taking, the simulated samples are overlaid with minimum-bias collisions, where the number of additional collisions approximate the pileup distributions observed in data. Since the pileup conditions changed over time, three distinct Monte Carlo campaigns are necessary to completely reproduce the pileup conditions in data. The mc16a campaign corresponds to data taken in 2015 and 2016 and is represented by tags `r9364_r9315`, mc16d corresponds to data taken in 2017 and is considered in tags `r10201_r10210`, while tags `r10724_r10726` are used for the mc16e campaign representing the 2018 data. 10K events are simulated for each signal point and Monte Carlo production campaign, with the exception of two samples per model for which 100K events per campaign have been simulated. These high-statistics samples are intended for detailed signal studies and correspond to ($m_{\pi_D}$ = 400 GeV, $\eta = 0.45$) and ($m_{\pi_D}$ = 800 GeV, $\eta = 0.25$) for $\mathrm{SU(2)_L}$ models, and for $\mathrm{SU(2)_R}$ models ($m_{\pi_D}$ = 300 GeV, $\eta = 0.45$) and ($m_{\pi_D}$ = 400 GeV, $\eta = 0.35$). All

simulated signal samples are processed in an unskimmed `TOPQ1` derivation which can be used by both the all-hadronic and the 1-lepton channel. A detailed list of all signal MC samples is given in appendix B.1, an overview of all simulated signal points and their distribution in the $\eta$-$m_{\pi_D}$ parameter space is provided in the signal sample documentation.

The effect of multiple interactions in the same and neighbouring bunch crossings (pile-up) was modelled by overlaying the simulated hard-scattering event with inelastic proton–proton events generated with Pythia.186 Sjöstrand et al. (2008) using the NNPDF2.3 set of parton distribution functions (PDF) Ball et al. (2013b) and the A3 set of tuned parameters ATLAS Collaboration (2016g).

**5.11.2 Signal Efficiencies.** Events are separated into all-hadronic, single-lepton, and multi-lepton; events with taus are not included in this multi-lepton study. Signal efficiencies are computed out of 10,000 events per sample. The dark pion to SM particle branching fractions in figure 67 are used to verify the signal efficiencies. The resulting signal efficiencies are plotted in figure 68. The signal samples are similar to the expected efficiencies and no further verification was deemed necessary. Low efficiencies reflect the small fraction of *ttbb* and *tttb* final states.

**5.11.3 Trigger Efficiencies.** Events out of 10,000 that pass a multi-lepton trigger are used to calculate absolute trigger efficiencies for each gridpoint. An event that meets the $p_T$ threshold of any of the multi-lepton triggers is considered as passing the trigger. The multi-lepton triggers used in this study are as follows: HLT_2e17_lhvloose_nod0_L12EM15VHI, HLT_2mu14, HLT_e17_lhloose_nod0_mu14,

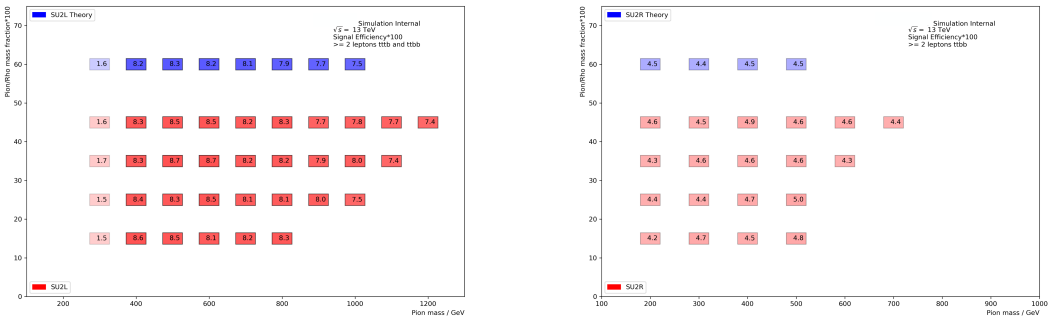


*Figure 68.* Multi-lepton channel signal efficiencies for $SU(2)_L$ (left) and $SU(2)_R$ (right) out of 10,000 events. The blue gridpoints are the expected efficiencies for comparison.

HLT_e7_lhmedium_nod0_mu24, HLT_e12_lhloose_nod0_2mu10, and HLT_2e12_lhloose_nod0_mu10. The results are plotted in figure 69.

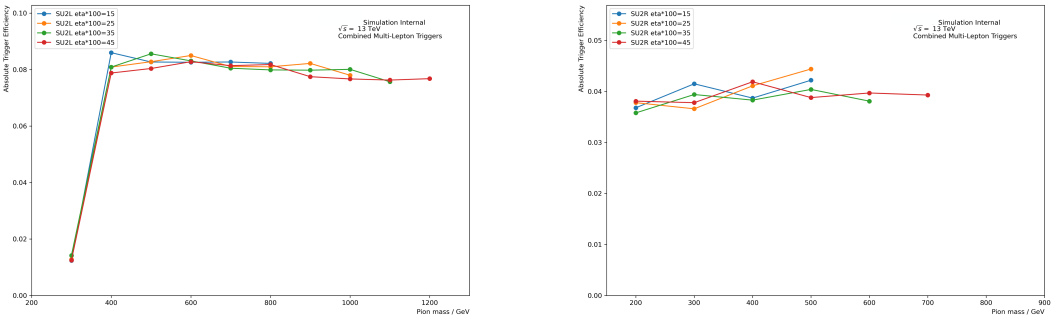


*Figure 69.* Absolute multi-lepton trigger efficiencies as a function of the dark pion mass and $\eta$ out of 10,000 events. $SU(2)_L$ is plotted on the left and $SU(2)_R$ on the right.

As expected, only a small fraction of events pass a multi-lepton trigger, with similar efficiencies across $\eta$ values. The $SU(2)_R$ model has very low efficiencies as it is made up of mostly *ttbb* final states.

Finally, events that pass a multi-lepton trigger exclusively with the correct weighting applied for 139 $fb^{-1}$ are shown in figure 70. Gridpoints at high $\eta$ and low dark pion mass are the most notable. This is a consequence of the high cross sections at those points, and figure 54 plots these cross sections as functions of $\eta$ and dark pion/rho mass for reference. Prior to weighting, most gridpoints contained, at most, 10's of unique events out of 10,000. It was notice that most multi-lepton event's leading lepton passed a single lepton $p_T$ threshold, causing the low count of exclusive events.

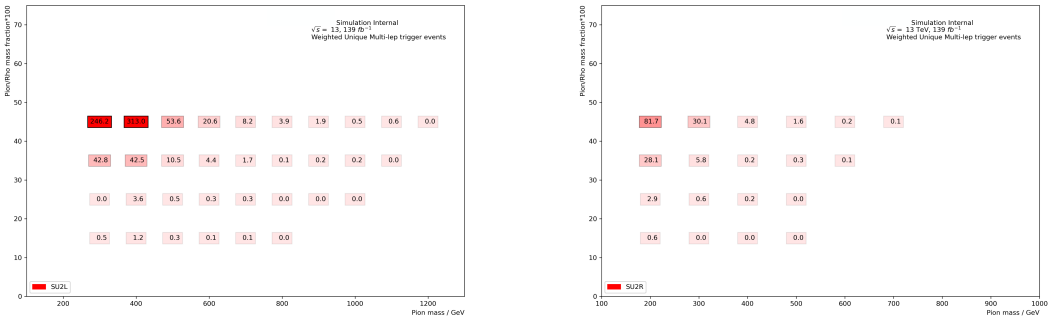


*Figure 70.* Weighted exclusive multi-lepton trigger events for the full $SU(2)_L$ (left) $SU(2)_R$ (right) gridpoints.

**5.11.4 Conclusions.** Based on the findings of this preliminary truth study, a stand-alone multi-lepton analysis is not justified. The amount of multi-lepton events are too few without considering backgrounds in an optimized multi-lepton signal region. However, the single-lepton search is sensitive to the high $\eta$, low dark pion mass gridpoints. It may be beneficial to make the single-lepton search inclusive, but a more detailed study addressing backgrounds would need to be done.

### 5.12 Preselection yields for the all-hadronic channel

In addition to the trigger, good run list, jet/muon cleaning, and derivation requirements, the selections listed in table 10 are applied for the all-hadronic channel. This preselection requires zero loose-leptons, $H_{\mathrm{T}} > 1150$ GeV, and at least six jets in an event with $p_T > 25$ GeV. This $H_{\mathrm{T}}$ selection has been chosen to exclude the vast majority of the trigger onset region where the $H_{\mathrm{T}}$ trigger does not have full efficiency yet and where the analysis would be susceptible to a mismodeling of the onset behaviour in simulation. A flavour tagging requirement of three b-tagged jets is applied to reject low b-tag backgrounds. The two large-R jets with the largest $p_{\mathrm{T}}$ are required to have masses above 190 GeV to exclude SM processes.

Table 10. Summary of the preselection cuts used in the all-hadronic channel.

| Cut | Preselection |
|---|---|
| loose $\ell$ | 0 |
| $H_{\mathrm{T}}$ | $>$ 1150 GeV |
| $p^{6}_{T,jet}$ | $>$ 25 GeV |
| $\mathrm{N}_{b\text{-jets}}$ | $\geq 3$ |
| $m^{1}_{\mathrm{jet,R=1.2}}$ | $>$ 190 GeV |
| $m^{2}_{\mathrm{jet,R=1.2}}$ | $>$ 190 GeV |

Event yields with this preselection applied are shown in table 11. SM processes with final states containing multiple top or bottom quarks were investigated as potential backgrounds and are included in this table. The dominant background originates from multijet events as can be inferred by the large data yield compared to the sum of MC backgrounds. In signal and validation regions this multijet background is determined through a data driven method. The major MC background is $t\bar{t}$, with additional contributions from $V$ + jets, single-top and $t\bar{t}$ +X. Multiboson backgrounds are almost entirely excluded by the preselection.

Table 11. All-hadronic preselection yields for data and Monte Carlo samples.

| Sample | Yield | Percent SM MC sum |
|---|---|---|
| $t\bar{t}$ | 8756.9 | 78.0 |
| $V$ + jets | 1688.3 | 15.0 |
| $t\bar{t}$ + X | 405.6 | 3.6 |
| SingleTop | 375.0 | 3.3 |
| Multiboson | 0.8 | $< 1$ |
| SM sum | 11226.5 | 100 |
| SU2L-45-400 | 804.7 | |
| SU2L-35-500 | 867.3 | |
| SU2L-25-500 | 549.5 | |
| Data | 67339 | |

Applying the event quality, trigger, and preselection cuts results in the data, MC and example signal point yields listed in the cutflow in table 12. Each row of this table shows the weighted events yields after application of all cuts listed above. For completeness the table also contains event counts for the final selection which will be described in detail in section 5.5.1. The preselection cutflow for raw event counts is included in the appendix for reference.

Signal yields across the original signal point grid with the preselection applied are shown in figure 71. The preselection cuts were optimised using the $\eta = 0.25$ and $m_{\pi_D} = 500$ GeV signal point as a benchmark. The signal yields drop significantly at high dark pion masses and for small $\eta$ values due to the large decrease in production cross section. Additionally, for the samples with $\eta = 0.15$ Drell-Yan-type dark pion production becomes relevant and takes over as dominant production mechanism for $m_{\pi_D} > 400$ GeV resulting in further reduced signal yields.

### 5.13 Extended ABCD method for single bin SR estimate

The dominant background for the all-hadronic channel, QCD mutli-jet, is estimated using a data-driven approach to extrapolate from the observed

Table 12. All-hadronic preselection cutflow for data and all considered simulated backgrounds at 140 fb$^{-1}$ integrated luminosity.

| Cut | data | All MC | $t\bar{t}$ allhad | $t\bar{t}$ nonallhad | $V$+jets | $t\bar{t}+X$ | single top | multiboson | Signal-25-500 |
|---|---|---|---|---|---|---|---|---|---|
| Derivation | 559740475 | 74686277.3 | 700250.6 | 485751.5 | 52752296.7 | 234104.3 | 20387641.6 | 126232.6 | 2650.2 |
| GRL | 417309494 | 74686277.3 | 700250.6 | 485751.5 | 52752296.7 | 234104.3 | 20387641.6 | 126232.6 | 2650.2 |
| Good Calo | 412694354 | 74686277.3 | 700250.6 | 485751.5 | 52752296.7 | 234104.3 | 20387641.6 | 126232.6 | 2650.2 |
| Primary vertex | 412692263 | 74686277.3 | 700250.6 | 485751.5 | 52752296.7 | 234104.3 | 20387641.4 | 126232.6 | 2650.2 |
| Trigger | 205205611 | 3413076.8 | 650091.2 | 419676.5 | 2188774.2 | 21031.8 | 132246.8 | 1256.3 | 2464.4 |
| Bad muon veto | 205203444 | 3412881.3 | 650081.8 | 419566.8 | 2188717.7 | 21028.4 | 132231.3 | 1255.3 | 2464.2 |
| Jet cleaning | 202840649 | 3401193.6 | 647806.6 | 418105.5 | 2181341.8 | 20951.7 | 131736.3 | 1251.7 | 2457.2 |
| $H_T > 1150$ GeV | 87703211 | 1701555 | 399278.5 | 258393.7 | 970739.3 | 10700.4 | 61920.1 | 523.0 | 2270.1 |
| $N_{\text{jets}} \geq 6$ | 45304007 | 1207437.7 | 363798.8 | 207361.1 | 581846.0 | 9943.0 | 44267.4 | 221.4 | 2039.9 |
| $N_{\text{jets, R=1.2}} \geq 2$ | 45005443 | 1196438.1 | 363209.0 | 201599.1 | 578272.9 | 9792.5 | 43347.0 | 217.6 | 1996.0 |
| $N_{\text{b-jets}} \geq 3$ | 576239 | 89564.5 | 48886.3 | 24779.6 | 8697.4 | 2696.3 | 4484.4 | 20.5 | 1340.9 |
| electron veto | 568304 | 80167.3 | 82489.7 | 18600.3 | 8682.5 | 2359.6 | 4094.0 | 20.5 | 1133.9 |
| muon veto | 561409 | 74916.9 | 48686.5 | 12526.6 | 8667.2 | 2048.2 | 3707.3 | 20.5 | 941.6 |
| $m^{1,2}_{\text{jet},R=1.2} > 190$ GeV | 69879 | 82489.7 | 7205.5 | 1660.0 | 1734.0 | 409.0 | 384.2 | 0.8 | 560.0 |
| $p^{6}_{T,\text{jet}} > 25$ GeV | 67339 | 11220.6 | 7127.8 | 1629.1 | 1687.4 | 405.6 | 375.0 | 0.8 | 549.2 |
| preselected | 67339 | 11220.6 | 7127.8 | 1629.1 | 1687.4 | 405.6 | 375.0 | 0.8 | 549.2 |
| lead. $m_{bb}/p_{\text{T},bb} > 0.25$ | 59299 | 10048 | 6364.7 | 1472.5 | 1507.8 | 365.1 | 337.1 | 0.8 | 492.9 |
| sub. $m_{bb}/p_{\text{T},bb} > 0.25$ | 52917 | 9075.8 | 5782.9 | 1309.9 | 1347.9 | 330.3 | 304.3 | 0.4 | 449.9 |
| lead. $m_{\text{jet,R=1.2}} > 300$ GeV | 20018 | 3447.5 | 2156.6 | 514.2 | 510.0 | 138.7 | 128.0 | 0.0 | 363.6 |
| sub. $m_{\text{jet,R=1.2}} > 250$ GeV | 11444 | 2040 | 1234.5 | 302.5 | 343.6 | 83.3 | 76.0 | 0.0 | 302.7 |
| lead. $\Delta R\,(j, b_2) < 1.0$ | 3365 | 575.7 | 411.1 | 63.9 | 52.5 | 26.5 | 21.7 | 0.0 | 167.0 |
| sub. $\Delta R\,(j, b_2) < 1.0$ | 234 | 46.2 | 28.3 | 7.9 | 5.0 | 3.4 | 1.5 | 0.0 | 66.6 |

contribution in low signal contamination regions to an estimate in the signal region. This four feature generalization of the ABCD method is similar to multi-jet estimation described in ATLAS Collaboration (2016a), but with tag definitions which select dark pions rather than tops. The top tags are replaced by $\pi_d$ tags and single b-tags by bb-tags as defined in table 13. The bin selections select a SR bin as described in the main body. In this appendix a QCD multijet exptrapolation for a single bin SR is shown for simplicity. In this selection the leading jet selection is $m_{\text{jet,R=1.2}} > 300$ GeV and the subleading selection is $m_{\text{jet,R=1.2}} > 250$ GeV.

The equations used here are derived in appendix C.

Table 13. All-hadronic binned tag selections applied to each signal-region bin.

| Large-R jet | Tag | Variable | Tag selection | Anti-tag selection |
|---|---|---|---|---|
| Both large-R jets | | $m_{bb}/p_{\text{T},bb}$ | $> 0.25$ | |
| Leading large-R jet | $\pi_{d,1}$ | $m_{\text{jet,R=1.2}}$ | bin selection | $\leq 300$ GeV |
| Subleading large-R jet | $\pi_{d,2}$ | $m_{\text{jet,R=1.2}}$ | bin selection | $\leq 250$ GeV |
| Leading large-R jet | $bb_1$ | $\Delta R\,(j, b_2)$ | $< 1.0$ | $\geq 1.0$ |
| Subleading large-R jet | $bb_2$ | $\Delta R\,(j, b_2)$ | $< 1.0$ | $\geq 1.0$ |

The conventional ABCD method uses selections on two uncorrelated features to define four regions and then estimates the background in one region using the other three. Consider applying this method to regions ACEF,

$$\frac{N_F}{N_C} = \frac{N_E N_C}{N_A}$$
$$N_F = \frac{N_E}{N_A}$$

using data - MC values from the ABCD region tables. The estimate shown is 16% low for this region implying that there is a correlation between these tag states.

$$k_{d1,bb1} = \frac{FA}{CE}$$
$$k_{d2,bb2} = \frac{OA}{CI}$$
$$k_{d1,bb2} = \frac{DA}{BC}$$
$$k_{d2,bb2} = \frac{GA}{EI}$$
$$k_{d1,d2} = \frac{JA}{BE}$$
$$k_{bb1,bb1} = \frac{HA}{BC}$$

In the extended ABCD method we compute the ratio of the QCD estimate to data - MC for each pair of features to determine correlation correction factors k. We then perform an ABCD estimate for region S using the zero and one tag regions with the k factors shown above included to correct for correlations.

$$\hat{S} = \hat{S}'_{\leq 1\ tag} \cdot k_{d1,bb1} \cdot k_{d2,bb2} \cdot k_{d1,bb2} \cdot k_{d2,bb} \cdot k_{d1,d2} \cdot k_{bb1,bb1}$$
$$\hat{S}'_{\leq 1\ tag} = \prod_{j=1}^{n} \frac{N_{(j)}}{N_A^{n-1}}$$

We check that the three and four correlations between tag states are small through comparing the ABCD estimate to data - MC in a validation region.

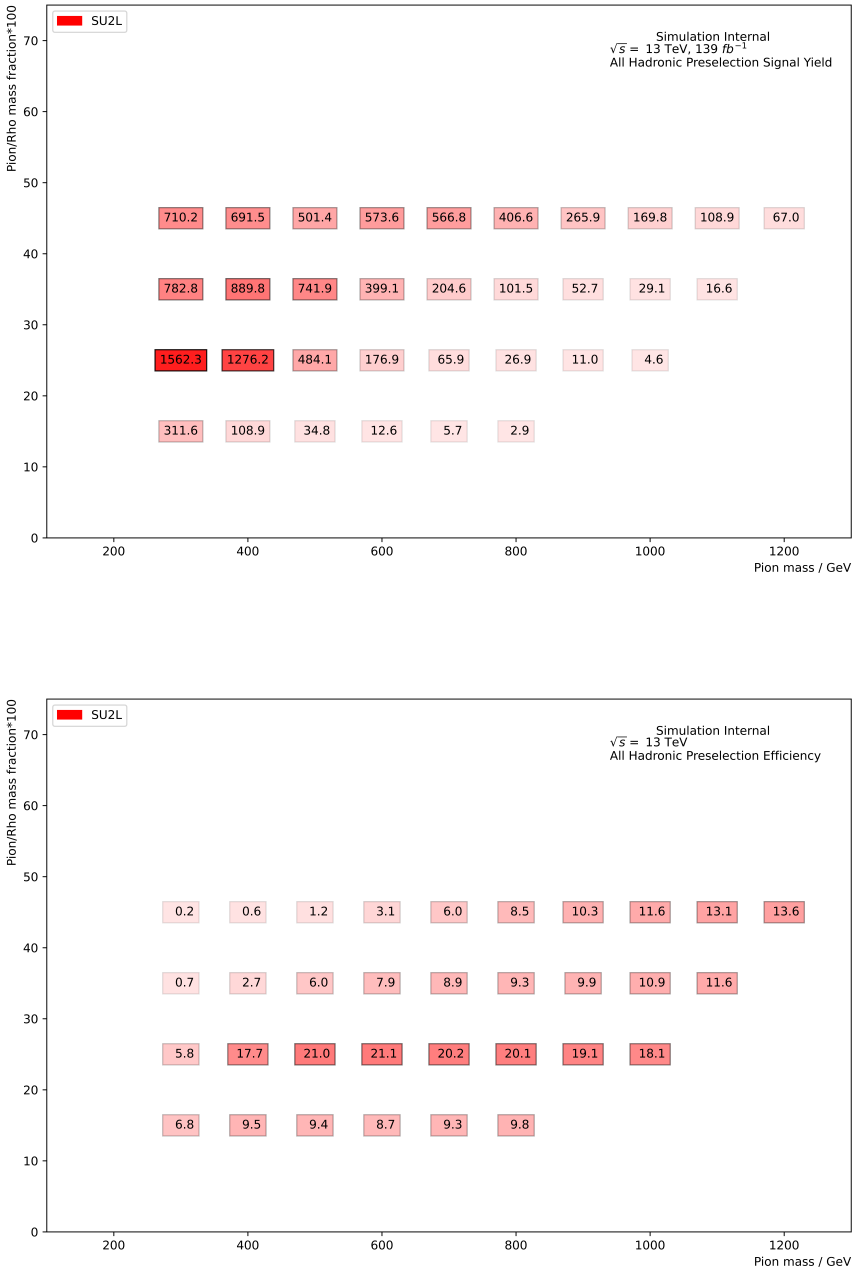


*Figure 71.* All-hadronic preselection yield and efficiency for SU2L signal points. The signal region has been optimized for $\eta = 0.25$ and $m_{\pi_D} = 500$ GeV. SU2R is not targeted in the all hadronic channel due to the low cross section at large $\pi_D$ and $\rho_D$ masses in this model. Note that these plots were created with the old luminosity tag corresponding to 139 fb$^{-1}$, however we expect differences with the new luminosity tag at 140 fb$^{-1}$ to be small.

*Figure 72.* Regions used for ABCD method.

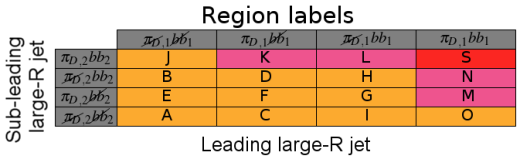


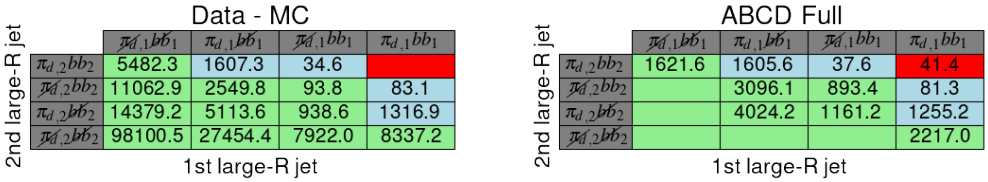


*Figure 73.* Data - MC and QCD estimates for VR ABCD regions. The ABCD estimate shown is 2D, 3D or 4D depending on region.

# CHAPTER VI

# A SEARCH FOR DARK PHOTONS FROM HIGGS DECAYS IN THE GLUON-GLUON FUSION PRODUCTION MODE

## 6.1 Introduction

This chapter focuses on a Run 3 search for dark photons in from Higgs decays with the ATLAS detector. As mentioned in Chapter 2.2.2, the BSM decay of the Higgs boson to a photon and dark photon is a well motivated signature for BSM physics, especially dark sector models with an additional $U(1)_D$ gauge group. In addition, the signature can arise from models with very low-scale supersymmetry breaking where the Higgs boson can decay into a gravitino ($\tilde{G}$) and a bino ($\tilde{B}$) that subsequently decays via $\tilde{B} \rightarrow \gamma\tilde{G}$ Petersson, Romagnoni, and Torre (2012), in the Peccei-Quinn limit of Next to Minimal Supersymmetric Models (NMSSM) Suematsu (1998), or in the decay of the Higgs boson into a pair of right-handed neutrinos (N) subsequently decaying via $N \rightarrow \nu\nu$ and $N \rightarrow \gamma N$ Graesser (2007). The search is optimized for the gluon-gluon fusion (ggF) production mode as seen in Fig. 74, which is an order of magnitude larger than the vector boson fusion (VBF) channel, but was not accessible in Run 2 due to trigger limitations. Results are combined with the Run 2 search, and the diagrams for the VBF and ZH channels are shown in Fig. 74 as well. Previous best limits on the braching ratio of Higgs to a photon and dark photon were set by ATLAS with a full Run 2 dataset of 139 fb$^{-1}$ in the VBF and ZH channels, with a combined limit of 1.3% (1.5% expected) ATLAS Collaboration (2024). The analysis is performed with 134.6 fb$^{-1}$ of data collected by ATLAS in 2023 and 2024 at $\sqrt{s} = 13.6$ TeV. A novel boosted decision tree was trained to identify events with misidentified primary vertices, and a new composite trigger was implemented to allow lower thresholds

on the photon transverse momentum and $E_{\mathrm{T}}^{\mathrm{miss}}$, increasing the acceptance of ggF events. The results of this Run 3 search represent the most stringent limits on the branching ratio of Higgs to a photon and dark photon to date.

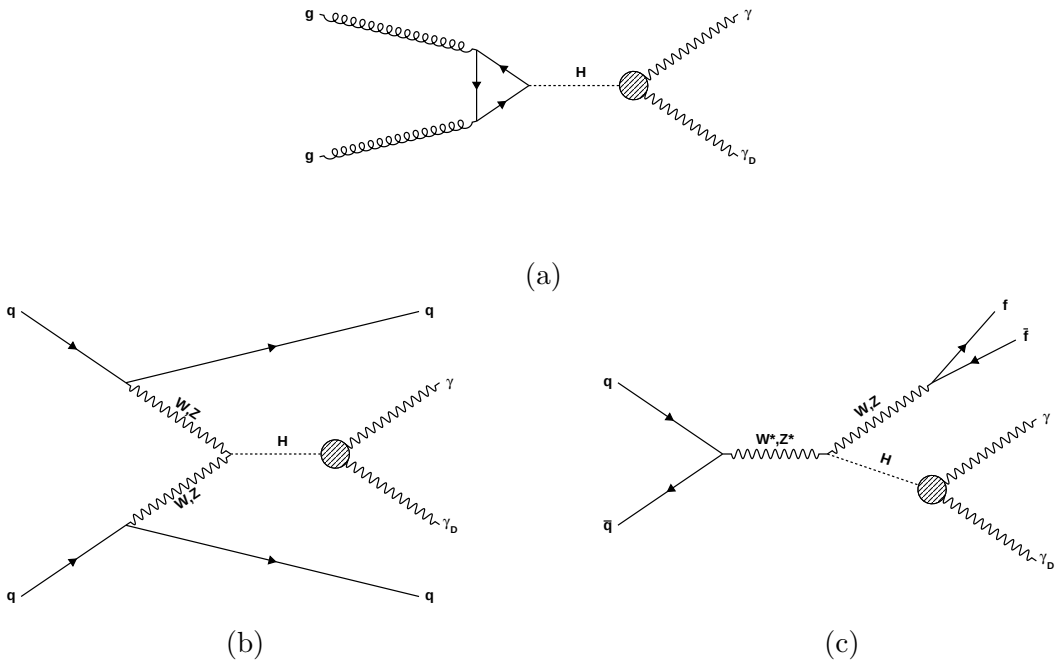


*Figure 74.* Feynman diagrams illustrating the Higgs boson production via gluon-gluon fusion process (a), vector-boson fusion (b), and Higgsstrahlung (c), all followed by the decay into a photon and a dark photon ($H \rightarrow \gamma\gamma_{\mathrm{D}}$). The hatched circle in the $H\gamma\gamma_{\mathrm{D}}$ vertex represents the interaction through messenger fields.

The signature for the ggF channel is a single photon and $E_{\mathrm{T}}^{\mathrm{miss}}$ in association with initial state radiation (ISR) jets. The ggF channel is made accessible by developments in the trigger between Run 2 and Run 3, which has led to a lower threshold $E_{\mathrm{T}}^{\mathrm{miss}}$ trigger in combination with photon $p_T$ and transverse mass requirements. Events are mostly constituted by Higgs bosons recoiling against jets, leading to a boosted event topology. Although the ggF channel has a higher cross section than the VBF or ZH channels, it comes with significant analysis challenges.

The phase space is significantly affected by electrons and jets misidentified as photons, as well as events with a large fake $E_{\mathrm{T}}^{\mathrm{miss}}$ due to mismeasurement or misreconstruction of physics objects. A low track activity topology, which leads to a non-negligible probability of primary-vertex misidentification, further enhances the contribution from fake $E_{\mathrm{T}}^{\mathrm{miss}}$ due to the removal of hard-scatter jets incorrectly classified as pile-up.

The author of this thesis made significant contributions to the analysis, including the development and implementation of the fitting regions for the statistical analysis, validation of the background estimation methods and vertex BDT, optimization of the signal region, studies to improve the primary vertex selection, and studies of a new neural network method to reconstruct $E_{\mathrm{T}}^{\mathrm{miss}}$.
In this chapter, the analysis will be presented, along with studies on vertexing improvement for a future iteration of the analysis.

## 6.2 Data and simulation

This search uses proton–proton ($pp$) collision data at a centre-of-mass energy of 13.6 TeV, collected in 2023 and 2024 by the ATLAS experiment. Only data recorded during stable beam conditions and with all sub-detectors operational are considered, corresponding to a total integrated luminosity of 134.6 fb$^{-1}$, with an uncertainty of 1.9% ATLAS Collaboration (2025). Events are selected using a dedicated trigger ("analysis trigger") optimised for the $\gamma + p_T^{\mathrm{miss}}$ final state and described in Section 6.3. In addition, samples with $e^+e^-$, $\gamma e$ and $\gamma\mu$ final states, used for the modelling of the background from electrons misidentified as photons (Sections 6.5, 6.7.1) and for the trigger efficiency studies (Section 6.3), are selected using a logical OR of dielectron, single-electron, and single-muon triggers, respectively.

Monte Carlo (MC) simulations are used to model the signal and a subset of the background processes. In particular, among the dominant backgrounds affecting the analysis (described in Section 6.5), those containing genuine photons are largerly based on MC simulations. For the remaining ones, the data-driven methods described in Section 6.7 are employed, with $W$+jets and $Z$+jets MC samples used as input for the background induced by jets misidentified as photons (Section 6.7.2). The list of samples used in the analysis is summarised in appendix D.

The simulation of the geometry and response of the ATLAS detector is performed using GEANT4, and all simulated events are processed through the same reconstruction chain as collision data. The effect of multiple interactions in the same and neighbouring bunch crossings (pile-up, PU), is modeled by overlaying ATLAS Collaboration (2021b) the simulated hard-scattering event with inelastic $pp$ events generated using EPOS Werner et al. (2006) and PYTHIA 8.308 Bierlich et al. (2022). The EPOSevents are generated with the EPOSLHC tune Pierog et al. (2015) and the PYTHIAevents with the A3 tune ATLAS Collaboration (2016g) and the NNPDF2.3lo Ball et al. (2013a) set of parton distribution functions (PDF). PYTHIAPU events include either a high $p_{\mathrm{T}}$ jet, a prompt photon, or a lepton from a $b$-hadron decay, while events generated using EPOSare filtered to simulate all remaining PU events in the overlay sample. The individual simulations are first reweighted to ensure a smooth connection across jet $p_{\mathrm{T}}$. The combination is then reweighted to match the distribution of the actual number of interactions per bunch crossing measured in data.

The signal samples include multiple Higgs production channels: the dominant process and main target of the analysis is the ggF channel, but

non-negligible contribution arises from the VBF and from the $WH$ and $ZH$ channels. One MC sample for each production mode is generated, with $WH$ production divided into $W^+H$ and $W^-H$. The matrix elements are estimated using POWHEG,v2 Alioli et al. (2010); Frixione, Nason, and Oleari (2007) at NLO, with the NNPDF3.0 parton density libraries Martin, Stirling, Thorne, and Watt (2009). The samples are generated with the SM Higgs boson mass of 125 GeV, a width set to 4 MeV and the complex pole scheme turned off. The decay into photon and dark photons, as well as the hadronisation and showering, is simulated using PYTHIA 8.245 with the CTEQ6L1 PDF set and the AZNLO tune Pumplin et al. (2002). The Hidden Valley scenario Carloni and Sjöstrand (2010) is used for modelling the $H \to \gamma\gamma_{\mathrm{D}}$ decay.

The $V\gamma$ and $V$+jets processes are generated using SHERPA 2.2.14 generator Bothmann et al. (2019), with up to 1 (2) jet at NLO and up to 3 additional jets at LO for $Z\gamma$ and $W\gamma$ ($Z$+jets and $W$+jets). The matrix elements are matched and merged with the SHERPAparton shower Schumann and Krauss (2008), using the MEPS@NLO prescription Catani et al. (2001); Höche et al. (2012) and the NNPDF3.0 NNLO PDF set Martin et al. (2009) with the dedicated SHERPA tune. The $\gamma$(direct)+jets sample is generated at LO using PYTHIA 8.186 Mrenna and Skands (2016); Sjöstrand et al. (2008), and showered using the NNPDF2.3 LO PDF set and the A14 tune. Table 14 summarises the configurations used for the signal and background MC simulations used in the analysis.

### 6.3 Analysis trigger

The "analysis trigger" combines selections on the photon $p_{\mathrm{T}}$, the $E_{\mathrm{T}}^{\mathrm{miss}}$ and the $m_T$. At L1, the trigger selects electrons or photons with $p_{\mathrm{T}}$ of 26 GeV. The HLT further requires a 50 GeV photon fulfilling tight identification criteria. As the

Table 14. The configurations used for event generation of signal and background MC samples. The matrix element (ME) order refers to the order in the strong coupling constant of the perturbative calculation in the MC event generation. PDF refers to the parton density libraries used with the generator. The tune refers to the underlying-event tune of the parton shower model.

| Process | Generator | ME order | PDF | Parton shower | Tune |
|---|---|---|---|---|---|
| $(ggF, VBF, VH)H \rightarrow \gamma\gamma_{\mathrm{D}}$ | Powheg,v2 | NLO | PDF4LHC21 | Pythia 8.245 | AZNLO |
| $Z\gamma, W\gamma$ | Sherpa v2.2.14 | 0,1j@NLO + 2,3,4j@LO | NNPDF3.0 NNLO | Sherpa | Sherpa |
| $Z$+jets, $W$+jets | Sherpa v2.2.14 | 0,1,2j@NLO + 3,4,5j@LO | NNPDF3.0 NNLO | Sherpa | Sherpa |
| $\gamma$(direct)+jets | Pythia 8.186 | LO | NNPDF2.3 LO | Pythia 8.186 | A14 |

input rate of L1 electrons can reach 20 kHz, a two-stage sequence of algorithms is employed, starting with the "cell" $p_T^{\mathrm{miss}}$ computed using only the calorimeter cells as input ATLAS Collaboration (2020g). This fast step is followed by a more sophisticated $p_T^{\mathrm{miss}}$ algorithm using particle flow ATLAS Collaboration (2017f) constituents with a dedicated PU subtraction algorithm unique to the HLT ("pfopufit") ATLAS Collaboration (2022e). A threshold of 40 GeV is applied for the first "cell" $p_T^{\mathrm{miss}}$ requirement, while the second "pfopufit" step has a threshold of 70 GeV. To further reduce the rate, the trigger requires a minimum $m_T$ of 80 GeV. As muons deposit less than a GeV of energy in the calorimeters, they are invisible to the "cell" $p_T^{\mathrm{miss}}$ algorithm ATLAS Collaboration (2010d); Ordonez Sanz (2009). Furthermore, to preserve the same behaviour in "pfopufit", particle flow constituents consistent with muons are removed. Therefore both the "cell" and the "pfopufit" algorithms are insensitive to the presence of muons, which are treated as invisible in the computation of $p_T^{\mathrm{miss}}$. This feature allows to use the analysis trigger also to select samples with reconstructed muons in the final state.

The accuracy of the simulation of the analysis trigger has been investigated. The trigger efficiency curve, as a function of reconstructed $p_{\mathrm{T}}^{\gamma}$, $p_T^{\mathrm{miss}}$ and $m_T$, is

studied in $\gamma\mu$ final states, using a baseline muon-trigger. The muon is treated as invisible in the computation of $p_T^{\text{miss}}$ and $m_T$. The result is displayed in Figure 75, where MC simulation and data are compatible within statistical uncertainty. For this reason, no trigger SF is needed.

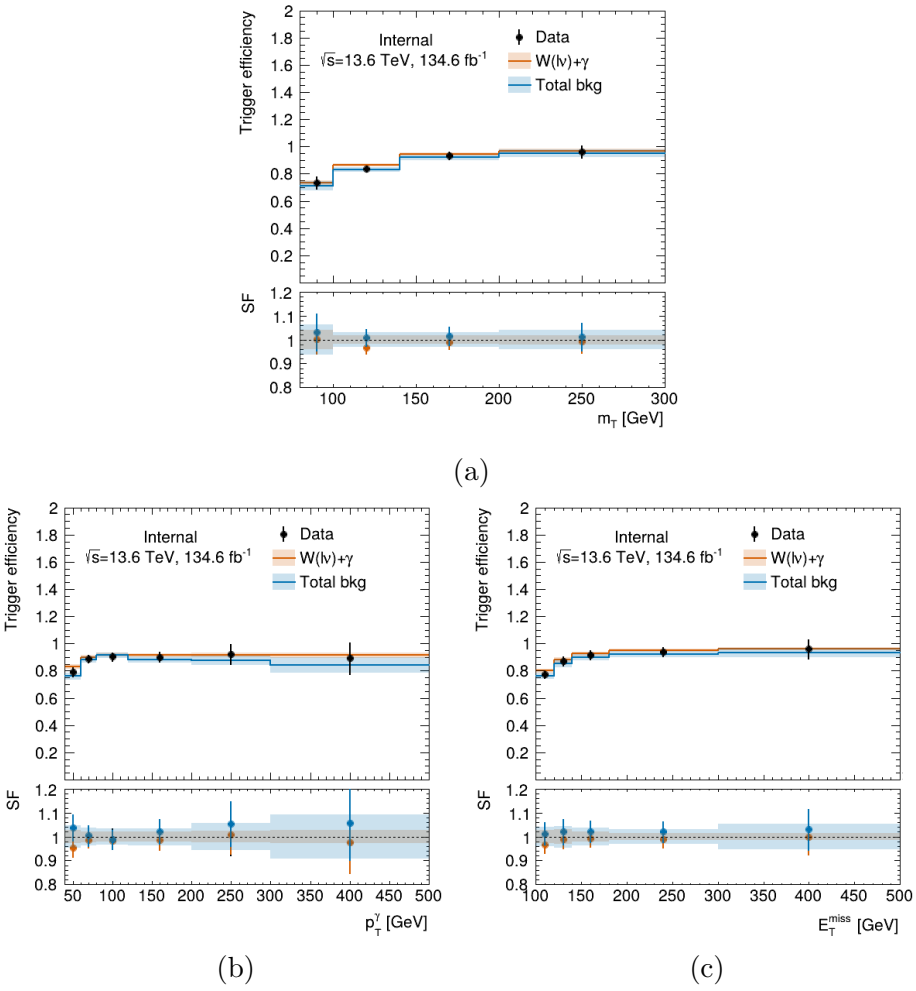


*Figure 75.* Trigger efficiency curves as function of $m_T$ (a), $p_{\text{T}}^{\gamma}$ (b), and $p_T^{\text{miss}}$ (c), for data, MC simulation of the dominant background $W\gamma$ and total background. The *baseline* selections are applied together with the selection $\Delta\phi(E_{\text{T}}^{\text{miss}}, E_{\text{T}}^{\gamma}) > 1.25$. Events selected by single-muon baseline trigger, containing one photon and one muon treated as invisible in the evaluation of $p_T^{\text{miss}}$ and $m_T$, are used.

## 6.4 Event reconstruction

For each event, primary vertex (PV) candidates are required to have at least two associated tracks with $p_{\mathrm{T}} > 500$ MeV. Among the reconstructed PV candidates, the hard-scattering (HS) PV is selected as the one with the highest sum of squared transverse momenta of contributing tracks ATLAS Collaboration (2015b).

Electrons are reconstructed by matching energy clusters in the ECAL to tracks in the ID ATLAS Collaboration (2019c, 2019d). Baseline electrons must satisfy $p_{\mathrm{T}} > 10$ GeV and $|\eta| < 2.47$ and be consistent with originating from the PV through requirements on the longitudinal and transverse impact parameters, $|z_0 \sin(\theta)| < 5$ mm and $|d_0/\sigma(d_0)| < 5$. All baseline electron candidates are required to satisfy *loose* likelihood-based identification criteria ATLAS Collaboration (2014b), based on calorimeter, tracking and combined variables that provide separation between electrons and jets. Selected electrons are further required to satisfy *tight* identification and *tight* isolation requirements.

Muons are reconstructed by matching ID tracks to MS tracks or track segments, by matching ID tracks to calorimeter energy deposits compatible with a minimum-ionizing particle, or by identifying MS tracks passing the *loose* requirement and compatible with the interaction point ATLAS Collaboration (2016d, 2021d). Baseline muon candidates must satisfy $p_{\mathrm{T}} > 10$ GeV and $|\eta| < 2.7$ and *medium* identification criteria. Similar selections on the impact parameter as for electrons are applied, but with $|d_0/\sigma(d_0)| < 3$. Selected muons are further required to satisfy *loose* isolation selections.

Photon candidates are reconstructed from clustered energy deposits in the ECAL ATLAS Collaboration (2019c, 2019d). Baseline photons must satisfy

$p_{\mathrm{T}}^{\gamma} > 25$ GeV, $|\eta| < 2.37$, outside the transition region between the ECAL barrel and endcaps ($1.37 < |\eta| < 1.52$). Photon candidates undergo a `Tight` identification criterion, based on several requirements on the "shower shape" variables ATLAS Collaboration (2016b, 2019g), that can be grouped into three categories: energy leakage in the HCAL, width in the middle layer of the ECAL, and shape in the strips. Selected photon candidates are additionally required to be isolated: a dimensionless isolation variable is introduced:

$$\Upsilon = \frac{E_{\mathrm{T}}^{\mathrm{cone}} - 2450 \text{ MeV}}{p_{\mathrm{T}}^{\gamma}}, \tag{6.1}$$

where $E_{\mathrm{T}}^{\mathrm{cone}}$ is the transverse energy flow measured by the ECAL in a cone of size $\Delta R = 0.4$ around the photon candidate, from which an offset is subtracted in order to centre the distribution around zero. Isolated photons are required to satisfy $\Upsilon < 0.022$. Non-isolated photons are used in the evaluation of the background induced by jets misidentified as photons (see Sections 6.5, 6.7.2). In this context, a `Loose` photon selection is also exploited, with relaxed cuts on the HCAL and middle layer, and no strips cuts. Removing `Tight` photons from the `Loose` sample, provides a `Loose`$'$ sample enriched in fake photons from hadronic jets. Further photon selections `Loose`$'' \subset$ `Loose`$'$ are introduced by applying to the HCAL and middle layer shower shapes the same cuts as for `Tight`, but no cuts or at most one cut on the strips shower shapes.

Particle flow (PFlow) jets are reconstructed using the anti-$k_t$ algorithm Cacciari et al. (2008), as implemented in FastJet Cacciari (n.d.), with a radius parameter $R = 0.4$. The algorithm takes PFlow objects as inputs, which combine measurements from the ATLAS ID and the calorimeters ATLAS Collaboration (2017f). Central jets ($|\eta| < 2.5$) are classified as originating from the HS interaction using a neural-network-based jet-vertex-tagger (NN-JVT) (evolution of the JVT

described in Ref. ATLAS Collaboration (2016e)), while a forward jet vertex tagging (fJVT) algorithm ATLAS Collaboration (2017e) is applied to forward jets ($|\eta| > 2.5$). Jets containing b-hadrons ($b$-jets) are identified using a Graph Neural Network tagger with 85% efficiency b-tagging efficiency ATLAS Collaboration (2026). In order to suppress the background originating from detector noise, hardware issues, beam-induced background or cosmic-ray muons, events containing jets failing *loose* jet-quality criteria are rejected ATLAS Collaboration (2012b).

Hadronically decaying $\tau$-leptons ($\tau_{\text{had}}$) are seeded by anti-$k_t$ jets with R=0.4 and identified using a recurrent neural network algorithm that uses as inputs tracks and calorimeter clusters associated to $\tau_{\text{had}}$ candidates, as well as high-level discriminating variables ATLAS Collaboration (2019f). Baseline $\tau_{\text{had}}$ are required to satisfy a *Medium* identification working point and have $p_{\text{T}} > 20$ GeV and $|\eta| < 2.5$.

The $\vec{p}_T^{miss}$, with magnitude $p_T^{\text{miss}} = |\vec{p}_T^{miss}|$, is defined as the negative vector sum of the transverse momenta of all *selected* objects and of the "soft term" estimated from charged PFlow objects associated with the primary vertex and not matched to any of the hard reconstructed objects ATLAS Collaboration (2020c); ATLAS Collaboration (2025); Balunas et al. (2024). In the $\vec{p}_T^{miss}$ calculation, a NN-JVT selection is applied to the jets for PU subtraction. An alternative $\vec{p}_T^{miss}$ with no PU subtraction, denoted as $\vec{p}_{\text{T,noJVT}}^{\text{miss}}$, is also exploited in this analysis to help tagging events with misidentified PV, as explained in section 6.6. In addition, a key quantity to identify events with fake $E_{\text{T}}^{\text{miss}}$ is the $E_{\text{T}}^{\text{miss}}$ significance $\mathcal{S}_{p_T^{\text{miss}}} = \frac{E_{\text{T}}^{\text{miss}}}{[\sigma_L^2(1-\rho_{LT}^2)]^{1/2}}$, where $\sigma_L$ is the total standard deviation in the longitudinal plane with respect to $E_{\text{T}}^{\text{miss}}$, and $\rho_{LT}$ is the correlation factor between the longitudinal and transverse measurements.

Scale factors (SFs) are derived in data control samples for all reconstructed objects and applied to MC simulations to correct the identification, reconstruction, and isolation efficiencies to match those observed in data. After the reconstruction of all physics objects, a sequential overlap removal procedure (Table 15) is applied to resolve ambiguities by keeping only one object in cases of overlap, based on $\Delta R$ matching or shared ID tracks, according to a predefined priority.

Table 15. Overview of the sequential overlap removal procedure applied to reconstructed objects and the corresponding matching criteria based on the $\Delta R$ separation and shared Inner Detector (ID) tracks.

| Remove | Keep | Matching criteria |
|---|---|---|
| Muon | Electron | muon with calorimeter deposits and shared ID track |
| Electron | Muon | shared ID track |
| Jet | Electron | $\Delta R < 0.2$ |
| Electron | Jet | $0.2 < \Delta R < 0.4$ |
| Electron | Electron | shared ID track, electron with lower $p_{\mathrm{T}}$ removed |
| Jet | Muon | number of tracks ¡ 3 and $\Delta R < 0.2$ |
| Muon | Jet | $0.2 < \Delta R < 0.4$ |
| Tau | Electron | $\Delta R < 0.2$ |
| Tau | Muon | $\Delta R < 0.2$ |
| Jet | Tau | $\Delta R < 0.2$ |
| Photon | Electron | $\Delta R < 0.4$ |
| Photon | Muon | $\Delta R < 0.4$ |
| Jet | Photon | $\Delta R < 0.4$ |

### 6.5 Signature and backgrounds

The $H \to \gamma\gamma_d$ signal is characterised by the presence of a single photon and $E_{\mathrm{T}}^{\mathrm{miss}}$. Though the $z$-component of the $\gamma_{\mathrm{D}}$ momentum escapes the detector, the $m_T$ results in a broad peak around the Higgs boson mass. In the ggF channel, the final state contains no leptons or $b$-tagged jets, while hadronic jets may originate from initial- or final-state radiation. The same final state also covers the VBF channel and the VH production with hadronic decay of the $V$ bosons.

Due to the limitations imposed by the trigger thresholds on $E_{\mathrm{T}}^{\mathrm{miss}}$ and photon $p_{\mathrm{T}}^{\gamma}$ (Section 6.3), optimised as a compromise between signal acceptance and trigger rate, the accepted signal events are mostly constituted by Higgs bosons recoiling against jets, leading to a boosted event topology.

This analysis phase space is significantly affected by background from jets and electrons misidentified as photons (hereafter referred to as *jet* or *electron faking photon*), as well as by events reconstructed with large $E_{\mathrm{T}}^{\mathrm{miss}}$, due to mismeasurement or misreconstruction of physics objects (referred to as *fake* $E_{\mathrm{T}}^{\mathrm{miss}}$). In addition, the low track activity leads to a non-negligible probability of PV misidentification, further enhancing the contribution from fake $E_{\mathrm{T}}^{\mathrm{miss}}$ due to the removal of HS jets incorrectly classified as PU. The SM background events with similar signatures can be classified in the following categories:

- **genuine photon**: $Z(\rightarrow \nu\nu)\gamma$ (irreducible background) or $W(\rightarrow \ell\nu)\gamma$ and $Z(\rightarrow \ell\ell)\gamma$ with non reconstructed leptons;
- **genuine photon and fake $p_T^{\mathbf{miss}}$**: $\gamma$ + jets processes with a direct photon, $\gamma$(direct)+jets;
- **electron faking photon ($e \rightsquigarrow \gamma$)**: mostly $W(\rightarrow e\nu)$ + jets events;
- **jet faking photon ($j \rightsquigarrow \gamma$)**: dominantly multijets and $\gamma$+jets with a fragmentation photon embedded into a hadronic jet ($\gamma$(frag)+jets), as well as $Z(\rightarrow \nu\nu)$+jets or $W(\rightarrow \ell\nu)$+jets, to a lesser extent. Multijets and $\gamma$(frag)+jets passing the analysis selections are also characterised by fake $E_{\mathrm{T}}^{\mathrm{miss}}$.

## 6.6 Event selection

Events passing the trigger selections described in Section 6.3 are further required to satisfy a set of *offline* requirements on reconstructed variables, designed to isolate the signal.

**6.6.1 Baseline selection.** Events are required to have exactly one selected photon with $p_{\mathrm{T}}^{\gamma} > 50$ GeV and $E_{\mathrm{T}}^{\mathrm{miss}} > 100$ GeV, a transverse mass $m_T > 80$ GeV, no reconstructed leptons nor $b$-tagged jets, and at most three central jets. The requirements on $p_{\mathrm{T}}^{\gamma}$ and $m_T$ are aligned with the trigger thresholds, exploiting the fast trigger turn-on, while a more conservative requirement is applied on $E_{\mathrm{T}}^{\mathrm{miss}}$ as a compromise between signal acceptance and background rejection.

As discussed in Section 6.5, the low track activity can lead to an incorrect identification of the PV. This effect has a significant impact on $E_{\mathrm{T}}^{\mathrm{miss}}$-related observables, particularly when HS jets are misclassified as PU jets and consequently excluded from the $E_{\mathrm{T}}^{\mathrm{miss}}$ reconstruction. In such events, the reconstructed $E_{\mathrm{T}}^{\mathrm{miss}}$ distribution becomes artificially harder for $\gamma$+jets and multijet backgrounds and softer for the signal, enhancing background acceptance while reducing signal efficiency. Moreover, the PV misidentification distorts the transverse mass distribution, resulting in values of $m_T \sim 150$ GeV for both signal and background, thereby degrading the signal-to-background discrimination. To mitigate this effect, a boosted decision tree (BDT) is trained on signal and background simulations using TMVA AdaBoost Freund and Schapire (1997), to identify and reject events with a misidentified PV. The BDT uses information related to the reconstructed vertex properties, jet multiplicity, and the angular separation between the photon, jets, and $E_{\mathrm{T}}^{\mathrm{miss}}$, as summarised in Table 16. As shown in Figure 76, a requirement on the vertex BDT score of $\mathrm{BDT}_{\mathrm{vertex}} > 0.1$ provides an almost complete

suppression of events with misidentified PV for both signal and background, especially when combined with the Signal Region selections described in Section 6.6.2.

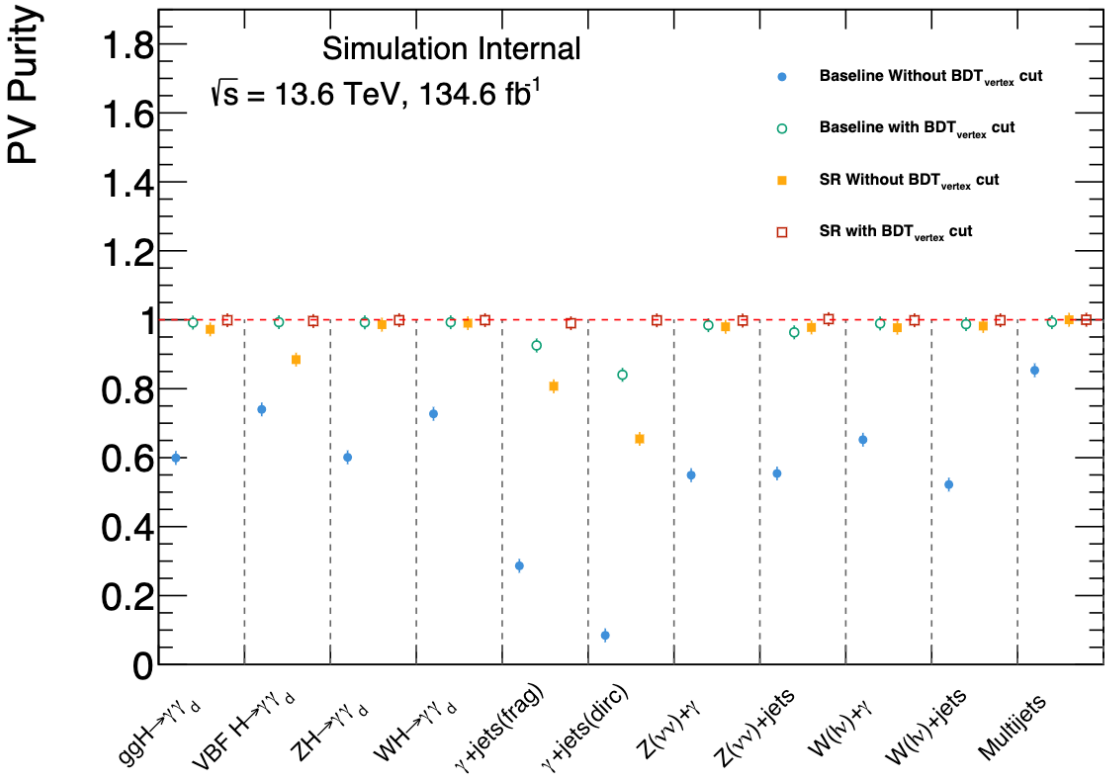


*Figure 76.* Fraction of events with correct primary vertex (PV) for the $H \to \gamma\gamma_d$ signals and for different background processes, with different selections applied: baseline selection are shown in blue and green, signal region (SR) selections are shown in orange and red. No selection on the $\mathrm{BDT}_{\mathrm{vertex}}$ is applied for the blue and orange dots, while $\mathrm{BDT}_{\mathrm{vertex}} \geq 0.1$ is applied for the green and red ones.

**6.6.2 Signal Region.** In addition to the *baseline* selections, the signal region (SR) definition includes requirements on the photon kinematics, angular separations between the photon, $E_{\mathrm{T}}^{\mathrm{miss}}$ and jets, as well as further $E_{\mathrm{T}}^{\mathrm{miss}}$-related variables. These include the $\mathcal{S}_{p_T^{\mathrm{miss}}}$ and the difference $\Delta p_{\mathrm{T}}^{\mathrm{miss}} = E_{\mathrm{T,noJVT}}^{\mathrm{miss}} - E_{\mathrm{T}}^{\mathrm{miss}}$, where $E_{\mathrm{T,noJVT}}^{\mathrm{miss}}$ is defined in Section 6.4. In particular, the requirement of $\mathcal{S}_{p_T^{\mathrm{miss}}} > 6$ further suppresses events with *fake* $E_{\mathrm{T}}^{\mathrm{miss}}$ which typically exhibit lower significance

Table 16. Description of the input features of the vertex BDT, in order of importance.

| **Variable** | **Description** |
|---|---|
| $\log\big(\sum p_{\mathrm{T}}^2(\text{tracks})\big)$ | Logarithm of the sum of the squared transverse momenta of tracks associated with the vertex. |
| $\lvert\Delta\phi(\vec{p}_{\text{vtx}}, \vec{p}_{\gamma})\rvert$ | Azimuthal separation between the vertex momentum vector and the photon direction. |
| $\Delta\phi(E_{\mathrm{T}}^{\text{miss}}, E_{\mathrm{T}}^{jet})$ | Azimuthal separation between the missing transverse momentum and the leading jet. |
| $\lvert\Delta\phi(\mathrm{j}_1, \mathrm{j}_2)\rvert$ | Azimuthal separation between the two leading jets. |
| $\Delta p_{\mathrm{T}}^{\text{miss}}$ | Difference between the missing transverse momentum computed without JVT requirements and the nominal reconstruction. |
| $\mathcal{S}_{p_T^{\text{miss}}}$ | Significance of the missing transverse momentum. |
| $(z_{\text{vtx}} - z_{\gamma})/\sigma(z_{\gamma})$ | Distance along $z$ between the reconstructed primary vertex and the vertex position inferred from the photon trajectory (photon pointing), normalized by the photon pointing resolution. The photon trajectory is reconstructed using its energy deposits in the first and second layer of the ECAL. |
| $z_{\text{skew}}$ | Skewness of the longitudinal ($z$) distribution of tracks associated with the vertex. |
| Number of central jets | Number of reconstructed jets in the central region ($\lvert\eta\rvert < 2.5$). |
| $(p_T^{\text{miss}} + p_{\mathrm{T}}^{\gamma})/\sum p_{\mathrm{T}}^{\text{jet}}$ | Transverse momentum balance between the photon+$E_{\mathrm{T}}^{\text{miss}}$ system and the reconstructed jets. |
| $z_{\text{kurt}}$ | Kurtosis of the longitudinal ($z$) distribution of tracks associated with the vertex. |

values. Moreover, events are required to satisfy $\Delta p_{\mathrm{T}}^{\mathrm{miss}} > -10$ GeV to reduce the contribution from wrong PV identification. If a PU vertex is identified as the HS one, the standard $E_{\mathrm{T}}^{\mathrm{miss}}$ computation rejects the HS jets while retaining PU jets. In this scenario, the $E_{\mathrm{T,noJVT}}^{\mathrm{miss}}$ is expected to be closer to the true $E_{\mathrm{T}}^{\mathrm{miss}}$ than the standard reconstruction, resulting in negative $\Delta p_{\mathrm{T}}^{\mathrm{miss}}$ values. Additionally, restricting the photon pseudorapidity to $|\eta_\gamma| < 1.75$ reduces background contributions from $W/Z + \gamma$ processes. Finally the requirements $\Delta\phi(E_{\mathrm{T}}^{\mathrm{miss}}, E_{\mathrm{T}}^{\gamma}) > 1.25$, $\Delta\phi(E_{\mathrm{T}}^{\mathrm{miss}}, E_{\mathrm{T}}^{jet}) < 0.75$, and $|\Delta\phi(j_1, j_2)| < 2.5$ are imposed, where $\vec{p}_{\mathrm{T}}^{\,\mathrm{miss},\gamma}$ and $\vec{p}_{\mathrm{T}}^{\,\mathrm{miss,jet}}$ are the jet and photon term of the $p_T^{\mathrm{miss}}$, i.e. the inverse vector sum of the $p_{\mathrm{T}}$ of all photons or jets in the event. The selection on $\Delta\phi(E_{\mathrm{T}}^{\mathrm{miss}}, E_{\mathrm{T}}^{\gamma})$ is particularly effective in rejecting residual background from misidentified PV while preserving the acceptance of the boosted Higgs signal. The full list of selection is summarised in Table 17, together with the definition of three control regions (CR) defined in Section 6.7.

Table 17. Summary of the selections applied in the signal (SR) and control (CR) regions. In the CRs with muons, the $E_{\mathrm{T}}^{\mathrm{miss}}$ is recomputed treating muons as invisible particles.

| Selection | SR | Low $\mathcal{S}_{p_T^{\mathrm{miss}}}$ CR | $1\mu$ CR | $2\mu$ CR |
|---|---|---|---|---|
| Photon | 1 (selected) with $p_{\mathrm{T}} > 50$ GeV | | | |
| $E_{\mathrm{T}}^{\mathrm{miss}}$ | $> 100$ GeV | | | |
| $m_T$ | $> 80$ GeV | | | |
| $\mathrm{BDT}_{\mathrm{vertex}}$ | $> 0.1$ | | | |
| $N_{e,\tau}$ | 0 (baseline) | | | |
| $N_{\mathrm{jet}}^{\mathrm{central}}$ | $\leq 3$ | | | — |
| $N_\mu$ | 0 (baseline) | | 1 (selected) | 2 (selected) |
| $\mathcal{S}_{p_T^{\mathrm{miss}}}$ | $> 6$ | $[2, 6]$ | $> 6$ | — |
| $\Delta\phi(E_{\mathrm{T}}^{\mathrm{miss}}, E_{\mathrm{T}}^{\gamma})$ | $> 1.25$ | | | |
| $\Delta p_{\mathrm{T}}^{\mathrm{miss}}$ | $> -10$ GeV | | | — |
| $\Delta\phi(E_{\mathrm{T}}^{\mathrm{miss}}, E_{\mathrm{T}}^{jet})$ | $< 0.75$ | | | — |
| $\lvert\Delta\phi(j_1, j_2)\rvert$ | $< 2.5$ | | | — |
| $m_{\mu\mu\gamma}$ | — | | | $> 100$ GeV |

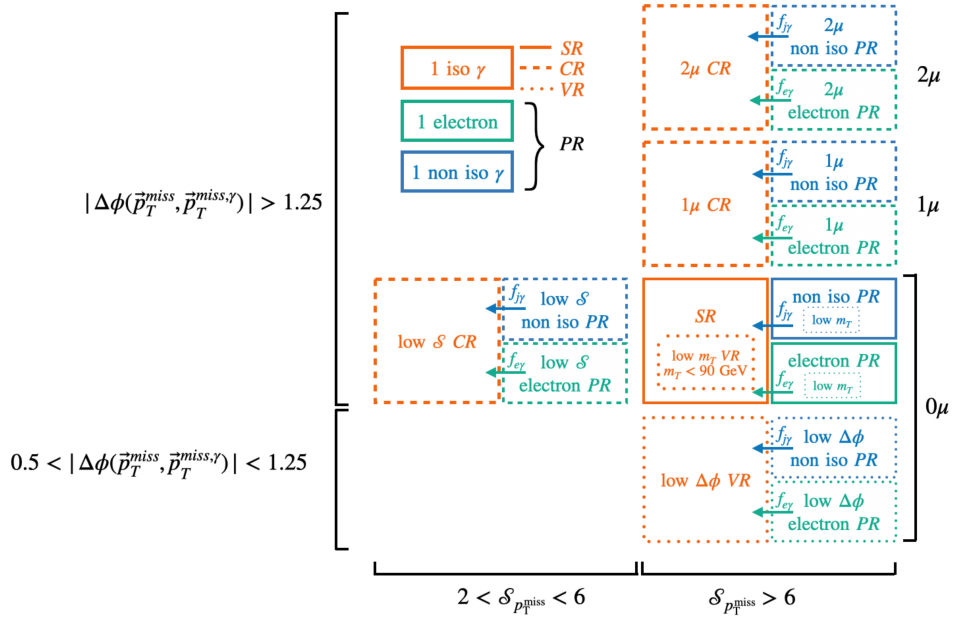


*Figure 77.* Schematic overview of the signal (SR), control (CR), validation (VR) and probe (PR) regions used in the analysis. Different colours correspond to different final states: events with one isolated photons are selected in the SR (continuous lines), CRs (dashed lines) and VRs (dotted lines), while events with single electron or non isolated photon are used for the corresponding PRs. Data in the PRs are scaled by the fake factors indicated by the blue and green arrows ($f_{e\gamma}$ and $f_{j\gamma}$) to estimate the $j \rightsquigarrow \gamma$ and $e \rightsquigarrow \gamma$ contribution in each analysis region.

## 6.7 Analysis strategy and background modelling

The analysis strategy is based on a binned maximum-likelihood fit to the $m_{\mathrm{T}}$ distribution, performed in the SR and in the three CRs summarised in Table 17.

The $1\mu$ CR and the $2\mu$ CR are employed to normalise the MC simulations of $W\gamma$ and $Z\gamma$ respectively to data. They are defined similarly to the SR, but requiring one or two selected muons. To emulate the SR kinematics, muons are treated as invisible in the $E_{\mathrm{T}}^{\mathrm{miss}}$ reconstruction. In the $2\mu$ CR, some SR selections are loosened or removed to increase the available statistics. The contribution from the $\gamma$(direct)+jets background due to fake $E_{\mathrm{T}}^{\mathrm{miss}}$ is subdominant, accounting for few percent of the total, and therefore it is estimated purely from MC.

The background from fake photons, either $e \rightsquigarrow \gamma$ or $j \rightsquigarrow \gamma$, is estimated in all the analysis regions by rescaling data in probe regions (PR), illustrated in Figure 77, by fake factors evaluated as described in Sections 6.7.1 and 6.7.2. For $e \rightsquigarrow \gamma$ background, electron PRs are defined for each analysis region, replacing the selected photon by a selected electron, passing a single electron trigger. Similarly, for $j \rightsquigarrow \gamma$ background, non-isolated PRs are introduced, by requiring the photon to be non isolated, $\gamma^{\mathrm{non-isol}}$, with $\Upsilon > 0.1$ as defined in eq. 6.1. Due to the large systematic uncertainty affecting the $j \rightsquigarrow \gamma$ component, the low $\mathcal{S}_{p_T^{\mathrm{miss}}}$ CR, defined by requiring $2 < \mathcal{S}_{p_T^{\mathrm{miss}}} < 6$, is included in the fit to provide an additional constraint on this background. The $e \rightsquigarrow \gamma$ contribution is further constrained in the low $m_T$ region of the SR, dominated by $W(e\nu)$+jets events with the electron being misidentified as a photon, yielding a $m_T$ value close to the $W$ mass. In particular, the low $m_T$ validation vegion (VR), with $80 < m_T < 90$ GeV, is well depleted of signal, and it is used also to validate the $e \rightsquigarrow \gamma$ background before performing

the fit. In addition, a low $\Delta\phi$ VR, with $0.8 < \Delta\phi(E_{\mathrm{T}}^{\mathrm{miss}}, E_{\mathrm{T}}^{\gamma}) < 1.1$, provides a sample orthogonal both to the SR and the low $\mathcal{S}_{p_T^{\mathrm{miss}}}$ CR to validate the modeling of the $j \rightsquigarrow \gamma$ background also at high $\mathcal{S}_{p_T^{\mathrm{miss}}}$ values. The two VRs are illustrated in Figure 77.

Table 18. Objects and data samples used for the $e \rightsquigarrow \gamma$ background. In the electron probe region (PR) an electron replaces the photon.

| Evaluation of $f_{e\gamma}$ | | | Electron PR | |
|---|---|---|---|---|
| $\gamma$ | from $\gamma e$ | $e$-trigger | | |
| $e$ | from both $e^+$, $e^-$ | $ee$-trigger | 1 $e$ and no $\gamma$ | $e$-trigger && analysis trigger |

**6.7.1 Estimation of $e \rightsquigarrow \gamma$.** The fake factor for $e \rightsquigarrow \gamma$ estimation is defined as:

$$f_{e\gamma} = \frac{N(e \rightsquigarrow \gamma)}{N(e \rightsquigarrow e)}. \tag{6.2}$$

The values of $f_{e\gamma}$ are computed directly from data, exploiting the $Z \rightarrow e^+e^-$ process, where genuine photons are absent. $N(e \rightsquigarrow \gamma)$ is counted from reconstructed $\gamma e$ final state selected by a single electron trigger, while $N(e \rightsquigarrow e)$ is counted from both $e^+$ and $e^-$ in $e^+e^-$ final state selected by a dielectron trigger — see Table 18. Both counts are collected in an invariant mass window $m_{inv} \in [80, 100]$ GeV about the $Z$-peak.

While the $e^+e^-$ events provide a rather pure sample of $Z \rightarrow e^+e^-$, the $\gamma e^{\pm}$ events contain a large amount of genuine photons, mostly from the $W(\rightarrow e^{\pm}\nu)\gamma$ process, which needs to be subtracted. This is achieved by exploiting the lepton universality, and selecting a sample of $\gamma\mu$ events. To account for the different reconstruction efficiency for $e$ and $\mu$, the invariant mass spectrum of the $\gamma\mu$ events is normalised to that of the $\gamma e$ on the two sidebands $m_{inv} < 70$ GeV and $m_{inv} > 110$ GeV, as displayed in Figure 78. The master formula of the fake factor is

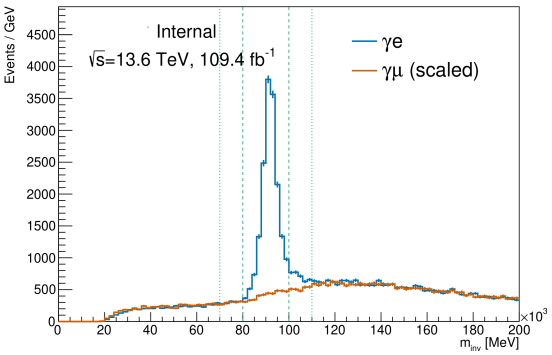


*Figure 78.* Invariant mass for reconstructed $\gamma e$ and $\gamma\mu$ pairs from data, the latter being rescaled such to match its sidebands to those of the former. The vertical dashed lines limit the window used to compute $f_{e\gamma}$, while the vertical dotted lines mark the sidebands used for the renormalization of the $\gamma\mu$ distribution.

therefore

$$f_{e\gamma} = \frac{N_{\gamma e}^{\text{peak}} - N_{\gamma\mu}^{\text{peak}} \dfrac{N_{\gamma e}^{\text{side}}}{N_{\gamma\mu}^{\text{side}}}}{N_{ee}^{\text{peak}}}. \tag{6.3}$$

The value of $f_{e\gamma}$ is computed, separately for 2023 and 2024, as a function of $\eta^{\gamma}$, as it appears flat versus $p_{\text{T}}^{\gamma}$. The values of $f_{e\gamma}$ are weakly dependent on the choice of the peak width and on the sidebands: each variation is treated as a systematic uncertainty, and are all combined in quadrature with the statistical uncertainty. The values of $f_{e\gamma}$ range between $\sim 0.027$ in the barrel, and $\sim 0.054$ in the endcaps, with overall relative uncertainties between 3% and 8%.

The $e$-PR must fulfil both the analysis trigger, to guarantee the same event topology as the SR and CRs, and the electron trigger, for consistency with the $f_{e\gamma}$ evaluation — as detailed in Table 18. However, the $f_{e\gamma}$ evaluation does not consider the analysis trigger, therefore a further correction is needed, to account for the efficiency of the analysis trigger on reconstructed $\gamma$ and $e$:

$$f_{e\gamma}^{\text{corr}} = f_{e\gamma} \frac{\epsilon_{\gamma}^{\text{trig}}}{\epsilon_{e}^{\text{trig}}}. \tag{6.4}$$

The only trigger requirement affecting the evaluation of $f_{e\gamma}$ is that on the reconstructed photon, therefore the effects of the $p_T^{\text{miss}}$ and $m_T$ selections need to be disentangled. This is achieved by applying offline cuts on $p_T^{\text{miss}}$ and $m_T$ higher than the trigger-level cuts, to ensure being in the plateau of the trigger efficiency turn-on curves. To evaluate $\epsilon_\gamma^{\text{trig}}$, $\gamma\mu$ events are selected from data by a muon trigger are used. The muon is treated as invisible in the offline evaluation of $p_T^{\text{miss}}$, and requirements $(p_T^{\text{miss}})^{\mu\text{-inv}} > 150$ GeV and $(m_T)^{\mu\text{-inv}} > 100$ GeV are applied. The trigger-level evaluation of $p_T^{\text{miss}}$ does not consider muons, therefore they are treated as invisible also by the analysis trigger. The fraction of events that pass the analysis trigger provides the value of $\epsilon_\gamma^{\text{trig}}$. Similarly, $\epsilon_e^{\text{trig}}$ is evaluated on events with an electron, selected from data by an electron trigger, and fulfilling $p_T^{\text{miss}} > 200$ GeV and $m_T > 100$ GeV. The fraction of events that pass the analysis trigger provides the value of $\epsilon_e^{\text{trig}}$. Both $\epsilon_\gamma^{\text{trig}}$ and $\epsilon_e^{\text{trig}}$ are computed as functions of $p_{\text{T}}$, to better track the trigger efficiency turn-on. While $\epsilon_\gamma^{\text{trig}}$ reaches full efficiency for $p_{\text{T}} > 60$ GeV, $\epsilon_e^{\text{trig}}$ saturates at about 90%, as a photon trigger is not fully optimal for electrons. The variations of $\epsilon_\gamma^{\text{trig}}$, $\epsilon_e^{\text{trig}}$ when applying different cuts on $p_T^{\text{miss}}$ and $m_T$ are treated as systematic uncertainties and combined in quadrature. The resulting trigger correction factor is between 1.06 and 1.26 with an overall relative uncertainty between 3% and 12%.

The validation of the $e \rightsquigarrow \gamma$ background in the low $m_T$ VR is displayed in Figure 79, showing a good agreement already before the fit.

**6.7.2 Estimation of $j \rightsquigarrow \gamma$.** The $j \rightsquigarrow \gamma$ fake factor is defined as

$$f_{j\gamma} = \frac{N(j \rightsquigarrow \gamma)}{N(j \rightsquigarrow \gamma^{\text{non-isol}})}. \tag{6.5}$$

Isolated and non-isolated reconstructed photons are defined by requiring isolation $\Upsilon < 0.022$ and $\Upsilon > 0.1$, respectively: the former cut is standard in

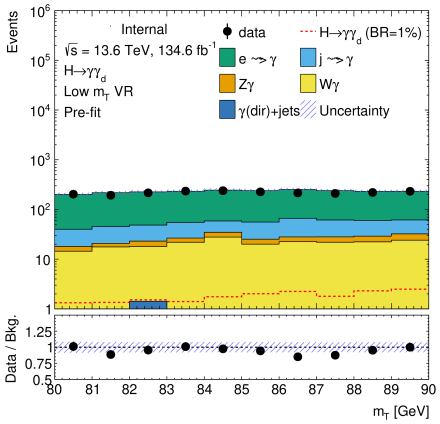


*Figure 79.* Comparison between data and pre-fit background estimates in the low $m_T$ VR. The uncertainty includes both statistical and systematic contributions from the $e \rightsquigarrow \gamma$ and $j \rightsquigarrow \gamma$ data-driven methods.

ATLAS analyses, while the latter is chosen to ensure a negligible contamination from genuine photons. The evaluation of the fake factor relies on the distribution $\Phi^{\texttt{Tight}}(\Upsilon)$ of the isolation for $j \rightsquigarrow \gamma$ passing the `Tight` identification:

$$f_{j\gamma} = \frac{\int_{-\infty}^{+0.022} d\Upsilon \, \Phi^{\texttt{Tight}}(\Upsilon)}{\int_{+0.1}^{+\infty} d\Upsilon \, \Phi^{\texttt{Tight}}(\Upsilon)}. \tag{6.6}$$

The $\Phi^{\texttt{Tight}}(\Upsilon)$ distribution cannot be directly extracted from data, as the `Tight` photon sample contains comparable contributions from $j \rightsquigarrow \gamma$ and genuine $\gamma$. Moreover, the MC modeling of $\Phi^{\texttt{Tight}}(\Upsilon)$ is not accurate and depends on the used MC generator. On the other hand, photons passing the `Loose′` selection[1] (see Section 6.4) are enriched of $j \rightsquigarrow \gamma$, therefore the isolation distribution $\Phi^{\texttt{Loose}'}(\Upsilon)$ can be extracted from data. However, the photon selection affects the isolation, making $\Phi^{\texttt{Loose}'}$ broader than $\Phi^{\texttt{Tight}}$. To extrapolate $\Phi^{\texttt{Tight}}$ from $\Phi^{\texttt{Loose}'}$, an affine transform is applied:

$$\Upsilon^{\texttt{Tight}}_{\text{data}} = m^{\texttt{Tight}}_{\text{data}} + \frac{w^{\texttt{Tight}}_{\text{data}}}{w^{\texttt{Loose}'}_{\text{data}}} \left( \Upsilon^{\texttt{Loose}'}_{\text{data}} - m^{\texttt{Loose}'}_{\text{data}} \right), \tag{6.7}$$

[1] `Loose′` photons are collected from events passing the analysis trigger: this is possible, as the `Tight` selection at trigger level is looser than at analysis level.

where $m$ and $w$ are the median and the 16%-to-84% half-width of the isolation distributions in $\texttt{Loose}'$ and $\texttt{Tight}$ samples. While $m_{\text{data}}^{\texttt{Loose}'}$ and $w_{\text{data}}^{\texttt{Loose}'}$ can be computed on data from the observed $\Phi^{\texttt{Loose}'}$, $m_{\text{data}}^{\texttt{Tight}}$ and $w_{\text{data}}^{\texttt{Tight}}$ must be inferred, assuming that the change in shape from $\Phi^{\texttt{Loose}'}$ to $\Phi^{\texttt{Tight}}$ is similar in data and in $j \rightsquigarrow \gamma$ MC. This assumption is encoded into the following equations:

$$\left(\frac{m_{\text{data}}^{\texttt{Tight}} - m_{\text{data}}^{\texttt{Loose}'}}{w_{\text{data}}^{\texttt{Loose}'}}\right) = R_m \left(\frac{m_{j\rightsquigarrow\gamma}^{\texttt{Tight}} - m_{j\rightsquigarrow\gamma}^{\texttt{Loose}'}}{w_{j\rightsquigarrow\gamma}^{\texttt{Loose}'}}\right) \quad ; \quad \left(\frac{w_{\text{data}}^{\texttt{Tight}}}{w_{\text{data}}^{\texttt{Loose}'}}\right) = R_w \left(\frac{w_{j\rightsquigarrow\gamma}^{\texttt{Tight}}}{w_{j\rightsquigarrow\gamma}^{\texttt{Loose}'}}\right). \tag{6.8}$$

The values of $R_m$ and $R_w$ are computed exploiting the $\texttt{Loose}''$ photon selection (see Section 6.4), that is closer to the $\texttt{Tight}$ selection, but non-overlapping: the $\texttt{Loose}''$ sample in data is still dominated by $j \rightsquigarrow \gamma$, therefore $m^{\texttt{Loose}''}$ and $w^{\texttt{Loose}''}$ can be evaluated on data from the observed $\Phi^{\texttt{Loose}''}$, and Equation 6.8 can be used with the $\texttt{Loose}''$ instead of the $\texttt{Tight}$ sample, to derive $R_m$ and $R_w$. In synthesis, the affine transform of equation 6.7 depends on the $R_m$ and $R_w$ parameters: these are evaluated to achieve a $\texttt{Loose}' \rightarrow \texttt{Loose}''$ extrapolation that reproduces at best the observed $\texttt{Loose}''$ sample, and then applied to the $\texttt{Loose}' \rightarrow \texttt{Tight}$ extrapolation. This process is symbolised as $\texttt{Loose}'(\rightarrow \texttt{Loose}'') \rightarrow \texttt{Tight}$. The observed isolation distribution for $\texttt{Loose}'$ photons and the extrapolated one for $\texttt{Tight}$ photons are displayed in Figure 80.

There are several ways to define the $\texttt{Loose}''$ selection, depending on the requirements on the strips shower shapes. The reliability of the extrapolation has been validated with several combinations of them, comparing the isolation of the $\texttt{Loose}'(\rightarrow \texttt{Loose}''_a) \rightarrow \texttt{Loose}''_b$ extrapolation with that of the observed $\texttt{Loose}''_b$ sample, as shown in Figure 80. For each $\texttt{Loose}''_a$ selection, a different extrapolated distribution $\Phi_a^{\texttt{Tight}}(\Upsilon)$ is obtained, and therefore a different fake factor

$(f_{j\gamma})_a$. The final fake factor is computed as the arithmetic mean of all $(f_{j\gamma})_a$, and a conservative systematic uncertainty is set as half the envelope of all their values.

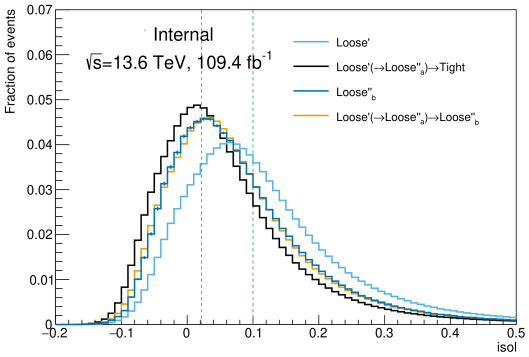


*Figure 80.* Isolation distributions for reconstruted photons, used for the $j \rightsquigarrow \gamma$ background estimate. The figure displays the distribution from the `Loose′` photon sample (enriched of $j \rightsquigarrow \gamma$), and an example of extrapolated distribution for the `Tight` sample (`Loose′`$(\rightarrow$ `Loose″`$_a) \rightarrow$ `Tight`), using a `Loose″`$_a$ sample to compute $R_m$ and $R_w$. The two dashed vertical lines mark the "isolated" ($\Upsilon < 0.022$) and the "non-isolated" ($\Upsilon > 0.1$) regions. The figure also shows the observed and extrapolated distributions for a different `Loose″`$_b$ sample.

The fake factor, separately for 2023 and 2024, is computed as a function of $\eta^\gamma$: the limited MC statistics does not allow to study the dependence on $p_{\mathrm{T}}^\gamma$. The values of $f_{j\gamma}$ range from $\sim$ 1.5 in the ECAL barrel, up to $\sim$ 2.5 in the endcaps, with relative uncertainties between 10% and 15%.

The obtained $j \rightsquigarrow \gamma$ prediction is validated, before the fit, in both the low $\mathcal{S}_{p_T^{\mathrm{miss}}}$ CR and the low $\Delta\phi$ VR, as shown in Figure 81.

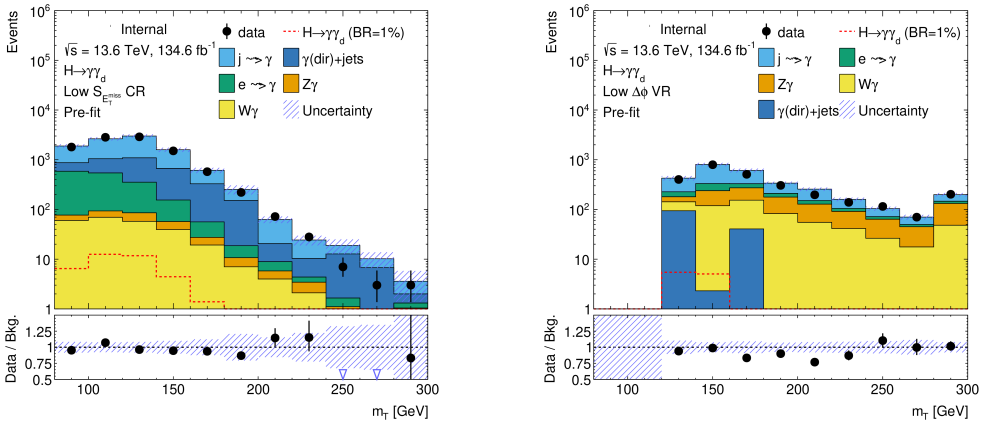


(a) (b)

*Figure 81.* Comparison between data and pre-fit background estimates in the low $\mathcal{S}_{p_T^{\text{miss}}}$ CR (a) and the low $\Delta\phi$ VR (b), enriched of $j \rightsquigarrow \gamma$. The uncertainty includes both statistical and systematic contributions from the $e \rightsquigarrow \gamma$ and $j \rightsquigarrow \gamma$ data-driven methods.

### 6.8 Systematic uncertainties

Multiple sources of systematic uncertainty are considered in the analysis. The experimental and theoretical uncertainties are applied only to the MC simulations of the signal and $V\gamma$ background, while their impact on the $\gamma$(direct)+jets simulation is expected to be negligible compared to its statistical fluctuations. Additional systematic uncertainties arise from the data-driven background estimates. The impact of the different sources of uncertainty on the fitted value of $\text{BR}_{\gamma\gamma_d}$ is summarised in Table 19. The contributions are evaluated using the covariance matrix decomposition method and include both statistical and systematic components. The total uncertainty is dominated by the statistical component (80%), including both the statistical uncertainty on the data and on the background. The dominant systematic contribution arises from experimental systematic uncertainties (29%), primarily driven by jet-related effects, followed by

uncertainties on the $e \rightsquigarrow \gamma$ and $j \rightsquigarrow \gamma$ data-driven methods (17%) and theoretical uncertainties (11%).

Table 19. Impact of each category of uncertainty on the signal yields, as obtained through the covariance matrix decomposition method.

| **Category** | **Contribution to uncertainty on the** $\mathrm{BR}_{\gamma\gamma_d}$ |
|---|---|
| **Statistical** | 80% |
| Data | 65% |
| Background | 47% |
| **Experimental systematic** | 29% |
| Pile-up reweighting | 5.7% |
| Pile-up corrections in jets calibration | 22% |
| Jets | 18% |
| Photons | 5.2% |
| Muons | 2.3% |
| $E_{\mathrm{T}}^{\mathrm{miss}}$ | ¡1% |
| **Systematic on data-driven methods** | 17% |
| $j \rightsquigarrow \gamma$ | 11% |
| $e \rightsquigarrow \gamma$ | 13% |
| **Theoretical systematic** | 11% |

**6.8.1 Experimental uncertainties.** Luminosity and PU modelling uncertainties affect the event as a whole. The uncertainty on the integrated luminosity is 1.9%, derived from the calibration of the LUCID-2 detector and complemented by information from the ID and the calorimeters ATLAS Collaboration (2023). This uncertainty is applied as a global normalization uncertainty to all MC samples, including both signal and background processes. The uncertainty associated with the modelling of PU interactions is estimated

by varying the average number of interactions per bunch crossing by 4% in the simulation.

Further uncertainties are associated with the reconstruction and isolation efficiency and with the energy calibration and resolution of photons, muons and jets. Photon efficiency uncertainties are estimated using Run-2 data and MC simulations ATLAS Collaboration (2019d), with an additional uncertainty included to account for differences between Run-2 and Run-3, as derived from simulation. The uncertainties related to photons energy calibration and resolution are evaluated following the methodology described in Ref. ATLAS Collaboration (2019c), using the Run-3 data collected between 2022 and 2024. All contributions are summed in quadrature and considered fully correlated in photon $\eta$, resulting in one systematic associated to the energy calibration, and one to the energy resolution.

Multiple sources of uncertainties are considered for muons. The uncertainties affecting the muon momentum scale and resolution are separated into charge-dependent and charge-independent components ATLAS Collaboration (2021d). The former include statistical uncertainties, data–MC non-closure effects, and non-sagitta effects in the end-cap region, while the latter accounts for track resolution and momentum scale variations. Additional uncertainties are associated with muon reconstruction and isolation efficiencies, as well as with the track-to-vertex association efficiency; each of these is split into statistical and systematic components ATLAS Collaboration (2016d).

Jet reconstruction is affected by uncertainties related to jet vertex tagging and to the jet energy scale (JES) and resolution (JER). The uncertainty on the NN-JVT and fJVT calibrations ATLAS Collaboration (2016e, 2017e) is derived from $Z \to \mu\mu$ and $Z \to ee$ events in 2022–2023 data and is dominated

by PU modelling uncertainties, particularly at low $p_{\mathrm{T}}$. The JES and JER uncertainties ATLAS Collaboration (2017f, 2017j, 2020b) include contributions from area subtraction, PU residual corrections, absolute energy scale, and Global Sequential Calibration, and are evaluated using Run-3 MC simulations. The uncertainty on the in-situ calibration is derived from Run-2 data, with an additional non-closure uncertainty included to cover differences between Run-2 and Run-3. Further non-closure uncertainties account for residual effects related to variations in the vertexing algorithm, calorimeter noise thresholds, and modelling differences in the forward calorimeter region. Among these systematic uncertainties, the dominant contribution arises from PU residual corrections, which is quoted separately in Table 19. An additional jet-related source of systematic uncertainty arises from flavour tagging ATLAS Collaboration (2019a).

Finally, the $E_{\mathrm{T}}^{\mathrm{miss}}$ is affected by three sources of systematic uncertainty ATLAS Collaboration (2020c); Balunas et al. (2024), related to the modelling of its soft term and evaluated using Run-3 data collected in 2022–2023 and the corresponding MC simulations. One scale uncertainty is obtained by scaling the soft-term magnitude up and down along the direction of the hard term, while two resolution uncertainties are derived by smearing the soft-term magnitude in directions parallel and perpendicular to the hard-term direction.

**6.8.2 Uncertainties on data-driven methods.** Three additional sources of systematic uncertainty are associated with the data-driven estimates of the $e \rightsquigarrow \gamma$ and $j \rightsquigarrow \gamma$ backgrounds. As described in Section 6.7.1, for the $e \rightsquigarrow \gamma$ background, one systematic uncertainty accounts for the dependence of the $f_{e\gamma}$ fake factor on the peak width and the definition of the sidebands, while the second contribution is associated to the trigger correction factors. The third data-driven

systematic uncertainty is associated to the extrapolation from $\Phi^{\texttt{Loose}'}$ to $\Phi^{\texttt{Tight}}$ in the $j \rightsquigarrow \gamma$ estimation, as described in Section 6.7.2.

**6.8.3 Theoretical uncertainties.** Theoretical uncertainties related to the modelling of QCD effects are considered, arising from variations of the renormalisation and factorisation scales, the value of the strong coupling constant, and the choice of parton distribution functions (PDFs). Their contribution is evaluated following the PDF4LHC21 prescription Ball et al. (2022).

The uncertainty associated with missing higher-order corrections is evaluated by independently varying the renormalisation and factorisation scales by factors of 0.5 and 2.0 with respect to their nominal values. The resulting variations are combined using the envelope method.

The uncertainty related to the strong coupling constant $\alpha_S$ is obtained by varying its value by $\pm 0.001$, while the PDF uncertainty is evaluated accounting for both the internal uncertainties of the nominal PDF set and the differences with respect to alternative PDF sets. These two PDF contributions are combined using the envelope method. For the signal samples, the `CT18NLO` and `MSHT20nlo_as118` PDF sets are used as systematic variations with respect to the nominal PDF4LHC21 set. For the background samples, the `CT18NNLO` and `MSHT20nnlo_as118` sets are compared to the nominal `NNPDF3.0` set.

## 6.9 Statistical treatment and results

**6.9.1 Likelihood fitting.** Most analyses with the ATLAS experiment are essentially counting experiments, where the number of events observed in data is compared to the number of events expected from the background-only hypothesis and the signal-plus-background hypothesis. The likelihood function is a powerful tool that quantifies the agreement between observed data and these hypotheses,

taking into account both statistical and systematic uncertainties. By maximizing the likelihood function, we can estimate the parameters of interest, such as the signal strength, and determine how well our data supports the presence of a signal. In this section, the fitting techniques used in this analysis will be described, using the statistical framework from TRExFitter and data/MC events from the dark photon analysis as described in appendix D.

The likelihood function is written as:

$$\mathcal{L}(\mu, \boldsymbol{\theta}, \gamma, \tau) = \prod_{i=1}^{N_{\text{bins}}} \text{Pois}(N_i \mid \mu s_i(\boldsymbol{\theta}) + b_i(\boldsymbol{\theta}, \gamma, \tau)) \prod_{\theta \in \boldsymbol{\theta}} \frac{1}{\sqrt{2\pi}} e^{-\theta_k^2/2} \prod_{i=1}^{N_{\text{bins}}} G\big(n_i^{MC} \mid \gamma_i\big) \,. \tag{6.9}$$

where $\mu$ is the signal strength, $\boldsymbol{\theta}$ are the nuisance parameters associated with systematic uncertainties, $\gamma$ are the parameters associated with the MC statistical uncertainties, and $\tau$ are the background normalization factors. The first product runs over the terms per bin of the histograms used in the fit. This includes the number of data events, number of expected signal events $s_i$, and number of expected background events $b_i$. $\mu$ scales the signal yield, while the nuisance parameters $\boldsymbol{\theta}$ affect both signal and background yields, and the $\gamma$ parameters affect only the background yields. The second product runs over the nuisance parameters, or systematic uncertainties, which are constrained by Gaussian distributions centered at zero with a width of one. Examples of systematic uncertainties include those related to the reconstruction of physics objects or detector related effects, calibration, theoretical modeling, MC modeling, and data-driven background estimation. This adds degrees of freedom to the fit, allowing the fit to adjust the expected yields within the uncertainties to better match the observed data. Nuisance parameters can affect the shape of the distributions used in the fit, as well

as the overall normalization. Systematic uncertainties in the dark photon analysis are described in more detail in Section 6.8. Ideally, MC simulations would have infinite statistics, but in practice they are limited by computational resources, leading to statistical uncertainties in the predicted yields. The final product in the likelihood function accounts for the statistical uncertainties in the MC predictions, which can be modeled as Poisson or Gaussian distributions depending on the number of MC events in each bin. $\gamma$ nuisance parameters are introduced in this final product, and scale the total signal plus background yields in each bin. It is important to note that there is only one $\gamma$ parameter per bin, which means that the MC statistical uncertainty is treated as a single source of uncertainty that affects all processes in that bin, rather than having separate $\gamma$ parameters for each process. It is common to use the negative log-likelihood (NLL) for numerical stability and convenience, as it transforms the product of probabilities into a sum, which is easier to handle computationally. The NLL is defined as:

$$\begin{aligned} -\ln \mathcal{L}(\mu, \boldsymbol{\theta}, \gamma, \tau) = &- \sum_{i=1}^{N_{\text{bins}}} \ln \text{Pois}(N_i \mid \mu s_i(\boldsymbol{\theta}) + b_i(\boldsymbol{\theta}, \gamma, \tau)) \\ &- \sum_{\theta \in \boldsymbol{\theta}} \ln \left( \frac{1}{\sqrt{2\pi}} e^{-\theta_k^2/2} \right) - \sum_{i=1} \ln G\big(n_i^{MC} \mid \gamma_i\big) \,. \end{aligned} \tag{6.10}$$

Maximizing the likelihood function (or equivalently minimizing the NLL) allows us to find the best-fit values of the parameters, including the signal strength $\mu$ and the nuisance parameters $\boldsymbol{\theta}$ and $\gamma$. The parameter of interest (POI) is the signal strength $\mu$, which quantifies the presence of a signal in the data, and in the case of the dark photon analysis, the branching ratio $BR(H \to \gamma\gamma_d)$ is considered a free parameter, as well as the k-factors used for the normalization of $Z\gamma$ and $W\gamma$ background.

**6.9.2 TRExFitter Framework.** The likelihood function is implemented and maximized in the dark photon analysis using the TRExFitter framework[2], which is a software tool developed by the ATLAS collaboration for performing statistical analysis in particle physics. TRExFitter is run using a configuration file that specifies the details of the fit, including the input histograms, the parameters to be fitted, and the systematic uncertainties to be included. A workspace is created for the fit, containing the the parameters of interest, the physics samples, and the systematic uncertainties. The fit is performed on the workspace, either with real data or with Asimov samples. Asimov samples are generated based on the expected yields from the MC templates, without any statistical fluctuations, and are used to evaluate the expected sensitivity of the analysis Cowan, Cranmer, Gross, and Vitells (2011b). The fit results include the best-fit values of the parameters, a breakdown of their uncertainties, and the correlations between the parameters. There are multiple regions defined and fed into the fit. A signal region (SR) is optimized with selections that enhance the signal contribution, while control regions (CRs) are defined to constrain the background contributions. Validation regions (VRs) can also be defined to check the modeling of the backgrounds. They are constrained by the fit, but the fit parameters are used to check for closure in the region. The various regions used in the dark photon analysis are described in more detail in section 6.6. Prefit and postfit distributions can be produced to visualize the agreement between the data and the fitted model in all regions, as well as the impact of the systematic uncertainties on the fit results. Diagnostic plots such as the ranking of the nuisance parameters and the correlation matrix can be produced to understand the impact

[2]TRExFitter documentation

of each systematic uncertainty on the fit results and the correlations between the parameters. When two or more parameters are correlated, checking if the correlation is expected based on the analysis or the fit configuration is important, as unexpected correlations could indicate issues with the fit or the modeling of the systematic uncertainties. In the ranking, the impact of each nuisance parameter on the signal strength $\mu$ is shown, which indicates how much the signal strength would change if that nuisance parameter were fixed to its prefit value. Understanding which systematics have the largest impact on the POI or the fit results can help identify areas of improvement in the analysis, or allow for corrections to the fit configuration or the modeling of the systematic uncertainties. Pull plots can also be produced to show the pulls of the fitted parameters, which indicate how much the fitted values deviate from their expected values based on the input MC templates and the data. Ideally, the nuisance parameters should center around zero, and can be slightly constrained by the fit, but they should not be pulled to extreme values, which could indicate issues with the fit configuration or the modeling of the systematic uncertainties. Expected or observed limits on the POI can be extracted from the fit, providing a quantitative measure of the sensitivity of the analysis on the Higgs to photon and dark photon decay. Examples of the various diagnostic plots and fit results will be shown in the next section, where a walkthrough of the fitting procedure in the dark photon analysis will be provided.

**6.9.3 Walkthrough of the dark photon fit.** This section provides a walkthrough of the fitting procedure in the dark photon analysis, using the TRExFitter framework and the likelihood function described above. Note that theoretical uncertainties are not included in the plots shown in this section, but they are included in section 6.9.4 for the final fit results of the analysis. There are

two fits conducted in the dark photon analysis: a signal-plus-background fit that is blinded, and a signal-plus-background fit that is unblinded. Fitting is performed in bins of transverse mass $m_T$, calculated using the photon and the $E_{\mathrm{T}}^{\mathrm{miss}}$. The blinded fit is performed on Asimov data in the signal region, with real data in the control regions. The unblinded fit is performed on real data in both the signal and control regions, with the data summarized in section 6.2.

As seen in Fig. 82, asimov data matches exactly with the expected yields from the background MC templates, with no statistical fluctuations. This allows for the evaluation of the expected sensitivity of the analysis without biasing the results by looking at the real data in the signal region, as well as acting as a check of the fit configuration and the implementation of the systematic uncertainties.

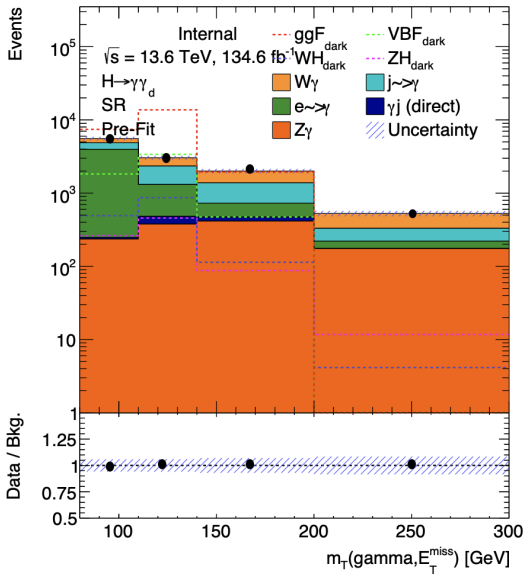


*Figure 82.* Prefit distribution of the transverse mass $m_T$ in the signal region, with Asimov sample.

***6.9.3.1 Control Regions.*** The various backgrounds in an analysis can be very correlated, and it can be difficult to disentangle their contributions in the signal region. One way to address this is to define control regions that are

enriched in specific backgrounds, and use the data in these control regions to constrain the normalizations of the backgrounds in the fit. These backgrounds can then be free to "float" in the fit, and the fit will adjust their normalization factors to best match the data in the control regions, which in turn constrains their contributions in the signal region. This is fitting is done simultaneously with the fit in the signal region for the dark photon analysis. Ideally, the control regions should be designed to be as orthogonal as possible to the signal region to avoid signal contamination, while still being close enough in phase space to the signal region to ensure that the background compositions are similar.

There are three control regions defined in the dark photon analysis, each enriched with a specific background: The one and two muon control regions, which are enriched in $W\gamma$ and $Z\gamma$ backgrounds respectively, and the low $E_{\mathrm{T}}^{\mathrm{miss}}$ significance control region, which is used to constrain the jets faking photons background. These regions are defined in section 6.6. An example of the prefit distributions in the CRs can be seen in Fig. 83, where the data is compared to the yields from the background MC templates.

***6.9.3.2 Impact of the jets faking photons background.*** The low $E_{\mathrm{T}}^{\mathrm{miss}}$ significance control region was originally a validation region to check the modeling of the jets faking photons background. During fitting, however, the jets faking photons background was found to have a large impact on the fit results. The uncertainty on the fake factor was significant, surpassing the statistical uncertainties and all other systematic uncertainties. Correlations between the jets faking photons background and the signal strength were observed, as well as with the normalization factors of the $W\gamma$ and $Z\gamma$ backgrounds. The breakdown of the

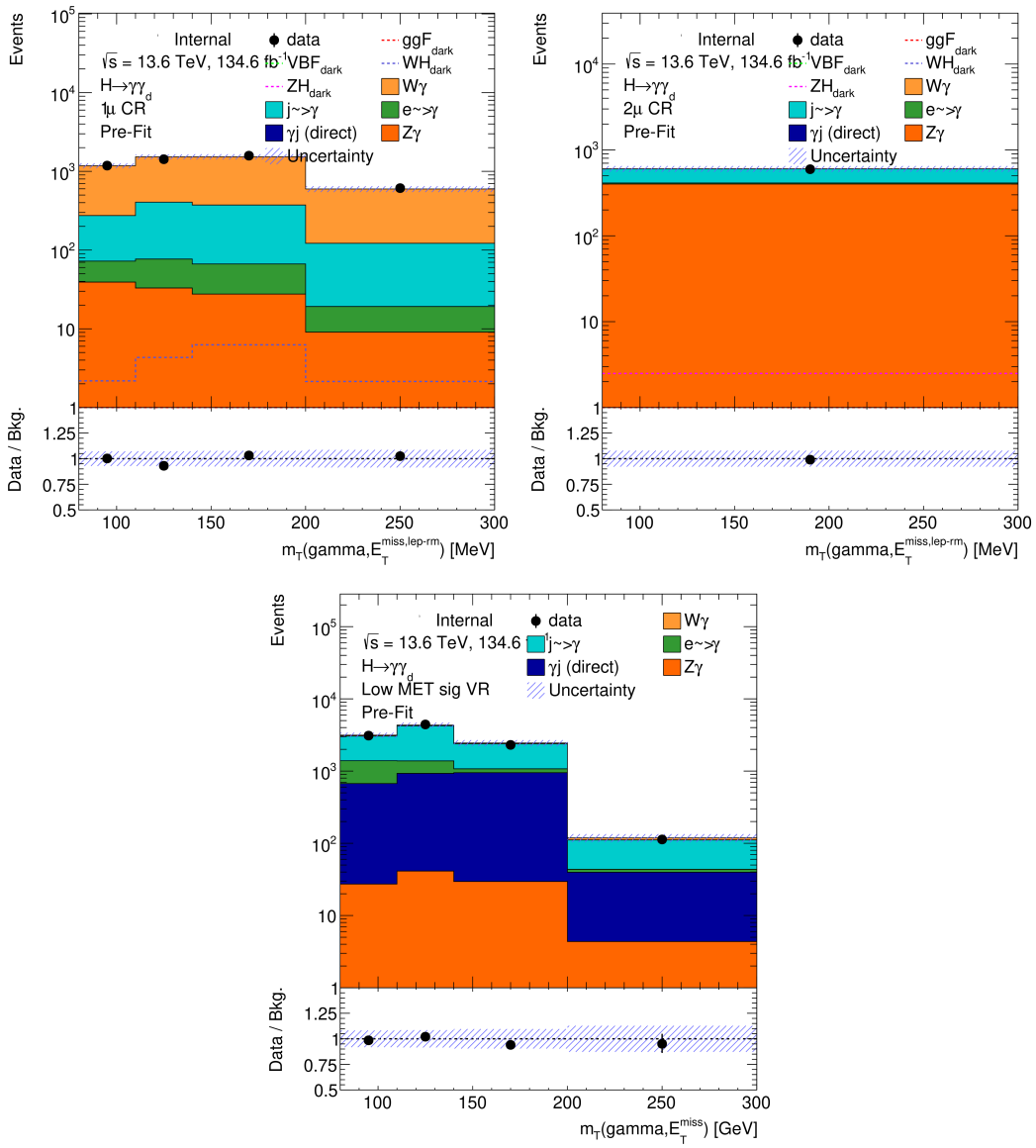


*Figure 83.* Prefit distributions of the transverse mass $m_T$ in the control regions.

nuisance parameter ranking in the fit, as well as the correlation matrix are shown in Fig. 84.

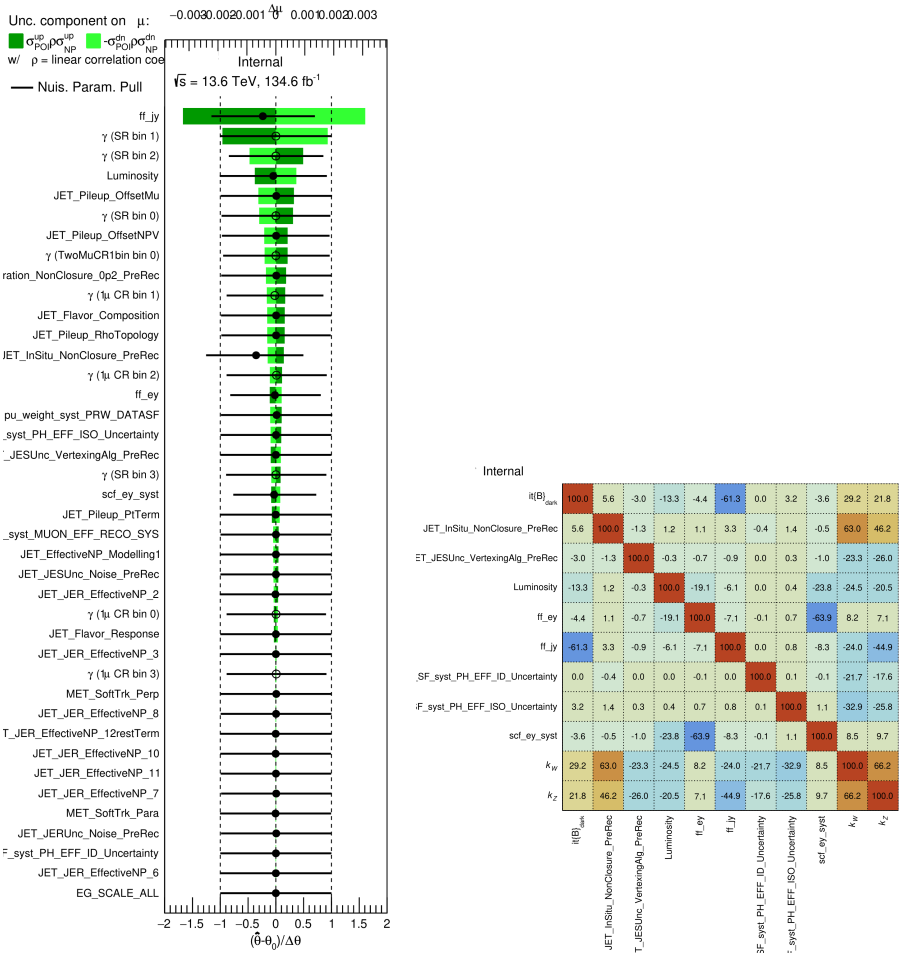


*Figure 84.* Ranking of the nuisance parameters in the fit, showing the impact of each nuisance parameter on the signal strength $\mu$ (left). Correlation matrix of the fit parameters (right). Both plots are with the low $E_{\mathrm{T}}^{\mathrm{miss}}$ significance validation region included in the fit.

It was proposed to transform the low $E_{\mathrm{T}}^{\mathrm{miss}}$ significance validation region into a control region to constrain the jets faking photons background, and this was implemented in the fit. The argument for this was that if the low $E_{\mathrm{T}}^{\mathrm{miss}}$ significance validation region is stable and well modeled, it is then safe to rerun the fit with this region included as a control region, which would help constrain the jets faking

photons background and reduce its impact on the fit results. As seen in Fig. 85, the fit confirms that the low $E_{\mathrm{T}}^{\mathrm{miss}}$ significance validation region is stable, and can be safely used as a control region.

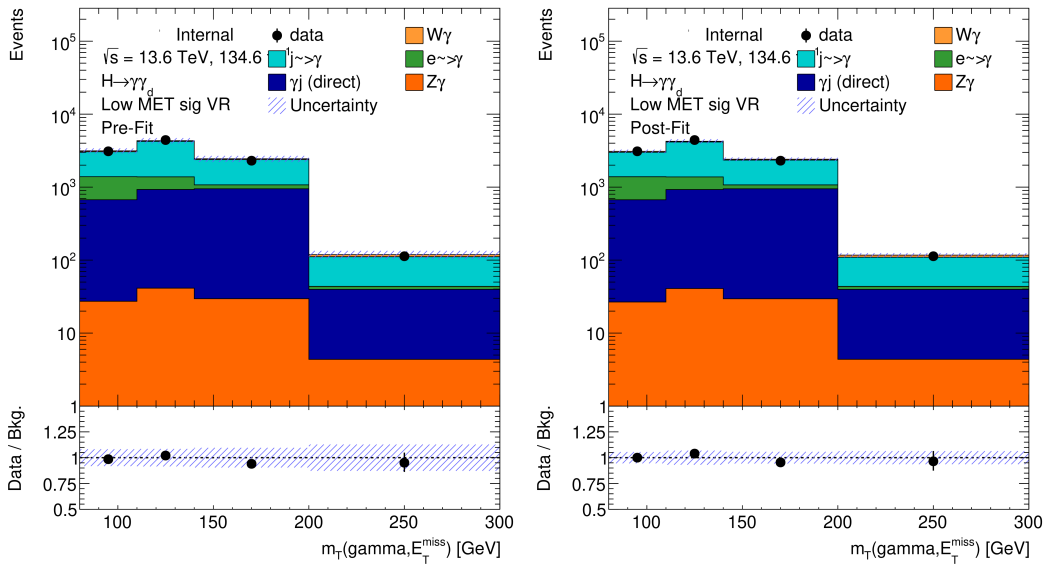


*Figure 85.* Prefit (left) and postfit (right) distributions of the transverse mass $m_T$ in the low $E_{\mathrm{T}}^{\mathrm{miss}}$ significance validation region. The fit confirms that the low $E_{\mathrm{T}}^{\mathrm{miss}}$ significance region is stable, and can be safely used to constrain the jets faking photons background.

The low $E_{\mathrm{T}}^{\mathrm{miss}}$ significance control region was then included in the fit, and studied with data and Asimov samples. Postfit distributions of the low $E_{\mathrm{T}}^{\mathrm{miss}}$ significance control region can be seen in Fig. 86. The background expectations are stable with all configurations of the fit, and the data is well modeled. It can be seen in Fig. 87 that the jets faking photons fake factor uncertainty is better constrained, and the correlations with the signal strength and the normalization factors are reduced. Along with the low $\Delta\phi(E_T^{miss}, E_T^{\gamma})$ VR as described in section 6.6, the low $E_{\mathrm{T}}^{\mathrm{miss}}$ significance control region also serves as a cross check of the modelling of the jets faking photons background and the $E_{\mathrm{T}}^{\mathrm{miss}}$ significance variable.

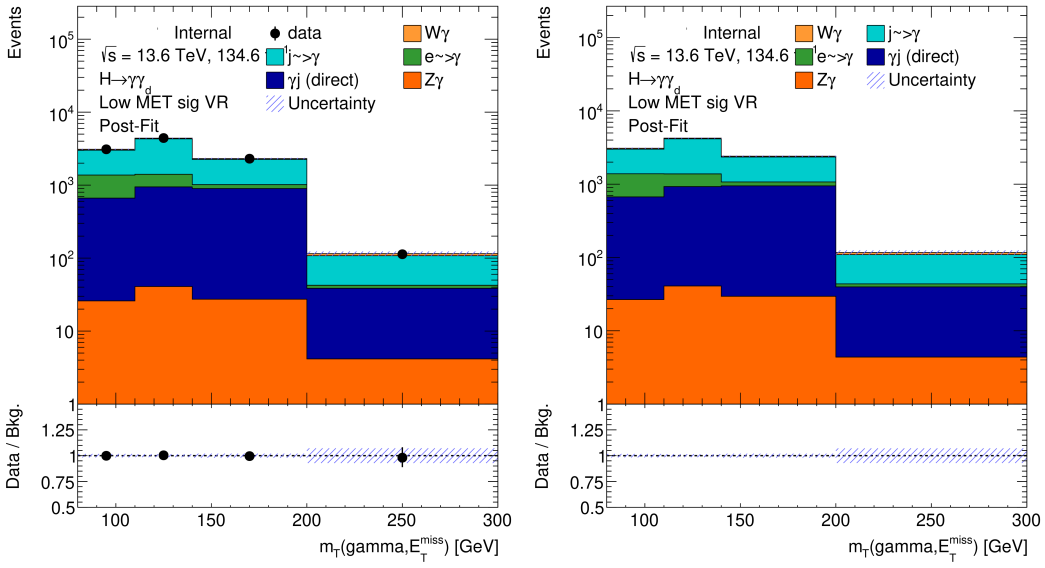


*Figure 86.* Postfit distributions of the transverse mass $m_T$ in the low $E_{\mathrm{T}}^{\mathrm{miss}}$ significance control region with data (left) and Asimov samples (right). The background expectations are stable with all configurations of the fit, and the data is well modeled.

Another check of how the fit compares with and without the low $E_{\mathrm{T}}^{\mathrm{miss}}$ significance control region is to look at the normalization factor pulls of the backgrounds. Prefit values are always at 1, and are constrained by data in the fit. Even though the two normalization factors should mostly be constrained by the one and two muon control regions, as said above, there were correlations between the backgrounds, and the jets faking photons background had a large impact on the fit results. Now that the jets faking photons background is better constrained, the normalization factors should still be consistent with the values obtained without the low $E_{\mathrm{T}}^{\mathrm{miss}}$ significance control region. This is indeed the case, as seen in Fig. 88, where the normalization factor pulls of the $W\gamma$ and $Z\gamma$ backgrounds are consistent between the fit with and without the low $E_{\mathrm{T}}^{\mathrm{miss}}$ significance control region.

The final metric to compare the fit results with and without the low $E_{\mathrm{T}}^{\mathrm{miss}}$ significance control region is the expected limits on the branching ratio $\mathcal{B}(H \rightarrow$

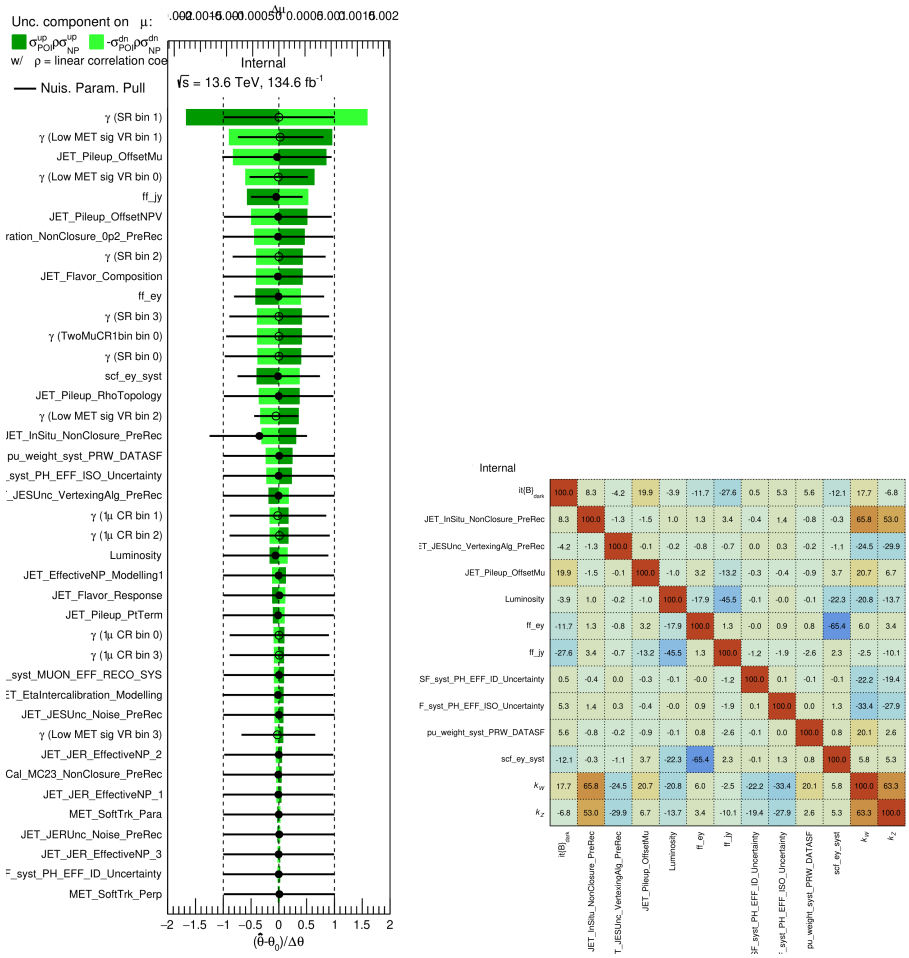


*Figure 87.* Ranking of the nuisance parameters in the fit after including the low $E_{\mathrm{T}}^{\mathrm{miss}}$ significance control region, showing the impact of each nuisance parameter on the signal strength $\mu$ (right). Correlation matrix of the fit parameters, showing the correlations between the signal strength $\mu$ and the normalization factors of the backgrounds (left). Both plots are with the low $E_{\mathrm{T}}^{\mathrm{miss}}$ significance control region included in the fit.




*Figure 88.* Normalization factor pulls of the $W\gamma$ and $Z\gamma$ backgrounds with the low $E_{\mathrm{T}}^{\mathrm{miss}}$ significance control region included in the fit (left) and without it (right). The normalization factors are consistent between the two fits, showing that the inclusion of the low $E_{\mathrm{T}}^{\mathrm{miss}}$ significance control region does not bias the fit results.

$\gamma\gamma_d$). Expected limits were extracted from the blinded fit with and without the low $E_{\mathrm{T}}^{\mathrm{miss}}$ significance control region, and are shown in Table 20.

| Fit Configuration | $-2\sigma$ | $-1\sigma$ | Median | $+1\sigma$ | $+2\sigma$ |
|---|---|---|---|---|---|
| With low $E_{\mathrm{T}}^{\mathrm{miss}}$ significance CR | .0049 | .0066 | .0095 | .014 | .020 |
| Without low $E_{\mathrm{T}}^{\mathrm{miss}}$ significance CR | .0059 | .008 | .011 | .016 | .023 |

Table 20. Expected 95% CL limits on $\mathcal{B}(H \to \gamma\gamma_d)$ at $-2\sigma$, $-1\sigma$, median, $+1\sigma$, and $+2\sigma$, with and without the low $E_{\mathrm{T}}^{\mathrm{miss}}$ significance control region included in the fit. There is a roughly 10% improvement in the expected limits when the low $E_{\mathrm{T}}^{\mathrm{miss}}$ significance control region is included.

In summary, the inclusion of the low $E_{\mathrm{T}}^{\mathrm{miss}}$ significance control region in the fit has a significant impact on the fit results, as it helps constrain the jets faking photons background, decouples it from the signal strength and the normalization factors of the other backgrounds, and improves the expected limits on the branching ratio $\mathcal{B}(H \to \gamma\gamma_d)$ by roughly 10%. The full fitting procedure and results for the blinded and unblinded fits are described in the next sections.

**6.9.4 Simultaneous fit and results.** To maximise the sensitivity to the Higgs boson mass peak, the transverse mass $m_T$ is used as the discriminating variable in the binned maximum-likelihood fit in all regions, except for the $2\mu$ CR, which is treated as a single inclusive bin due to limited statistical precision. The $m_T$ binning is optimised such that the bulk of the expected signal is contained in the two central bins, defined as $110 < m_T < 140$ GeV and $140 < m_T < 200$ GeV, while the lower and upper bins provide additional constraints on the background normalisation. In particular, the first bin ($80 < m_T < 110$ GeV) contains the low-$m_T$ VR and is dominated by the $e \rightsquigarrow \gamma$ background, allowing an effective constraint on this contribution.

The likelihood function is constructed as the product of Poisson probability distribution functions describing the event counts in each $m_T$ bin of the SR and

CRs, as functions of the expected signal and background yields. The branching ratio $\mathrm{BR}_{\gamma\gamma_d}$ is included in the fit as the Parameter of Interest (POI). In addition, two normalisation factors, $k_{W\gamma}$ and $k_{Z\gamma}$, are applied to the $W\gamma$ and $Z\gamma$ background processes respectively, and included as free parameters in the fit, primarily constrained by the corresponding $1\mu$ and $2\mu$ CRs. Systematic uncertainties affecting the signal and background yields are incorporated into the likelihood model as nuisance parameters with a Gaussian constraint centered at zero with a width corresponding to the associated uncertainty. The experimental and data-driven systematics are treated as fully correlated across all regions, and experimental systematics are also correlated among the background MC samples. Theoretical uncertainties are treated as fully uncorrelated. All nuisance parameters are assumed to be mutually uncorrelated.

A background-only fit is first performed in the SR and CRs, with $\mathrm{BR}_{\gamma\gamma_d}$ set to zero, and the $k_{W\gamma}$ and $k_{Z\gamma}$ normalisation factors left free to float. The fitted values are $k_{W\gamma} = 0.92^{+0.08}_{-0.07}$ and $k_{Z\gamma} = 1.04^{+0.12}_{-0.11}$. The post-fit $m_T$ distributions for data and the expected SM background are shown in Figure 89, while the corresponding yields are reported in Table 21. The yields and background composition in each analysis region, including the VRs, are also summarised in Figure 90. Good agreement is observed between data and the SM background expectation in all the analysis regions, and the data are consistent with the background-only hypothesis with an observed $p_0$-value of 0.31.

A second fit is then performed including the signal contribution and the branching ratio $\mathrm{BR}_{\gamma\gamma_d}$ as POI. The results are consistent with the background-only hypothesis, with the best-fit value $\mathrm{BR}_{\gamma\gamma_d} = 0.002^{+0.05}_{-0.04}$. Since no significant excess over the SM prediction is observed, upper limits on the branching ratio of

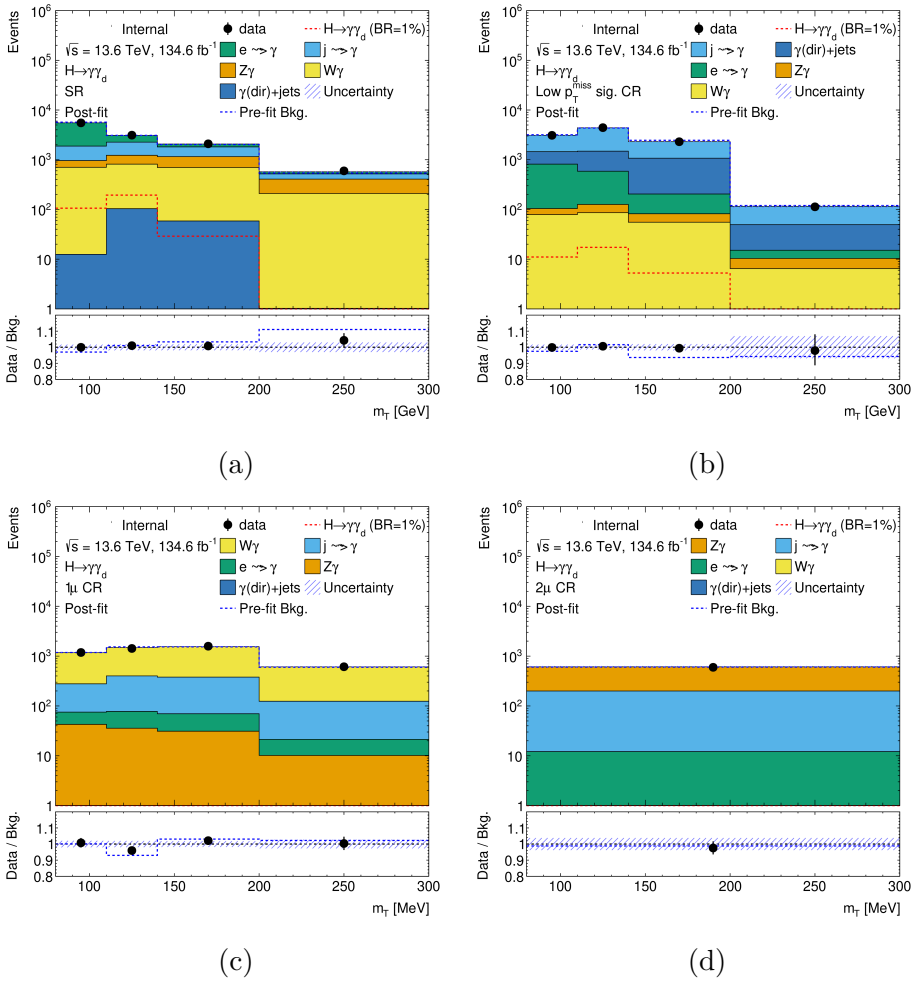


*Figure 89.* Distribution of $m_T$ for data and for the expected SM background after the background-only fit, in the SR (a) and CRs (b), (c), and (d). The $H \to \gamma\gamma_d$ signal with $\mathrm{BR}_{\gamma\gamma_d} = 1\%$ is shown as a dashed red line, including the ggF, VBF, WH and ZH channels. The pre-fit prediction is overlaid as a dashed blue line. The uncertainties include both the statistical and the systematic component determined by the multiple-bin fit. The lower panel shows the ratio of data to expected background event yields post-fit (black dots) and pre-fit (dashed blue line).

Table 21. Data and background yields in the SR and CRs, after the background-only fit. Uncertainties include statistical and systematic components.

| | SR | low $\mathcal{S}_{E_{\mathrm{T}}^{\mathrm{miss}}}$ CR | 1 $\mu$ CR | 2 $\mu$ CR |
|---|---|---|---|---|
| $Z\gamma$ | 1337 ± 93 | 93.8 ± 21 | 120.6 ± 8.8 | 412 ± 25 |
| $W\gamma$ | 2251 ± 69 | 221 ± 57 | 3634 ± 80 | 0.679 ± 0.058 |
| $e \rightsquigarrow \gamma$ | 4808 ± 113 | 1302 ± 43 | 124.5 ± 3.5 | 11.46 ± 0.45 |
| $j \rightsquigarrow \gamma$ | 2727 ± 106 | 5882 ± 150 | 941 ± 37 | 188 ± 10 |
| $\gamma$(direct)+jets | 175.7 ± 3.6 | 2438 ± 62 | 0.0468 ± 0.0010 | $(2.84 \pm 0.08) \times 10^{-6}$ |
| Total | 11299 ± 101 | 9936 ± 98 | 4820 ± 69 | 612 ± 23 |
| Data | 11327 | 9934 | 4802 | 596 |

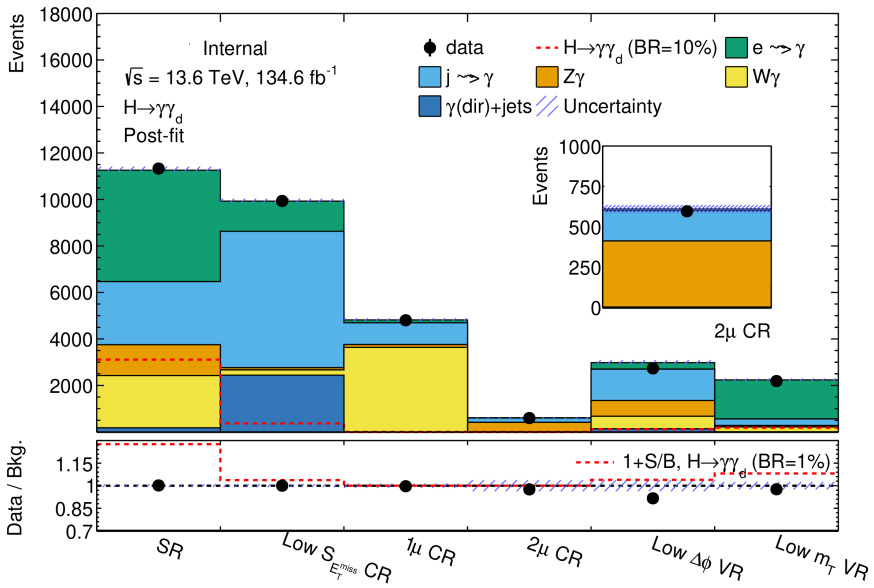


*Figure 90.* Observed data and post-fit background yields in the SR, CRs, and VRs after the background-only fit. The expected signal yields are overlaid assuming $\mathrm{BR}_{\gamma\gamma_d} = 10\%$ for visualisation purposes. The lower panel shows the signal contamination, defined as $1 + S/B$, where $S$ denotes the signal yield with $\mathrm{BR}_{\gamma\gamma_d} = 1\%$ and $B$ the total background yield.

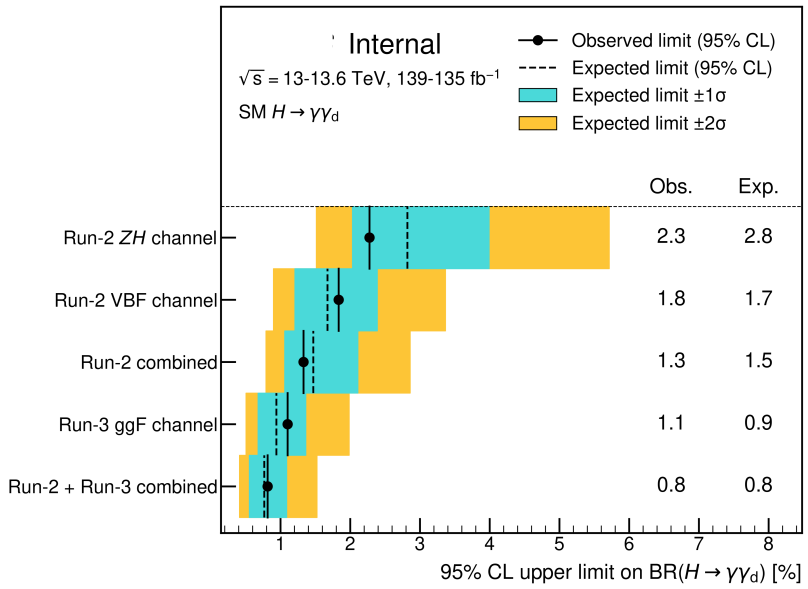


*Figure 91.* Summary of the 95% CL upper limits on $\mathrm{BR}_{\gamma\gamma_d}$, achieved by the Run-2 searches (top three rows: $ZH$ ATLAS Collaboration (2022d), VBF ATLAS Collaboration (2021e), and their combination ATLAS Collaboration (2024)) and by the present analysis (4th row). The overall Run2+Run3 combination is displayed in the bottom row.

the exotic decay $H \to \gamma\gamma_d$ are set using the profile likelihood ratio test statistic and the $\mathrm{CL_s}$ approach Read (2002), in the asymptotic approximation Cowan, Cranmer, Gross, and Vitells (2011a). An observed (expected) upper limit on $\mathrm{BR}_{\gamma\gamma_d}$ of 1.10% ($0.94^{+0.45}_{-0.29}$%) is obtained at 95% CL. This result can be compared with former searches carried out on the VBF ATLAS Collaboration (2021e) and $ZH$ ATLAS Collaboration (2022d) production channels in Run-2, as well as their combination ATLAS Collaboration (2024), as summarised in Figure 91: the present analysis improves the observed (expected) upper limit of 1.3% (1.5%) achieved in the Run-2, thanks to its sensitivity to the ggF production channel. The combination of Run-2 results with the present analysis, yields an observed (expected) upper limit of 0.82% (0.77%) on $\mathrm{BR}_{\gamma\gamma_d}$.

## 6.10 METNet Performance Studies

The following section presents studies of the METNet ML algorithm within the dark photon analysis. Within ATLAS, $E_T^{\text{miss}}$ is reconstructed using various working points. These working points differ in the selection criteria of input jets, such as $p_T$ and JVT tagging requirements. Each analysis selects a WP based on performance in the relevant phase space and pileup rejection. These WPs have a high dependence on event topology, and are not optimal for every event that might enter the signal region. A new NN tool, METNet Hodkinson (2023), has been developed to allow for WP selection on an event-by-event basis.

METNet classifies events based on Equation 6.11, and the outputs are N weights, $\omega_N$, corresponding to the likelihood that each WP is optimal for the event. The weights sum to unity, and are used to build a prediction for $E_T^{\text{miss}}$ as shown in Equation 6.12, summed in quadrature.

$$Class = \text{argmin}_{WP} \left[ (p_x^{miss,WP} - p_x^{miss,true})^2 + (p_y^{miss,WP} - p_y^{miss,true})^2 \right] \tag{6.11}$$

$$p_{x,y}^{miss,METNet} = \sum_{WP} \omega_{WP} p_{x,y}^{miss,WP} \tag{6.12}$$

Performance studies of METNet have been conducted previously and show an increase in performance on a variety of event topologies Hodkinson (2023); Horstmann and Past (2025), such as $t\bar{t}$ and $Z \rightarrow \mu\mu$. The CP task for the dark photon analysis is to validate the latest version of the METNet algorithm and to study the impact on our signal sensitivity. The METNet algorithm has been integrated into the analysis framework, and studies are presented here using four MC samples shown in table 22. A network file specific to Run 3 conditions was provided by the METNet developers.

Table 22. MC samples used for METNet studies.

| Process | Sample Name |
|---|---|
| $ggF \to H \to \gamma\gamma_D$ | mc23_13p6TeV.602402.PhPy8EG_ggH_H125yyd.deriv.DAOD_PHYS.e8537_e8528_s4159_s4114_r15224_r15225_p6320 |
| $\gamma$ + jets (frag) | mc23_13p6TeV.801649.Py8_gammajet_frag_DP8_17_FullSW.deriv.DAOD_PHYS.e8514_e8528_s4159_s4114_r15224_r15225_p6491 |
| | mc23_13p6TeV.801650.Py8_gammajet_frag_DP17_35_FullSW.deriv.DAOD_PHYS.e8514_e8528_s4159_s4114_r15224_r15225_p6491 |
| | mc23_13p6TeV.801651.Py8_gammajet_frag_DP35_50_FullSW.deriv.DAOD_PHYS.e8514_e8528_s4159_s4114_r15224_r15225_p6491 |
| | mc23_13p6TeV.801652.Py8_gammajet_frag_DP50_70_FullSW.deriv.DAOD_PHYS.e8514_e8528_s4159_s4114_r15224_r15225_p6491 |
| | mc23_13p6TeV.801653.Py8_gammajet_frag_DP70_140_FullSW.deriv.DAOD_PHYS.e8514_e8528_s4159_s4114_r15224_r15225_p6491 |
| | mc23_13p6TeV.801654.Py8_gammajet_frag_DP140_280_FullSW.deriv.DAOD_PHYS.e8514_e8528_s4159_s4114_r15224_r15225_p6491 |
| | mc23_13p6TeV.801655.Py8_gammajet_frag_DP280_500_FullSW.deriv.DAOD_PHYS.e8514_e8528_s4159_s4114_r15224_r15225_p6491 |
| | mc23_13p6TeV.801656.Py8_gammajet_frag_DP500_800_FullSW.deriv.DAOD_PHYS.e8514_e8528_s4159_s4114_r15224_r15225_p6491 |
| | mc23_13p6TeV.801657.Py8_gammajet_frag_DP800_1000_FullSW.deriv.DAOD_PHYS.e8514_e8528_s4159_s4114_r15224_r15225_p6491 |
| | mc23_13p6TeV.801658.Py8_gammajet_frag_DP1000_1500_FullSW.deriv.DAOD_PHYS.e8514_e8528_s4159_s4114_r15224_r15225_p6491 |
| | mc23_13p6TeV.801659.Py8_gammajet_frag_DP1500_2000_FullSW.deriv.DAOD_PHYS.e8514_e8528_s4159_s4114_r15224_r15225_p6491 |
| | mc23_13p6TeV.801660.Py8_gammajet_frag_DP2000_inf_FullSW.deriv.DAOD_PHYS.e8514_e8528_s4159_s4114_r15224_r15225_p6491 |
| $Z \to \mu\mu$ + jets | mc23_13p6TeV.700789.Sh_2214_Zmumu_maxHTpTV2_BFilter.deriv.DAOD_PHYS.e8514_e8528_s4159_s4114_r15224_r15225_p6491 |
| | mc23_13p6TeV.700790.Sh_2214_Zmumu_maxHTpTV2_CFilterBVeto.deriv.DAOD_PHYS.e8514_e8528_s4159_s4114_r15224_r15225_p6491 |
| | mc23_13p6TeV.700791.Sh_2214_Zmumu_maxHTpTV2_CVetoBVeto.deriv.DAOD_PHYS.e8514_e8528_s4159_s4114_r15530_r15514_p6491 |
| $Z \to \nu\nu + \gamma$ | mc23_13p6TeV.700776.Sh_2214_nunugamma.deriv.DAOD_PHYS.e8514_e8528_s4159_s4114_r15224_r15225_p6491 |

Besides the dark photon signal sample, three background samples are used for METNet studies: $\gamma$ + jets fragmentation, $Z \to \mu\mu$ + jets, and $Z \to \nu\nu + \gamma$. $Z \to \mu\mu$ + jets was chosen as a cross check for the performance studies conducted in Hodkinson (2023); Horstmann and Past (2025), while $Z \to \nu\nu + \gamma$ provides a true $E_T^{\text{miss}}$ environment. The $\gamma$ + jets fragmentation background enters the SR due to large amount of fake $E_T^{\text{miss}}$ from primary vertex misidentification, making it a useful test of METNet performance in a challenging $E_T^{\text{miss}}$ environment.

The cross check of METNet performance using $Z \to \mu\mu$ + jets is shown in Figure 92 without any analysis selections, with the RMS of the $E_T^{\text{miss}}$ in x and y used as the metric for resolution.

As expected, METNet more closely matches the truth $E_T^{\text{miss}}$ distribution compared to the tight WP. The resolution as a function of $N_{\text{PV}}$ outperforms the tight WP until reaching a high number of vertices. Interestingly, the difference in resolution for events with a bad reconstructed vertex is much larger for METNet

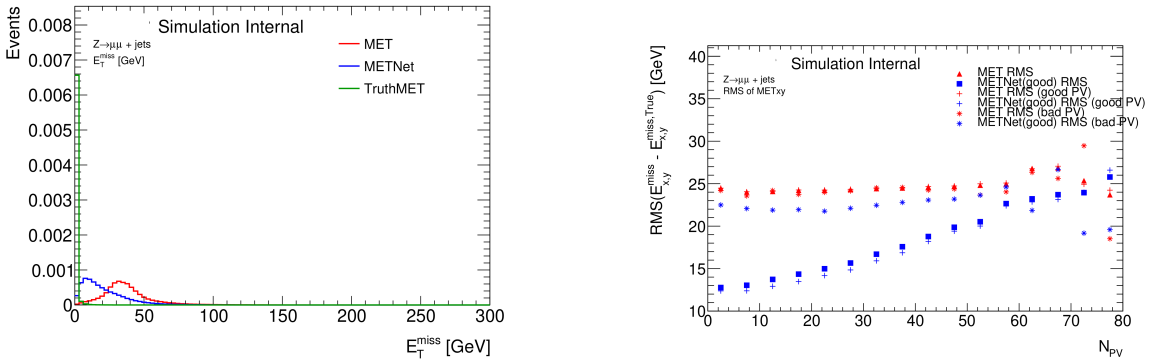


(a) $E_T^{\text{miss}}$ (b) RMS

*Figure 92.* $E_T^{\text{miss}}$ distribution (a) for METNet (blue), the tight WP (red), and truth (green) for $Z \rightarrow \mu\mu$ + jets. The resolution (b) is shown for all events in solid blue rectangles (METNet) and red triangles (tight WP), and plus marks and asterisks for good and bad reconstructed vertices respectively.

compared to the tight WP. This indicates that METNet is sensitive to the correct identification of the primary vertex. Overall, the results agree almost exactly with the previous studies Hodkinson (2023); Horstmann and Past (2025), confirming the proper integration of METNet into the analysis framework.

The $E_T^{\text{miss}}$ distributions for the four samples are shown in Figure 93 with the analysis preselections applied.

The METNet distributions trend slightly lower than the tight WP for all samples, with overall agreement in shape between the two. While this brings METNet marginally more in line with truth for signal and $\gamma$ + jets, it appears to shift slightly lower than truth for $Z \rightarrow \nu\nu + \gamma$. Note that the analysis trigger removes almost all $Z \rightarrow \mu\mu$ + jets events, rendering the sample less useful for comparison. Resolutions with preselections applied are shown in Figure 94.

The resolutions are generally comparable between METNet and the tight WP across all samples except for $Z \rightarrow \nu\nu + \gamma$. As seen before, METNet degrades in performance at high $N_{\text{PV}}$ for this sample, and is outperformed by the tight WP

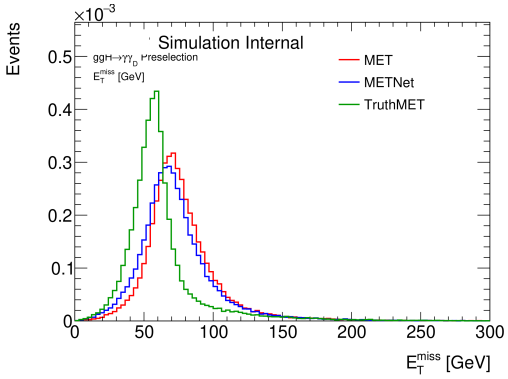


(a) ggF $H \to \gamma\gamma_D$

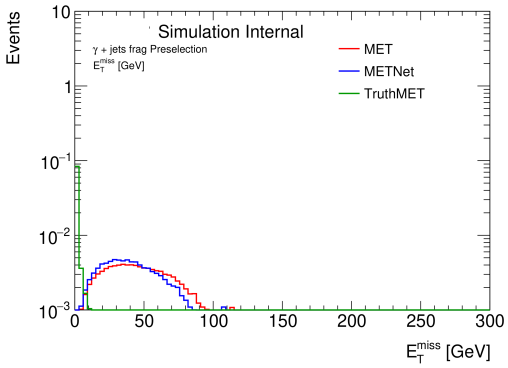


(b) $\gamma$ + jets fragmentation

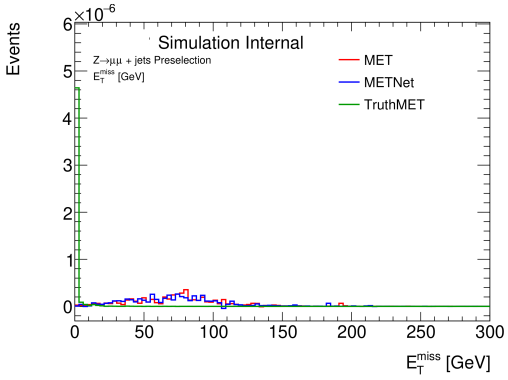


(c) $Z \to \mu\mu$ + jets

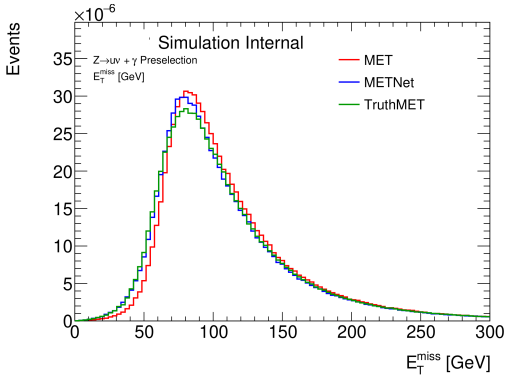


(d) $Z \to \nu\nu + \gamma$

*Figure 93.* $E_T^{\text{miss}}$ distributions for METNet (blue), the tight WP (red), and truth (green) for: (a) ggF $H \to \gamma\gamma_D$, (b) $\gamma$ + jets fragmentation, (c) $Z \to \mu\mu$ + jets, and (d) $Z \to \nu\nu + \gamma$. Analysis preselections applied.

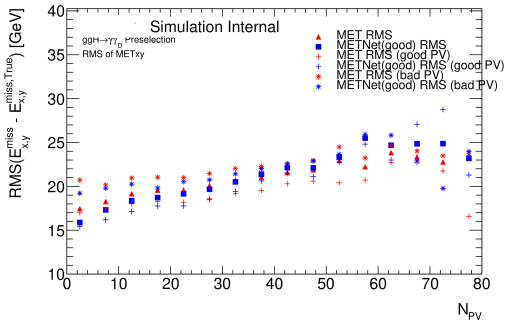


(a) ggF $H \to \gamma\gamma_D$

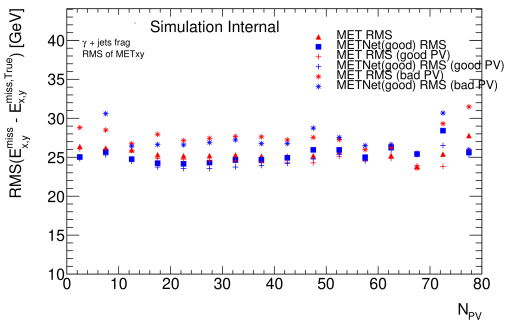


(b) $\gamma$ + jets fragmentation

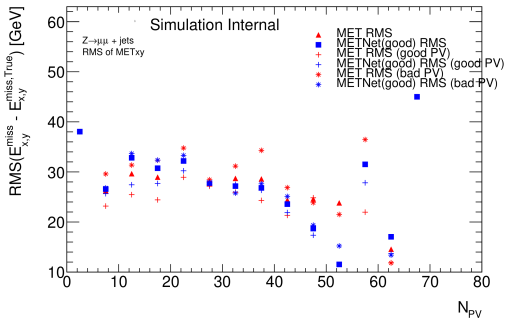


(c) $Z \to \mu\mu$ + jets

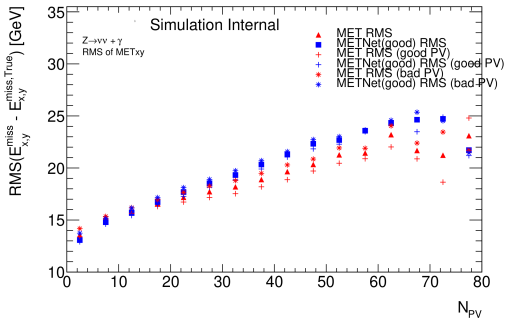


(d) $Z \to \nu\nu + \gamma$

*Figure 94.* Resolution as a function of $N_{\mathrm{PV}}$ for METNet (blue) and the tight WP (red) for: (a) ggF $H \to \gamma\gamma_D$, (b) $\gamma$ + jets fragmentation, (c) $Z \to \mu\mu$ + jets, and (d) $Z \to \nu\nu + \gamma$. Analysis preselections applied.

at an $N_{\mathrm{PV}}$ of 25. This could be due to the tight WP being specifically optimized for a true $E_T^{\mathrm{miss}}$ environment, while METNet may weight the other WPs too heavily for this topology. Most importantly, there is no siginificant increase in resolution for signal events using METNet. Acceptances for signal and the $\gamma$ + jets fragmentation background were calculated in comparison to the 100 GeV cut on $E_T^{\mathrm{miss}}$ used in the analysis. It was found that a 100 GeV cut on METNet achieves the same 1.43% acceptance for signal (1.71x10$^{-4}$% for $\gamma$ + jets fragmentation), giving no gain in efficiency.

In summary, these studies have validated METNet performance on $Z \rightarrow \mu\mu$ + jets events, in agreement with previous studies. When applying analysis preselections, METNet shows comparable performance to the tight WP in $E_T^{\mathrm{miss}}$ resolution across four samples, with some degradation at high pileup for $Z \rightarrow \nu\nu + \gamma$ events. There is no significant improvement in resolution or signal acceptance using METNet compared to the tight WP, and the current recommendation of the tight WP is maintained. However, the dark photon analysis presents a challenging environment for $E_T^{\mathrm{miss}}$ reconstruction due to the high rate of fake $E_T^{\mathrm{miss}}$ from primary vertex misidentification. It is recommended that METNet be trained more extensively on events with low track activity and fake $E_T^{\mathrm{miss}}$, and revisited in the next iteration of the analysis.

### 6.11 Vertex Tagging Efficiency Studies

The physics of the dark photon analysis necessarily creates a challenging environment for vertex tagging. In the ggF production mode, the observable signature is a photon, $E_{\mathrm{T}}^{\mathrm{miss}}$, and less than four initial state radiation jets. This is a low track multiplicitiy environment, and tradition vertex tagging techniques are shown to be not as efficient, as described in section 6.6. Briefly, the vertex

that is selected as the primary vertex is the one with the highest sum of track $p_{\mathrm{T}}$ squared, $\sum p_T^2$. The method is robust and performs well in high track multiplicity environments, but is shown to be less efficient in a low track multiplicity environment, such as the dark photon analysis. In this section, preliminary studies are shown using a neural network classifier approach to improve the vertex tagging efficiency for a future iteration of the dark photon analysis, potentially a full Run 3 search.

**6.11.1 Current vertex tagging performance and motivation.** As stated above, the standard ATLAS hard-scatter vertex selection chooses the vertex with the highest $\sum p_T^2$ of associated tracks as the primary vertex. In Run 3 with a $\langle\mu\rangle$ of 60, there are multiple reconstructed vertices per event, each built from at least two tracks, and a transverse momentum of at least 400 MeV. The final state of the dark photon analysis is a photon + $E_{\mathrm{T}}^{\mathrm{miss}}$, and as a result, the track activity is low. This is mainly due to the absence of charged leptons or jets in the final state. Relying on the standard vertex tagging method can lead to a pile-up vertex, the result of multiple soft scatter interactions, being incorrectly identified as the primary vertex since it may have a higher $\sum p_T^2$ than the actual hard-scatter vertex. This misidentification can lead to a significant inaccuracy in the $E_{\mathrm{T}}^{\mathrm{miss}}$ calculation, as seen in Fig. 95, and can degrade the overall sensitivity of the search for dark photons. When the primary vertex is misidentified, pile-up jets can be incorrectly associated with the hard-scatter vertex, leading to an overestimation of the $E_{\mathrm{T}}^{\mathrm{miss}}$.

How often the primary vertex is misidentified in the dark photon analysis varies, with up to 30 percent of signal events and 90 percent of $\gamma$ + jets background events incorrectly tagged with preselections applied. Misidentification presents

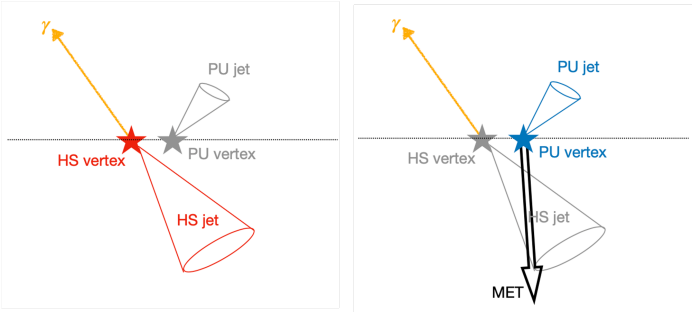


*Figure 95.* Diagram of a hard scatter jet and photon and a pile-up vertex with a jet, with the hard scatter vertex correctly identified as the primary vertex (left) and incorrectly identified as the pile-up vertex (right). The misidentification of the primary vertex leads to a significant miscalculation of the $E_{\mathrm{T}}^{\mathrm{miss}}$.

a gaussian distributed background if the reconstructed z position of the primary vertex is plotted against the true z position of the hard-scatter vertex, as shown in Fig. 96. It appears that either the correct vertex is identified exactly, or a random pile-up vertex is identified, leading to a gaussian distribution around the diagonal line representing perfect vertex tagging.

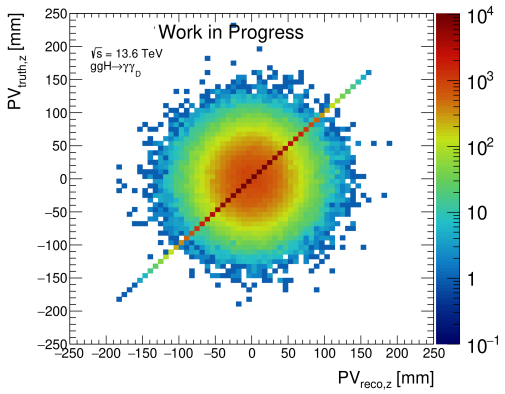


*Figure 96.* The reconstructed z position of the primary vertex plotted against the true z position of the hard-scatter vertex for signal events. The diagonal line represents perfect vertex tagging, while the gaussian distribution around the diagonal line represents misidentification.

With a $E_{\mathrm{T}}^{\mathrm{miss}}$ cut of 100 GeV in the signal region, this leads to a significant amount of background events entering the signal region, seen in Fig. 95, which can

degrade the sensitivity of the analysis. This motivates the need for improved vertex tagging techniques that can better distinguish between the hard-scatter vertex.

### 6.11.2 Preliminary studies with a neural network classifier.

To address the issue of vertex misidentification for the next iteration of the dark photon analysis, preliminary studies have been conducted using a neural network classifier approach. The goal of this approach is to improve the vertex tagging efficiency by training a neural network to distinguish between the hard-scatter vertex and pile-up vertices based on various features of the vertices, while also taking into account the geometic information from the photon showers in the calorimeter. The reconstructed photon showers in the first and second layers of the calorimeter are used in combination with the top three primary vertex candidates ordered in $\sum p_T^2$. A linear fit is then performed using the z and R positions of the photon showers and the z positions of the three primary vertex candidates to extract a $\chi^2$ value as an input to the neural network, also called a "geometric input" to the neural network. This fitting method can be seen in the diagrams in Fig. 97, showing the 2 layers of the EM calorimeter, the photon showers, and the three primary vertex candidates.

#### *6.11.2.1 Neural network architecture and training.*

A supervised binary MLP classifier from scikit-learn is used for this preliminary study, and the features used for training are listed in Table 23. This is a feed-forward network with the task of scoring the three primary vertex candidates, with the highest score being selected as the primary vertex. It is important to note that all features are candidate specific except for the $\Delta E_T^{miss}$ and photon pointing, which are the same for all three candidates in an event.

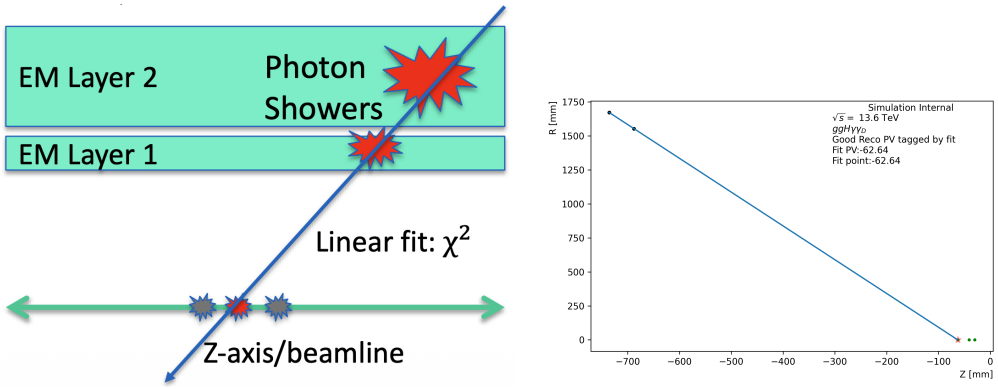


*Figure 97.* Diagram of the linear fit performed using the z and R positions of the photon showers and the z positions of the three primary vertex candidates (left). Actual line of best fit example for a signal event (right). The star is the true vertex, and the $\chi^2$ value from this fit is used as an input to the neural network classifier.

| Feature | Description |
|---|---|
| $log(\sum p_T^2)$ | Logarithm of the sum of the squared transverse momentum of tracks associated with the vertex |
| $N_{\text{tracks}}$ | Number of tracks associated with the vertex |
| $z_{\text{vertex}}$ | z position of the vertex |
| $\gamma$ pointing $= \frac{z_\gamma - z_{\text{vertex}}}{\sigma_{z_\gamma}}$ | Photon pointing variable |
| $\Delta E_T^{miss}$ | Difference between $E_{\text{T}}^{\text{miss}}$ calculation with and without pile-up jets |
| $\chi^2$ | Chi-squared value from the linear fit of photon showers and vertex positions |

Table 23. Features used for training the neural network classifier to improve vertex tagging efficiency.

The architecture of the neural network consists of two hidden layers with 32 and 16 neurons respectively, using the ReLU activation function, and an output layer with a single neuron using the sigmoid activation function for binary classification. Two-class softmax is used as the loss function, and the Adam optimizer is employed for training. The probability for class "True PV" is used as the score for each vertex candidate, and the candidate with the highest score is selected as the primary vertex. Training is done on 30% of the available signal and a $p_T$ slice from 70 GeV to 140 GeV of $\gamma$ + jets background events, with the remaining 70% used for testing and evaluation, with a maximum number of iterations set to 200. The background slice of events are weighted. Two sets of training are performed: one on events without selections, and one with preselections applied as defined in section 6.6, to evaluate the performance of the classifier in both scenarios. At most, there is one positive candidate per event, closest to the true vertex within .5 mm, else all candidates are labeled as negative. As seen in Fig. 98, the photon pointing variable is a powerful discriminator between the hard-scatter vertex and pile-up vertices, as the pointing for incorrectly identified vertices is much broader than the pointing for correctly identified vertices, which is more peaked around zero. The $log(\sum p_T^2)$ and $\chi^2$ variables also provide significant discrimination power as expected.

#### *6.11.2.2 Preliminary results and performance evaluation.*

Predicted probabilities from the neural network classifier are used to select the primary vertex candidate with the highest score, and the performance of the classifier is evaluated on the test set. These probabilities are plotted for candidates split into correctly identified vertices and incorrectly identified vertices, as shown in Fig. 99, for both the training with preselections and without preselections.

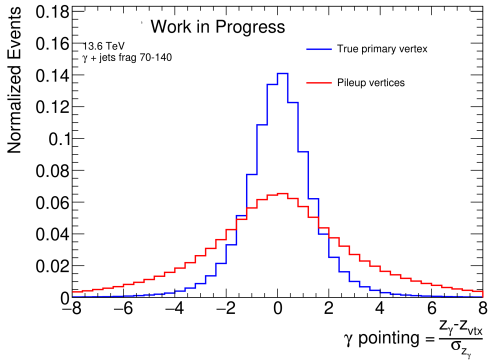


*Figure 98.* Distribution of the photon pointing variable for correctly identified vertices and incorrectly identified vertices in the background slice. The photon pointing variable shows good separation between correctly identified vertices and incorrectly identified vertices, with correctly identified vertices having a more peaked distribution around zero, while incorrectly identified vertices have a broader distribution.

For the $\gamma$ + jets background slice, the classifier shows excellent separation for no preselections, with the majority of true PV candidates having predicted probabilities close to 1. With preselections, the separation is still good, especially compared to the stand reconstruction. In signal events, there is a decent separation between the true PV candidates and pile-up vertices, but there is a large fraction of candidates centered around a probability of 0.2 without preselections. As expected, the preselections clean up the signal events, leading to a grouping of true PV candidates around higher predicted probabilities, while the pile-up vertices are grouped around zero.

The final performance of the classifier is evaluated using a simple accuracy metric, which is the percentage of events where the primary vertex is correctly identified. These percentages are listed in Table 100 for both the training with preselections and without preselections, and compared to the performance of the standard vertex tagging method. With preselections applied, the classifer shows a significant improvement in vertex tagging efficiency, especially in the background

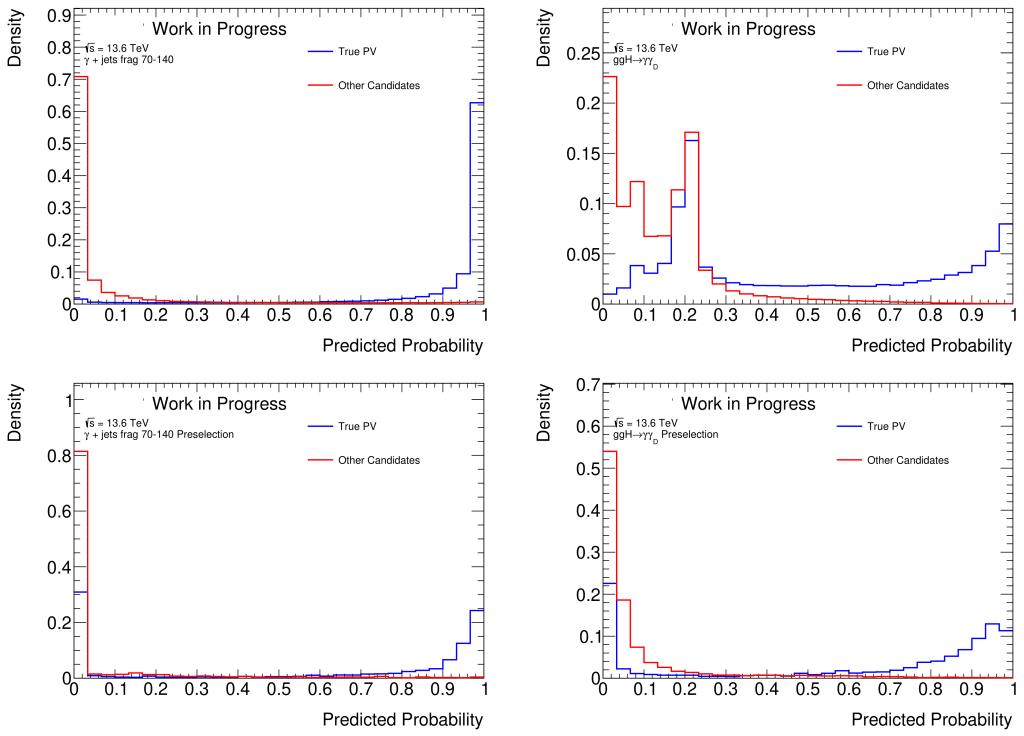


*Figure 99.* Predicted probabilities from the neural network classifier for candidates split into correctly identified vertices and incorrectly identified vertices, for both the training with preselections (bottom) and without preselections (top), and split by background (left) and signal (right). The classifier shows good separation between the true PV candidates and pile-up vertices, especially in the background slice.

slice, where the efficiency increases from 20% to 51%. In signal events, the efficiency also improves from 65% to 72%, which is a significant improvement. For a preliminary study, these results are very promising, especially in the background rejection potential of the classifier.

| | $ggH\gamma\gamma_D$ [%] | | $\gamma$ + jets frag 70-140 GeV [%] | |
|---|---|---|---|---|
| **Selection Applied** | Standard | NN | Standard | NN |
| All events | 44.0 | **48.5** | 71.5 | **80.4** |
| With preselections | 65.1 | **72.3** | 20.1 | **51.2** |

*Figure 100.* Table of the vertex tagging efficiency for the standard vertex tagging method and the neural network classifier, for both the training with preselections and without preselections, and split by background and signal. The neural network classifier shows a significant improvement in vertex tagging efficiency compared to the standard method, especially in the background slice.

The $\Delta z$ between the reconstructed primary vertex and the true vertex is also plotted for both the standard vertex tagging method and the neural network classifier, as shown in Fig. 101, for the training with preselections, and split by background and signal. There is a significant improvement in the $\Delta z$ distribution for the neural network classifier, with a sharper peak around zero for correctly identified vertices, especially in the background slice, indicating that the classifier is more accurately identifying the primary vertex compared to the standard method.

**6.11.3 Future work and conclusions.** While these preliminary results are promising, there is still work to be done to further optimize the neural network classifier and evaluate its performance in a full analysis context. Future work includes exploring different neural network architectures, such as a Boosted Decision Tree (BDT) or a more complex deep learning model, and performing a more detailed evaluation of the classifier's performance in terms of its impact on the overall sensitivity of the dark photon analysis by including more backgrounds.

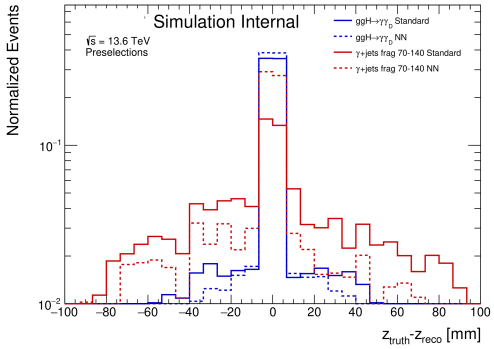


*Figure 101.* The $\Delta z$ between the reconstructed primary vertex and the true vertex for both the standard vertex tagging method (solid) and the neural network classifier (dashed) with preselections applied, and split by background (red) and signal (blue). The neural network classifier shows a significant improvement in the $\Delta z$ distribution, with a sharper peak around zero for correctly identified vertices, especially in the background slice.

Additionally, a more comprehensive metric for performance evaluation would be to run the full particle flow reconstruction and evaluate the $E_{\mathrm{T}}^{\mathrm{miss}}$ resolution and the impact on the signal significance in the analysis. With these preliminary studies, a conservative estimate for the improvement in signal sensitivity for the dark photon analysis with the neural network classifier is around 10%. This is based on the asymptotic scaling of the signal significance with the square root of background reduction over the increase in signal events. In conclusion, these preliminary studies show that a neural network approach to vertex tagging has the potential to significantly improve the vertex tagging efficiency in the dark photon analysis for a full Run 3 search.

# CHAPTER VII

# CONCLUSION

This thesis describes two searches for new physics with the ATLAS detector at the LHC, with the focus of discovering or excluding dark matter signals. The search for dark matter and BSM physics will continue to be a major focus of the ATLAS physics program in the coming years. By setting new and competitive limits on the production of dark mesons and dark photons, the dark sector phase space is further constrained, and the results of these searches will be used to guide future searches for dark sectors at the LHC and beyond.

The dark meson search utilized the full Run 2 dataset of 140 fb$^{-1}$ of $pp$ collisions at $\sqrt{s} = 13$ TeV, collected by the ATLAS experiment, and focused on the all-hadronic and one-lepton final states. Though no excess above the SM was observed in the Run 2 dark meson search, the strongest limits to date are obtained from the one-lepton channel. For SU(2)$_L$ signals with $m_{\pi_D}/m_{\rho_D} = .45$, dark pions with masses below 940 GeV are excluded at 95% CL, while for $m_{\pi_D}/m_{\rho_D} = .25$, the exclusion extends up to 740 GeV. The dark meson results remain the first and most stringent limit on this type of model, extending the exclusion reach significantly compared to previous re-interpretations of LHC searches for similar signatures. A Run 3 analysis has the potential to extend the exclusion reach with a dataset that is over twice as large as the Run 2 dataset. With the large-R jet identification in the gFEX, the all-hadronic channel might be able to use direct triggering on boosted topologies, and lower the large $H_T$ requirement that cut out a siginificant fraction of the signal in the Run 2 analysis. A lower $H_T$ requirement has the potential to increase signal acceptance by up to 30-80% for lower $m_{\pi_D}/m_{\rho_D}$ ratios and lower dark pion masses in SU(2)$_L$ and SU(2)$_R$ models, as seen in Figure

102. With generic multi-jet events being filtered more efficiently, combined with a larger dataset, a revised all-hadronic channel may be able to reach sensitivities comparable to the one-lepton channel. An extrapolation of sensitivity to a dark meson signal point in Run 3 that was not excluded in the all-hadronic channel of Run 2 is shown in Figure 102.

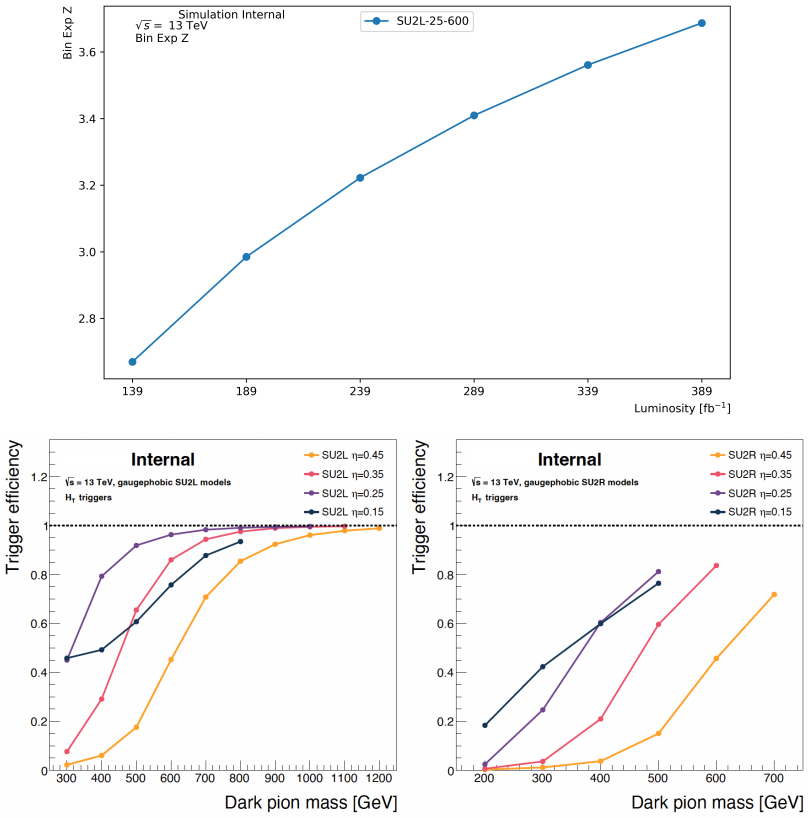


*Figure 102.* Extrapolation search sensitivity for a dark meson signal point with a 600 GeV dark pion in Run 3 that was not excluded in the all-hadronic channel of Run 2 as a function of luminosity (top). A conservative 50% multijet systematic uncertainty is included. $H_T$ trigger efficiencies as a function of dark pion mass and mass ratio $m_{\pi_D}/m_{\rho_D}$ (bottom).

The dark photon search was performed using Run-3 *pp* collision data at $\sqrt{s}$ = 13.6 TeV, collected by the ATLAS experiment in 2023 and 2024, corresponding to an integrated luminosity of 134.6 fb$^{-1}$. For the dark photon

search, the results of the Run 3 analysis represent the most stringent limits on the branching ratio of Higgs to a photon and dark photon to date, with an observed (expected) upper limit of 1.10% (0.94%) at 95% CL, superseding the current best limits of 1.3% (1.5%) from the ATLAS Run-2 combination ATLAS Collaboration (2024). Combining this analysis with the Run-2 results, an observed (expected) upper limit of 0.82% (0.77%) at 95% CL is achieved. The inclusion of the ggF channel, which is an order of magnitude larger production cross section than the VBF and ZH channels, was made possible by the implementation of a new composite trigger that allows lower thresholds on the photon transverse momentum and $E_{\mathrm{T}}^{\mathrm{miss}}$, greatly increasing the acceptance of ggF events. This allowed the search to reach a previously unexplored phase space down to $E_{\mathrm{T}}^{\mathrm{miss}} > 100$ GeV and $p_{\mathrm{T}}^{\gamma} > 50$ GeV. A natural next step for this search is to include the full Run 3 dataset, which is expected to reach an integrated luminosity of around 300 $\mathrm{fb}^{-1}$; more than double the dataset used in this search. While the trained vertex BDT was effective at suppressing events with misidentified primary vertices, the analysis would greatly benefit from improvements in the vertex reconstruction and identification algorithms, which would further reduce the background and increase the sensitivity of the search as discussed in Section 6.11. In addition, a newly optimized signal region combining machine learning techniques with multi-dimensional phase space could further improve the sensitivity of the search, especially in the ggF channel where the kinematics are more challenging.

The HL-LHC will provide an unprecedented amount of data, with an expected integrated luminosity above 3000 $\mathrm{fb}^{-1}$. This will allow for significant improvements in the sensitivity of dark sector searches. In addition, the ATLAS detector will undergo significant upgrades to cope with the increased luminosity

and pile-up conditions. Among the upgrades, the new Global Trigger will allow for offline-like algorithms to be implemented at the L0 Trigger level. The work discussed in Chapter IV on the development of the USCA topological clustering algorithm will allow for significant improvements in object reconstruction, including for jets and taus, at the L0 Trigger level. With efficient and dynamic firmware algorithms within the Global Trigger, as well as the multiple improvements in the detector subsystems, ATLAS will be able to increase the sensitivity of dark sector searches and explore new areas of BSM phase space in the years to come.

# APPENDIX A

## SHELL COUNT STUDIES FOR THE USCA ALGORITHM

Other shell counts for the growth section of the USCA algorithm were considered, between 1 and 5. Preliminary physics studies shown in this section were conducted to narrow down to 2 and 3 shells. As seen in Fig. A.103, 1 shell of growth does not seem to capture enough of the detector response to particles even with the merging stage, leading to lower energy clusters. The cluster multiplicities are higher for the 1-shell clusters, averaging at $\tilde{7}0$ more clusters per event than the 2-shell clusters. The opposite is seen for the 4-shell clusters, there does not seem to be much of a benefit at the cluster energy or multiplicity level by going to a higher shell count. Further studies have shown that most clusters do not reach more than a few shells of $2\sigma$ cells, and the merging stage takes care of the clusters that are physically larger. More evidence of this is seen in the jet $p_T$ distributions shown in Fig. A.105. The distributions are almost identical for the different shell counts. Fixed threshold trigger efficiency curves are shown in Fig. A.106. Again, there is diminishing returns seen for higher shell counts, with the 1-shell algorithm leading to a shallower turn-on curve. These studies led to the conclusion that 1-shell clusters are not ideal since the multiplicities are too high and the performance does not meet the needs of the Global Trigger, and 4-shell clusters are more computational work without a large benefit to performance.

More work with other shell counts could be done to really study the difference, but this is not of the highest priority since the Global Trigger is assumed to have the bandwidth for at least 2-shell clusters. A study of where the USCA algorithm breaks down could also be done, meaning push the shell count very high.

This could be used to see if over-merged clusters are formed, or the creation of large R jets that contain the detector response to multiple particles.

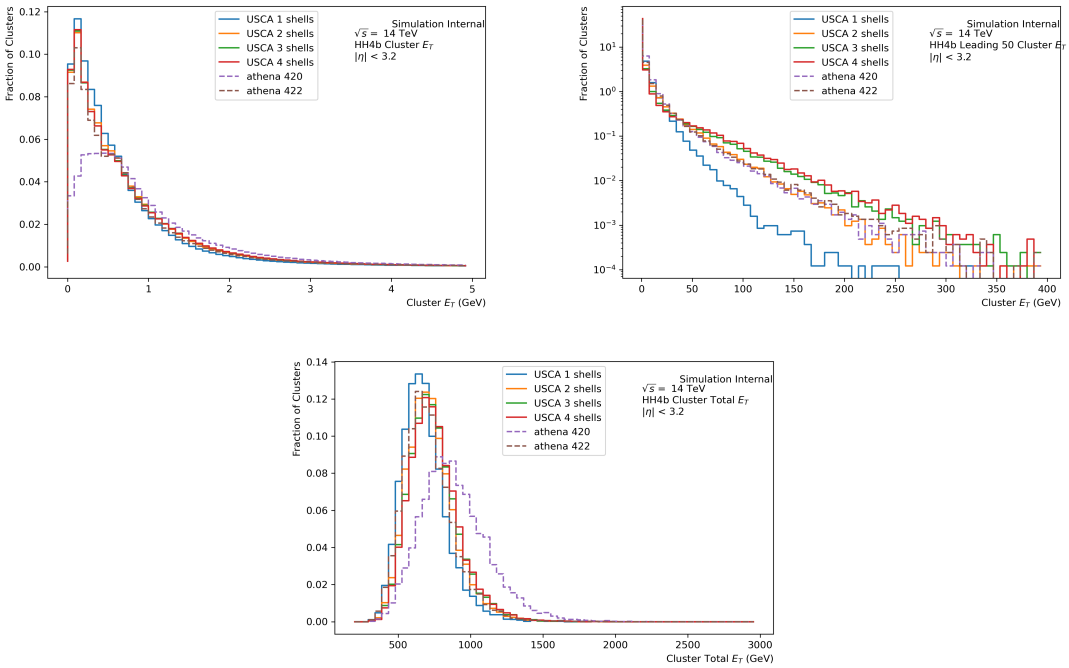


*Figure A.103.* Cluster $E_T$ plots for a HH $\rightarrow$ 4b sample with 1-4 shells used during the algorithm growth stage.

## A.1 Jet $p_T$ 2-D and Ratio Plots

Through the comparisons in this paper, the reconstructed jets from USCA and 422 clusters were concluded to have small differences as expected. More in-depth comparisons between the highest $p_T$ jets are shown in this appendix to reinforce the conclusions. The $p_T$ differences between $\Delta$R matched jets for the leading 6 jets are plotted in Fig. A.107. Jets from the HH $\rightarrow$ 4b sample are more similar between algorithms compared to the background sample. Both clustering algorithms are more likely to contain the detector response to particles if the cells are more closely clustered and at higher $E_T$. In the JZ0 sample plots, the scattering of USCA jets that are higher in $p_T$ than their 422 counterparts is believed to come

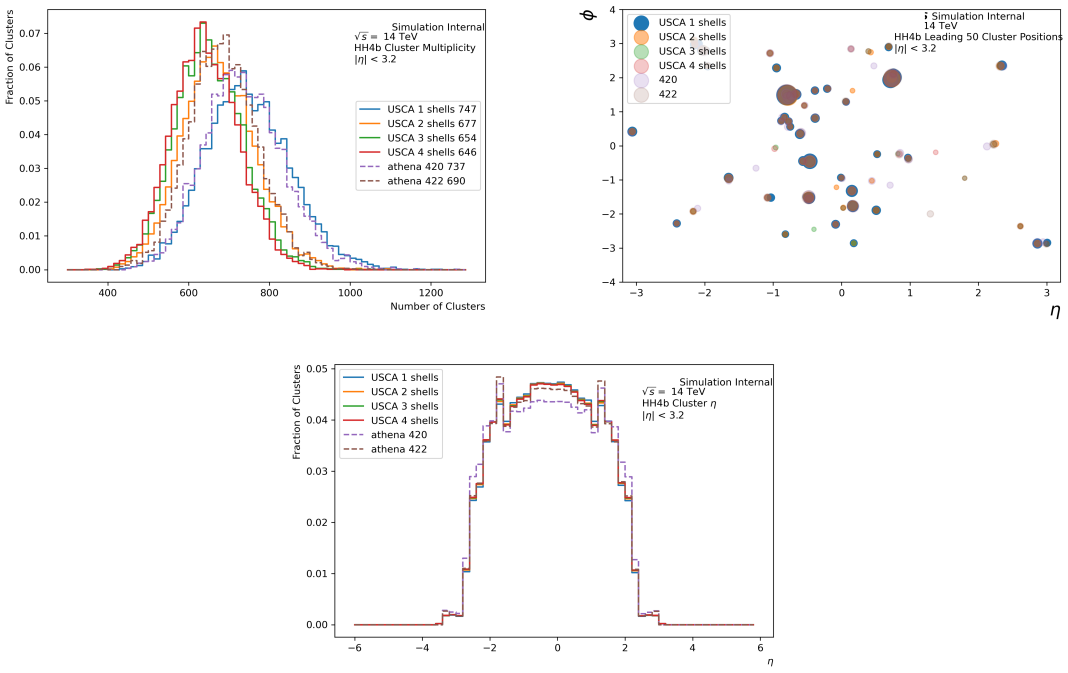


*Figure A.104.* Cluster multiplicities, $\eta$, and positions for a HH $\rightarrow$ 4b sample with 1-4 shells used during the algorithm growth stage.

from the fact that there is no splitting. This leads to more jets that contain too many clustered cells from nearby background QCD jets. Fig. A.108 shows the ratio of USCA leading jet $p_T$ to their matched 422 jets for reference. As expected, the ratio is near 1 for signal events, and centered at 1, but larger in spread for the background events.

A next step for the topoclustering studies is to calculate the jet energy resolution, and calibrate the USCA jets. Plotted in Fig. A.109 are ratio plots, USCA $p_T$/420 $p_T$ vs 420 $p_T$, for the leading jets using the background sample. These are a first step in making the aforementioned calculations. USCA jets will be much lower in $p_T$ compared to their 420 counterparts on average, but there is a clear increase in the ratios for the 3-shell version of the algorithm. For the background sample, jets from USCA clusters tend to be higher in $p_T$, so there is

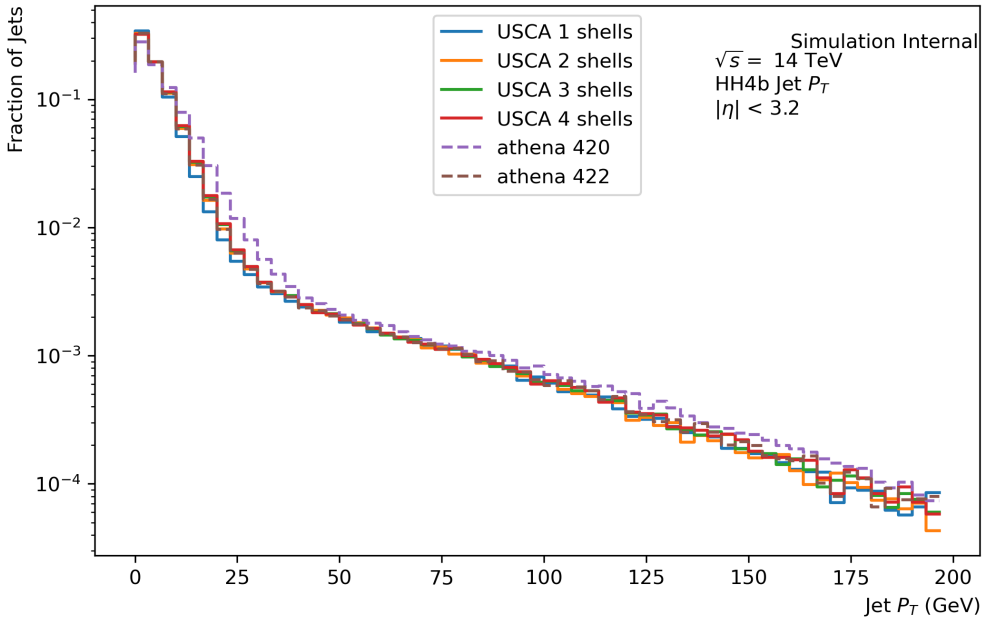


*Figure A.105.* Reconstructed jet $p_T$ for a HH $\rightarrow$ 4b sample with 1-4 shells used during the algorithm growth stage.

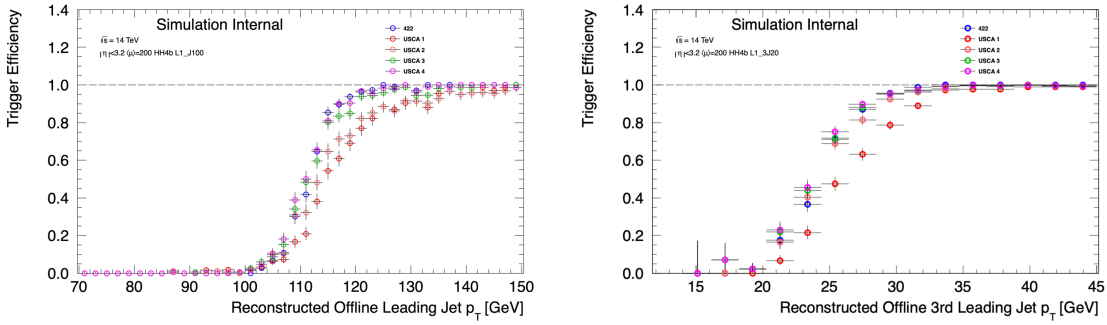


*Figure A.106.* Fixed threshold trigger efficiency curves for leading and 3rd leading jets using a HH $\rightarrow$ 4b sample with 1-4 shells used during the algorithm growth stage.

a large population of USCA jets that are at or above a ratio of 1, especially past 100 GeV, and near 10 GeV. For the jets near 10 GeV, mis-reconstruction may be the main cause of being higher in $p_T$ than the 420 counterparts.

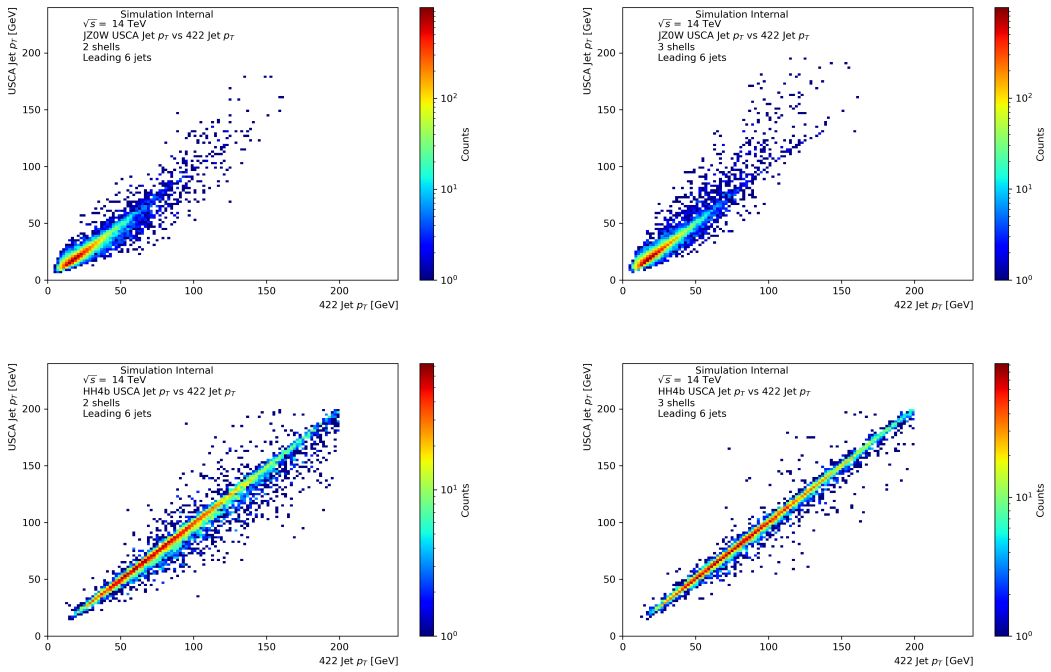


*Figure A.107.* 2-D Comparisons between the leading 6 in $p_T$ reconstructed jets from USCA and 422 clusters for background (top) and HH $\rightarrow$ 4b (bottom). The plots are divided between 2-shell (left) and 3-shell (right) USCA jets.

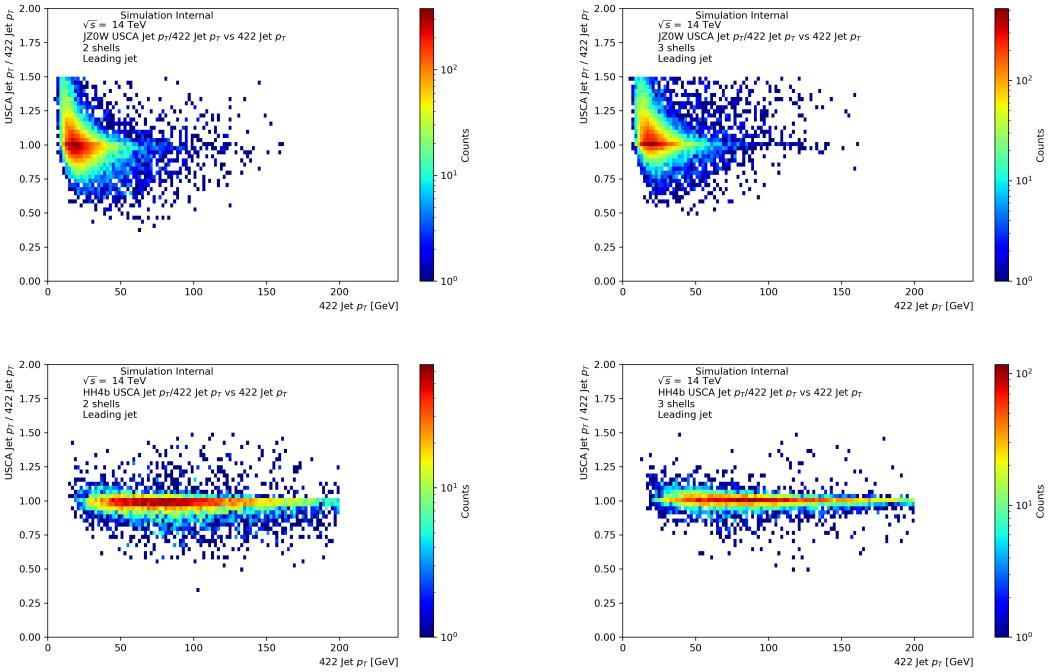


*Figure A.108.* Ratio of USCA jet $p_T$ over 422 jet $p_T$ as a function of 422 jet $p_T$. Background (top) and HH $\rightarrow$ 4b (bottom) samples are shown divided between 2-shell (left) and 3-shell (right) USCA jets.

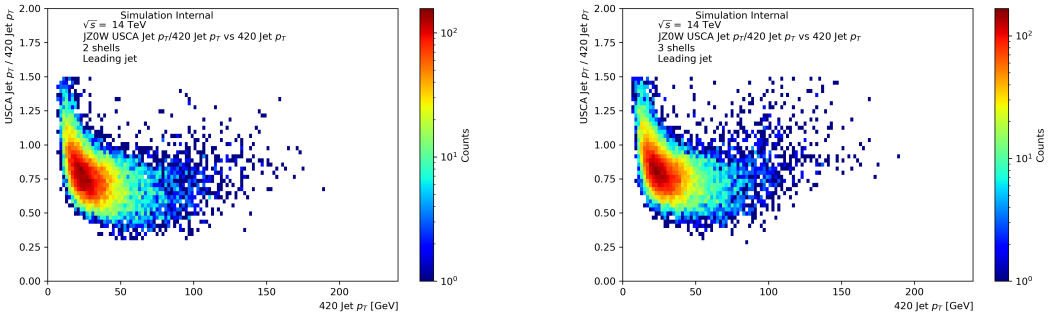


*Figure A.109.* Ratio of USCA jet $p_T$ over 420 jet $p_T$ as a function of 420 jet $p_T$ for a background sample.

# APPENDIX B

# DARK MESON MC SAMPLES

## B.1 List of MC samples

The following tables are automatically generated with values directly extracted from AMI. It can happen that cross sections are missing or that the number of AOD events is zero when an AOD sample has been deleted. For now we do not fix these problems by hand. They do not necessarily indicate a problem with that corresponding sample.

**B.1.1 Signal samples.** All signal samples used for the multi-lepton truth studies are listed in Table B.1.

| DSID | Name of Sample | Tags | TOPQ1 | TOPQ4 | $\sigma \times \epsilon$ [fb] | $N_{\text{events}}$ (AOD) | Int. Lumi [fb$^{-1}$] |
|---|---|---|---|---|---|---|---|
| 313258 | MGPy8EG_A14NNPDF23LO_DarkPions_SU2L_gaugephobic_45_300 | e8005_s3126_r9364 | p4346 | - | 2457.7 | 10000 | 4.1 |
| 313259 | MGPy8EG_A14NNPDF23LO_DarkPions_SU2L_gaugephobic_45_400 | e8005_s3126_r9364 | p4346 | - | 793.89 | 100000 | 126.0 |
| 313260 | MGPy8EG_A14NNPDF23LO_DarkPions_SU2L_gaugephobic_45_500 | e8005_s3126_r9364 | p4346 | - | 312.33 | 10000 | 32.0 |
| 313261 | MGPy8EG_A14NNPDF23LO_DarkPions_SU2L_gaugephobic_45_600 | e8005_s3126_r9364 | p4346 | - | 139.17 | 10000 | 71.9 |
| 313262 | MGPy8EG_A14NNPDF23LO_DarkPions_SU2L_gaugephobic_45_700 | e8005_s3126_r9364 | p4346 | - | 67.297 | 10000 | 148.6 |
| 313263 | MGPy8EG_A14NNPDF23LO_DarkPions_SU2L_gaugephobic_45_800 | e8005_s3126_r9364 | p4346 | - | 34.51 | 10000 | 289.8 |
| 313264 | MGPy8EG_A14NNPDF23LO_DarkPions_SU2L_gaugephobic_45_900 | e8005_s3126_r9364 | p4346 | - | 18.552 | 10000 | 539.0 |
| 313265 | MGPy8EG_A14NNPDF23LO_DarkPions_SU2L_gaugephobic_45_1000 | e8005_s3126_r9364 | p4346 | - | 10.253 | 10000 | 975.3 |
| 313266 | MGPy8EG_A14NNPDF23LO_DarkPions_SU2L_gaugephobic_45_1100 | e8005_s3126_r9364 | p4346 | - | 5.83 | 10000 | 1715.3 |
| 313267 | MGPy8EG_A14NNPDF23LO_DarkPions_SU2L_gaugephobic_45_1200 | e8005_s3126_r9364 | p4346 | - | 3.4008 | 10000 | 2940.5 |
| 313271 | MGPy8EG_A14NNPDF23LO_DarkPions_SU2L_gaugephobic_35_600 | e8005_s3126_r9364 | p4346 | - | 36.863 | 10000 | 271.3 |
| 313272 | MGPy8EG_A14NNPDF23LO_DarkPions_SU2L_gaugephobic_35_700 | e8005_s3126_r9364 | p4346 | - | 16.468 | 10000 | 607.2 |
| 313273 | MGPy8EG_A14NNPDF23LO_DarkPions_SU2L_gaugephobic_35_800 | e8005_s3126_r9364 | p4346 | - | 7.7397 | 10000 | 1292.0 |
| 313274 | MGPy8EG_A14NNPDF23LO_DarkPions_SU2L_gaugephobic_35_900 | e8005_s3126_r9364 | p4346 | - | 3.8212 | 10000 | 2617.0 |
| 313275 | MGPy8EG_A14NNPDF23LO_DarkPions_SU2L_gaugephobic_35_1000 | e8005_s3126_r9364 | p4346 | - | 1.9263 | 10000 | 5191.3 |
| 313276 | MGPy8EG_A14NNPDF23LO_DarkPions_SU2L_gaugephobic_35_1100 | e8005_s3126_r9364 | p4346 | - | 0.99927 | 10000 | 10007.3 |
| 313277 | MGPy8EG_A14NNPDF23LO_DarkPions_SU2L_gaugephobic_25_300 | e8005_s3126_r9364 | p4346 | - | 196.25 | 10000 | 51.0 |
| 313278 | MGPy8EG_A14NNPDF23LO_DarkPions_SU2L_gaugephobic_25_400 | e8005_s3126_r9364 | p4346 | - | 52.148 | 10000 | 191.8 |
| 313279 | MGPy8EG_A14NNPDF23LO_DarkPions_SU2L_gaugephobic_25_500 | e8005_s3126_r9364 | p4346 | - | 16.79 | 9000 | 536.0 |
| 313280 | MGPy8EG_A14NNPDF23LO_DarkPions_SU2L_gaugephobic_25_600 | e8005_s3126_r9364 | p4346 | - | 6.0813 | 10000 | 1644.4 |
| 313281 | MGPy8EG_A14NNPDF23LO_DarkPions_SU2L_gaugephobic_25_700 | e8005_s3126_r9364 | p4346 | - | 2.3695 | 10000 | 4220.3 |
| 313282 | MGPy8EG_A14NNPDF23LO_DarkPions_SU2L_gaugephobic_25_800 | e8005_s3126_r9364 | p4346 | - | 0.97055 | 95000 | 97882.6 |
| 313283 | MGPy8EG_A14NNPDF23LO_DarkPions_SU2L_gaugephobic_25_900 | e8005_s3126_r9364 | p4346 | - | 0.41262 | 10000 | 24235.4 |
| 313284 | MGPy8EG_A14NNPDF23LO_DarkPions_SU2L_gaugephobic_25_1000 | e8005_s3126_r9364 | p4346 | - | 0.1782 | 10000 | 56116.7 |
| 313285 | MGPy8EG_A14NNPDF23LO_DarkPions_SU2L_gaugephobic_15_300 | e8005_s3126_r9364 | p4346 | - | 33.558 | 10000 | 298.0 |
| 313286 | MGPy8EG_A14NNPDF23LO_DarkPions_SU2L_gaugephobic_15_400 | e8005_s3126_r9364 | p4346 | - | 8.502 | 10000 | 1176.2 |
| 313287 | MGPy8EG_A14NNPDF23LO_DarkPions_SU2L_gaugephobic_15_500 | e8005_s3126_r9364 | p4346 | - | 2.7447 | 10000 | 3643.4 |
| 313288 | MGPy8EG_A14NNPDF23LO_DarkPions_SU2L_gaugephobic_15_600 | e8005_s3126_r9364 | p4346 | - | 1.0483 | 10000 | 9539.3 |
| 313289 | MGPy8EG_A14NNPDF23LO_DarkPions_SU2L_gaugephobic_15_700 | e8005_s3126_r9364 | p4346 | - | 0.45058 | 10000 | 22193.6 |
| 313290 | MGPy8EG_A14NNPDF23LO_DarkPions_SU2L_gaugephobic_15_800 | e8005_s3126_r9364 | p4346 | - | 0.21085 | 10000 | 47427.1 |
| 313291 | MGPy8EG_A14NNPDF23LO_DarkPions_SU2R_gaugephobic_45_200 | e8207_s3126_r9364 | p4346 | - | 393.5 | 10000 | 25.4 |
| 313292 | MGPy8EG_A14NNPDF23LO_DarkPions_SU2R_gaugephobic_45_300 | e8207_s3126_r9364 | p4346 | - | 90.212 | 100000 | 1108.5 |
| 313293 | MGPy8EG_A14NNPDF23LO_DarkPions_SU2R_gaugephobic_45_400 | e8207_s3126_r9364 | p4346 | - | 29.39 | 10000 | 340.3 |
| 313294 | MGPy8EG_A14NNPDF23LO_DarkPions_SU2R_gaugephobic_45_500 | e8207_s3126_r9364 | p4346 | - | 11.63 | 10000 | 859.8 |
| 313295 | MGPy8EG_A14NNPDF23LO_DarkPions_SU2R_gaugephobic_45_600 | e8207_s3126_r9364 | p4346 | - | 5.206 | 10000 | 1920.9 |
| 313296 | MGPy8EG_A14NNPDF23LO_DarkPions_SU2R_gaugephobic_45_700 | e8207_s3126_r9364 | p4346 | - | 2.5385 | 10000 | 3939.3 |
| 313297 | MGPy8EG_A14NNPDF23LO_DarkPions_SU2R_gaugephobic_35_200 | e8207_s3126_r9364 | p4346 | - | 148.6 | 9000 | 60.6 |
| 313298 | MGPy8EG_A14NNPDF23LO_DarkPions_SU2R_gaugephobic_35_300 | e8207_s3126_r9364 | p4346 | - | 31.825 | 10000 | 314.2 |
| 313299 | MGPy8EG_A14NNPDF23LO_DarkPions_SU2R_gaugephobic_35_400 | e8207_s3126_r9364 | p4346 | - | 9.707 | 100000 | 10301.8 |
| 313300 | MGPy8EG_A14NNPDF23LO_DarkPions_SU2R_gaugephobic_35_500 | e8207_s3126_r9364 | p4346 | - | 3.6025 | 10000 | 2775.9 |
| 313301 | MGPy8EG_A14NNPDF23LO_DarkPions_SU2R_gaugephobic_35_600 | e8207_s3126_r9364 | p4346 | - | 1.512 | 10000 | 6613.8 |
| 313302 | MGPy8EG_A14NNPDF23LO_DarkPions_SU2R_gaugephobic_25_200 | e8207_s3126_r9364 | p4346 | - | 52.91 | 10000 | 189.0 |
| 313303 | MGPy8EG_A14NNPDF23LO_DarkPions_SU2R_gaugephobic_25_300 | e8207_s3126_r9364 | p4346 | - | 10.575 | 10000 | 945.6 |
| 313304 | MGPy8EG_A14NNPDF23LO_DarkPions_SU2R_gaugephobic_25_400 | e8207_s3126_r9364 | p4346 | - | 3.0065 | 10000 | 3326.1 |
| 313305 | MGPy8EG_A14NNPDF23LO_DarkPions_SU2R_gaugephobic_25_500 | e8207_s3126_r9364 | p4346 | - | 1.0385 | 10000 | 9629.3 |
| 313306 | MGPy8EG_A14NNPDF23LO_DarkPions_SU2R_gaugephobic_15_200 | e8207_s3126_r9364 | p4346 | - | 14.79 | 10000 | 676.1 |
| 313307 | MGPy8EG_A14NNPDF23LO_DarkPions_SU2R_gaugephobic_15_300 | e8207_s3126_r9364 | p4346 | - | 2.698 | 10000 | 3706.4 |
| 313308 | MGPy8EG_A14NNPDF23LO_DarkPions_SU2R_gaugephobic_15_400 | e8207_s3126_r9364 | p4346 | - | 0.7182 | 10000 | 13923.7 |
| 313309 | MGPy8EG_A14NNPDF23LO_DarkPions_SU2R_gaugephobic_15_500 | e8207_s3126_r9364 | p4346 | - | 0.2366 | 10000 | 42265.4 |
| 512607 | MGPy8EG_DarkPions_SU2L_gphobic_20_400 | e8419_s3126_r9364 | p4514 | - | 21.383 | 20000 | 935.3 |
| 512608 | MGPy8EG_DarkPions_SU2L_gphobic_20_500 | e8419_s3126_r9364 | p4514 | - | 6.1667 | 20000 | 3243.2 |
| 512609 | MGPy8EG_DarkPions_SU2L_gphobic_30_500 | e8419_s3126_r9364 | p4514 | - | 50.212 | 20000 | 398.3 |
| 512610 | MGPy8EG_DarkPions_SU2L_gphobic_25_550 | e8419_s3126_r9364 | p4514 | - | 11.127 | 20000 | 1797.4 |
| 512611 | MGPy8EG_DarkPions_SU2L_gphobic_30_550 | e8419_s3126_r9364 | p4514 | - | 30.82 | 20000 | 648.9 |
| 512612 | MGPy8EG_DarkPions_SU2L_gphobic_20_300 | e8419_s3126_r9364 | p4514 | - | 89.139 | 20000 | 224.4 |
| 512613 | MGPy8EG_DarkPions_SU2L_gphobic_20_250 | e8419_s3126_r9364 | p4514 | - | 203.02 | 20000 | 98.5 |
| 512614 | MGPy8EG_DarkPions_SU2L_gphobic_25_250 | e8419_s3126_r9364 | p4514 | - | 493.68 | 20000 | 40.5 |
| 512615 | MGPy8EG_DarkPions_SU2L_gphobic_30_250 | e8419_s3126_r9364 | p4514 | - | 1053.0 | 20000 | 19.0 |
| 512616 | MGPy8EG_DarkPions_SU2L_gphobic_25_200 | e8419_s3126_r9364 | p4514 | - | 1207.8 | 20000 | 16.6 |
| 512617 | MGPy8EG_DarkPions_SU2L_gphobic_35_200 | e8419_s3126_r9364 | p4514 | - | 4488.2 | 20000 | 4.5 |
| 512618 | MGPy8EG_DarkPions_SU2L_gphobic_47_550 | e8419_s3126_r9364 | p4514 | - | 293.82 | 20000 | 68.1 |
| 512619 | MGPy8EG_DarkPions_SU2L_gphobic_47_450 | e8419_s3126_r9364 | p4514 | - | 685.15 | 20000 | 29.2 |
| 512620 | MGPy8EG_DarkPions_SU2L_gphobic_47_500 | e8419_s3126_r9364 | p4514 | - | 442.05 | 20000 | 45.2 |
| 512621 | MGPy8EG_DarkPions_SU2L_gphobic_45_550 | e8419_s3126_r9364 | p4514 | - | 238.98 | 20000 | 83.7 |
| 512622 | MGPy8EG_DarkPions_SU2L_gphobic_40_300 | e8419_s3126_r9364 | p4514 | - | 1692.7 | 120000 | 70.9 |
| 512623 | MGPy8EG_DarkPions_SU2L_gphobic_40_550 | e8419_s3126_r9364 | p4514 | - | 131.73 | 20000 | 151.8 |
| 512624 | MGPy8EG_DarkPions_SU2L_gphobic_45_1300 | e8419_s3126_r9364 | p4514 | - | 2.1705 | 20000 | 9214.5 |
| 510907 | MGPy8EG_DarkPions_SU2L_gphobic_40_400 | e8419_s3126_r9364 | p4514 | - | 533.33 | 100000 | 187.5 |
| 510908 | MGPy8EG_DarkPions_SU2L_gphobic_40_500 | e8419_s3126_r9364 | p4514 | - | 203.39 | 100000 | 491.7 |
| 510909 | MGPy8EG_DarkPions_SU2L_gphobic_35_300 | e8419_s3126_r9364 | p4514 | - | 948.83 | 100000 | 105.4 |
| 510910 | MGPy8EG_DarkPions_SU2L_gphobic_35_350 | e8419_s3126_r9364 | p4514 | - | 504.85 | 100000 | 198.1 |
| 510911 | MGPy8EG_DarkPions_SU2L_gphobic_35_400 | e8419_s3126_r9364 | p4514 | - | 285.63 | 100000 | 350.1 |
| 510912 | MGPy8EG_DarkPions_SU2L_gphobic_35_450 | e8419_s3126_r9364 | p4514 | - | 169.18 | 20000 | 118.2 |
| 510913 | MGPy8EG_DarkPions_SU2L_gphobic_35_500 | e8419_s3126_r9364 | p4514 | - | 103.8 | 99000 | 953.8 |
| 510914 | MGPy8EG_DarkPions_SU2L_gphobic_35_550 | e8419_s3126_r9364 | p4514 | - | 65.512 | 20000 | 305.3 |
| 510915 | MGPy8EG_DarkPions_SU2L_gphobic_30_300 | e8419_s3126_r9364 | p4514 | - | 505.16 | 100000 | 198.0 |
| 510916 | MGPy8EG_DarkPions_SU2L_gphobic_30_350 | e8419_s3126_r9364 | p4514 | - | 263.02 | 20000 | 76.0 |
| 510917 | MGPy8EG_DarkPions_SU2L_gphobic_30_400 | e8419_s3126_r9364 | p4514 | - | 145.4 | 20000 | 137.6 |
| 510918 | MGPy8EG_DarkPions_SU2L_gphobic_20_600 | e8419_s3126_r9364 | p4514 | - | 1.9923 | 20000 | 10038.6 |

Table B.1. List of all used MC16a signal samples with associated TOPQ1 and TOPQ4 derivation tags, cross sections, number of produced events and equivalent integrated luminosity.

APPENDIX C

N-DIMENSIONAL ABCD METHOD FOR THE DARK MESON SEARCH

## C.1 The extended ABCD method

The dominant background for this analysis, mutlijet, is estimated using a data-driven approach to extrapolate from the observed contribution in low signal contamination regions to an estimate in the signal region. This four feature generalization of the ABCD method is similar to multi-jet estimation described in ATLAS Collaboration (2016a), but with tag definitions which select dark pions rather than tops. The top tags are replaced by $\pi_D$ tags and single b-tags by bb-tags.

*Figure C.1.* 4D ABCD estimate region definitions. These labels have been chosen to agree with the notation used in ATLAS Collaboration (2016a). Tag definitions are described in the main body in table 6.

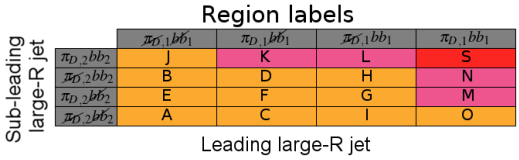


The method can be defined using $N_D$ different features. For $N_D = 2$, define $N_{11}$ as the number of events passing both selections and $N_{ij}$ as the number of events passing some combination of selections and inverse selections specified by 1 or 0 for the $N$ subscripts. We define $f_i$ as the ratio of events passing and not passing selection $i$. We can write

$$f_1 = \frac{N_{10}}{N_{00}} \tag{C.1}$$

$$f_2 = \frac{N_{01}}{N_{00}}. \tag{C.2}$$

In the case of uncorrelated selections,

$$f_1 = \frac{N_{11}}{N_{01}}, \tag{C.3}$$

$$f_2 = \frac{N_{11}}{N_{10}}, \tag{C.4}$$

and

$$N_{10} = f_1 N_{00}, \tag{C.5}$$

$$\hat{N}_{11} = f_2 N_{10}, \tag{C.6}$$

$$= f_2 f_1 N_{00}, \tag{C.7}$$

$$= \frac{N_{10} N_{01}}{N_{00}}. \tag{C.8}$$

Which reproduces the conventional 2D ABCD method (with different notation) for extrapolating into signal region A,

$$\hat{N}_{A^*} = \frac{N_{B^*} N_{C^*}}{N_{D^*}}. \tag{C.9}$$

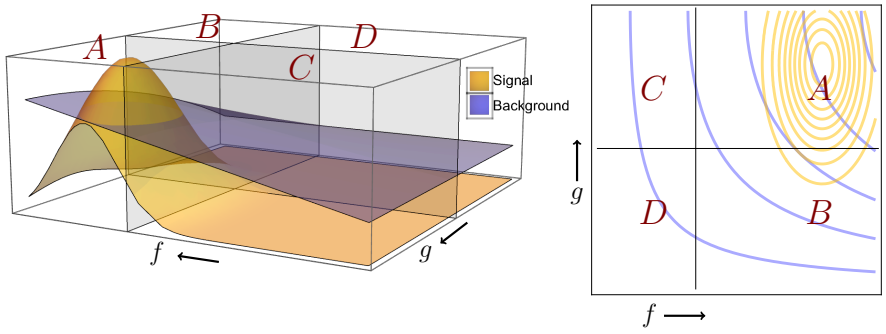


*Figure C.2.* Regions used in a conventional 2D ABCD estimate. Figure taken from Kasieczka et al. (2021). Discriminating variables are f and g in this plot.

The ratio of the estimated region yield $N_{11}$ to the observed yield $\hat{N}_{11}$ is defined as the correlation between these selections,

$$k_{12} = \frac{N_{11}}{\hat{N}_{11}} = \frac{N_{11} N_{00}}{N_{10} N_{01}}. \tag{C.10}$$

In the notation of figure C.1 there are 6 k factors which are each determined by comparing the 2D ABCD estimate of the multijet background to data - MC in the two tag region,

$$k_{\pi_{D,1},\pi_{D,2}} = \frac{FA}{CE}, \tag{C.11}$$

$$k_{\pi_{D,1},bb1} = \frac{OA}{CI}, \tag{C.12}$$

$$k_{\pi_{D,1},bb2} = \frac{DA}{BC}, \tag{C.13}$$

$$k_{\pi_{D,2},bb1} = \frac{GA}{EI}, \tag{C.14}$$

$$k_{\pi_{D,2},bb2} = \frac{JA}{BE}, \tag{C.15}$$

$$k_{bb1,bb2} = \frac{HA}{BI}. \tag{C.16}$$

In the case of three discriminating variables with correlations between pairs of features,

$$f_1 = \frac{N_{100}}{N_{000}}, \tag{C.17}$$

$$f_2 = \frac{N_{010}}{N_{000}}, \tag{C.18}$$

$$f_3 = \frac{N_{001}}{N_{000}}, \tag{C.19}$$

$$k_{12} = \frac{N_{110}}{f_1 f_2 N_{000}}, \tag{C.20}$$

$$k_{13} = \frac{N_{101}}{f_1 f_3 N_{000}}, \tag{C.21}$$

$$k_{23} = \frac{N_{011}}{f_2 f_3 N_{000}}. \tag{C.22}$$

The expectation value of the two tag correlation terms $k_{ij}$ is 1 for the case of uncorrelated variables.

Assuming that the correlation between any two 2-features does not depend on the third feature,

$$\hat{N}_{111} = f_1 f_2 f_3 k_{12} k_{23} k_{13} N_{000}. \tag{C.23}$$

In the notation of figure C.1 there are four 3-tag regions which are estimated using the six k-factors defined in equations C.11-C.16. The four-region validation region estimates are,

$$\hat{K} = \frac{JC}{A} k_{\pi_{D,1},\pi_{D,2}} k_{\pi_{D,1},bb_2}, \tag{C.24}$$

$$\hat{L} = \frac{JI}{A} k_{\pi_{D,2},bb_1} k_{bb_1,bb_2}, \tag{C.25}$$

$$\hat{M} = \frac{OE}{A} k_{\pi_{D,1},\pi_{D,2}} k_{\pi_{D,2},bb_1}, \tag{C.26}$$

$$\hat{N} = \frac{OB}{A} k_{\pi_{D,1},bb_2} k_{bb_1,bb_2}. \tag{C.27}$$

These multijet estimates are used to estimate the SM background in the VRs and define non-closure systematic uncertainties,

$$\sigma_{ABCD} = |1 - k_K k_L k_M k_N|. \tag{C.28}$$

The VR k-factors are estimates of the 3-tag correlations,

$$k_{VR} = \frac{N_{VR}}{\hat{N}_{VR}} \quad , \tag{C.29}$$

where $N$ is the data minus SM MC yield for a region.

Extending to 4 variables and assuming that there are no 4-correlations,

$$\hat{N}_{1111} = f_1 f_2 f_3 f_4 k_{12} k_{13} k_{14} k_{23} k_{24} k_{34} N_{0000}, \tag{C.30}$$

$$= \frac{N_{1000} N_{0100} N_{0010} N_{0001}}{N_{0000}^3} k_{12} k_{13} k_{14} k_{23} k_{24} k_{34}. \tag{C.31}$$

Expressing this relation in the region notation used in this analysis,

$\pi_{D,1}, bb_1, \pi_{D,2}, bb_2 = 1, 2, 3, 4,$

$$\hat{S}'_{\leq 1 \text{ tag}} = \prod_{\text{tags}=1} \frac{N_{(j)}}{N_A^3}, \tag{C.32}$$

$$\hat{S}'_{\leq 1 \text{ tag}} = \frac{N_B N_E N_C N_I}{N_A^3}, \tag{C.33}$$

$$\hat{S} = \hat{S}'_{\leq 1 \text{ tag}} k_{\pi_{D,1}, bb_1} k_{\pi_{D,1}, \pi_{D,2}} k_{\pi_{D,1}, bb_2} k_{\pi_{D,2}, bb_1} k_{bb_1, bb_2} k_{\pi_{D,2}, bb_2}. \tag{C.34}$$

This is the 4-variable 2-correlation corrected ABCD estimate. The statistical uncertainty of this estimate is computed from the uncertainties on data minus SM MC for each 1- and 2-tag regions,

$$\sigma_S^2 = \sum_{\text{1tag,2tag}} \left( \frac{\partial S}{\partial N_i} \right)^2 \sigma_{N_i}^2. \tag{C.35}$$

# APPENDIX D

## DARK PHOTON MC SAMPLES

The MC samples were processed with p-tag p6697.

The signal samples were showered from common Higgs LHE samples generated using Powheg. The decay process implemented as part of the shower was implemented using Pythia. The relevant JIRA tickets can be found at: ATLMCPROD-10733, ATLMCPROD-10819, ATLMCPROD-10916 and the sample validation at: MC23HLRSHyydValidation. The signal sample paths are shown in table D.1.

Table D.1. List of signal MCd samples used in this analysis.

| MC23d |
|---|
| mc23_13p6TeV.602403.PhPy8EG_VBF_H125yyd.deriv.DAOD_PHYS.e8523_e8528_s4159_s4114_r15224_r15225_p6697 |
| mc23_13p6TeV.602913.PhPy8EG_qqZH_H125yyd.deriv.DAOD_PHYS.e8523_e8528_s4159_s4114_r15224_r15225_p6697 |
| mc23_13p6TeV.602914.PhPy8EG_WpH_H125yyd.deriv.DAOD_PHYS.e8523_e8528_s4159_s4114_r15224_r15225_p6697 |
| mc23_13p6TeV.602915.PhPy8EG_WmH_H125yyd.deriv.DAOD_PHYS.e8523_e8528_s4159_s4114_r15224_r15225_p6697 |
| mc23_13p6TeV.602402.PhPy8EG_ggH_H125yyd.deriv.DAOD_PHYS.e8537_e8528_s4159_s4114_r15224_r15225_p6320 |
| MC23e |
| mc23_13p6TeV.602403.PhPy8EG_VBF_H125yyd.deriv.DAOD_PHYS.e8537_e8586_s4369_s4370_r16083_r15970_p6697 |
| mc23_13p6TeV.602913.PhPy8EG_qqZH_H125yyd.deriv.DAOD_PHYS.e8537_e8586_s4369_s4370_r16083_r15970_p6697 |
| mc23_13p6TeV.602914.PhPy8EG_WpH_H125yyd.deriv.DAOD_PHYS.e8537_e8586_s4369_s4370_r16083_r15970_p6697 |
| mc23_13p6TeV.602915.PhPy8EG_WmH_H125yyd.deriv.DAOD_PHYS.e8537_e8586_s4369_s4370_r16083_r15970_p6697 |
| mc23_13p6TeV.602402.PhPy8EG_ggH_H125yyd.deriv.DAOD_PHYS.e8537_e8586_s4369_s4370_r16083_r15970_p6697 |

The primary backgrounds for the analysis include processes with a true photon in the final states and genuine $E_{\mathrm{T}}^{\mathrm{miss}}$. These samples include: $Z\gamma$ and $W\gamma$, where the vector boson can decay to a lepton that is not reconstructed or to neutrinos. Additional background processes originate from a fake photon due to misidentified jets or electrons, and/or fake $E_{\mathrm{T}}^{\mathrm{miss}}$. The background due to jets or electrons misidentified as photons is mainly given by $Zjets$, $Wjets$, di-jets and $\gamma jets$ with fragmentation photon. The $Zjets$, di-jets and $\gamma(frag)jets$ events are also characterized by fake $E_{\mathrm{T}}^{\mathrm{miss}}$ due to mismeaured or not reconstructed

jets. Finally, $\gamma jets$ with direct photon ($\gamma(direct)jets$) enter the analysis regions exclusively due to the presence of fake $E_{\mathrm{T}}^{\mathrm{miss}}$.

The list of MC samples used in this analysis is shown in table D.2 for $\gamma(direct)jets$ and table D.3 for $W\gamma/Z\gamma$, table D.4 for $W/Z$. As detailed later, in section 6.7, MC simulations are eventually employed only for true photon backgrounds (including the $\gamma(direct)jets$), while the contribution from events with fake photons are estimated through data-driven methods. The $W/Z$ MC samples are used as part of the $j \rightsquigarrow \gamma$ method and therefore listed in the following tables, while $\gamma(direct)jets$ and di-jets have been used exclusively for preliminary studies and initial optimization of the analysis selection and are not reported here.

Table D.2. List of $\gamma jets$ MC23d and MC23e samples used in this analysis.

| MC23d |
|---|
| mc23_13p6TeV.801663.Py8_gammajet_direct_DP8_17_FullSW.deriv.DAOD_PHYS.e8514_e8528_s4159_s4114_r15224_r15225_p6697 |
| mc23_13p6TeV.801664.Py8_gammajet_direct_DP17_35_FullSW.deriv.DAOD_PHYS.e8514_e8528_s4159_s4114_r15224_r15225_p6697 |
| mc23_13p6TeV.801665.Py8_gammajet_direct_DP35_50_FullSW.deriv.DAOD_PHYS.e8514_e8528_s4159_s4114_r15224_r15225_p6697 |
| mc23_13p6TeV.801666.Py8_gammajet_direct_DP50_70_FullSW.deriv.DAOD_PHYS.e8514_e8528_s4159_s4114_r15224_r15225_p6697 |
| mc23_13p6TeV.801667.Py8_gammajet_direct_DP70_140_FullSW.deriv.DAOD_PHYS.e8514_e8528_s4159_s4114_r15224_r15225_p6697 |
| mc23_13p6TeV.801668.Py8_gammajet_direct_DP140_280_FullSW.deriv.DAOD_PHYS.e8514_e8528_s4159_s4114_r15224_r15225_p6697 |
| mc23_13p6TeV.801669.Py8_gammajet_direct_DP280_500_FullSW.deriv.DAOD_PHYS.e8514_e8528_s4159_s4114_r15224_r15225_p6697 |
| mc23_13p6TeV.801670.Py8_gammajet_direct_DP500_800_FullSW.deriv.DAOD_PHYS.e8514_e8528_s4159_s4114_r15224_r15225_p6697 |
| mc23_13p6TeV.801671.Py8_gammajet_direct_DP800_1000_FullSW.deriv.DAOD_PHYS.e8514_e8528_s4159_s4114_r15224_r15225_p6697 |
| mc23_13p6TeV.801672.Py8_gammajet_direct_DP1000_1500_FullSW.deriv.DAOD_PHYS.e8514_e8528_s4159_s4114_r15224_r15225_p6697 |
| mc23_13p6TeV.801673.Py8_gammajet_direct_DP1500_2000_FullSW.deriv.DAOD_PHYS.e8514_e8528_s4159_s4114_r15224_r15225_p6697 |
| mc23_13p6TeV.801674.Py8_gammajet_direct_DP2000_2500_FullSW.deriv.DAOD_PHYS.e8514_e8528_s4159_s4114_r15224_r15225_p6697 |
| mc23_13p6TeV.801675.Py8_gammajet_direct_DP2500_3000_FullSW.deriv.DAOD_PHYS.e8514_e8528_s4159_s4114_r15224_r15225_p6697 |
| mc23_13p6TeV.801676.Py8_gammajet_direct_DP3000_inf_FullSW.deriv.DAOD_PHYS.e8514_e8528_s4159_s4114_r15224_r15225_p6697 |
| MC23e |
| mc23_13p6TeV.801663.Py8_gammajet_direct_DP8_17_FullSW.deriv.DAOD_PHYS.e8514_e8528_s4369_s4370_r16083_r15970_p6697 |
| mc23_13p6TeV.801664.Py8_gammajet_direct_DP17_35_FullSW.deriv.DAOD_PHYS.e8514_e8528_s4369_s4370_r16083_r15970_p6697 |
| mc23_13p6TeV.801665.Py8_gammajet_direct_DP35_50_FullSW.deriv.DAOD_PHYS.e8514_e8528_s4369_s4370_r16083_r15970_p6697 |
| mc23_13p6TeV.801666.Py8_gammajet_direct_DP50_70_FullSW.deriv.DAOD_PHYS.e8514_e8528_s4369_s4370_r16083_r15970_p6697 |
| mc23_13p6TeV.801667.Py8_gammajet_direct_DP70_140_FullSW.deriv.DAOD_PHYS.e8514_e8528_s4369_s4370_r16083_r15970_p6697 |
| mc23_13p6TeV.801668.Py8_gammajet_direct_DP140_280_FullSW.deriv.DAOD_PHYS.e8514_e8528_s4369_s4370_r16083_r15970_p6697 |
| mc23_13p6TeV.801669.Py8_gammajet_direct_DP280_500_FullSW.deriv.DAOD_PHYS.e8514_e8528_s4369_s4370_r16083_r15970_p6697 |
| mc23_13p6TeV.801670.Py8_gammajet_direct_DP500_800_FullSW.deriv.DAOD_PHYS.e8514_e8528_s4369_s4370_r16083_r15970_p6697 |
| mc23_13p6TeV.801671.Py8_gammajet_direct_DP800_1000_FullSW.deriv.DAOD_PHYS.e8514_e8528_s4369_s4370_r16083_r15970_p6697 |
| mc23_13p6TeV.801672.Py8_gammajet_direct_DP1000_1500_FullSW.deriv.DAOD_PHYS.e8514_e8528_s4369_s4370_r16083_r15970_p6697 |
| mc23_13p6TeV.801673.Py8_gammajet_direct_DP1500_2000_FullSW.deriv.DAOD_PHYS.e8514_e8528_s4369_s4370_r16083_r15970_p6697 |
| mc23_13p6TeV.801674.Py8_gammajet_direct_DP2000_2500_FullSW.deriv.DAOD_PHYS.e8514_e8528_s4369_s4370_r16083_r15970_p6697 |
| mc23_13p6TeV.801675.Py8_gammajet_direct_DP2500_3000_FullSW.deriv.DAOD_PHYS.e8514_e8528_s4369_s4370_r16083_r15970_p6697 |
| mc23_13p6TeV.801676.Py8_gammajet_direct_DP3000_inf_FullSW.deriv.DAOD_PHYS.e8514_e8528_s4369_s4370_r16083_r15970_p6697 |

Table D.3. List of $W\gamma/Z\gamma$ MC23d and MC23e samples used in this analysis

| MC23d |
|---|
| mc23_13p6TeV.700770.Sh_2214_eegamma.deriv.DAOD_PHYS.e8514_e8528_s4159_s4114_r15224_r15225_p6697 |
| mc23_13p6TeV.700771.Sh_2214_mumugamma.deriv.DAOD_PHYS.e8514_e8528_s4159_s4114_r15224_r15225_p6697 |
| mc23_13p6TeV.700772.Sh_2214_tautaugamma.deriv.DAOD_PHYS.e8514_e8528_s4159_s4114_r15224_r15225_p6697 |
| mc23_13p6TeV.700773.Sh_2214_enugamma.deriv.DAOD_PHYS.e8514_e8528_s4159_s4114_r15224_r15225_p6697 |
| mc23_13p6TeV.700774.Sh_2214_munugamma.deriv.DAOD_PHYS.e8514_e8528_s4159_s4114_r15224_r15225_p6697 |
| mc23_13p6TeV.700775.Sh_2214_taunugamma.deriv.DAOD_PHYS.e8514_e8528_s4159_s4114_r15224_r15225_p6697 |
| mc23_13p6TeV.700776.Sh_2214_nunugamma.deriv.DAOD_PHYS.e8514_e8528_s4159_s4114_r15224_r15225_p6697 |
| MC23e |
| mc23_13p6TeV.700770.Sh_2214_eegamma.deriv.DAOD_PHYS.e8514_e8528_s4369_s4370_r16083_r15970_p6697 |
| mc23_13p6TeV.700771.Sh_2214_mumugamma.deriv.DAOD_PHYS.e8514_e8528_s4369_s4370_r16083_r15970_p6697 |
| mc23_13p6TeV.700772.Sh_2214_tautaugamma.deriv.DAOD_PHYS.e8514_e8528_s4369_s4370_r16083_r15970_p6697 |
| mc23_13p6TeV.700773.Sh_2214_enugamma.deriv.DAOD_PHYS.e8514_e8528_s4369_s4370_r16083_r15970_p6697 |
| mc23_13p6TeV.700774.Sh_2214_munugamma.deriv.DAOD_PHYS.e8514_e8528_s4369_s4370_r16083_r15970_p6697 |
| mc23_13p6TeV.700775.Sh_2214_taunugamma.deriv.DAOD_PHYS.e8514_e8528_s4369_s4370_r16083_r15970_p6697 |
| mc23_13p6TeV.700776.Sh_2214_nunugamma.deriv.DAOD_PHYS.e8514_e8528_s4369_s4370_r16083_r15970_p6697 |

Table D.4. List of $W/Z$ MC23d and MC23e samples used in this analysis.

| MC23d |
|---|
| mc23_13p6TeV.700777.Sh_2214_Wenu_maxHTpTV2_BFilter.deriv.DAOD_PHYS.e8514_e8528_s4159_s4114_r15224_r15225_p6697 |
| mc23_13p6TeV.700778.Sh_2214_Wenu_maxHTpTV2_CFilterBVeto.deriv.DAOD_PHYS.e8514_e8528_s4159_s4114_r15224_r15225_p6697 |
| mc23_13p6TeV.700779.Sh_2214_Wenu_maxHTpTV2_CVetoBVeto.deriv.DAOD_PHYS.e8514_e8528_s4159_s4114_r15530_r15514_p6697 |
| mc23_13p6TeV.700780.Sh_2214_Wmunu_maxHTpTV2_BFilter.deriv.DAOD_PHYS.e8514_e8528_s4159_s4114_r15224_r15225_p6697 |
| mc23_13p6TeV.700781.Sh_2214_Wmunu_maxHTpTV2_CFilterBVeto.deriv.DAOD_PHYS.e8514_e8528_s4159_s4114_r15224_r15225_p6697 |
| mc23_13p6TeV.700782.Sh_2214_Wmunu_maxHTpTV2_CVetoBVeto.deriv.DAOD_PHYS.e8514_e8528_s4159_s4114_r15530_r15514_p6697 |
| mc23_13p6TeV.700783.Sh_2214_Wtaunu_maxHTpTV2_BFilter.deriv.DAOD_PHYS.e8514_e8528_s4159_s4114_r15224_r15225_p6697 |
| mc23_13p6TeV.700784.Sh_2214_Wtaunu_maxHTpTV2_CFilterBVeto.deriv.DAOD_PHYS.e8514_e8528_s4159_s4114_r15224_r15225_p6697 |
| mc23_13p6TeV.700785.Sh_2214_Wtaunu_maxHTpTV2_CVetoBVeto.deriv.DAOD_PHYS.e8514_e8528_s4159_s4114_r15530_r15514_p6697 |
| mc23_13p6TeV.700786.Sh_2214_Zee_maxHTpTV2_BFilter.deriv.DAOD_PHYS.e8514_e8528_s4159_s4114_r15224_r15225_p6697 |
| mc23_13p6TeV.700787.Sh_2214_Zee_maxHTpTV2_CFilterBVeto.deriv.DAOD_PHYS.e8514_e8528_s4159_s4114_r15224_r15225_p6697 |
| mc23_13p6TeV.700788.Sh_2214_Zee_maxHTpTV2_CVetoBVeto.deriv.DAOD_PHYS.e8514_e8528_s4159_s4114_r15530_r15514_p6697 |
| mc23_13p6TeV.700789.Sh_2214_Zmumu_maxHTpTV2_BFilter.deriv.DAOD_PHYS.e8514_e8528_s4159_s4114_r15224_r15225_p6697 |
| mc23_13p6TeV.700790.Sh_2214_Zmumu_maxHTpTV2_CFilterBVeto.deriv.DAOD_PHYS.e8514_e8528_s4159_s4114_r15224_r15225_p6697 |
| mc23_13p6TeV.700791.Sh_2214_Zmumu_maxHTpTV2_CVetoBVeto.deriv.DAOD_PHYS.e8514_e8528_s4159_s4114_r15530_r15514_p6697 |
| mc23_13p6TeV.700792.Sh_2214_Ztautau_maxHTpTV2_BFilter.deriv.DAOD_PHYS.e8514_e8528_s4159_s4114_r15224_r15225_p6697 |
| mc23_13p6TeV.700793.Sh_2214_Ztautau_maxHTpTV2_CFilterBVeto.deriv.DAOD_PHYS.e8514_e8528_s4159_s4114_r15224_r15225_p6697 |
| mc23_13p6TeV.700794.Sh_2214_Ztautau_maxHTpTV2_CVetoBVeto.deriv.DAOD_PHYS.e8514_e8528_s4159_s4114_r15530_r15514_p6697 |
| mc23_13p6TeV.700795.Sh_2214_Znunu_pTV2_BFilter.deriv.DAOD_PHYS.e8514_e8528_s4159_s4114_r15224_r15225_p6697 |
| mc23_13p6TeV.700796.Sh_2214_Znunu_pTV2_CFilterBVeto.deriv.DAOD_PHYS.e8514_e8528_s4159_s4114_r15224_r15225_p6697 |
| mc23_13p6TeV.700797.Sh_2214_Znunu_pTV2_CVetoBVeto.deriv.DAOD_PHYS.e8514_e8528_s4159_s4114_r15530_r15514_p6697 |
| MC23e |
| mc23_13p6TeV.700777.Sh_2214_Wenu_maxHTpTV2_BFilter.deriv.DAOD_PHYS.e8514_e8528_s4369_s4370_r16083_r15970_p6697 |
| mc23_13p6TeV.700778.Sh_2214_Wenu_maxHTpTV2_CFilterBVeto.deriv.DAOD_PHYS.e8514_e8528_s4369_s4370_r16083_r15970_p6697 |
| mc23_13p6TeV.700779.Sh_2214_Wenu_maxHTpTV2_CVetoBVeto.deriv.DAOD_PHYS.e8514_e8528_s4159_s4114_r15530_r15514_p6697 |
| mc23_13p6TeV.700780.Sh_2214_Wmunu_maxHTpTV2_BFilter.deriv.DAOD_PHYS.e8514_e8528_s4369_s4370_r16083_r15970_p6697 |
| mc23_13p6TeV.700781.Sh_2214_Wmunu_maxHTpTV2_CFilterBVeto.deriv.DAOD_PHYS.e8514_e8528_s4369_s4370_r16083_r15970_p6697 |
| mc23_13p6TeV.700782.Sh_2214_Wmunu_maxHTpTV2_CVetoBVeto.deriv.DAOD_PHYS.e8514_e8528_s4159_s4114_r15530_r15514_p6697 |
| mc23_13p6TeV.700783.Sh_2214_Wtaunu_maxHTpTV2_BFilter.deriv.DAOD_PHYS.e8514_e8528_s4369_s4370_r16083_r15970_p6697 |
| mc23_13p6TeV.700784.Sh_2214_Wtaunu_maxHTpTV2_CFilterBVeto.deriv.DAOD_PHYS.e8514_e8528_s4369_s4370_r16083_r15970_p6697 |
| mc23_13p6TeV.700785.Sh_2214_Wtaunu_maxHTpTV2_CVetoBVeto.deriv.DAOD_PHYS.e8514_e8528_s4159_s4114_r15530_r15514_p6697 |
| mc23_13p6TeV.700786.Sh_2214_Zee_maxHTpTV2_BFilter.deriv.DAOD_PHYS.e8514_e8528_s4369_s4370_r16083_r15970_p6697 |
| mc23_13p6TeV.700787.Sh_2214_Zee_maxHTpTV2_CFilterBVeto.deriv.DAOD_PHYS.e8514_e8528_s4369_s4370_r16083_r15970_p6697 |
| mc23_13p6TeV.700788.Sh_2214_Zee_maxHTpTV2_CVetoBVeto.deriv.DAOD_PHYS.e8514_e8528_s4159_s4114_r15530_r15514_p6697 |
| mc23_13p6TeV.700789.Sh_2214_Zmumu_maxHTpTV2_BFilter.deriv.DAOD_PHYS.e8514_e8528_s4369_s4370_r16083_r15970_p6697 |
| mc23_13p6TeV.700790.Sh_2214_Zmumu_maxHTpTV2_CFilterBVeto.deriv.DAOD_PHYS.e8514_e8528_s4369_s4370_r16083_r15970_p6697 |
| mc23_13p6TeV.700791.Sh_2214_Zmumu_maxHTpTV2_CVetoBVeto.deriv.DAOD_PHYS.e8514_e8528_s4159_s4114_r15530_r15514_p6697 |
| mc23_13p6TeV.700792.Sh_2214_Ztautau_maxHTpTV2_BFilter.deriv.DAOD_PHYS.e8514_e8528_s4369_s4370_r16083_r15970_p6697 |
| mc23_13p6TeV.700793.Sh_2214_Ztautau_maxHTpTV2_CFilterBVeto.deriv.DAOD_PHYS.e8514_e8528_s4369_s4370_r16083_r15970_p6697 |
| mc23_13p6TeV.700794.Sh_2214_Ztautau_maxHTpTV2_CVetoBVeto.deriv.DAOD_PHYS.e8514_e8528_s4159_s4114_r15530_r15514_p6697 |
| mc23_13p6TeV.700795.Sh_2214_Znunu_pTV2_BFilter.deriv.DAOD_PHYS.e8514_e8528_s4369_s4370_r16083_r15970_p6697 |
| mc23_13p6TeV.700796.Sh_2214_Znunu_pTV2_CFilterBVeto.deriv.DAOD_PHYS.e8514_e8528_s4369_s4370_r16083_r15970_p6697 |
| mc23_13p6TeV.700797.Sh_2214_Znunu_pTV2_CVetoBVeto.deriv.DAOD_PHYS.e8514_e8528_s4159_s4114_r15530_r15514_p6697 |

REFERENCES CITED


Aaboud, M., Aad, G., Abbott, B., et al. (2016). Measurement of the inelastic proton-proton cross section at $\sqrt{s} = 13$ TeV with the ATLAS detector at the LHC. *Phys. Rev. Lett.*, *117*(18), 182002. doi: 10.1103/PhysRevLett.117.182002

Abbott, B., et al. (2018). Production and integration of the ATLAS Insertable B-Layer. *JINST*, *13*, T05008. doi: 10.1088/1748-0221/13/05/T05008

AC Team. (1999). *https://cds.cern.ch/record/40524.* Retrieved from `https://cds.cern.ch/record/40524`

Alioli, S., Nason, P., Oleari, C., & Re, E. (2009). NLO single-top production matched with shower in POWHEG: $s$- and $t$-channel contributions. *JHEP*, *09*, 111. doi: 10.1088/1126-6708/2009/09/111

Alioli, S., Nason, P., Oleari, C., & Re, E. (2010). A general framework for implementing NLO calculations in shower Monte Carlo programs: the POWHEG BOX. *JHEP*, *06*, 043. doi: 10.1007/JHEP06(2010)043

Alwall, J., Frederix, R., Frixione, S., Hirschi, V., Maltoni, F., Mattelaer, O., ... Zaro, M. (2014). The automated computation of tree-level and next-to-leading order differential cross sections, and their matching to parton shower simulations. *JHEP*, *07*, 079. doi: 10.1007/JHEP07(2014)079

Anastasiou, C., Dixon, L., Melnikov, K., & Petriello, F. (2004). High-precision QCD at hadron colliders: Electroweak gauge boson rapidity distributions at next-to-next-to leading order. *Phys. Rev. D*, *69*, 094008. doi: 10.1103/PhysRevD.69.094008

Artoisenet, P., Frederix, R., Mattelaer, O., & Rietkerk, R. (2013). Automatic spin-entangled decays of heavy resonances in Monte Carlo simulations. *JHEP*, *03*, 015. doi: 10.1007/JHEP03(2013)015

ATLAS Collaboration. (1996a). *ATLAS Liquid Argon Calorimeter: Technical Design Report* (ATLAS-TDR-2; CERN-LHCC-96-041). Retrieved from `https://cds.cern.ch/record/331061`

ATLAS Collaboration. (1996b). *ATLAS Tile Calorimeter: Technical Design Report* (ATLAS-TDR-3; CERN-LHCC-96-042). Retrieved from `https://cds.cern.ch/record/331062`

ATLAS Collaboration. (1997a). *ATLAS Inner Detector: Technical Design Report, Volume 1* (ATLAS-TDR-4; CERN-LHCC-97-016). Retrieved from https://cds.cern.ch/record/331063

ATLAS Collaboration. (1997b). *ATLAS Muon Spectrometer: Technical Design Report* (ATLAS-TDR-10; CERN-LHCC-97-022). CERN. Retrieved from https://cds.cern.ch/record/331068

ATLAS Collaboration. (1998). *ATLAS Pixel Detector: Technical Design Report* (ATLAS-TDR-11; CERN-LHCC-98-013). Retrieved from https://cds.cern.ch/record/381263

ATLAS Collaboration. (2008). The ATLAS Experiment at the CERN Large Hadron Collider. *JINST*, *3*, S08003. doi: 10.1088/1748-0221/3/08/S08003

ATLAS Collaboration. (2010a). *ATLAS Insertable B-Layer: Technical Design Report* (ATLAS-TDR-19; CERN-LHCC-2010-013). Retrieved from https://cds.cern.ch/record/1291633

ATLAS Collaboration. (2010b). The ATLAS Simulation Infrastructure. *Eur. Phys. J. C*, *70*, 823. doi: 10.1140/epjc/s10052-010-1429-9

ATLAS Collaboration. (2010c). Drift Time Measurement in the ATLAS Liquid Argon Electromagnetic Calorimeter using Cosmic Muons. *Eur. Phys. J. C*, *70*, 755. doi: 10.1140/epjc/s10052-010-1403-6

ATLAS Collaboration. (2010d). Readiness of the ATLAS Tile Calorimeter for LHC collisions. *Eur. Phys. J. C*, *70*, 1193. doi: 10.1140/epjc/s10052-010-1508-y

ATLAS Collaboration. (2012a). Observation of a new particle in the search for the Standard Model Higgs boson with the ATLAS detector at the LHC. *Phys. Lett. B*, *716*, 1. doi: 10.1016/j.physletb.2012.08.020

ATLAS Collaboration. (2012b). *Selection of jets produced in proton–proton collisions with the ATLAS detector using 2011 data.* ATLAS-CONF-2012-020. Retrieved from https://cds.cern.ch/record/1430034

ATLAS Collaboration. (2013a). *ATLAS Liquid Argon Calorimeter Phase-I Upgrade: Technical Design Report* (ATLAS-TDR-022; CERN-LHCC-2013-017). Retrieved from https://cds.cern.ch/record/1602230

ATLAS Collaboration. (2013b). *ATLAS New Small Wheel: Technical Design Report* (ATLAS-TDR-020; CERN-LHCC-2013-006). Retrieved from https://cds.cern.ch/record/1552862

ATLAS Collaboration. (2013c). Characterisation and mitigation of beam-induced backgrounds observed in the ATLAS detector during the 2011 proton–proton run. *JINST*, *8*, P07004. doi: 10.1088/1748-0221/8/07/P07004

ATLAS Collaboration. (2013). *Performance of the atlas liquid argon calorimeter after three years of lhc operation and plans for a future upgrade.* Retrieved from `https://arxiv.org/abs/1306.6756`

ATLAS Collaboration. (2014a). *ATLAS Pythia 8 tunes to* 7 *TeV data.* ATL-PHYS-PUB-2014-021. Retrieved from `https://cds.cern.ch/record/1966419`

ATLAS Collaboration. (2014b). Electron reconstruction and identification efficiency measurements with the ATLAS detector using the 2011 LHC proton–proton collision data. *Eur. Phys. J. C*, *74*, 2941. doi: 10.1140/epjc/s10052-014-2941-0

ATLAS Collaboration. (2014c). Operation and performance of the ATLAS semiconductor tracker. *JINST*, *9*, P08009. doi: 10.1088/1748-0221/9/08/P08009

ATLAS Collaboration. (2015a). *Selection of jets produced in* 13 *TeV proton–proton collisions with the ATLAS detector.* ATLAS-CONF-2015-029. Retrieved from `https://cds.cern.ch/record/2037702`

ATLAS Collaboration. (2015b). *Vertex Reconstruction Performance of the ATLAS Detector at* $\sqrt{s} = 13$ *TeV.* ATL-PHYS-PUB-2015-026. Retrieved from `https://cds.cern.ch/record/2037717`

ATLAS Collaboration. (2016a). *ATL-COM-PHYS-2016-1696.* ATLAS internal note.

ATLAS Collaboration. (2016b). Measurement of the photon identification efficiencies with the ATLAS detector using LHC Run-1 data. *Eur. Phys. J. C*, *76*, 666. doi: 10.1140/epjc/s10052-016-4507-9

ATLAS Collaboration. (2016c). Measurements of top-quark pair differential cross-sections in the lepton+jets channel in $pp$ collisions at $\sqrt{s} = 8\,\text{TeV}$ using the ATLAS detector. *Eur. Phys. J. C*, *76*, 538. doi: 10.1140/epjc/s10052-016-4366-4

ATLAS Collaboration. (2016d). Muon reconstruction performance of the ATLAS detector in proton–proton collision data at $\sqrt{s} = 13\,\text{TeV}$. *Eur. Phys. J. C*, *76*, 292. doi: 10.1140/epjc/s10052-016-4120-y

ATLAS Collaboration. (2016e). Performance of pile-up mitigation techniques for jets in $pp$ collisions at $\sqrt{s} = 8\,\text{TeV}$ using the ATLAS detector. *Eur. Phys. J. C*, *76*, 581. doi: 10.1140/epjc/s10052-016-4395-z

ATLAS Collaboration. (2016f). The performance of the jet trigger for the ATLAS detector during 2011 data taking. *Eur. Phys. J. C*, *76*, 526. doi: 10.1140/epjc/s10052-016-4325-0

ATLAS Collaboration. (2016g). *The Pythia 8 A3 tune description of ATLAS minimum bias and inelastic measurements incorporating the Donnachie–Landshoff diffractive model.* ATL-PHYS-PUB-2016-017. Retrieved from `https://cds.cern.ch/record/2206965`

ATLAS Collaboration. (2016h). *Studies on top-quark Monte Carlo modelling for Top2016.* ATL-PHYS-PUB-2016-020. Retrieved from `https://cds.cern.ch/record/2216168`

ATLAS Collaboration. (2017a). *ATLAS Inner Tracker Strip Detector: Technical Design Report* (ATLAS-TDR-025; CERN-LHCC-2017-005). Retrieved from `https://cds.cern.ch/record/2257755`

ATLAS Collaboration. (2017b). *ATLAS LAr Calorimeter Phase-II Upgrade: Technical Design Report* (ATLAS-TDR-027; CERN-LHCC-2017-018). Retrieved from `https://cds.cern.ch/record/2285582`

ATLAS Collaboration. (2017c). *ATLAS TDAQ Phase-II Upgrade: Technical Design Report* (ATLAS-TDR-029; CERN-LHCC-2017-020). Retrieved from `https://cds.cern.ch/record/2285584`

ATLAS Collaboration. (2017d). *ATLAS Tile Calorimeter Phase-II Upgrade: Technical Design Report* (ATLAS-TDR-028; CERN-LHCC-2017-019). Retrieved from `https://cds.cern.ch/record/2285583`

ATLAS Collaboration. (2017e). Identification and rejection of pile-up jets at high pseudorapidity with the ATLAS detector. *Eur. Phys. J. C*, *77*, 580. doi: 10.1140/epjc/s10052-017-5081-5

ATLAS Collaboration. (2017f). Jet reconstruction and performance using particle flow with the ATLAS Detector. *Eur. Phys. J. C*, *77*, 466. doi: 10.1140/epjc/s10052-017-5031-2

ATLAS Collaboration. (2017g). *Optimisation and performance studies of the ATLAS b-tagging algorithms for the 2017-18 LHC run.* ATL-PHYS-PUB-2017-013. Retrieved from `https://cds.cern.ch/record/2273281`

ATLAS Collaboration. (2017h). Performance of the ATLAS trigger system in 2015. *Eur. Phys. J. C*, *77*, 317. doi: 10.1140/epjc/s10052-017-4852-3

ATLAS Collaboration. (2017i). Search for new high-mass phenomena in the dilepton final state using $36\,\mathrm{fb}^{-1}$ of proton–proton collision data at $\sqrt{s} = 13\,\mathrm{TeV}$ with the ATLAS detector. *JHEP*, *10*, 182. doi: 10.1007/JHEP10(2017)182

ATLAS Collaboration. (2017j). Topological cell clustering in the ATLAS calorimeters and its performance in LHC Run 1. *Eur. Phys. J. C*, *77*, 490. doi: 10.1140/epjc/s10052-017-5004-5

ATLAS Collaboration. (2018). Measurements of $t\bar{t}$ differential cross-sections of highly boosted top quarks decaying to all-hadronic final states in $pp$ collisions at $\sqrt{s} = 13\,\mathrm{TeV}$ using the ATLAS detector. *Phys. Rev. D*, *98*, 012003. doi: 10.1103/PhysRevD.98.012003

ATLAS Collaboration. (2019a). ATLAS $b$-jet identification performance and efficiency measurement with $t\bar{t}$ events in $pp$ collisions at $\sqrt{s} = 13\,\mathrm{TeV}$. *Eur. Phys. J. C*, *79*, 970. doi: 10.1140/epjc/s10052-019-7450-8

ATLAS Collaboration. (2019b). *ATLAS FTAG note FTAG-2019-02.* ATLAS internal/public note.

ATLAS Collaboration. (2019c). Electron and photon energy calibration with the ATLAS detector using 2015–2016 LHC proton–proton collision data. *JINST*, *14*, P03017. doi: 10.1088/1748-0221/14/03/P03017

ATLAS Collaboration. (2019d). Electron and photon performance measurements with the ATLAS detector using the 2015–2017 LHC proton–proton collision data. *JINST*, *14*, P12006. doi: 10.1088/1748-0221/14/12/P12006

ATLAS Collaboration. (2019e). Electron reconstruction and identification in the ATLAS experiment using the 2015 and 2016 LHC proton–proton collision data at $\sqrt{s} = 13\,\mathrm{TeV}$. *Eur. Phys. J. C*, *79*, 639. doi: 10.1140/epjc/s10052-019-7140-6

ATLAS Collaboration. (2019f). *Identification of hadronic tau lepton decays using neural networks in the ATLAS experiment.* ATL-PHYS-PUB-2019-033. Retrieved from `https://cds.cern.ch/record/2688062`

ATLAS Collaboration. (2019g). Measurement of the photon identification efficiencies with the ATLAS detector using LHC Run 2 data collected in 2015 and 2016. *Eur. Phys. J. C*, *79*, 205. doi: 10.1140/epjc/s10052-019-6650-6

ATLAS Collaboration. (2019h). Measurements of inclusive and differential fiducial cross-sections of $t\bar{t}$ production with additional heavy-flavour jets in proton–proton collisions at $\sqrt{s} = 13\,\text{TeV}$ with the ATLAS detector. *JHEP*, *04*, 046. doi: 10.1007/JHEP04(2019)046

ATLAS Collaboration. (2020a). *A High-Granularity Timing Detector for the ATLAS Phase-II Upgrade: Technical Design Report* (ATLAS-TDR-031; CERN-LHCC-2020-007). Retrieved from `https://cds.cern.ch/record/2719855`

ATLAS Collaboration. (2020b). Jet energy scale and resolution measured in proton–proton collisions at $\sqrt{s} = 13\,\text{TeV}$ with the ATLAS detector. *Eur. Phys. J. C*, *81*, 689. doi: 10.1140/epjc/s10052-021-09402-3

ATLAS Collaboration. (2020c). *JETM-2020-03.* ATLAS jet/met performance note.

ATLAS Collaboration. (2020d). Operation of the ATLAS trigger system in Run 2. *JINST*, *15*, P10004. doi: 10.1088/1748-0221/15/10/P10004

ATLAS Collaboration. (2020e). Performance of electron and photon triggers in ATLAS during LHC Run 2. *Eur. Phys. J. C*, *80*, 47. doi: 10.1140/epjc/s10052-019-7500-2

ATLAS Collaboration. (2020f). Performance of the ATLAS muon triggers in Run 2. *JINST*, *15*, P09015. doi: 10.1088/1748-0221/15/09/p09015

ATLAS Collaboration. (2020g). Performance of the missing transverse momentum triggers for the ATLAS detector during Run-2 data taking. *JHEP*, *08*, 080. doi: 10.1007/JHEP08(2020)080

ATLAS Collaboration. (2021a). The ATLAS Inner Detector Trigger performance in *pp* collisions at 13 TeV during LHC Run 2. *Eur. Phys. J. C*, *82*, 206. doi: 10.1140/epjc/s10052-021-09920-0

ATLAS Collaboration. (2021b). Emulating the impact of additional proton–proton interactions in the ATLAS simulation by pre-sampling sets of inelastic Monte Carlo events. *Comput. Softw. Big Sci.*, *6*, 3. doi: 10.1007/s41781-021-00062-2

ATLAS Collaboration. (2021c). Measurement of the $c$-jet mistagging efficiency in $t\bar{t}$ events using $pp$ collision data at $\sqrt{s} = 13\,\text{TeV}$ collected with the ATLAS detector. *Eur. Phys. J. C*, *82*, 95. doi: 10.1140/epjc/s10052-021-09843-w

ATLAS Collaboration. (2021d). Muon reconstruction and identification efficiency in ATLAS using the full Run 2 $pp$ collision data set at $\sqrt{s} = 13\,\text{TeV}$. *Eur. Phys. J. C*, *81*, 578. doi: 10.1140/epjc/s10052-021-09233-2

ATLAS Collaboration. (2021e). Observation of electroweak production of two jets in association with an isolated photon and missing transverse momentum, and search for a Higgs boson decaying into invisible particles at 13 TeV with the ATLAS detector. *Eur. Phys. J. C*, *82*, 105. doi: 10.1140/epjc/s10052-021-09878-z

ATLAS Collaboration. (2021f). *Simulation-based extrapolation of b-tagging calibrations towards high transverse momenta in the ATLAS experiment.* ATL-PHYS-PUB-2021-003. Retrieved from `https://cds.cern.ch/record/2753444`

ATLAS Collaboration. (2022a). *ATLAS EXOT note EXOT-2022-14.* ATLAS internal/public note.

ATLAS Collaboration. (2022b). *ATLAS flavour-tagging algorithms for the LHC Run 2 pp collision dataset.*

ATLAS Collaboration. (2022c). *Luminosity determination in pp collisions at* $\sqrt{s} = 13$ *TeV using the ATLAS detector at the LHC.*

ATLAS Collaboration. (2022d). *Search for dark photons from Higgs boson decays via ZH production with a photon plus missing transverse momentum signature from pp collisions at* $\sqrt{s} = 13$ *TeV with the ATLAS detector.*

ATLAS Collaboration. (2022e). *TRIG-2022-01.* ATLAS trigger performance note.

ATLAS Collaboration. (2023). *ATL-DAPR-PUB-2023-001.* ATLAS public note.

ATLAS Collaboration. (2024a, May). The atlas experiment at the cern large hadron collider: a description of the detector configuration for run 3. *Journal of Instrumentation*, *19*(05), P05063. Retrieved from `http://dx.doi.org/10.1088/1748-0221/19/05/P05063` doi: 10.1088/1748-0221/19/05/p05063

ATLAS Collaboration. (2024b). *ATLAS Inner Tracker (ITk) Schematics.* Retrieved from `https://cds.cern.ch/record/2908925` (General Photo)

ATLAS Collaboration. (2024). Combination of searches for Higgs boson decays into a photon and a massless dark photon using pp collisions at $\sqrt{s}$= 13 TeV with the ATLAS detector. *JHEP*, *08*, 153. doi: 10.1007/JHEP08(2024)153

ATLAS Collaboration. (2024a, December). Measurement of the w-boson mass and width with the atlas detector using proton–proton collisions at

$$\sqrt{s} = 7$$

tev. *The European Physical Journal C*, *84*(12). Retrieved from `http://dx.doi.org/10.1140/epjc/s10052-024-13190-x` doi: 10.1140/epjc/s10052-024-13190-x

ATLAS Collaboration. (2024b, September). Search for dark mesons decaying to top and bottom quarks in proton-proton collisions at

$$\sqrt{\mathrm{s}}$$

= 13 tev with the atlas detector. *Journal of High Energy Physics*, *2024*(9). Retrieved from `http://dx.doi.org/10.1007/JHEP09(2024)005` doi: 10.1007/jhep09(2024)005

ATLAS Collaboration. (2024). *Software and computing for Run 3 of the ATLAS experiment at the LHC.*

ATLAS Collaboration. (2025). *Atlas public plots — 2025 data summary: mu_run123.* Retrieved 2025-11-18, from `https://atlas.web.cern.ch/Atlas/GROUPS/DATAPREPARATION/PublicPlots/2025/DataSummary/figs/mu_run123.pdf` (Online image; ATLAS Data Preparation Public Plots)

ATLAS Collaboration. (2025). *ATL-DAPR-PUB-2025-001.* ATLAS public note.

ATLAS Collaboration. (2025, June). The performance of missing transverse momentum reconstructionand its significance with the atlas detector using 140 fb$^{-1}$ of $\sqrt{s} = 13$ tev pp collisions. *The European Physical Journal C*, *85*(6). Retrieved from `http://dx.doi.org/10.1140/epjc/s10052-025-14062-8` doi: 10.1140/epjc/s10052-025-14062-8

ATLAS Collaboration. (2026). Transforming jet flavour tagging at ATLAS . *Nature Communications*, *17*. doi: 10.1038/s41467-025-65059-6

Avoni, G., et al. (2018). The new lucid-2 detector for luminosity measurement and monitoring in atlas. *JINST*, *13*(07), P07017. doi: 10.1088/1748-0221/13/07/P07017

Bähr, M., et al. (2008). Herwig++ physics and manual. *Eur. Phys. J. C*, *58*, 639. doi: 10.1140/epjc/s10052-008-0798-9

Ball, R. D., et al. (2013a). Parton distributions with LHC data. *Nucl. Phys. B*, *867*, 244. doi: 10.1016/j.nuclphysb.2012.10.003

Ball, R. D., et al. (2013b). Parton distributions with LHC data. *Nucl. Phys. B*, *867*, 244–289. doi: 10.1016/j.nuclphysb.2012.10.003

Ball, R. D., et al. (2015). Parton distributions for the LHC run II. *JHEP*, *04*, 040. doi: 10.1007/JHEP04(2015)040

Ball, R. D., et al. (2022). The path to proton structure at 1 percent accuracy. *Eur. Phys. J. C*, *82*, 428. doi: 10.1140/epjc/s10052-022-10328-7

Balunas, W., et al. (2024). Machine-learning-based reconstruction of missing transverse momentum in ATLAS. *JINST*, *19*, P05073. doi: 10.1088/1748-0221/19/05/P05073

Bärnreuther, P., Czakon, M., & Mitov, A. (2012). Percent-Level-Precision Physics at the Tevatron: Next-to-Next-to-Leading Order QCD Corrections to $q\bar{q} \to t\bar{t} + X$. *Phys. Rev. Lett.*, *109*, 132001. doi: 10.1103/PhysRevLett.109.132001

Begel, M., & Sankey, D. (2021). *System Specification for the Global Trigger* (Tech. Rep.). Geneva: CERN. Retrieved from `https://cds.cern.ch/record/2791119`

Bellm, J., et al. (2016). Herwig 7.0/Herwig++ 3.0 release note. *Eur. Phys. J. C*, *76*(4), 196. doi: 10.1140/epjc/s10052-016-4018-8

Beneke, M., Falgari, P., Klein, S., & Schwinn, C. (2012). Hadronic top-quark pair production with NNLL threshold resummation. *Nucl. Phys. B*, *855*, 695-741. doi: 10.1016/j.nuclphysb.2011.10.021

Bierlich, C., Chakraborty, S., Desai, N., Gellersen, L., Helenius, I., Ilten, P., ... Verheyen, R. (2022). *A comprehensive guide to the physics and usage of pythia 8.3.* arXiv. Retrieved from `https://arxiv.org/abs/2203.11601` doi: 10.48550/ARXIV.2203.11601

Bierlich, C., et al. (2022). A comprehensive guide to the physics and usage of PYTHIA 8.3. *SciPost Phys. Codebases*, *8*, 1. doi: 10.21468/SciPostPhysCodeb.8

Biswas, S., Gabrielli, E., & Mele, B. (2022, July). Dark photon searches via higgs boson production at the lhc and beyond. *Symmetry*, *14*(8), 1522. doi: 10.3390/sym14081522

Bothmann, E., et al. (2019). Event generation with Sherpa 2.2. *SciPost Phys.*, *7*(3), 034. doi: 10.21468/SciPostPhys.7.3.034

Botje, M., Butterworth, J., Cooper-Sarkar, A., de Roeck, A., Feltesse, J., Forte, S., ... Thorne, R. (2011). *The pdf4lhc working group interim recommendations.* arXiv. doi: 10.48550/ARXIV.1101.0538

Buccioni, F., Lang, J.-N., Lindert, J. M., Maierhöfer, P., Pozzorini, S., Zhang, H., & Zoller, M. F. (2019). OpenLoops 2. *Eur. Phys. J. C*, *79*(10), 866. doi: 10.1140/epjc/s10052-019-7306-2

Butterworth, J. M., Corpe, L., Kong, X., Kulkarni, S., & Thomas, M. (2022). New sensitivity of LHC measurements to composite dark matter models. *Phys. Rev. D*, *105*(1), 015008. doi: 10.1103/PhysRevD.105.015008

Cacciari, M. (n.d.). FastJet: A Code for fast $k_t$ clustering, and more. In *Proceedings, Deep inelastic scattering, 14th International Workshop, DIS 2006* (p. 487-490).

Cacciari, M., Czakon, M., Mangano, M., Mitov, A., & Nason, P. (2012). Top-pair production at hadron colliders with next-to-next-to-leading logarithmic soft-gluon resummation. *Phys. Lett. B*, *710*, 612-622. doi: 10.1016/j.physletb.2012.03.013

Cacciari, M., Salam, G. P., & Soyez, G. (2008). The anti-$k_t$ jet clustering algorithm. *JHEP*, *04*, 063. doi: 10.1088/1126-6708/2008/04/063

Cacciari, M., Salam, G. P., & Soyez, G. (2012). FastJet user manual. *Eur. Phys. J. C*, *72*, 1896. doi: 10.1140/epjc/s10052-012-1896-2

Carloni, L., & Sjöstrand, T. (2010, September). Visible effects of invisible hidden valley radiation. *Journal of High Energy Physics*, *2010*(9). Retrieved from http://dx.doi.org/10.1007/JHEP09(2010)105 doi: 10.1007/jhep09(2010)105

Carrazza, S., Forte, S., Kassabov, Z., Latorre, J. I., & Rojo, J. (2015). An unbiased Hessian representation for Monte Carlo PDFs. *Eur. Phys. J. C*, *75*(8), 369. doi: 10.1140/epjc/s10052-015-3590-7

Cascioli, F., Maierhöfer, P., & Pozzorini, S. (2012). Scattering Amplitudes with Open Loops. *Phys. Rev. Lett.*, *108*, 111601. doi: 10.1103/PhysRevLett.108.111601

Catani, S., Krauss, F., Webber, B. R., & Kuhn, R. (2001). QCD Matrix Elements + Parton Showers. *JHEP*, *11*, 063. doi: 10.1088/1126-6708/2001/11/063

CDF Collaboration. (1995, Apr). Observation of top quark production in $\overline{p}p$ collisions with the collider detector at fermilab. *Phys. Rev. Lett.*, *74*, 2626–2631. Retrieved from https://link.aps.org/doi/10.1103/PhysRevLett.74.2626 doi: 10.1103/PhysRevLett.74.2626

CDF Collaboration. (2022). High-precision measurement of the ¡i¿w¡/i¿ boson mass with the cdf ii detector. *Science*, *376*(6589), 170-176. Retrieved from https://www.science.org/doi/abs/10.1126/science.abk1781 doi: 10.1126/science.abk1781

CERN. (2004). *LHC Design Report*. Geneva: CERN. Retrieved from https://cds.cern.ch/record/782076 doi: 10.5170/CERN-2004-003-V-1

CERN. (2017). *High-Luminosity Large Hadron Collider (HL-LHC)*. Geneva: CERN. Retrieved from `https://cds.cern.ch/record/2284929` doi: 10.23731/CYRM-2017-004

CMS Collaboration. (2008). The CMS Experiment at the CERN LHC. *JINST*, *3*, S08004. doi: 10.1088/1748-0221/3/08/S08004

CMS Collaboration. (2012). Observation of a new boson at a mass of 125 GeV with the CMS experiment at the LHC. *Phys. Lett. B*, *716*, 30. doi: 10.1016/j.physletb.2012.08.021

CMS Collaboration. (2018). Search for high-mass resonances in dilepton final states in proton–proton collisions at $\sqrt{s} = 13\,\text{TeV}$. *JHEP*, *06*, 120. doi: 10.1007/JHEP06(2018)120

Corbelli, E., & Salucci, P. (2000). The extended rotation curve and the dark matter halo of m33. *Monthly Notices of the Royal Astronomical Society*, *311*(2), 441–447.

Cowan, G., Cranmer, K., Gross, E., & Vitells, O. (2011a). Asymptotic formulae for likelihood-based tests of new physics. *Eur. Phys. J. C*, *71*, 1554. doi: 10.1140/epjc/s10052-011-1554-0

Cowan, G., Cranmer, K., Gross, E., & Vitells, O. (2011b, February). Asymptotic formulae for likelihood-based tests of new physics. *The European Physical Journal C*, *71*(2). Retrieved from `http://dx.doi.org/10.1140/epjc/s10052-011-1554-0` doi: 10.1140/epjc/s10052-011-1554-0

Czakon, M., Fiedler, P., & Mitov, A. (2013). Total Top-Quark Pair-Production Cross Section at Hadron Colliders Through $O(\alpha_S^4)$. *Phys. Rev. Lett.*, *110*, 252004. doi: 10.1103/PhysRevLett.110.252004

Czakon, M., Heymes, D., Mitov, A., Pagani, D., Tsinikos, I., & Zaro, M. (2017). Top-pair production at the LHC through NNLO QCD and NLO EW. *JHEP*, *10*, 186. doi: 10.1007/JHEP10(2017)186

Czakon, M., & Mitov, A. (2012). NNLO corrections to top-pair production at hadron colliders: the all-fermionic scattering channels. *JHEP*, *12*, 054. doi: 10.1007/JHEP12(2012)054

Czakon, M., & Mitov, A. (2013). NNLO corrections to top pair production at hadron colliders: the quark-gluon reaction. *JHEP*, *01*, 080. doi: 10.1007/JHEP01(2013)080

Czakon, M., & Mitov, A. (2014). Top++: A program for the calculation of the top-pair cross-section at hadron colliders. *Comput. Phys. Commun.*, *185*, 2930. doi: 10.1016/j.cpc.2014.06.021

D0 Collaboration. (1995, Apr). Observation of the top quark. *Phys. Rev. Lett.*, *74*, 2632–2637. Retrieved from `https://link.aps.org/doi/10.1103/PhysRevLett.74.2632` doi: 10.1103/PhysRevLett.74.2632

de Florian, D., et al. (2016). *Handbook of LHC Higgs Cross Sections: 4. Deciphering the Nature of the Higgs Sector.* doi: 10.23731/CYRM-2017-002

Denner, A., Dittmaier, S., & Hofer, L. (2017). COLLIER: A fortran-based complex one-loop library in extended regularizations. *Comput. Phys. Commun.*, *212*, 220-238. doi: 10.1016/j.cpc.2016.10.013

Dominguez, D. (2015). *Standard Model.* urlhttps://cds.cern.ch/record/2002395. Retrieved from `https://cds.cern.ch/record/2002395` (CERN Document Server record)

Evans, L., & Bryant, P. (2008). LHC Machine. *JINST*, *3*, S08001. doi: 10.1088/1748-0221/3/08/S08001

Frederix, R., Pagani, D., & Zaro, M. (2018). Large NLO corrections in $t\bar{t}W^{\pm}$ and $t\bar{t}t\bar{t}$ hadroproduction from supposedly subleading EW contributions. *JHEP*, *02*, 031. doi: 10.1007/JHEP02(2018)031

Frederix, R., Re, E., & Torrielli, P. (2012). Single-top $t$-channel hadroproduction in the four-flavour scheme with POWHEG and aMC@NLO. *JHEP*, *09*, 130. doi: 10.1007/JHEP09(2012)130

Freund, Y., & Schapire, R. E. (1997). A decision-theoretic generalization of on-line learning and an application to boosting. *Journal of Computer and System Sciences*, *55*(1), 119-139. Retrieved from `https://www.sciencedirect.com/science/article/pii/S002200009791504X` doi: https://doi.org/10.1006/jcss.1997.1504

Frixione, S., Laenen, E., Motylinski, P., & Webber, B. R. (2007). Angular correlations of lepton pairs from vector boson and top quark decays in Monte Carlo simulations. *JHEP*, *04*, 081. doi: 10.1088/1126-6708/2007/04/081

Frixione, S., Laenen, E., Motylinski, P., White, C., & Webber, B. R. (2008). Single-top hadroproduction in association with a $W$ boson. *JHEP*, *07*, 029. doi: 10.1088/1126-6708/2008/07/029

Frixione, S., Nason, P., & Oleari, C. (2007). Matching NLO QCD computations with parton shower simulations: the POWHEG method. *JHEP*, *11*, 070. doi: 10.1088/1126-6708/2007/11/070

Frixione, S., Ridolfi, G., & Nason, P. (2007). A positive-weight next-to-leading-order Monte Carlo for heavy flavour hadroproduction. *JHEP*, *09*, 126. doi: 10.1088/1126-6708/2007/09/126

GEANT4 Collaboration, Agostinelli, S., et al. (2003). GEANT4 – a simulation toolkit. *Nucl. Instrum. Meth. A*, *506*, 250. doi: 10.1016/S0168-9002(03)01368-8

Gleisberg, T., & Höche, S. (2008). Comix, a new matrix element generator. *JHEP*, *12*, 039. doi: 10.1088/1126-6708/2008/12/039

Graesser, M. L. (2007). *Experimental constraints on higgs boson decays to tev-scale right-handed neutrinos.* Retrieved from `https://arxiv.org/abs/0705.2190`

Harland-Lang, L. A., Martin, A. D., Motylinski, P., & Thorne, R. S. (2015). Parton distributions in the LHC era: MMHT 2014 PDFs. *Eur. Phys. J. C*, *75*(5), 204. doi: 10.1140/epjc/s10052-015-3397-6

Hartanto, H. B., Jäger, B., Reina, L., & Wackeroth, D. (2015). Higgs boson production in association with top quarks in the POWHEG BOX. *Phys. Rev. D*, *91*(9), 094003. doi: 10.1103/PhysRevD.91.094003

Hatlo, M., James, F., Mato, P., Moneta, L., Winkler, M., & Zsenei, A. (2005). Developments of mathematical software libraries for the lhc experiments. *IEEE Trans. Nucl. Sci.*, *52*(6), 2818-2822. doi: 10.1109/TNS.2005.860152

Höche, S., Krauss, F., Schönherr, M., & Siegert, F. (2012). A critical appraisal of NLO+PS matching methods. *JHEP*, *09*, 049. doi: 10.1007/JHEP09(2012)049

Höche, S., Krauss, F., Schönherr, M., & Siegert, F. (2013). QCD matrix elements + parton showers. The NLO case. *JHEP*, *04*, 027. doi: 10.1007/JHEP04(2013)027

Höche, S., Krauss, F., Schumann, S., & Siegert, F. (2009). QCD matrix elements and truncated showers. *JHEP*, *05*, 053. doi: 10.1088/1126-6708/2009/05/053

Höche, S., Mrenna, S., Payne, S., Preuss, C. T., & Skands, P. (2022). A Study of QCD Radiation in VBF Higgs Production with Vincia and Pythia. *SciPost Phys.*, *12*(1), 010. doi: 10.21468/SciPostPhys.12.1.010

Hodkinson, B. (2023). *Enhancing the sensitivity of the atlas experiment to electroweak supersymmetry* (Doctoral dissertation, Apollo - University of Cambridge Repository). doi: 10.17863/CAM.104677

Horstmann, M., & Past, V. (2025, January). *Metnet - z mumu data and plots with the performance framework.* Retrieved from URL_TO_THE_PDF_IF_AVAILABLE (Presentation slides)

Hu, W., & Dodelson, S. (2002, September). Cosmic microwave background anisotropies. *Annual Review of Astronomy and Astrophysics*, *40*(1), 171–216. Retrieved from http://dx.doi.org/10.1146/annurev.astro.40.060401.093926 doi: 10.1146/annurev.astro.40.060401.093926

Ježo, T. (2019). *Powheg-box-res ttbb source code.* Retrieved from https://gitlab.cern.ch/tjezo/powheg-box-res_ttbb/

Ježo, T., Lindert, J. M., Moretti, N., & Pozzorini, S. (2018). New NLOPS predictions for $t\bar{t} + b$-jet production at the LHC. *Eur. Phys. J. C*, *78*(6), 502. doi: 10.1140/epjc/s10052-018-5956-0

Kasieczka, G., Nachman, B., Schwartz, M., & Shih, D. (2021, 02). Automating the abcd method with machine learning. *Physical Review D*, *103*. doi: 10.1103/PhysRevD.103.035021

Kribs, G. D., Martin, A., Ostdiek, B., & Tong, T. (2019). Dark Mesons at the LHC. *JHEP*, *07*, 133. doi: 10.1007/JHEP07(2019)133

Kribs, G. D., Martin, A., & Tong, T. (2019a). Effective Theories of Dark Mesons with Custodial Symmetry. *JHEP*, *08*, 020. doi: 10.1007/JHEP08(2019)020

Kribs, G. D., Martin, A., & Tong, T. (2019b, aug). Effective theories of dark mesons with custodial symmetry. *Journal of High Energy Physics*, *2019*(8). Retrieved from https://doi.org/10.1007%2Fjhep08%282019%29020 doi: 10.1007/jhep08(2019)020

Kribs, G. D., & Neil, E. T. (2016a). Review of strongly-coupled composite dark matter models and lattice simulations. *Int. J. Mod. Phys. A*, *31*(22), 1643004. doi: 10.1142/S0217751X16430041

Kribs, G. D., & Neil, E. T. (2016b, August). Review of strongly-coupled composite dark matter models and lattice simulations. *International Journal of Modern Physics A*, *31*(22), 1643004. Retrieved from http://dx.doi.org/10.1142/S0217751X16430041 doi: 10.1142/s0217751x16430041

Lange, D. J. (2001). The EvtGen particle decay simulation package. *Nucl. Instrum. Meth. A*, *462*, 152. doi: 10.1016/S0168-9002(01)00089-4

Lattice Strong Dynamics (LSD) Collaboration. (2015). Stealth Dark Matter: Dark scalar baryons through the Higgs portal. *Phys. Rev. D*, *92*(7), 075030. doi: 10.1103/PhysRevD.92.075030

LHCb Collaboration. (2008). The LHCb Detector at the LHC. *JINST*, *3*, S08005. Retrieved from `https://cds.cern.ch/record/1129809` (Also published by CERN Geneva in 2010) doi: 10.1088/1748-0221/3/08/S08005

Martin, A. D., Stirling, W. J., Thorne, R. S., & Watt, G. (2009). Parton distributions for the LHC. *Eur. Phys. J. C*, *63*, 189. doi: 10.1140/epjc/s10052-009-1072-5

Massey, R., Kitching, T., & Richard, J. (2010, July). The dark matter of gravitational lensing. *Reports on Progress in Physics*, *73*(8), 086901. Retrieved from `http://dx.doi.org/10.1088/0034-4885/73/8/086901` doi: 10.1088/0034-4885/73/8/086901

Mrenna, S., & Skands, P. (2016). Automated parton-shower variations in PYTHIA 8. *Phys. Rev. D*, *94*, 074005. doi: 10.1103/PhysRevD.94.074005

Nachman, B., Nef, P., Schwartzman, A., Swiatlowski, M., & Wanotayaroj, C. (2015, feb). Jets from jets: re-clustering as a tool for large radius jet reconstruction and grooming at the LHC. *JHEP*, *02*, 075. doi: 10.1007/jhep02(2015)075

Nason, P. (2004). A new method for combining NLO QCD with shower Monte Carlo algorithms. *JHEP*, *11*, 040. doi: 10.1088/1126-6708/2004/11/040

Ordonez Sanz, G. (2009). *Muon identification in the ATLAS calorimeters* (Unpublished doctoral dissertation). Nijmegen U., Nijmegen U.

Petersson, C., Romagnoni, A., & Torre, R. (2012, October). Higgs decay with monophoton + signature from low scale supersymmetry breaking. *Journal of High Energy Physics*, *2012*(10). Retrieved from `http://dx.doi.org/10.1007/JHEP10(2012)016` doi: 10.1007/jhep10(2012)016

Pierog, T., et al. (2015). EPOS LHC: Test of collective hadronization with LHC data. *Phys. Rev. C*, *92*, 034906. doi: 10.1103/PhysRevC.92.034906

Pumplin, J., et al. (2002). New Generation of Parton Distributions with Uncertainties from Global QCD Analysis. *JHEP*, *07*, 012. doi: 10.1088/1126-6708/2002/07/012

Re, E. (2011). Single-top $Wt$-channel production matched with parton showers using the POWHEG method. *Eur. Phys. J. C*, *71*, 1547. doi: 10.1140/epjc/s10052-011-1547-z

Read, A. L. (2002). Presentation of search results: the $CL_S$ technique. *J. Phys. G*, *28*, 2693. doi: 10.1088/0954-3899/28/10/313

Rubin, V. C., Ford, W. K., Jr., & Thonnard, N. (1980, June). Rotational properties of 21 SC galaxies with a large range of luminosities and radii, from NGC 4605 (R=4kpc) to UGC 2885 (R=122kpc). *ApJ*, *238*, 471-487. doi: 10.1086/158003

Schumann, S., & Krauss, F. (2008). A parton shower algorithm based on Catani–Seymour dipole factorisation. *JHEP*, *03*, 038. doi: 10.1088/1126-6708/2008/03/038

Sjöstrand, T., Ask, S., Christiansen, J. R., Corke, R., Desai, N., Ilten, P., ... Skands, P. Z. (2015). An introduction to PYTHIA 8.2. *Comput. Phys. Commun.*, *191*, 159. doi: 10.1016/j.cpc.2015.01.024

Sjöstrand, T., Mrenna, S., & Skands, P. (2008). A brief introduction to PYTHIA 8.1. *Comput. Phys. Commun.*, *178*, 852-867. doi: 10.1016/j.cpc.2008.01.036

Suematsu, D. (1998, February). Neutralino decay in the mu problem solvable extra u(1) models. *Physical Review D*, *57*(3), 1738–1754. Retrieved from `http://dx.doi.org/10.1103/PhysRevD.57.1738` doi: 10.1103/physrevd.57.1738

The ALICE Collaboration. (2008, aug). The alice experiment at the cern lhc. *Journal of Instrumentation*, *3*(08), S08002. Retrieved from `https://doi.org/10.1088/1748-0221/3/08/S08002` doi: 10.1088/1748-0221/3/08/S08002

The ATLAS Collaboration. (2016, jun). The atlas data acquisition and high level trigger system. *Journal of Instrumentation*, *11*(06), P06008. Retrieved from `https://doi.org/10.1088/1748-0221/11/06/P06008` doi: 10.1088/1748-0221/11/06/P06008

Tommasini, D. (2010). *The PS Booster, PS and SPS Magnets for the next 25 years.* urlhttps://cds.cern.ch/record/1233948. Retrieved from `https://cds.cern.ch/record/1233948` (Available at: urlhttps://cds.cern.ch/record/1233948)

Vanden Broeck, R. (2019). *The cern accelerator complex (complexe des accélérateurs du cern)* (Tech. Rep.). CERN. Retrieved from `https://cds.cern.ch/record/2693837` (CERN Document Server record 2693837)

Verkerke, W., & Kirkby, D. (2003). *The RooFit toolkit for data modeling.*

Vogelsberger, M., Marinacci, F., Torrey, P., & Puchwein, E. (2020, January). Cosmological simulations of galaxy formation. *Nature Reviews Physics*, *2*(1), 42-66. doi: 10.1038/s42254-019-0127-2

Werner, K., et al. (2006). Parton ladder splitting and the rapidity dependence of transverse momentum spectra in deuteron-gold collisions at RHIC. *Phys. Rev. C*, *74*, 044902. doi: 10.1103/PhysRevC.74.044902